On the Development of Praseodymium-Doped Radioluminescent Nanoparticles and Their Use In X-ray Mediated Photodynamic Therapy Of Glioblastoma Cells

Gabrielle Mandl

A Thesis
in
The Department
of
Chemistry and Biochemistry

Presented in Partial Fulfillment of the Requirements
for the Degree of Doctor of Philosophy (Chemistry) at
Concordia University
Montréal, Québec, Canada

March 2023

CONCORDIA UNIVERSITY

SCHOOL OF GRADUATE STUDIES

This is to certify that the thesis prepared

By: Gabrielle Mandl

Entitled: On the Development of Praseodymium-Doped Radioluminescent Nanoparticles and Their Use in X-ray Mediated Photodynamic Therapy of Glioblastoma Cells

and submitted in partial fulfillment of the requirements for the degree of

Doctor Of Philosophy (Chemistry)

complies with the regulations of the University and meets the accepted standards with respect to originality and quality.

Signed by the final examining committee:

_____ Chair
Dr. William Bukowski

_____ External Examiner
Dr. Jean-Claude Bünzli

_____ External to Program
Dr. Yves Gelinas

_____ Examiner
Dr. Rafik Naccache

_____ Examiner
Dr. Ashlee Howarth

_____ Thesis Supervisor
Dr. John Capobianco

Approved by

_____
Dr. Louis Cuccia, Graduate Program Director

April 28, 2023

_____
Dr. Pascale Sicote, Dean (Faculty of Arts and Science)

ABSTRACT

On the Development of Praseodymium-Doped Radioluminescent Nanoparticles and Their Use in X-ray Mediated Photodynamic Therapy of Glioblastoma Cells

Gabrielle Mandl, PhD
Concordia University, 2023

Despite decades of research, few advancements have been made toward improving the prognosis of patients with glioblastoma, a lethal and invasive form of brain cancer. The current standard of care is fluorescence-guided surgical resection followed by radiotherapy and chemotherapy. Fluorescence guided surgery is performed using 5-aminolevulinic acid (5-ALA), a prodrug that induces the accumulation of fluorescent protoporphyrin IX (PPIX) in malignant cells. Conveniently, 5-ALA mediated production of PPIX is also renowned as the most popular photodynamic therapy (PDT) agent in the world. PDT is a treatment that uses visible light to stimulate a photosensitizer to produce reactive oxygen species, which can damage and kill cells. However, the technique is limited by the tissue depth penetration of light. The advent of nanomedicine has enabled the possibility to achieve PDT by using luminescent nanoparticles to alter the incident excitation source. When X-rays are used to excite the nanoparticles, the process is called X-ray mediated photodynamic therapy (X-PDT).

Herein, we have developed $NaLuF_4:Pr^{3+}$ radioluminescent nanoparticles to achieve X-PDT. The emission spectrum of Pr^{3+} exhibits strong spectral overlap with the absorption spectrum of PPIX, an endogenous photosensitizer. A reproducible route to synthesizing uniform $NaLuF_4:Pr^{3+}$ nanoparticles at sizes relevant for cell uptake was developed, and the spectroscopic properties of the nanoparticles were evaluated prior to *in vitro* studies. The nanoparticles were found to exhibit persistent luminescence, and a mechanism was developed to explain the charge (de-)trapping process. The nanoparticle composition was optimized for excitation of PPIX and studied in the human glioblastoma cell line called U251. We evaluated the therapeutic effect of the nanoparticles with and without 5-ALA to establish the radiosensitization capability as well as the X-PDT effect. Three nanoparticle concentrations were studied using 4 radiation doses, including those relevant for intraoperative radiotherapy which is performed on the tumor cavity immediately after resection. The

effects on stress, death, damage, senescence and proliferation were studied. and demonstrate promising results at a proof-of-concept level. Throughout this work, current clinical practice guided our experimental design, providing a strong foundation toward using Pr^{3+}-doped nanoparticles for X-PDT in an intraoperative setting using endogenous PPIX as the photosensitizer.

“Art is I, science is we.” – Claude Bernard

Acknowledgements

Words cannot describe how grateful I am to everyone who has participated in this journey of mine. I will do my best to write it down, but there is simply nothing I can say that would convey my appreciation and deep respect for all of you. If you know me well, you won't be surprised that this acknowledgement is going to be many, many pages long.

To my incredible mother, you have gone above and beyond toward helping me reach this goal. I am so honored to be your daughter, I picked incredibly well. I hope you know how much I love you, and how much your support has meant to me each and every day. This thesis is a testament to your hard work and your unwavering love for me, it would not exist otherwise. Cheers to you my beautiful momma, we did it.

Boss, I don't know how to describe how much your guidance and support has meant to me. You have been so much more to me than just a supervisor over the past 8 years. I know my dad is watching us and is grateful to you for the role you have played in my life. Thank you for taking a chance on me when so many told you not to. Thank you for believing in me when I didn't believe in myself. Thank you for bringing me into the incredible research we do, and thank you for teaching me all of the aspects behind the scenes that go into making the research possible. You have changed my life profoundly, and I am so proud to be your student. You have thoroughly ruined anyone else's chances of being my favorite mentor and role model, I have no idea how I will ever work for another boss. I promise I will never become a common garden vegetable, and I will continue cooking with gas.

To my committee members, Professor Ashlee Howarth and Professor Rafik Naccache, thank you for your time and support during my graduate studies. To Professor Jean-Claude Bünzli and Professor Yves Gelinas, thank you so much for being part of this final chapter as my external committee members. You have each impacted my life in different ways beyond being simple committee members, as you'll see below.

Professor Howarth, thank you for being a role model to female scientists everywhere, your success and drive have inspired me tremendously. Also, thank you for teaching me about the power of social media in academia, it has opened doors I couldn't imagine existed. Thank you for also

introducing me to MOFs and their beauty, unravelling their radioluminescent properties was a highlight of my time as a grad student. Finally, thank you for advocating for the well-being of graduate students, I am glad to know there is always someone in our corner.

Rafik, I don't even know where to begin. WBTY truly no one. I still have the (unused) Kleenex you passed me after my CHEM 450 presentation in my undergrad that says "not bad" on it. Thank you for helping me become stronger mentally, I am no longer the cry-on-command girl I was when we first met, and you have been a big part of that. Thank you for failing me on the midterm in CHEM 498 when I correctly answered a question that was not even being asked. That experience taught me to be okay with failure, and to forgive myself for it and move forward regardless. Thank you for showing me there's a place in academia for metal-heads, that fountain pens are truly the GOAT, and that dry humor works in almost every situation. If I turn out to be half as great of a mentor and scientist as you are, I will be anti-Stoked.

Professor Bünzli, I still cannot believe you are reading my thesis; I am so incredibly honored and grateful for your time. For the past 8 years, I have always turned to your words for guidance, you have influenced this thesis more than you know. Thank you for all of your contributions to science, and to making the complex nature of lanthanide luminescence accessible to anyone who is interested in learning about it.

Yves, you have always been such a bright light in a very stressful world. Thank you for helping me get my NSERC MSc award all of those years ago, I know it was your edits that made me successful. Thank you for being a constant source of peace, and for always helping me in your capacity as GPD and my capacity as president, we made a great team. I appreciate you so much for taking the time to read my thesis and be part of my defence, I know you are doing it despite having 100000x other things on your plate at all times. Please never change, you are a gift to everyone who is lucky enough to cross paths with you.

To Philippe Smet, David Van der Heggen and Jonas Joos, my incredible collaborators. Thank you for teaching me everything there is to know about persistent luminescence, for all of your time and efforts on this project, and for putting up with my enthusiasm at all hours of the day. I am in awe of each of you, and I appreciate you taking the time you did to help morph me into a persistent

luminescence girl. Also thank you for letting me keep the LOLs, despite it being a very silly acronym.

To Ursula Stochaj, thank you for taking me under your wing these past few years as my biology mentor and collaborator. I have learned so much from you, both academically and professionally. Thank you for always pushing me to be thorough, careful, and precise. I cherish all of the moments we have shared, and I am so glad I got to be the one to start working with you and Dana all of those years ago. To Kais, thank you for showing me the beauty of statistics, and the wisdom of silence. You both have been so patient with me, and I am more grateful than I know how to convey.

To my incredible labmates, past and present, thank you for making research everything I ever wished it would be. It is the environment each of you cultivated that enabled me to become comfortable and blossom throughout this experience. To Rachel Hall, who introduced me to Professor Capobianco, I am forever indebted to you for literally changing my life and putting me on this path. To Diana, Suraj, Tarek, Gaurav, Devesh, Tang, Anne, Laura and Pedro, thank you for putting up with me at all times, and for laughing and crying with me. To Maddie and Kyle, thank you for taking a chance as undergrads and joining the lab with me. I loved every moment and I am grateful to call you my friends.

To Mannu Kaur, I thank you for being an incredible labmate and friend. Thank you for always being there to help me, and for being a calm presence in a chaotic world. Your humility, perseverance and kindness inspires me to be better every day. I am so grateful to have done grad school at the same time as you and to spend time with you almost everyday.

To Paola Rojas-Gutierrez, my first mentor. Paola, you are an angel, you have been like a big sister to me. Thank you for all of the time you spent teaching me how to do research, and for introducing me to the beauty of azobenzene and cell culture. Thank you for putting up with me as an undergrad, especially for the time I accidentally filled your acetone bottle with acetonitrile (I don't know if I ever told you the truth about this haha!) and ruined a column you were teaching me to run. Thank you for all of the times you held me when I cried, you have always been there for me when I needed you and that is a gift I am forever grateful for. I cherish every memory we share: BFZ, molletes, making videos for your parents, lunches at Bano, our roadtrip through the Canadian

Rockies, the buckle song, you name it. Besitos doritos, always and forever. Thank you for always loving me for who I am, even though I am infinitely more of a couch potato than you are.

To Gabriella Tessitore, you too have been like a big sister to me…between you and Paola, I am set! Gabs, I have never knew such an unapologetically smart, talented, strong, funny and deeply kind person could exist. You are an enigma, and I love every bit of you. Thank you for teaching me that it is okay to be silly, even when everything is hard and stressful and serious. Thank you for always being honest and reliable. I am so grateful for your commitment to helping me become a scientist, and for your love and time and support. I am so proud to know you, to work with you and to call you my friend. You are my hero.

To Steven Maurizio, my bear. I cherish every single time we have ever screamed at each other. I cherish every single tear you have made me shed in frustration. I cherish every snarky comment, every piercing insult. I don't know who I would be if I had never met you. I love you so much, and to be honest I didn't cry for any of these until I started writing to you….that's how much you mean to me. Thank you for being confidently wrong, and in doing so, teaching me to trust myself. Thank you for answering every question I have, even at the most inopportune times, I trust your judgement implicitly. Thank you for dealing with my constant messes. You are the brother I never had, and I am committed to haunting you for the rest of your life.

To Freesia Vettier, my partner in crime. We are two peas in a pod, the perfect balance of everything good and bad on this earth. Fridgey, I love you with my whole entire soul, I could not have survived grad school without you. Thank you for taking a chance on me, thank you for loving me unconditionally and supporting me at every opportunity. There has not been a single day in four years that we haven't spoken at least once, that is how much I rely on you. Your strength, bravery, humility, and innocence are refreshing and inspiring. Your willingness to try anything you want to try, even if it might be embarrassing, is amazing to me. I am in awe of how hard you have worked, and how you do it with grace even when you are at your worst. I will continue to strive to be the person you see in me, and I thank you for reminding me that she exists.

To my Aunt Suzy, Aunt Huguette and Uncle Jacques, I am grateful for your constant love and praise. I am so lucky to have aunts and uncles that are there for me at a moment's notice, for the good and the bad. I love you all so much and I am proud to be your niece. To my Aunt Nan and

Uncle Pete, I am so blessed to have you in my life. I never imagined we would be so close and I know my dad is so happy we are. Thank you for your constant encouragement and unwavering love.

To my grandfather, Laszlo Mandl, besides my mom, I don't think there is anyone that makes me feel more special. I am so grateful for the bond we share, and I am so glad I moved to Montreal and got to become close to you. Thank you for being one of my biggest fans and believing I could do this. I am so proud to be a Mandl.

To my oldest friend, Kendra Byrd. The little girls dressed as pirates on Halloween probably never imagined we'd be here now. We were barely out of diapers when we met, you have been there for every single stage of my life. Every milestone. Every tragedy. And somehow, you willingly stayed. I love you so much, thank you for helping me become Dr. Mandl.

To my sweet Daliah Farajat and Cynthia Messina. We are family. I trust you both with my life. Thank you for loving me unconditionally, and for treasuring me as I am. There aren't words for the part of my soul you belong to. Thank you for everything, from the bottom of my heart. I truly believe part of the reason I ended up in Montreal was so that we would meet. You are forever inscribed in the story of my life and my success would not be possible without you both. Chris Liczner, with you, the tetramer is completed, and I am so grateful for our little team. You've had my back since ABACUS in 2014, and it's been an absolute dream growing up together. Thank you.

To Jackie Shapiro Grinberg, one of the best friends I've ever had. I feel so lucky that out of everyone, you chose me. You are everything I want to be, and I am so inspired and motivated by you. Thank you for being patient with me, and for never giving up on me despite all of the times I cancelled on you. Thank you for showing me what it means to love and respect yourself. I am in awe of the life you have made for yourself, and how you have handled every challenge thrown your way. Watching you become a wife and mother has been one of the great joys of my life. To Daniel, thank you for showing me that there are real, wonderful men in this world and that I am deserving of a partner who will treat me the way you treat Jackie. I can't wait to hear all of your dad jokes. I love you both tremendously, thank you for supporting me on this journey.

To Anic Imfeld, thank you for showing me the importance of family, and that there is always a way if you try hard enough and wait long enough. Thank you for all of the dark humor, I never felt

alone during grad school because I knew you were right there with me. From the CBGRC to COVID, we have grown so much together, I am so lucky to have you in my life. Thank you for making sure Yves doesn't rip his eyes out when he reads the mass spec part of my thesis. To Jeremy, much like Daniel, you have shown me what a good partner should be. Thank you for loving Anic, and for putting up with me when Anic and I go overboard, and thank you for reminding us that grad school isn't all there is to life.

To Daniel Cooper, I owe you so much. It is because of your brilliance, guidance, patience, love and kindness that I was able to bring this project to life. Thank you for introducing me to radioluminescence, 5-ALA and praseodymium. It has been a more complicated ride than I could've ever imagined, but you gave me the foundation to pull through. Thank you for teaching me the importance of reading the literature, it is because of you that there are so many references in this thesis. Thank you for teaching me to ask as many questions as possible, and that it is okay to want to answer those questions, even if they are not flashy.

To Ms. Hilary Scuffell, the first person I ever met at Concordia. You have been like a mother to me, I am so grateful for your kindness and support over the past 11 years. This thesis exists in part because of your guidance and advice, which I will always treasure. Thank you for always looking out for me.

To Ms. Jennifer Sachs, you have become such an important role model, guide and friend to me. Thank you for showing me that it is okay to go above and beyond, and that the right people will appreciate it. You are one of the most thoughtful, resourceful, and loving people that I know. I feel so lucky to have been in grad school while you were here. Thank you for always being there for me, professionally and personally. Whereas Ms. Hilary is like a mom, you are like the cool aunt!

To Cerrie Rogers, you've been here for me every step of the way, from undergrad to now. I aspire to be everything you are, kind, funny, humble, clever, and real. Thank you for giving me the opportunity to discover and pursue my love of teaching, and for showing me that even the most incredible people are human too. And to Xavier Ottenwaelder, you have also taught me so much. Thank you for all of your incredible insights, for understanding that sometimes traditional teaching doesn't work for me, and for believing in my potential anyways. Thank you both for letting me into

your home and giving me the chance to spend time with Chloe and Liam, they have been a great source of joy and comfort to me throughout these years as well.

I am so blessed to have a truly incredible circle of people around me, who will give me just as much love and effort as I will give them. I treasure each of you tremendously, and this thesis would not be possible without you. To Jean-Louis Do, Adryanne Clermont-Paquette, Maria Elena Radu, Emma Shaver, Phil Prevost, Keegan McKibbon, Caroline Bergeron, and John Chin. Each of you have profoundly impacted my life academically and personally in the past few years and I am truly grateful.

Finally, I have kept a list of every person who has helped me and made this thesis possible in some way, in addition to those above. I am grateful to each of you for going out of your way to help me whether it was for an experiment or to help me grow. It truly does take a village.

Alain Tessier	David Kwan	Jeremy Hall	Neema Chirwa
Alex Kanso	Donna Craven	Judith Kornblatt	Nhat Pham
Alissa Piekny	Elvis Tzanetakos	Kevin Laroque	Nooshin Movahed
Angela Quach	Geoffrey Ozin	Louis Cuccia	Richard Ford
Cameron Skinner	Heidi Muchall	Paul Joyce	Sara Ouadhi
Chris Law	Heng Jiang	Marika Dochia	Suzanne Groulx
Christine DeWolf	Jan Seuntjens	Miriam Posner	Vincent Lau
Dan Duru	Jean-Philippe Masse	Mohamed Nasr	William Chicoine

Table of Contents

List of Figures

List of Tables

List of Abbreviations

5-ALA	5-aminolevulinic acid
ABCB6	ATP-binding cassette super-family B member 6
ABCG2	ATP-binding cassette super-family G member 2
AGuIX	Activation and Guidance of irradiation by X-ray
ALAD	Aminolevulinic acid dehydrogenase
ATM	Ataxia telangiectasia mutated
ATR	Ataxia telangiectasia and Rad3-related
AxV-FITC	Annexin V fluorescein isothiocyanate
BAX	Bcl-2 associated X protein
CB	Conduction band
CCD	charge coupled device
Cit/PLL	Citrate coated with poly-L-lysine
CNS	Central nervous system
CPO	Coproporphyrinogen oxidase
CT	computed tomography
DAMPs	Damage associated molecular patterns
DCF	Dichlorofluorescein
DCHF-DA	2',7'-Dichlorohydrofluorescein diacetate
DFT	Density functional theory
DIC	Differential imaging contrast
DLS	Dynamic light scattering
DMEM	Dulbecco's modified Eagle's medium
DMR	Dose modifying ratio
DNA	Deoxyribonucleic acid
DNA-PK	Deoxyribonucleic acid protein kinase
DOTA	(1,4,7,10-tetra-azacyclododecane-1-glutaric anhydride-4,7,10-triacetic acid)
DSB	Double strand break
EBRT	external beam radiotherapy
EDS	Energy dispersive spectroscopy
EGFR	Epidermal growth factor receptor
EMCCD	electron multiplying charge coupled device
EPR	Electron paramagnetic resonance
ET	energy transfer
EURATOM	European Atomic Energy Community
FACS	fluorescence activated cell sorting
FAD	Flavin adenine dinucleotide
FBS	fetal bovine serum
FDA	Food and Drug Administration (United States of America)
FECH	Ferrochelatase
FRET	Förster resonance energy transfer
FSC	side scatter
FT-IR-ATR	Fourier-transform infrared attenuated total reflectance
GBM	Glioblastoma multiforme
Grp78	Glucose related protein 78
Grp94	Glucose related protein 94
H2AX	Histone h2a family member X
HAADF	High angle annular dark field
HpD	Hematoporphyrin derivative
HRBE	Host referred binding energy
ICP-MS	Inductively-coupled plasma-mass spectrometry

ICRU	The International Commission on Radiation Units and Measurements
IDH	Isocitrate dehydrogenase
IORT	Intraoperative radiotherapy
iPDT	Interstitial photodynamic therapy
ISC	intersystem crossing
ISO	International Organization for Standardization
kVp	peak kilovoltage
LET	linear energy transfer
LEX-IORT	Low-energy X-ray intraoperative radiotherapy
LINAC	linear particle accelerator
LOL	Lower optical levels
LQ	Linear quadratic
MID	Mean inactivation dose
MOF	Metal-organic framework
MRI	Magnetic resonance imaging
MRN complex	MRE11, RAD50 and NBS1 complex
NA	numerical aperture
NAD	Nicotinamide adenine dinucleotide
NADPH	Nicotinamide adenine dinucleotide phosphate
NCL	Nanoparticle Characterization Laboratory at the National Institute of Health
MRN complex	MRE11, RAD50 and NBS1 complex
NfκB	Nuclear factor kappa-light-chain enhancer of activated B cells
NIR	Near infrared
NIST	National Institute of Standards and Technology
Nrf2	Nuclear factor erythroid 2–related factor 2
OA	Oleic acid
ODE	1-octadecene
OSL	optically-stimulated luminescence
PARP1	Poly-ADP-ribosylation-polymerase 1
SSC	Forward scatter
PBDG	Porphobilinogen deaminase
PBS	phosphate buffered saline
PCE	Photon cascade emission
PDF	Powder diffraction file
PDT	Photodynamic therapy
PE	Plating efficiency
PET	positron emission tomography
PI	Propidium iodide
PL	Photoluminescence
PLL	Poly-L-lysine
PPIX	Protoporphyrin IX
PPO	Protoporphyrinogen oxidase
PR	Power regression
PS	Photosensitizer
PTEN	Phosphatase and tensin homolog
PUMA	P53 upregulated mediator of apoptosis
PXRD	Powder X-ray diffraction
Rb	retinoblastoma protein
RE	Rare earth
RER	Radiation enhancement ratio
RL	Radioluminescence
RLNP	Radioluminescent nanoparticle
ROS	Reactive oxygen species
RPM	Rotations per minute
RS	Radiosensitizer
RTEL 1	Regulator of telomere elongation 1
SASP	senescence associated secretory phenotype
SER	Sensitizer enhancement ratio
SF	Survival fraction
SHMT	Single hit-multi-target
SHST	Single hit-single target

STE	Self-trapped exciton
STEM	Scanning transmission electron microscopy
TEM	Transmission electron microscopy
TERT	Telomerase reverse transcriptase
TL	Thermoluminescence
TP53	Tumor suppressor protein 53
TTI	Time to initiation
UPR	Unfolded protein response
URO3S	Uroporphyrinogen III synthase
UROD	Uroporphyrinogen III decarboxylase
VB	Valence band
VRBE	Vacuum referred binding energy
VUV	Vacuum ultraviolet
WBRT	whole brain radiotherapy
WHO	World Health Organization
X-PDT	X-ray mediated photodynamic therapy
YAG	$Y_3Al_5O_{12}$
γH2AX	phosphorylated histone h2a family member X

List of Symbols

I	Intensity
I_0	Initial intensity
μ	Linear attenuation coefficient
x	Path length
Z_{eff}	Effective atomic number
Z	Atomic number
E	Photon energy (equations 2 and 4)
	Energy of an electronic state (page 14)
	Activation energy (equation 5)
A	Atomic mass
τ	Photoelectric effect cross-section
σ	Compton scattering cross-section
κ	Pair production cross-section
η	Radioluminescence efficiency
B	Efficiency of electron-hole pair generation
S	Efficiency of host to activator energy transfer
	Total spin angular momentum
Q	Quantum efficiency
n_p	Number of electron-hole pairs produced by an incident ionizing photon
ξ	Average energy required to form an electron-hole pair
E_g	Electronic band gap energy
L	Total orbital angular momentum
s	Frequency factor
k	Boltzmann constant
T	Temperature
p	Probability
τ_e	Lifetime of a trapped electron
T_m	Maximum temperature
h^+	Hole

e^-	Electron
Ln^{3+}	Trivalent lanthanide ion
Ln^{2+}	Divalent lanthanide ion
$O_2^{\bullet-}$	Superoxide anion radical
$OH^{\bullet-}$	Hydroxyl radical
$^1O_2$	Singlet oxygen
R	Donor-acceptor distance
ϕ	Singlet oxygen yield
α	Cubic crystal phase
	Lethal single hit (equation 10)
β	Hexagonal crystal phase
	Sublethal component of linear quadratic equation (equation 10)
n	Number of electrons in a 4f orbital or 5d orbital
	number of hits (equations 11 and 12)
V_k	Self-trapped hole
λ	Wavelength
z	Depth as it pertains to microscopy images
D	Radiation dose delivered in a single fraction
D_0	Radiation dose that reduces survival to 1/*e* of previous value in the exponential portion of the dose response curve
$\overline{D}$	Mean inactivation dose

Chapter 1. Introduction

Complex challenges require creative solutions. With respect to modern medicine, this is especially true. Despite decades of progress and technological advancements, it is clear that there is no one-size-fits-all treatment for cancers like glioblastoma, where therapies are aggressive and yet the survival of most patients remains a year or two, at best. The advent of nanomedicine has brought forth the potential to develop unique routes to adjuvant therapies which were previously impractical or impossible to administer. X-ray mediated photodynamic therapy (X-PDT), is one such adjuvant treatment which combines radiotherapy and photodynamic therapy using a luminescent nanoparticle and a photosensitizer.[1–3] While X-PDT does indeed combine two highly established, currently used treatments, the road to the successful clinical implementation of nanoparticle-based X-PDT requires us to first understand the fundamental physicochemical properties of the nanoparticles, and their effects at the cellular level.

Herein, we set out to detail our efforts on the development of an X-PDT modality for the treatment of glioblastoma. First, the synthesis and spectroscopic properties of the nanoparticles are explored, providing a strong fundamental understanding of the luminescent properties of the nanoparticles. The second part of the work focuses on the biological studies undertaken using these nanoparticles to demonstrate an *in vitro* proof-of-concept for X-PDT. The multidisciplinary nature of this project requires solid foundational knowledge of nanochemistry, spectroscopy, radiobiology, medical physics, and the state-of-the-art of both clinical treatments of glioblastoma and the new nanoparticle-based treatments under development. This introduction aims to establish a basic foundation for the reader. Throughout this introduction, the reader is referred to several appendices which provide additional in-depth discussion on several topics that are relevant to the work presented herein and may be of interest.

Chapter 2. Introduction to lanthanide luminescence

2.1. On the interaction of ionizing radiation with matter

Ionizing radiation plays a key role in two aspects of X-PDT: radioluminescence (Section 2.2) and radiotherapy (Section 3.2.3). The general outcome of each aspect is quite different, but the physical principles are the same for both. First, we will detail how ionizing radiation interacts with matter and the properties which govern those mechanisms. We will then apply those principles to each of the above-mentioned aspects.

Ionizing radiation consists of photons or particles with sufficient energy to ionize an atom.[4,5] Interestingly, there is little consensus on the numerical threshold for the definition of ionizing radiation, even within the International Atomic Energy Agency.[6] Of practical interest for this work, however, we can define it to be a minimum photon energy of 12.4 eV (100 nm), in line with the EURATOM definition.[6] For the sake of relevance, we will restrict the discussion here to ionizing photons, with emphasis on X-rays in the keV energy range.

When a keV X-ray photon interacts with a material, energy is deposited in a two-step process, during which a cascade of events may occur.[7] The incident photon first transfers energy to an orbital electron, followed by energy deposition from the excited charged particle to the rest of the material and/or the surrounding medium. As shown in equation 1, X-ray attenuation by an absorber is related to the thickness of the material, x, and the linear attenuation coefficient, μ:

$$\boldsymbol{I = I_0 e^{-\mu x}} \quad (1)$$

Where I_0 and I are the initial and final X-ray intensities before and after the photon beam interacts with the material.[7] The linear attenuation coefficient, μ, is reported in units of cm^{-1} and is the probability as a function of distance (path length) that an X-ray photon will interact with the absorber. As shown in equation 2, μ is inversely proportional to the third power of the X-ray energy (E) and the atomic mass of the absorber (A). It is also proportional to the density of the absorber (ρ) and the fourth-power of the atomic number of the material, Z_{eff}.

$$\mu = \frac{\rho Z_{eff}{}^4}{E^3 A} \quad (2)$$

It became necessary to establish a means of estimating an atomic number (Z) for a composite material, since many ionizing radiation-matter interactions depend upon this property. As such, the effective atomic number, Z_{eff}, is used when the absorber is not a pure element with a characteristic Z. In many cases, Z_{eff} is colloquially referred to as Z when it is clear a multi-element material is being discussed. Z_{eff} can be calculated using a variety of methods, but most recently, there has been software developed to calculate it using photon cross-section data, and the Z_{eff} can be scaled according to the incident ionizing radiation source of interest.[8] The relationships between these variables are somewhat intuitive, and explain some of our experiences with X-ray-matter interactions. For example, high-energy X-rays can penetrate tissues more deeply than low-energy X-rays, and denser materials attenuate X-rays more efficiently. Combined, these interactions form the basis of X-ray radiography. The nature of the primary photon-matter interaction depends on the energy of the incident photon and the properties of the absorbing material. As shown in Figure 1A, there are three major types of interactions: the photoelectric effect, Compton scattering, and pair production.[5,7]

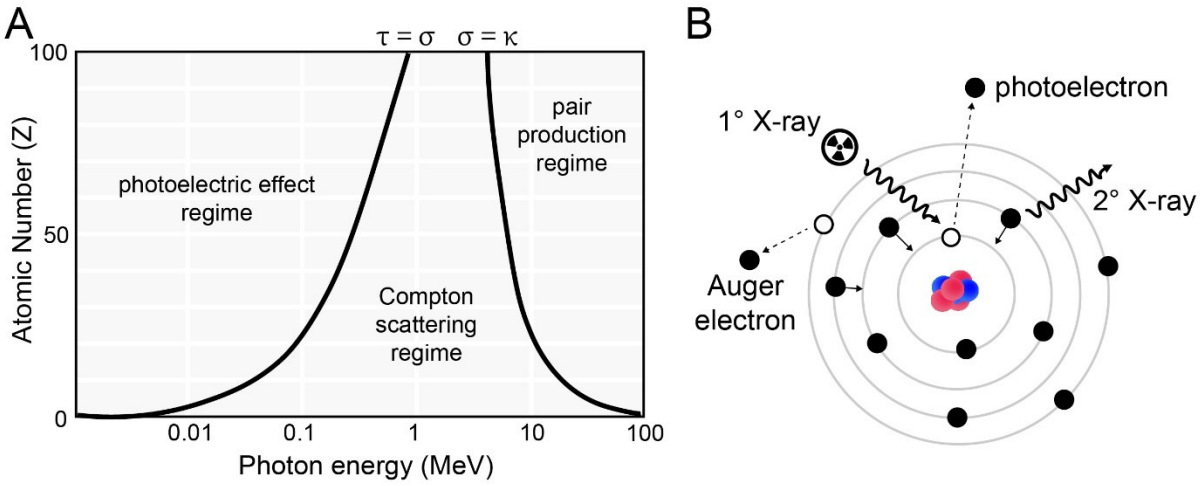

Figure 1. A) Graph of the different regimes of photon-matter interactions as a function of atomic number and photon energy. The curves represent the points at which the photoelectric effect (τ) cross-section is equivalent to the Compton scattering cross-section (σ) and where the Compton scattering and pair production (κ) cross-sections are equivalent. Adapted from References 5 and 7. B) Graphical depiction of the ejection of photoelectrons, Auger electrons and secondary X-rays upon interaction of an atom with ionizing radiation.

In the low-energy regime (up to a few hundred keV), interactions are dominated by the photoelectric effect. The middle range, from around 500 keV to 5 MeV, is dominated by Compton scattering, and finally pair-production is predominant in the high-energy regime. For the X-PDT system developed herein, we are particularly interested in the keV regime for several reasons:

- Intraoperative radiotherapy (IORT) for glioblastoma is performed using keV X-rays, as discussed in Section 3.3.2.[9]
- Physical radiosensitization occurs *via* the Auger effect, and is an effective means of inducing DNA damage (Section 3.4).[10] This is best achieved using high-density, high Z_{eff} materials.[11]
- The high density, high Z_{eff} materials that give rise to the Auger effect are also generally suitable for absorbing energy *via* the photoelectric effect and converting it into radioluminescence.[5]

As shown in Figure 1B, in the photoelectric effect, the energy of an incident X-ray photon is completely absorbed and causes the ejection of an electron (known as a photoelectron).[5,7] The vacancy left by the ejected photoelectron is then filled by a higher-energy electron. The energy equivalent to the binding energy of the ejected photoelectron is then emitted by the atom in the form of another electron (the Auger effect), or in the form of X-ray fluorescence.[7] The probability of the photoelectric effect to occur is inversely dependent on the photon energy ($1/E^3$) and approximately proportional to Z^3 of the absorber (Z_{eff} if it is a multi-element absorber).[1]

The secondary ionizations and X-ray photons generated can further interact with the surrounding medium and produce their own cascades, until all (or most) of the energy has been deposited and the cascade cannot continue. Finally, the deposited energy can result in radioluminescence, as discussed below, or in a biological effect, as discussed in Section 3.2.3. Compton scattering and pair production will not be discussed for the sake of relevance. The interested reader is referred to the textbook by Podgorsak[7] for discussions on the high-energy regime as it pertains to medical physics, and to the works by Blasse[12], and Lecoq[13] for this discussion in the context of radioluminescence.

2.2. Radioluminescence

Radioluminescence is the production of non-ionizing luminescence upon excitation with ionizing radiation.[14] Radioluminescence plays a role in a huge number of modern technologies. A class of radioluminescent materials, known as scintillators, are used in many applications, from detectors for medical imaging, to deep-space astrophysics, to nuclear weapons detection, among others.[13,15–18] Traditionally, an ideal scintillator is grown as a single crystal, and possesses extremely fast decay times (on the order of ps), thus not all radioluminescent materials fit that classification (especially those that take advantage of the forbidden 4f emissions of the lanthanide ions, as described in Section 2.3).[19] Herein, we choose not to use the term scintillator, though many of the references cited (especially for nanomaterials) use the terms radioluminescence and scintillation interchangeably.[1,15,20,21] Radioluminescence in inorganic materials occurs in three stages[19], and the efficiency of the radioluminescence process (η) is most basically described using equation 3:

$$\boldsymbol{\eta = BSQ} \tag{3}$$

Where B describes the efficiency of the absorption of the incident radiation and the formation of electron-hole pairs, S describes the efficiency of the energy transfer from the electron-hole pairs to a luminescent center, and Q describes the efficiency of the emission process (ie. the quantum yield of the luminescent center). The process is summarized in Figure 2.

As discussed previously, an incident photon can interact with an absorbing material *via* the photoelectric effect, Compton scattering or pair production, depending on its energy. With respect to radioluminescence, these primary interactions cause an excitation of the host material, generating electron-hole pairs. The theoretical maximum number of electron-hole pairs (n_p) that can be produced by an incident photon is given in equation 4[19]:

$$\boldsymbol{n_p = \frac{10^6 E}{\xi}} \tag{4}$$

Where E is the energy of the incident photon in MeV, and ξ is equal to the average energy in eV required to form a single electron-hole pair, including any losses in energy. While ξ in equation 4 considers losses, there is still intrinsically a minimum energy required to form a single

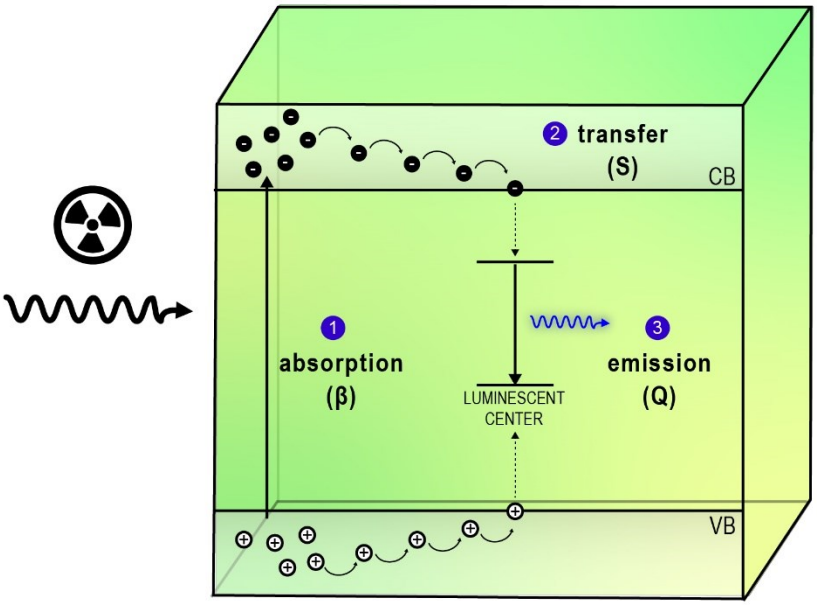

Figure 2. Graphical depiction of the radioluminescence process. 1) Incoming ionizing radiation is absorbed by the material causing excitation of the host lattice and production of electron-hole pairs. 2) Excited electrons and holes migrate through the conduction and valence bands, respectively, and then transfer their energy to the luminescent center. 3) The luminescent center radiatively relaxes to emit a photon. CB: conduction band, VB: valence band.

electron-hole pair (ξ_{min}). This minimum is approximated to energies between $1.5E_g$ and $3E_g$ depending on the model used, where E_g is the energy of the electronic band gap of the material.[19,22,23] Most often, $2.25E_g$ is the value encountered in the literature. From these relationships, we can estimate that a single 50 keV X-ray photon can produce over 2000 electron-hole pairs in a material with a 10 eV band gap if we take ξ as $2.25E_g$. As such, under constant irradiation with an X-ray beam, countless pairs are propagating throughout a crystalline lattice at a given time, even if only a fraction of the theoretical maximum number of pairs is produced. The generated electron-hole pairs eventually undergo thermalization, where phonons are emitted until the electrons and holes reach energies close to those of the band edges.[22] This is the end of the first part of the radioluminescence process.

The transfer of energy from thermalized charge carriers in the host conduction and valence bands to luminescent centers is the next phase of the process. The efficiency of this process, *S*, is the least understood part of the radioluminescence mechanism and no models are able to predict it at this time, to our knowledge.[19] While relatively little is understood about this process, it is

established that while the thermalized charges propagate through the host, one portion of these carriers is lost to interactions with defects and trap states (or can be self-trapped), and the remainder result in electron-hole recombination at the luminescent center, which then becomes promoted to a higher-energy electronic state. [24]

The final stage, emission of a non-ionizing photon from the luminescent center, is the most familiar process. The efficiency of this process, Q, is the quantum yield of the emitting center. Since the basic definition of quantum yield (number of photons emitted per number of photons absorbed) is practically not obtainable in the case of radioluminescence because the host excites the luminescent center, this value is typically obtained using lifetimes under a pulsed radiation source.[19,25]

2.2.1. Radioluminescence: Bulk vs. nanoscale

Our understanding of the radioluminescence process, and development of radioluminescent materials has mostly occurred due to the rapid advancement of technologies based on scintillation detectors.[5,13,14,19] Importantly, the majority of scintillator-based technologies use single crystals or bulk-scale polycrystalline materials, and our understanding of the radioluminescence process is based on these bulk materials. In 2014, Jung *et al.* reported a study comparing the radioluminescence of several materials at the bulk and nanoscale and concluded that a trend could not be established between their performance.[20] These discrepancies mean it is important to re-evaluate previously discarded compositions, as their performance may be much more impressive at the nanoscale.

The past two decades have seen a tremendous increase in the development of technologies based on nanomaterials. Nanomaterials, defined as having one dimension on the order of 100 nm or smaller, are known to exhibit properties that are different than their bulk counterparts owing to a much larger surface area-to-volume ratio.[26] The advancements made in nanomedicine[27,28] using nanoparticles have more recently inspired the development of radioluminescent nanoparticles (RLNPs), also commonly referred to as nanoscintillators. As recent as 2011, it was noted that the development of nanoscintillators had essentially been unexplored.[29]

A major consideration in nanocrystalline radioluminescent materials is the diffusion length

of charge carriers. In ionic crystals, the average diffusion (thermalization) length of excited electrons is around 70-100 nm before recombination at an activator ion occurs. [29,30] This effectively means that a free electron can traverse a nanoparticle, and either transfer its energy to a surface defect, or be ejected from the nanoparticle altogether.[31] The prevalence of luminescence quenching due to surface defects in nanomaterials extends beyond radioluminescence; it is a common phenomenon in upconversion and photoluminescence as well.[20] Sharp dependencies on the luminescence intensity of $LaPO_4:Pr^{3+}$ and $LuPO_4:Pr^{3+}$ have been observed in the range of 15-40 nm, and the correlation of radioluminescence intensity with RLNP size was modelled and confirmed to be affected by the average thermalization length of electrons.[31] In agreement with these results, it has been suggested on multiple occasions that relatively large nanoparticle sizes (around 70-100 nm) are beneficial for achieving higher radioluminescence efficiencies.[29,32,33]

Mentioned previously, the interaction of an initial primary electron is usually accompanied by a secondary cascade of Auger electrons and X-rays. In addition to the diffusion of hot electrons formed in the primary interaction, the migration distance of these secondary particles/photons are also on the order of a hundred nanometers.[34] The potential for primary and secondary electrons and photons to traverse multiple nanoparticles is a key factor in radioluminescence at the nanoscale, and in the use of nanoparticles as radiosensitizers (discussed in Section 3.4.1.1). Notably, Bulin *et al.* modelled the energy deposited into nanoparticles in an aqueous environment, and found that the majority of incident energy is deposited into the surrounding medium before interacting with the nanoparticles.[35] This is a particularly important consideration for RLNPs in the context of X-PDT, as most fundamental studies on radioluminescent materials are performed on powders or single crystals, where there is no surrounding medium to consider.

2.2.2. Material considerations

Radioluminescent materials can be classified by the type of luminescent center: intrinsic materials where luminescence comes from the "host" material itself, and extrinsic materials, in which luminescence comes from an activator ion introduced into a spectroscopically-silent host. The ability to introduce dopant ions into a lattice and precisely tune its radioluminescent properties makes extrinsic materials particularly interesting. Herein, we will focus on these types of radioluminescent materials.

Since radioluminescence is a host-mediated process, it follows that the choice of host is an essential consideration. The intended application of the material may be the best means of choosing a host. In our case, the host must fulfill the following criteria:

- It must be of sufficiently high density and effective atomic number to facilitate interactions *via* the photoelectric effect
- It must be chemically stable in biological medium such that it does not decompose upon introduction to cells or tissues
- It must be non-toxic in line with its use as a therapeutic agent
- It must have low phonon energies such that minimal luminescence quenching is caused
- It must be possible to synthesize at the nanoscale relatively easily, with high reproducibility and uniformity
- It must facilitate the desired emissions from the chosen luminescent ion

For these reasons, the ternary sodium lanthanide fluoride hosts are an ideal choice. Fluoride hosts have been very successfully used in the development of scintillators for a wide variety of applications, owing to their generally low hygroscopicity and wide band gaps.[36] The fluorides have also been the most widely-used hosts for the development of upconverting nanoparticles.[37,38] The low phonon energies of fluorides (300-500 cm^{-1}) facilitate upconversion by reducing the probability of non-radiative relaxation of the intermediate excited states. This is also an important property for radioluminescent materials when activator ions have states which are susceptible to such phenomena. Moreover, the rapid advancement of luminescent nanoparticles for biomedical applications has resulted in a wealth of *in vitro* and *in vivo* studies, which thus far have suggested fluoride nanoparticles are not toxic.[39–47]

$NaLuF_4$ is a particularly interesting host for use in X-PDT, as it fits all of the criteria above, and has been previously demonstrated by the Capobianco group to yield strong radioluminescence when doped with lanthanide ions.[48] Of major importance, the lanthanides have played a major role in the development and success of luminescent materials and are among the best choices for activators in radioluminescent materials.[21,36,49,50]

2.3. The lanthanides

Lanthanide means “to lie hidden” and refers to the 14 elements following lanthanum on the periodic table (Ce-Lu).[51] These elements are also referred to as lanthanoids when La is included, and when Y and Sc are included in the definition, they are known as the rare-earth elements. While La, Y and Sc do not possess 4f valence electrons, they are often found in the same ores as the other lanthanides and are chemically similar, thus they tend to be included in the definition of rare-earths.[52] The lanthanide elements are essential in modern society. First discovered in 1787[52], the rare-earth elements were initially difficult to identify and purify, owing to their similar ionic radii in the trivalent state, determining their similar properties. The interested reader is referred to Chapter 73 of the *Handbook of the Chemistry and Physics of Rare Earths* for a detailed discussion of the history of these elements. Nearly 300 years after their discovery, 243.3 thousand metric tons of lanthanides were produced in 2020.[53] Lanthanides are now crucial components of many commercial and government sectors, such as telecommunications, medicine, vehicles, displays, lighting, catalysis, security and defense. To further contextualize their importance, the global supply of rare-earth elements has even shaped world politics on several occasions.[54–56]

Of relevance to this work, the lanthanides are known for their luminescence. The key to their luminescent properties lies in their electronic structure. The lanthanides are most often found in the trivalent state, with the ground state electron configuration of $[Xe]4f^n$, where n=1 for Ce^{3+} and n=14 for Lu^{3+}. The 4f orbitals are shielded by the fully occupied 5s and 5p orbitals, and thus the 4f electrons are not greatly influenced by the surrounding environment. In contrast, the positions of the $4f^{n-1}5d$ levels are affected to a much greater extent by their environment, as discussed later in Section 2.3.2.[57]

Lanthanide luminescence can occur *via* interconfigurational 5d→4f transitions, or *via* intraconfigurational 4f→4f transitions.[58] In many cases, however, it is the luminescence arising from 4f→4f transitions that is desired because of the wide range of emissions that can be obtained, and their narrow bandwidths.[5,58]

Since the 4f electrons are not strongly affected by their environment, their energy states can be understood mostly from the electronic interactions within a free ion.[58,59] The 4f electronic

energy levels are generated due to Coulombic interactions with the nucleus, which generates sets of microstates that are described as spectroscopic terms, denoted by a term symbol ^{2S+1}L. *L* is the total orbital angular momentum and *S* is the total spin angular momentum of the 4f electrons. The two momenta are also coupled; this is known as Russell-Saunders coupling. This spin-orbit coupling gives rise to further splitting, where states are then described by an additional parameter, *J*, which is the total angular momentum. The complete term symbol, $^{2S+1}L_J$ encompasses all of the electronic interactions in the free ion (Figure 3).

Importantly, the 4f→4f transitions are forbidden by the selection rules; specifically, they are electric-dipole forbidden by the Laporte rule, as they are transitions involving states of the same parity. Magnetic-dipole transitions are allowed, but do not account for all the observed transitions.[49] So, how are the other transitions accounted for?

In 1937, Van Vleck first addressed this in what he called "the puzzle" of lanthanide emissions.[60] He attributed the emissions to indeed be due to the electric-dipole forbidden transitions, and proposed the now-accepted model for why the electric-dipole forbidden emissions are observed in solids, as described below. Since then, the nature of these transitions has been thoroughly studied, and we have a good understanding of why emissions are observed from forbidden transitions, as well as their relative intensities.[58,59,61,62]

Upon incorporation of a free lanthanide ion into a material (crystalline or amorphous),

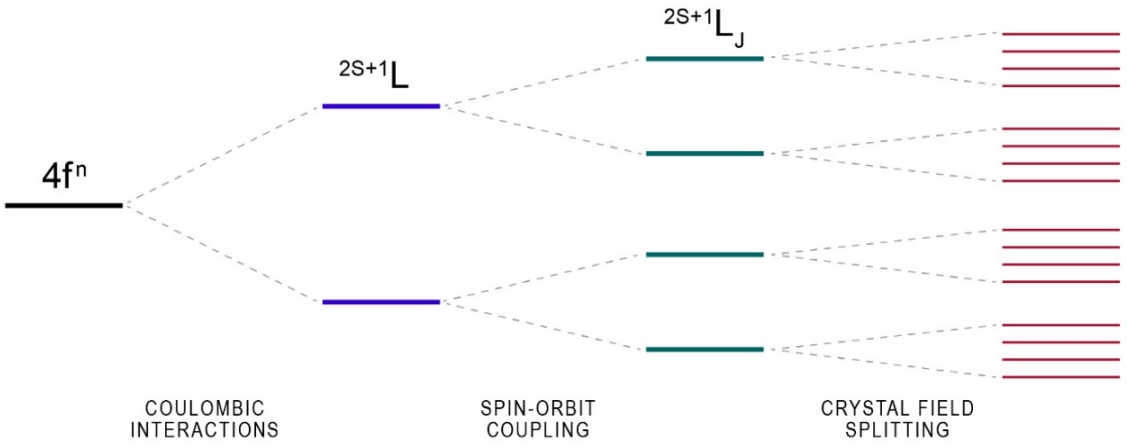

Figure 3. Graphical depiction of the 4f orbitals in a trivalent lanthanide ion and how the levels split due to Coulombic interactions, spin-orbit coupling and crystal field splitting.

additional splitting of the 4f states occurs due to interactions with the crystal field (Figure 3).[58] The interactions between neighboring ions in the material result in the mixing of the 5d and 4f wavefunctions. This mixing relaxes the selection rules, making the electric-dipole transitions partially allowed. Thus, the "forbidden" emissions are observed, and they remain narrow because of the relatively small effects of the crystal field. As mentioned before, the 4f electrons are largely uninfluenced by the surrounding environment, thus the 4f energy levels that give rise to these narrow emissions generally only change by a few hundred cm^{-1} (at most) when incorporated into different host lattices.[57] This allows for the researcher to choose a suitable host for an application, but still take advantage of the desired emissions from the lanthanide ion of choice.

The splitting of the energy levels gives rise to a myriad of different emissions. As previously mentioned, the lanthanides each have unique emission spectra. Herein, we are interested in Pr^{3+} because of its particularly good suitability for X-PDT in combination with PPIX as a photosensitizer, as will be discussed later.

2.3.1. Trivalent Praseodymium (Pr^{3+})

Praseodymium is the second element in the lanthanide series. It is most often found in the trivalent state, having an electron configuration of $[Xe]4f^2$. First isolated in 1842 by Carl Mosander, praseodymium and neodymium (the element after it in the series) were thought to be the same element, called didymium, which comes from the Greek word for "twins".[63,64] This belief persisted for nearly 50 years, until 1885 when Carl Auer von Welsbach separated didymium into two elements: praseodymium ('*green twin*' from the Greek translation) and neodymium ('*new twin*' from the Greek translation) while working in Robert Bunsen's laboratory.[52,64] Notably, the spectroscopic properties of didymium led chemists to realize it could not be a single element.

The energy level diagram of the Pr^{3+} ion is shown in Figure 4 up to 50000 cm^{-1}. The unique luminescent properties of Pr^{3+}-based materials occur because of its energy level structure and give rise to a myriad of 4f→4f emissions spanning the UV, visible and NIR regions. In some instances, the 5d→4f transitions are also observed, as described below. The $^1S_0$ state is found at 46,500 cm^{-1} and can only be accessed with relatively high energy sources (vacuum ultraviolet (VUV) or higher).[65] Transitions from the $^1S_0$ state give rise to UV-A, UV-B and UV-C emissions. In contrast, the energy levels below 30000 cm^{-1} (^3P_J, $^1I_6$, $^1D_2$, $^1G_4$, ^3F_J, and ^3H_J) are involved in transitions giving

rise to emissions in the visible and NIR regions and will be referred to herein as the lower optical levels (LOLs) when discussed in a general manner. Emissions from the $^1S_0$ state are often accompanied by LOL emissions, and emissions from these states can be also obtained using visible excitation (457.9 nm light from an Argon ion laser can be used to excite into the $^3P_0$ level, for example).[66] Since we are ultimately interested in radioluminescence from Pr^{3+}, the discussion below focuses on high-energy excitation.

As mentioned earlier, the positions of the $4f^{n-1}5d^1$ states change substantially in different hosts. When an interconfigurational transition occurs, the electron in the 5d state is no longer shielded to the same degree as it is in an 4f orbital, since the 5d orbitals extend past the filled 5s and 5p orbitals.[67] Thus, the 5d orbitals can interact with neighboring ions, thereby influencing their positions. Because of this variability, the emissions from the $^1S_0$ state may or may not be observed depending on the relative positions of these levels relative to the $^1S_0$ state.[65] The lowest-lying $4f^15d^1$ state can be found at energies below, nearly identical to, or above the $^1S_0$ state. Thus, the emission spectrum of Pr^{3+} can be quite different depending on the host material. If the $4f^15d^1$ configuration lies below the $^1S_0$ state, 5d→4f emissions will be observed (and no $^1S_0$ emissions), along with weak emissions from the LOL states, as in $LiYF_4:Pr^{3+}$, for example. When the $4f^15d^1$ states are slightly higher in energy than the $^1S_0$ state, both the $^1S_0$ and 5d→4f emissions are observed, as is the case in $LiLaPO_4:Pr^{3+}$.[68] Both types of emission occur in this case, due to non-radiative relaxation from the $4f^15d^1$ state to populate the $^1S_0$ state. Finally, when the $4f^15d^1$ states lie sufficiently above the $^1S_0$ state, only 4f→4f emissions are observed. This is a particularly interesting scenario and gives rise to one of the most desirable properties of Pr^{3+} phosphors, photon cascade emission (PCE) as described below.

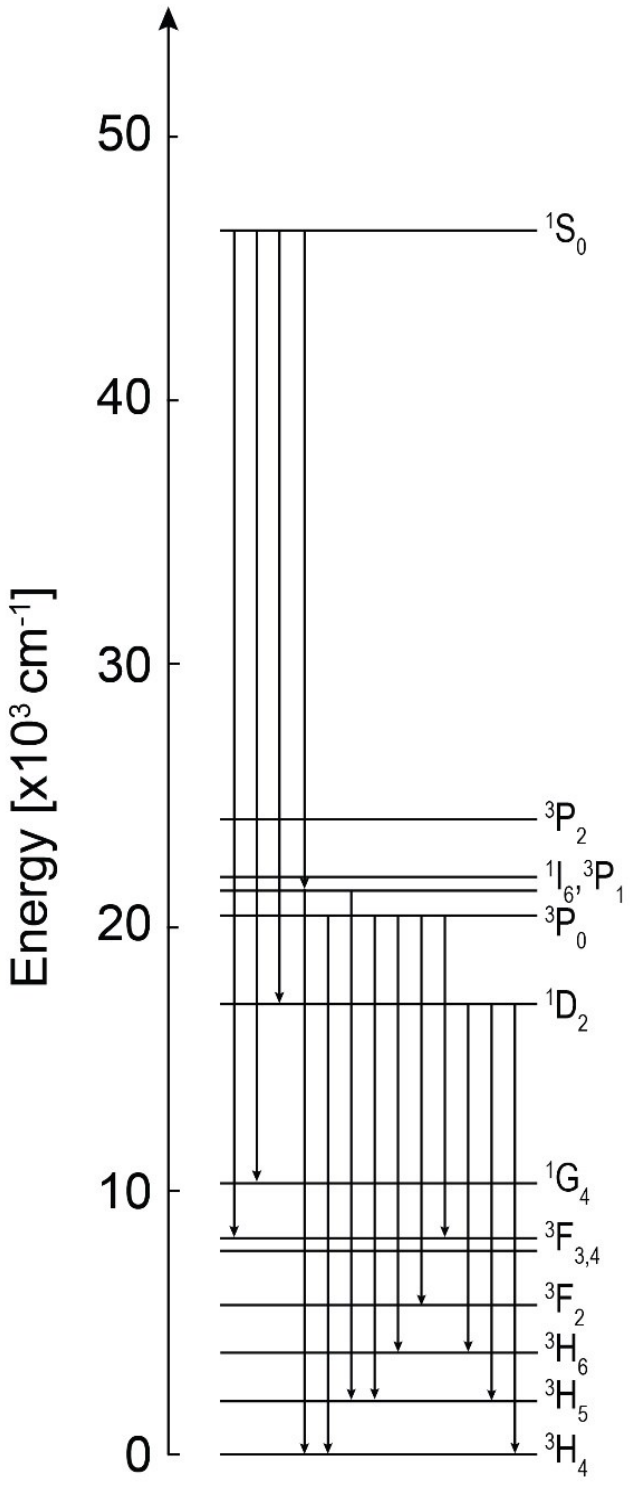

Figure 4. Energy level diagram of the Pr^{3+} ion up to 50000 cm^{-1}.

The wide energy gap between the $^1S_0$ and $^3P_J/^1I_6$ states (approximately 24600 cm^{-1}) is especially important for two main reasons. First, since the radiative probability increases with the third power of the energy gap between the initial and final states in the transition (ΔE^3), the likelihood of radiative relaxation is high from the $^1S_0$ state.[69] Second, the $^1S_0 \rightarrow {}^1I_6$ transition is spin allowed and tends to be the most intense of the $^1S_0$ emissions. Population of the $^1I_6$ state *via* this transition then leads to population of the $^3P_0$ state through non-radiative relaxation. As mentioned earlier, visible and NIR emissions are obtained from LOL transitions, many of them from the $^3P_0$ state. Thus, it is possible for Pr^{3+} to emit two photons from a single absorbed photon. This is known as photon cascade emission (PCE), or quantum cutting, and presents the highly attractive opportunity to obtain a quantum efficiency greater than 100%. Of all the lanthanide ions, Pr^{3+} is the best ion for achieving PCE based on calculations using the Judd-Ofelt theory.[70] However, PCE from Pr^{3+} can only be achieved in hosts satisfying the following criteria: the $4f^15d^1$ states must lie above the $^1S_0$ state, the energy gap between the $4f^15d^1$ state and the $^3H_4$ 4f ground state is at least 5.8 eV, and the entire 4f manifold of Pr^{3+} levels must fit within the band gap.[60] For these reasons, fluoride hosts are preferred as most of them satisfy these criteria.[71] Impressively, in 1974, researchers from the General Electric Company reported a quantum yield of 140% from $YF_3:Pr^{3+}$, the first Pr^{3+} material reported with a quantum yield greater than 100%.[72]

With respect to emissions from the LOLs, the excited states are much closer in energy to one another compared to the separation between them and the $^1S_0$ state discussed above. As such, the LOLs are susceptible to concentration quenching, and in particular, to a process known as cross-relaxation.[66] Cross-relaxation occurs between ions of the same element when there are multiple resonant transitions, leading to the de-population of one state and concurrent population of another state. This can either result in complete quenching of the emissions, or it can lead to altered ratios of the transitions as a function of concentration. Many of the cross-relaxation mechanisms between Pr^{3+} states were established in the Capobianco group from research undertaken by Rafik Naccache, and are depicted in Figure 66, Appendix 1.[66,73]

The search for phosphors employing Pr^{3+} led to the development and study of a huge number of different materials, mainly of fluoride and oxide/complex oxide hosts. These paved the way for the observation of Pr^{3+}-based materials that exhibited other useful properties in addition to scintillation and photoluminescence, such as upconversion[66,74–77], cathodoluminescence[78–80],

mechanoluminescence[81,82] and, of particular interest to us, persistent luminescence[81,83–86].

2.3.2. Lanthanide level location

Through the work of Dorenbos in the early 2000's, the ability to model the positions of the lanthanide energy levels within the forbidden band of different hosts became possible.[67,87–90] By studying the positions of the lanthanide energy levels in hundreds of materials[57,87,89,90] it became possible to predict different luminescent properties of lanthanide-doped materials. Mostly, these models are useful for engineering persistent luminescent materials and determining their mechanisms, but it is also useful for predicting what emissions may be favored or feasible in a material, especially for Pr^{3+} as discussed below. These predictions are based on the development of four models which build on one another: the red shift model, the centroid shift model, the charge transfer model, and the chemical shift model.[90]

The red shift model defines the method of predicting the position of the $4f^{n-1}5d^1$ states for all lanthanide ions in a host if knowledge of the energy of the d-f transitions of one ion is known in that host.[57] This is possible because (1) the difference in energy of the $4f^{n-1}5d^1$ states across the lanthanide series red shifts according to the same pattern observed for the binding energies of the 4f electrons for the free ions, and (2) because the influence of the host on the position of these states is independent of the number of electrons in the 4f manifold (ie. all lanthanides experience the same red shift in the same ion site in the same host). The centroid shift model predicts the red shift of the centroid position of the $4f^{n-1}5d$ states in a material relative to their positions in the free ion.[91] The centroid shift follows the nephelauxetic sequence, where a larger shift is observed with increasing covalency between the lanthanide ion and the neighboring anions coordinated to it, and the polarizability of the anion.[67] Thus, lanthanides in fluoride hosts experience a relatively small centroid shift compared to in sulfides, for example.

The charge transfer model takes the red shift and centroid shift models and uses them for the prediction of the placement of the ground states of the divalent and trivalent lanthanides relative to the top of the valence band. Specifically, knowledge of the charge transfer energies enable the placement of the ground state of the divalent ions relative to the top of the valence band.[88] The red shift and charge transfer models can then be combined to produce a host referred binding energy scheme (HRBE) that shows the 4f ground states within the forbidden band for the entire lanthanide

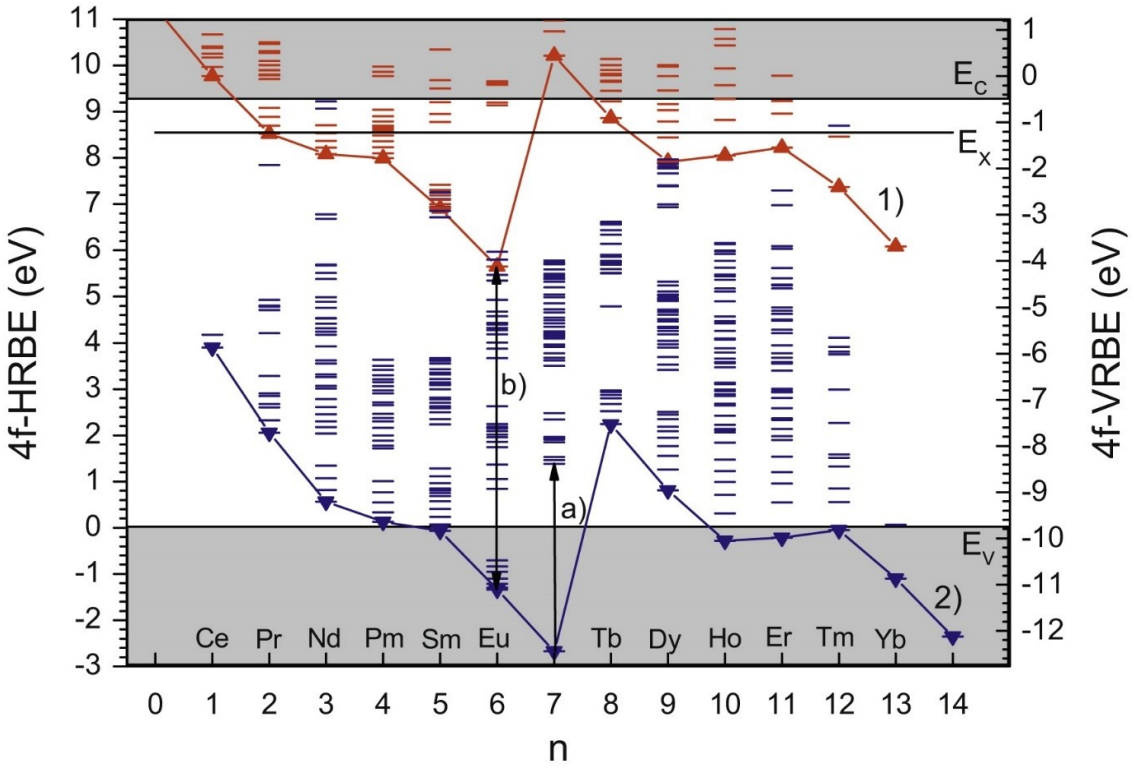

Figure 5. 4f-electron HRBE (left-hand scale) and VRBE (right-hand scale) in YPO_4. Upper curve (1) connects 4f-HRBE of divalent lanthanide ions in the ground state of the $4f^{n+1}$ configuration. The horizontal lines above curve (1) are binding energies in the excited states. Lower curve (2) and the horizontal lines above it pertain to the 4f-HRBE of trivalent lanthanide ions with $4f^n$ configuration. E_X and E_C indicate the binding energy of the electron in the exciton and at the bottom of the conduction band, respectively. Figure reproduced with permission from Reference 83.

series. The scheme for YPO_4 is well-established and often used by Dorenbos as a model material[83,92,93], it is shown as an example in Figure 5. The zig-zag curve takes its shape from the pattern observed due to the binding energies of the 4f electrons. In the HRBE, the energy scale is defined such that the top of the valence band is 0 eV, thus the relative positions can be obtained. The chemical shift model again builds upon the other models and allows for the absolute binding energies to be determined from the HRBE. The HRBE scheme is then framed in reference to the energy of a free electron at rest in a vacuum, and all other values are calculated in relation to this to obtain absolute binding energies.[67] When the absolute binding energies are used as the energy scale, a vacuum-referred binding energy scheme (VRBE) is developed instead.

In materials where the entire radiative 4f manifold does not fit within the forbidden band, the position of the trivalent lanthanide ground state relative to the top of the valence band will

inform on which excited states fit within the band, and thus which emissions are expected. This is important in Pr^{3+} materials, as the $^1S_0$ state is so well-separated from the other radiative states. For example, $CaTiO_3:Pr^{3+}$, has a bandgap around 3.5 eV.[94] Since the 4f manifold of Pr^{3+} is ~6 eV in energy from the $^3H_4$ ground state to the $^1S_0$ excited state, only the LOL states fit within the bandgap, and there is no possibility to observe emission from the $^1S_0$ state. HRBE and VRBE schemes find the bulk of their use in proposing persistent luminescence mechanisms, or in defect engineering to produce persistent luminescence materials.

2.4. Persistent luminescence

> "One of the basic rules of the universe is that nothing is perfect. Perfection simply doesn't exist...Without imperfection, neither you nor I would exist." – Stephen Hawking

At a glance, an imperfection, or defect, in a crystalline material would seem to be a highly undesirable thing. A perfect, defect-free material would have a dramatically higher luminescence efficiency, especially at the nanoscale. What is often forgotten, however, is that in many cases, defects are essential for generating some of the most desirable luminescence phenomena. Persistent luminescence is a phenomenon which cannot exist without the presence of defects. Much like Hawking's sentiment that we would not exist without imperfection, neither would persistent luminescence. It seems that perfection is not always so desirable!

Persistent luminescence is the continued emission of light after excitation has ceased. This so-called "glow-in-the-dark" phenomenon is not just used to make a night sky on the ceiling of a bedroom, it is commercially used in things from watch dials to safety signage, and is currently investigated for use in bioimaging.[95–98] Persistent luminescence is described as far back as the Song dynasty of China, over 1000 years ago, though the material is not precisely known.[99] The Bologna Stone, reported in 1602 represents the first modern persistent luminescence material. At the time, the phenomenon baffled amateurs and scientists alike, and reportedly even Galileo did not want to get involved in trying to explain it.[96] Today, the mechanisms that give rise to persistent luminescence are far from fully-understood and are routinely disputed.[96,99–102] Perhaps the only consensus is that the phenomenon arises due to the presence of defects.

Defects, as mentioned before, are imperfections in a crystal lattice. Some examples include

impurities (intentionally or accidentally introduced), vacancies, and interstitials.[97,103] Defects give rise to additional energy levels, known as trap states, from which persistent luminescence occurs. The nature of the traps, and their positions relative to luminescent centers and the conduction and valence bands, can be used to infer the mechanism through which persistent luminescence occurs in a material.

The general process giving rise to persistent luminescence is as follows: upon excitation of sufficiently high energy, excited charge carriers can migrate and become trapped in the potential energy well of a trap state. This can occur with electrons or holes, depending on the nature of the ion and host involved. When the trap states are at specific energies, thermal energy is required to liberate the trapped charge. This represents a metastable non-equilibrium state, which can remain for a certain period of time before equilibrium is restored *via* de-trapping.[104] When room temperatures provide enough thermal energy to cause de-trapping, persistent luminescence is observed, bringing the system back to equilibrium.

2.4.1. Kinetics of persistent luminescence

Perhaps the most obvious clue that a material may exhibit persistent luminescence is that its luminescence intensity changes as a function of irradiation time. $Sr_2AlO_4:Dy^{3+},Eu^{2+}$, which is perhaps the most widely-studied persistent luminescent material, is an exemplary material for such a phenomenon.[105] Typically, at the onset of irradiation, the luminescence intensity is at its lowest and then increases as a function of irradiation time until it reaches a plateau (Figure 6A). The change in intensity can inform on how long it takes to fill the traps in a material, as well as how the trap filling kinetics may change at different dose rates or temperatures, for example. Importantly, the type of irradiation necessary to induce trap filling depends on the material, and is typically UV or ionizing radiation, but there is recent work on developing NIR-chargeable persistent luminescence materials.[106]

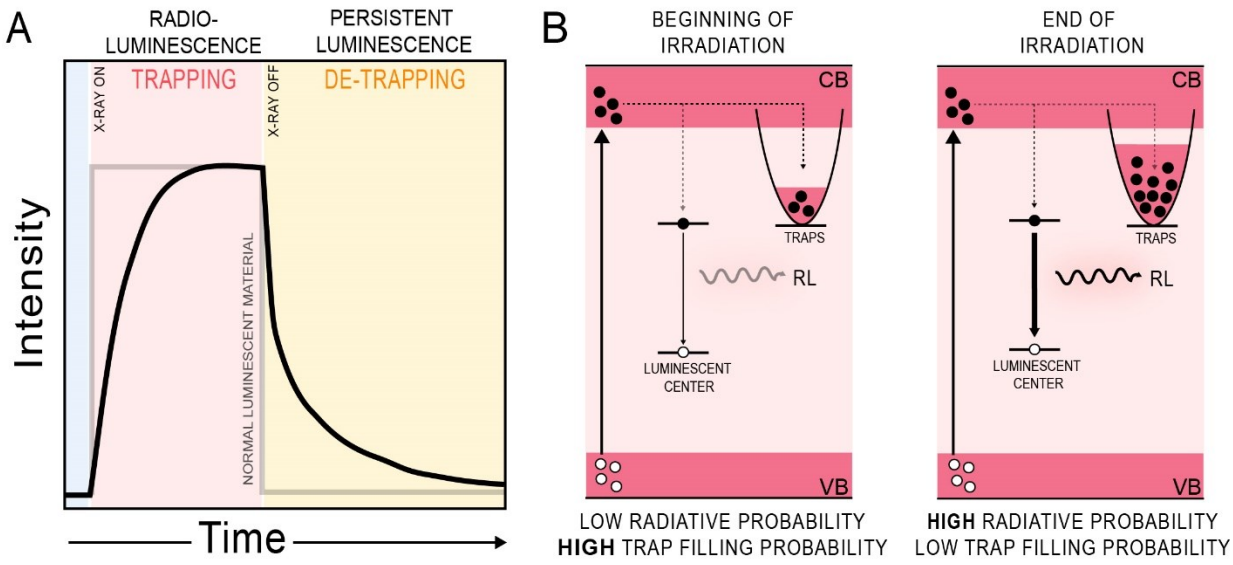

Figure 6. A) Graphical depiction of the commonly observed luminescence profile of a persistent luminescence material as a function of irradiation time, and subsequent persistent luminescence kinetics. In this case, the persistent luminescent material is excited with X-rays and is also radioluminescent B) Graphical depiction of the probability for electrons to become trapped or recombine at a luminescent center based on how populated the trap states are during irradiation as depicted in panel A. CB: conduction band, VB: valence band, RL: radioluminescence. Panel A is modified from Reference 109.

The change in intensity with time occurs due a competition between radiative recombination and trapping (Figure 6B). Prior to irradiation, the traps in the material are empty (ie. not populated). Thus, there is a high probability for trapping to occur at the onset of irradiation, which consequently results in a low radiative recombination probability. As the traps become filled, more electrons are free to recombine at luminescent centers and thus the luminescence intensity increases and plateaus at a maximum once the traps are filled. Just as the de-trapping process (persistent luminescence) can be complex, the trap filling process is also influenced by many parameters such as temperature, excitation dose rate/intensity, and excitation wavelength, for example.[107–109] In some cases, there is even a thermal barrier to charging the trap, in addition to the thermal barrier required to de-trap. Such is the case for YAG:Pr^{3+} and YAG:Ce^{3+}, which causes luminescence quenching at higher temperatures due to an introduced trapping pathway when the thermal barrier is reached.[110,111] This is an undesirable phenomenon in these materials that hinders their use as scintillators and white light phosphors. In contrast, materials like $Ca_2Si_5N_8$:Eu^{2+} and $SrAl_2O_4$:Eu^{2+},Dy^{3+} can be charged more quickly at higher temperatures, if

desired. Importantly, these types of complex charging dynamics can make it more difficult to understand the positions of trapping states, thus complicating the determination of a persistent luminescence mechanism.[108]

Thermoluminescence spectroscopy is an essential technique to determine the position of the trap states and is intimately tied to the understanding of persistent luminescence phenomena to achieve greater charge trapping capabilities (or reduce it if it is not desired).

2.4.2. Thermoluminescence

Thermoluminescence, more formally known as thermally-stimulated luminescence, is the emission of light when a material is heated after previously being irradiated with an excitation source.[104,112] Importantly, this is *not* the same phenomenon where a material emits black-body radiation upon heating. In thermoluminescence, a material must first have absorbed energy from a previous irradiation event and the material is simply emitting the absorbed energy when given enough thermal energy to do so. In the context of persistent luminescence, thermoluminescence gives us information on how much energy is required to release trapped charge. Formally, this is the activation energy to release the trapped charge, but it is often called the "trap depth" when it can be correlated with the position of the trap state relative to the conduction and valence bands.

Persistent luminescence is characterized by a significantly delayed recombination of trapped charge at a luminescent center. The degree to which this process is delayed is dependent on the amount of thermal energy required to release the trapped charge, as mentioned before. The probability of releasing an electron can be most basically described by the Arrhenius equation (equation 5):

$$\boldsymbol{p = se^{-\frac{E}{kT}}} \tag{5}$$

Where p is the probability, s is the frequency factor (described below), E is the activation energy (ie. the trap depth), k is the Boltzmann constant, and T is the temperature. From this equation we can deduce that the probability of releasing an electron from a trap changes with the ratio of E and T. At temperatures where $kT > E$, there is a high probability to release the charge and observe luminescence. The time it takes for de-trapping to occur (ie. the persistent

luminescence duration) is related to the trap depth, and the frequency factor, and is inversely proportional to the lifetime of the trapped electron (τ_e).[104,112] The frequency factor is a temperature-independent constant that is often called the "attempt to escape" factor; it is a constant that describes how difficult it is for a charge to overcome the thermal barrier and be de-trapped. Higher frequency factors generally mean more energy is required for de-trapping to occur, even if the trap depth is shallow.[104] If the combination of E and s allow for de-trapping to be probable at room temperature in such a way that τ_e is not too short, then persistent luminescence will be observed for an appreciable amount of time. At room temperature, if E is too shallow, τ_e would be very short and de-trapping would occur in seconds or less, while if it is too deep τ_e would be extremely long. For more context, McKeever states that the practical limit for an indefinitely long τ_e is the age of the solar system, 4.6×10^9 years.[112] This is an extremely simplistic description of these relationships, but illustrates how the trap depth and temperature affect the persistent luminescence duration. In thermoluminescence spectroscopy, the temperature is varied such that τ_e becomes short and we can stimulate de-trapping, thereby learning about the energy of the trap on a convenient timescale.

Most often, the goal of thermoluminescence spectroscopy is to produce a glow curve. This curve is obtained by plotting thermoluminescence intensity as a function of temperature. The thermoluminescence intensity I is related to the number of de-trapped charges/recombinations taking place at a specific temperature, which corresponds to the activation energy of the trap as mentioned before. A theoretical glow curve is shown below in Figure 7.

In this theoretical material, there are 5 distinct sets of trap states. The maximum of peak 1 is just above room temperature, but the peak begins below room temperature. As such, we expect that these trap states are very shallow and easily liberated at room temperature, but the ones slightly above room temperature at the maximum of peak 1 are positioned seemingly-adequately to give rise to persistent luminescence (assuming s does not significantly alter the relationship between E and T). Peaks 2 and 3 require more energy to liberate, and 4 and 5 even more. Peaks 4 and 5 require relatively high temperatures to liberate the trapped charge, and thus their presence could indicate the material may act as a stable charge storage material. Materials possessing traps deep enough to be stable at room temperature are commonly used as personal radiation dosimeters, such as LiF:Mg,Ti (TLD-100).[104,112] The shape of the glow curve also gives information on the nature of

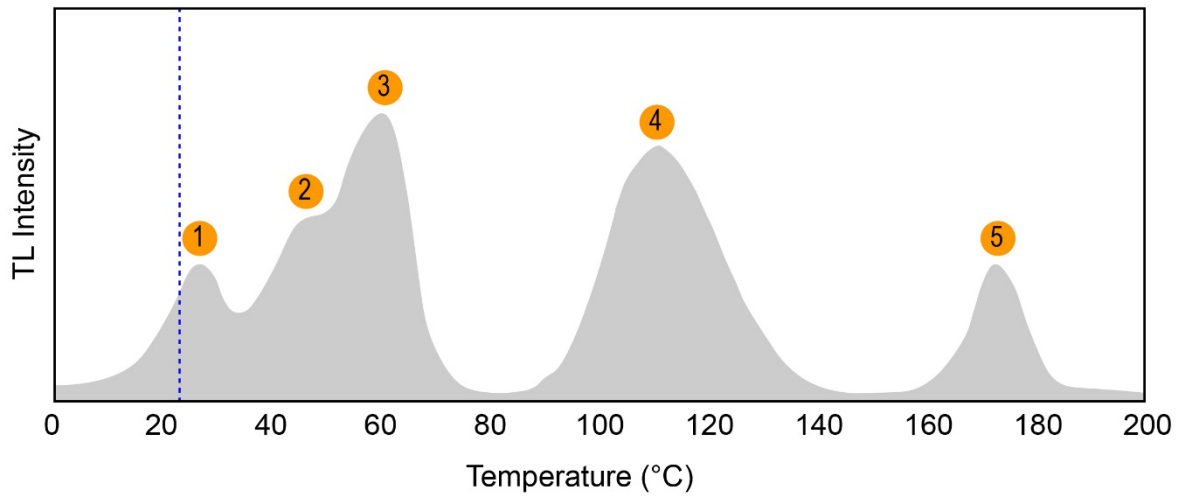

Figure 7. Graphical depiction of a thermoluminescence (TL) glow curve for an imaginary persistent luminescence material. Dotted blue line depicts room temperature (25 °C).

the trap states. Narrow curves are more indicative of a discrete, isolated trap energy state, as depicted by peak 5. More often, however, glow curves are broad and may have multiple local maxima, as depicted by peaks 1-3. The broad nature of these curves is indicative of a continuum of trap states of overlapping energy.[113] Peak 4 is also relatively broad, and may be deconvoluted into multiple curves. In inorganic phosphors, this is thought to be a more realistic representation of the situation based on the nature of the defects, the number of them, and how they may propagate throughout a crystal.[107] In this way, the value obtained for the trap depth represents an estimate for the shallowest edge of the trap state energy distribution.

A number of models have been developed to calculate a trap depth from a glow curve, with varying complexity. Usually, it is the ease of obtaining parameters necessary for the calculation that determines which model is used to obtain the depth estimation. The simplest method was developed by Urbach in 1930, where the trap depth E is approximated[114] by using equation 6:

$$\boldsymbol{E = \frac{T_m}{500}} \tag{6}$$

Where T_m is the temperature maximum of the glow curve peak, and 500 is a constant of proportionality. While this equation has been used frequently due to the ease of obtaining T_m from a single glow curve, it can result in inaccuracies since this calculation assumes the frequency factor, s, is the same for all peaks in a glow curve, and the shape and peak position can vary with

radiation dose and heating rate.[112,113] Based on this method, trap depths can be calculated with a precision of 0.1 eV.[101] Other methods such as those of Randall and Wilkins[115] (1945), Garlick and Gibson[116] (1948), Hoogenstraaten[117] (1958), Chen[118,119] (1969), Sweet and Urquhart[120] (1981), among others are certainly more accurate, but require additional information or experimental variables, and may have restrictions of use depending on the kinetics of the trapping or de-trapping processes.[100,101]

In summary, thermoluminescence spectroscopy provides information on the energies of a trap state or distribution of states based on the temperature required to produce luminescence after a material has been previously irradiated and charge has been trapped. The trap depth can be extracted from a thermoluminescence glow curve using a variety of different models with varying complexity. Further, the trap depth is related to the possibility for persistent luminescence, and also governs the duration that charge can be stored within a material at a given temperature. For these reasons, thermoluminescence is a powerful tool for determining persistent luminescence mechanisms.

2.4.3. Persistent Luminescence Models

Two main types of trapping/de-trapping mechanisms are known: global models that involve the valence and conduction bands (Figure 8), and local models where trap states interact directly with luminescent centers and bypass the conduction and valence bands altogether.[109,121–123] Each of these models will be explained in detail in Sections 2.4.3.1 and 2.4.3.2, respectively. The vast majority of lanthanide-based persistent luminescence materials employ Eu^{2+}, thus most of the mechanistic studies have been carried out on these materials. Given our interest in Pr^{3+}, however, we will focus on the persistent luminescence models with examples from Pr^{3+}-materials wherever possible. The observation of persistent luminescence from Pr^{3+} and subsequent development of Pr^{3+} persistent phosphors was driven by the need for red persistent luminescence materials, since most of the Eu^{2+} persistent luminescence phosphors emit green/blue. The $^1D_2 \rightarrow {}^3H_4$ and $^3P_0 \rightarrow {}^3H_6$ transitions of Pr^{3+} around 600 nm give rise to the desired red persistent luminescence. Nearly all of the singly-doped Pr^{3+} persistent luminescence materials are based on oxide/complex oxide hosts[83,124–128], with the majority of hosts being titanates[78,85,94,126,129–131],

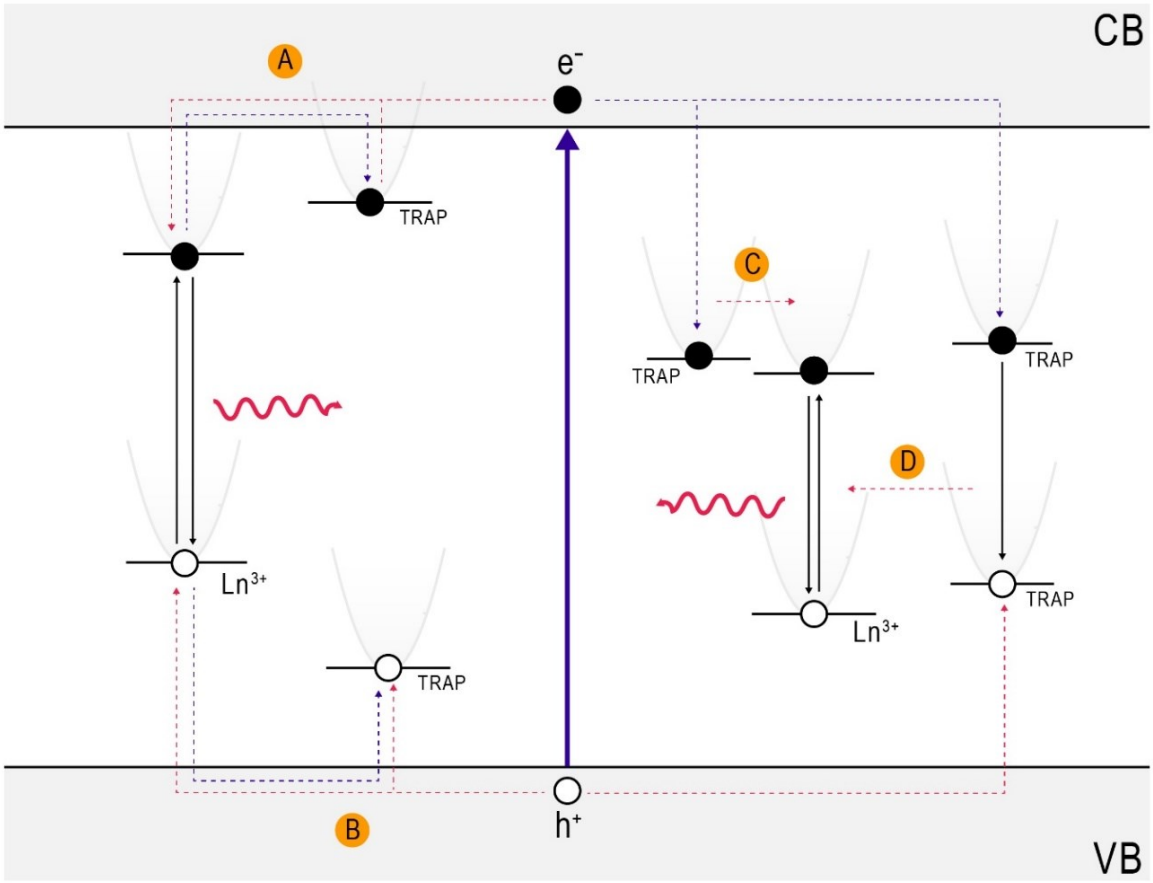

Figure 8. Schematic of the global and local trapping models. Dark blue arrows depict excitation/trap filling processes, pink arrows depict emission/de-trapping processes. Global models rely (A) on electrons being trapped after migration through the conduction band or (B) on holes being trapped after migration through the valence band before recombining at a luminescent lanthanide center (Ln^{3+}). Local models rely on direct de-trapping from traps to lanthanide centers in processes such as (C) tunneling or (D) self-trapped exciton (STE) mediated recombination and energy transfer to luminescent centers. Configuration coordinate parabolas are qualitative. CB: conduction band, VB: valence band.

gallates[81,132–135], and gallogermanates[84,136–139]. Notably, there are comparably few fluoride materials reported to exhibit persistent luminescence.[140,141]

2.4.3.1. Global (de-)trapping models

Global models rely on the concept that luminescence centers change oxidation states during the (de-)trapping processes, and that the bandgap of the material is narrow enough that prolonged charge delocalization is feasible.[142–144] As such, the likelihood for a lanthanide ion to form a +1, +2, +3, or +4 oxidation state becomes important, along with the positions of the energy states of

the lanthanides in these oxidation states relative to the conduction and valence bands.[123,145] For this reason, HRBE/VRBE diagrams usually incorporate the energy levels of lanthanides in both the +2 and +3 oxidation states. Evidence of the formation of different oxidation states is typically obtained from electron paramagnetic resonance (EPR) spectroscopy, or photoconductivity measurements.[116,146,147]

The first detailed persistent luminescence mechanism ever proposed was that of Matsuzawa *et al.* to describe the persistent luminescence from $SrAl_2O_4:Eu^{2+},Dy^{3+}$.[147] It is a global model which proposes that holes were the main charge carriers involved, and that trapping and de-trapping occurred through migration of holes *via* the valence band due to changes in the oxidation states of Eu^{2+} and Dy^{3+}. The model relied on the presence of Dy^{3+} and therefore did not account for persistent luminescence from singly-doped $SrAl_2O_4:Eu^{2+}$, and it described the highly unlikely formation of Eu^{+} and Dy^{4+} species. Thereafter, the models of Tanabe[148], Aitasalo[149], Dorenbos[150] and Clabau[151] were developed to account for these deficiencies of the original Matsuzawa model. Notably, Tanabe, Dorenbos and Clabau proposed models involving exclusively electron trapping/de-trapping *via* the conduction band, and Aitasalo later proposed a mechanism[152] combining those of Dorenbos and Clabau. Since then, the majority of mechanisms propose electrons as the main charge carriers in a variety of materials.[101,102] A graphical depiction of a global trapping model is shown in Figure 8.

The positions of the lanthanide energy states relative to the valence and conduction bands of the host for each oxidation state informs on the likelihood of an ion to act as either an electron trap or a hole trap, if the traps are not formed solely by defects. Dorenbos and Bos determined that the trap depth of a trivalent lanthanide (Ln^{3+}) to act as an electron trap is approximately the energy difference between the ground state of the divalent lanthanide (Ln^{2+}) and the bottom of the conduction band.[123] Conversely, when the ground state of Ln^{3+} is a few eV above the top of the valence band, Ln^{3+} may act as a hole trap and form Ln^{4+}. Generally, Sm^{3+}, Eu^{3+}, Gd^{3+} and Yb^{3+} form stable electron traps, while Ce^{3+}, Pr^{3+} and Tb^{3+} are common hole traps. All can act as recombination centers and can also be paired to engineer persistent luminescence materials with precisely tuned trap depths.[113]

$CaTiO_3:Pr^{3+}$ and $YPO_4:Pr^{3+},Ho^{3+}$ are well-understood examples of Pr^{3+} persistent

luminescence materials with mechanisms under the global model framework.[83,85] Both of these materials provide red persistent luminescence from Pr^{3+}, and in both cases Pr^{3+} acts as a hole trap. $CaTiO_3$ is unique because its predominant emission is from the $^1D_2$ state, whereas in most materials, Pr^{3+} luminescence comes predominately from the $^3P_0$ level.[146] For $CaTiO_3$, a defect cluster comprised of $[Pr^{3+}Ti^{3+}O_3]^+$ gives rise to charge trapping as determined by EPR spectroscopy.[146] Ti^{4+} acts as an electron trap and thus the mechanism ($Pr^{3+} + h^+ \rightarrow Pr^{4+}$, $Ti^{4+} + e^- \rightarrow Ti^{3+}$) involves charge transfer between the activator and the host material.[94,153] $CaTiO_3$ has a bandgap around 3.5-3.8 eV[94,154], thus charges are easily delocalized in this material, and charge transfer is quite feasible between the different ions. Notably, this charge transfer band is responsible for the quenching of the $^3P_0$ emissions, in addition to the persistent luminescence. In $YPO_4:Pr^{3+},Ho^{3+}$, the Ho^{3+} ions act as the electron traps, in line with the positions of its energy states relative to the conduction band in the +2 oxidation state, as previously mentioned. In this case, electron de-trapping occurs *via* the conduction band to recombine at Pr^{3+} and produce red luminescence. Importantly, however, an additional de-trapping pathway was observed in $YPO_4:Pr^{3+},Ho^{3+}$ that does not involve the conduction and valence bands. The bandgap of YPO_4 is 9.23 eV[92], thus charges are less-easily delocalized than in $CaTiO_3$ for example, and thus there are more opportunities for alternative mechanisms to occur. This material functions under both the global and local trapping mechanisms.

2.4.3.2. Local (de-)trapping model

In some cases, the persistent luminescence mechanism cannot be explained under the framework of lanthanides acting as electron and hole traps *via* the conduction and valence bands. In a local mechanism, charges directly recombine from two spatially-localized species with no involvement from the valence and conduction bands.[155] The direct trap-center recombination processes primarily occur *via* quantum tunnelling, but charge transfer between defect clusters, and exciton recombination that induces energy transfer to excite the luminescent center *via* energy transfer are also known (Figure 8).[122] In many cases, it is difficult to precisely ascertain if one or more of these processes is occurring. Local processes are generally more likely in wide bandgap materials where charge delocalization is not easily attained, or in singly-doped materials.[144] Often, the local processes are observed in addition to a global mechanism, as was the case for $YPO_4:Pr^{3+}$, Ho^{3+}.[83]

The local component of the persistent luminescence mechanism for $YPO_4:Pr^{3+}$, Ho^{3+} was determined to be due to tunnelling processes.[83] Electron tunneling is a quantum phenomenon; put simply, it is the phenomenon of an electron traversing through a classically-insurmountable potential energy barrier. Tunneling recombination depends on the energy required to surpass the tunnelling barrier (it is easiest to visualize this concept when energy states are viewed as potential energy parabolas), and on the distance between the separated charges.[122] In this case, the concentration of traps and recombination centers will strongly affect the tunneling process. Tunneling can be athermal or thermally-assisted. This is easily determined by observing whether or not persistent luminescence occurs at low temperatures, since usually thermal energy is required to liberate the trapped charge. Low-temperature thermoluminescence measurements are highly useful in these scenarios. Tunnelling is relatively common, and is reported in several Pr^{3+} materials such as $Ca_2Ga_2GeO_7:Pr^{3+}$, $(Gd_xLu_{3-x})Ga_3Al_2O_{12}:Pr^{3+}$, $LiSrAlF_6:Pr^{3+}$, $Cs_2NaYF_6:Pr^{3+}$ and $Lu_2Si_2O_7:Pr^{3+}$.[139–141,156]

In a local framework, the energy of the trap states and their position in the forbidden band relative to the excited states will also determine which bands give rise to persistent luminescence. When direct recombination takes place to generate persistent luminescence, it has been demonstrated that recombination at the ^3P_J levels of Pr^{3+} will occur when the trap energies are resonant with these levels, and emission from the higher states ($^1S_0$ and $4f^15d^1$) is either not observed[86,156,157], or occurs *via* an alternate mechanism involving the conduction band[140]. In $LiSrAlF_6:Pr^{3+}$, only LOL emissions are observed during persistent luminescence while all the 4f→4f emissions are observed during X-ray excitation (including from the $^1S_0$ level).[141] In this case, the presence of a broad emission overlapping with the emission from the $^1S_0 \rightarrow {}^1I_6$ transition of Pr^{3+} was observed and is attributed to the presence of a self-trapped exciton (STE). This feature allowed for the proposal of an STE-mediated local model of Pr^{3+} persistent luminescence, rather than a tunneling recombination. However, no thermoluminescence studies were performed so it is not clear whether or not tunneling recombination may also contribute to the observed persistent luminescence. Often, multiple potential mechanisms are proposed when a model doesn't fully exclude other options or can't fully explain the phenomenon. In summary, the mechanisms that can give rise to persistent luminescence are numerous, and can vary for the same ion in different materials depending on the likelihood of each mechanism.

2.4.4. Timescale of persistent luminescence

When reading about persistent luminescence, one aspect becomes rapidly evident: the means used to quantify the duration of the phenomenon vary, and often the method used to obtain the value is not even reported.[99,145,158] The traditionally established method to determine the persistent luminescence duration is to observe the time taken for the luminescence to decay to 0.32 $mcdm^{-2}$ measured at a viewer angle of 65.54°, which corresponds to 100 times the lower limit of the scotopic vision of the human eye.[145] This value was established based on the requirements for safety signage, and is not optimal for several reasons: it is not useful for UV and NIR wavelengths that are not visible to the human eye, the human eye is more sensitive to green wavelengths thus blue or red-emitting phosphors are at a disadvantage, and many phosphors are known to exhibit persistent luminescence that is visible to the unaided eye for far longer than this time.[107,158,159] However, perhaps the most important limitation is that this value does not have relevance for inducing a biological effect. Clearly, the requirements for safety signage would be different than those required to elicit a therapeutic effect in cells, for example. Because of this, it is commonly suggested that the durations reported in the literature should be taken based on the order of magnitude (minutes, hours, days) rather than the exact time.[101,102]

2.5. Summary

In summary, inorganic materials can exhibit a wide range of luminescence phenomena, especially when lanthanides are involved. The interaction of ionizing radiation with materials is dependent upon the energy of the incident photons and the properties of the absorbing material. Relevant to the work here, materials with high density and large effective atomic numbers tend to facilitate strong interactions with keV X-rays, and when doped with lanthanide ions, can undergo radioluminescence. Moreover, Pr^{3+} can exhibit a variety of different luminescence phenomena when excited with X-rays: photon cascade emission, radioluminescence and persistent luminescence. Each of these properties is facilitated by the energy level structure of Pr^{3+}, where the $^1S_0$ excited state is energetically-separated from the other excited states (called LOLs) by 26,500 cm^{-1}.

Persistent luminescence is a highly complex phenomenon with a history spanning hundreds of years. Presently, our understanding of the mechanisms behind this property are far from

complete. However, as more persistent phosphors are developed, our understanding of their operating principles becomes clearer, and trends can be identified through relations to other materials. We now know that there is strong evidence for both global and local models, and that the use of referred binding energy schemes can be very helpful in determining these mechanisms, along with thermoluminescence spectroscopy.

The rapid rise in nanomaterials research has also led to the idea of using persistent luminescence materials in bioimaging, owing to the advantage that there is no need for *in situ* excitation and therefore extremely high signal-to-noise ratios can be achieved.[160–163] This new application of persistent luminescence has spurred significant interest in the field, especially at the nanoscale, in combination with other luminescence-driven phenomena. The combined luminescence properties of Pr^{3+} in fluoride hosts under X-ray excitation enable the potential for their use in medicine, building upon advancements made in the medical field and addressing some challenges as well. Glioblastoma is a disease which may benefit from the new avenues of treatment brought about using nanoparticles.

Chapter 3. Introduction to therapeutics

Novel therapeutic and diagnostic agents based on lanthanide-doped nanomaterials have been at the core of the research into light-based nanomedicine. From radioluminescence to upconversion and persistent luminescence, the versatile luminescent properties that are enabled by lanthanides have the potential to produce new treatment modalities, but also to vastly improve current clinical practices. Since clinical treatments are (obviously) established to be sufficiently safe for humans, there is merit to finding ways of using nanoparticles to build upon these techniques, as there is a strong and valid foundation to build upon. In some instances, the addition of nanoparticles allows us to combine treatments that were previously not compatible in practice. The work herein aims to merge fluorescence-guided surgery, intraoperative radiotherapy and photodynamic therapy into a single treatment modality in the context of glioblastoma. To understand how we envision this to work, we will first discuss each of these techniques based on their use in treating cancer, with a focus on glioblastoma wherever possible.

3.1. Glioblastoma

Glioblastoma, also called glioblastoma multiforme (GBM) and high-grade glioma[164,165], is the most common type of brain/central nervous system (CNS) cancer, accounting for nearly half of brain/CNS cancers diagnosed in the United states in 2020.[166–168] Unfortunately, it is also the most aggressive type of brain/CNS cancer. As of 2021, the median overall survival of patients is 16-18 months, and the five year survival rate was 7% between 2013 and 2017.[167] Glioblastomas are a grade 4 (high-grade) cancer according to the World Health Organization (WHO); this is the highest grade possible. Most glioblastomas are primary (de novo) tumors, meaning they are grade 4 from the beginning, rather than progressing from a lower-grade tumor type.[169] Other than overexposure to ionizing radiation, there are no known etiologies of glioblastoma. Even more alarming, glioblastoma is considered to be inevitably recurrent, with the majority of recurrences occurring within 2 cm of the original tumor site.[170–172] For all of these reasons, it is suggested that palliative care be initiated at diagnosis.[169] Recently, advancements in the understanding of glioblastoma at a molecular level essentially revolutionized the way oncologists and researchers understood and diagnosed brain cancers. In 2016, the WHO re-classified brain tumors and introduced new schemes for identifying and diagnosing gliomas according to their molecular

presentations rather than their histological features, which was further revised and improved upon in the 2021 edition of the classification system.[168] By understanding the molecular biology of these tumors, there is hope that researchers can better understand how glioblastoma continually evades treatment and thus how to more effectively help patients diagnosed with this disease. An in-depth discussion on the molecular features of glioblastoma can be found in Appendix 2.

3.1.1. Features of glioblastoma

Classically, glioblastoma was thought to originate exclusively from glial cells (astrocytes, microglial cells or oligodendrocytes) due to their similar histologies. Today, there are three accepted possibilities for the origin of glioblastoma: mature glial cells, neural stem cells, and oligodendrocyte precursor cells.[173] In other words, it is currently not known what cells give rise to glioblastoma, but it is possible that many different cell types can give rise to it. This uncertainty makes it more difficult to understand the fundamental aspects and progression of the disease, which in turn makes it more difficult to develop an effective treatment.

Glioblastoma is a highly invasive cancer. As mentioned before, it is inevitably recurrent. The recurrence is due to the diffuse nature of the tumor, meaning there is little delineation between healthy and malignant cells at the tumor edges. Moreover, glioblastoma cells are able to detach from the primary tumor and travel along neural pathways to infiltrate healthy tissue, further contributing to their diffuse and highly recurrent nature.[174] The most common invasion route is through blood vessels. To be characterized as glioblastomas, the tumors must have strong microvascular angiogenesis; a necrotic core is a hallmark diagnostic feature of the disease.[168–170,174] Tumor hypoxia is considered to be a major factor in cell migration and invasion into nearby healthy tissue, where oxygen concentrations are higher since healthy tissues are not growing as rapidly.[175]

3.1.2. U251: An immortal glioblastoma cell line

The immortal human glioblastoma cell line, U251, was used for the studies throughout this thesis as an *in vitro* glioblastoma model. U251 was established in the 1960's at the Wallenberg laboratory in Uppsala, Sweden.[176] It is a line originating from a 75 year old Caucasian male originally diagnosed with astrocytoma in the parietal region of the brain.[177–179] Genetically, the line is characterized as isocitrate dehydrogenase (IDH) wildtype, has mutations in the telomerase

reverse transcriptase (TERT) promoter, a duplication of the epidermal growth factor receptor (EGFR) gene on chromosome 7, additional chromosomes 3, 7, 15 and 17, a deletion of chromosome 10, 13 and 14, a homozygous mutation in TP53, a deficiency in PTEN, deletions of p16 and p15, and a mutation in p21 (see Appendix 2 for more information).[176,178–181] Importantly, the U251 cell line has a homozygous missense mutation in the TP53 gene which encodes the $p53^{R273H}$ protein.[181–183] This mutation is associated with the accumulation of mutant p53 proteins in the nucleus of the cell, leading to a poor prognosis. This is somewhat counter-intuitive, as high levels of a tumor suppressor protein sound like a good means of suppressing tumors. However, because the mutated tumor suppressor cannot perform its intended function, and it has additional pro-cancer functions, high levels of it are deleterious. In essence, U251 has mutations in all of the main genes that correlate with high treatment resistance and a very poor prognosis.

3.2. Treatment options for glioblastoma

Despite the major advancements in the understanding of genetics and molecular biology of glioblastoma, there has been little progress over the past several decades in extending the lifespan of glioblastoma patients as previously mentioned. However, this has led to the development of a myriad of treatments, in an attempt to improve the prognosis for this disease. This section aims to give an overview of the current treatment options, and a discussion on some of the technologies that we aim to exploit in this work.

3.2.1. The current standard of care

In 2023, the standard line of treatment for patents newly-diagnosed with primary glioblastoma is maximal safe surgical resection, followed by radiotherapy and chemotherapy.[184] The current standard of care, known as the Stupp regimen, was introduced in 2005 after determining adjuvant chemoradiotherapy with temozolomide resulted in better treatment outcomes than radiotherapy alone post-resection.[185] In this protocol, the radiotherapy component consists of a 60 Gy dose given in 1.8-2 Gy fractions administered five days per week for a total of six weeks, and temozolomide is orally administered daily during radiotherapy, and intermittently for an additional 6 months thereafter.[186]

Importantly, chemo- and radiotherapy are only begun after a waiting period, up to 4 weeks,

to allow for healing after surgery.[169] The diffuse nature of glioblastoma tumors means that it is essentially impossible to completely remove all of the malignant cells, and thus the healing period unfortunately also allows time for the cells to begin proliferating again. When recurrence inevitably happens, there is no standard of care treatment. Instead, a combination of re-resection, radiotherapy, systemic therapies and palliative/supportive care are explored.[186]

3.2.2. Surgical Resection

Since maximal safe surgical resection is the first line treatment for glioblastoma, there has been a major push toward developing high-precision surgical techniques. A greater extent of resection is correlated with a longer progression-free survival.[169,184,186] However, this has to be balanced with saving as much healthy brain tissue as possible, since a major loss in neurological function would drastically reduce the quality of life of the patient, even if they were to survive. This is known as the "oncofunctional balance" and is a paramount reason that there is any tumor margin left behind at all.[187] This is especially true if the tumor is close to a particularly important structure like the brain stem, for example. Advancements in imaging both prior to and during surgery have enabled a more precise delineation of the tumor, leading to much higher extents of resection. The main techniques currently responsible for such advancements are intraoperative image-guided surgery using magnetic resonance imaging (MRI) and ultrasound, and fluorescence guided surgery. Real-time imaging represents an obvious advantage, but requires dedicated imaging suites for an operating room, and is not easily implemented in every hospital. Fluorescence guided surgery, however, can be implemented using only a simple light source attached to a pair of surgical loups.[188]

3.2.2.1. Fluorescence guided surgery

Fluorescence guided surgery relies on the visualization of fluorescence in malignant tissues as a marker to resect them. In this way, surgeons can directly visualize by eye what tissue needs to be resected without the need for expensive equipment and digital image processing. This technique is most commonly performed using 5-aminolevulinic acid (5-ALA), which is approved for this purpose, or sodium fluorescein which is under investigation as an alternative.[187,189] The main difference in the two approaches is 5-ALA is naturally converted into a fluorescent molecule that accumulates in cancer cells, and fluorescein is passively uptaken by malignant cells *via*

disruptions in the blood-brain barrier. Moreover, since 5-ALA is the only approved option, and it is also used in photodynamic therapy (see Section 3.5.4); we will focus on how fluorescence guided surgery is achieved using this treatment.

3.2.2.2. 5-Aminolevulinic acid

5-ALA is an amino acid that participates in the heme biosynthesis pathway in mammals.[190,191] 5-ALA is naturally produced in mammals from the condensation of glycine and succinyl coenzyme A, but is also administered orally as a pro-drug to induce the production and accumulation of PPIX with high specificity in malignant tissues.[192] Alterations in the heme biosynthesis pathway in malignant cells are what enable the specific accumulation of PPIX in

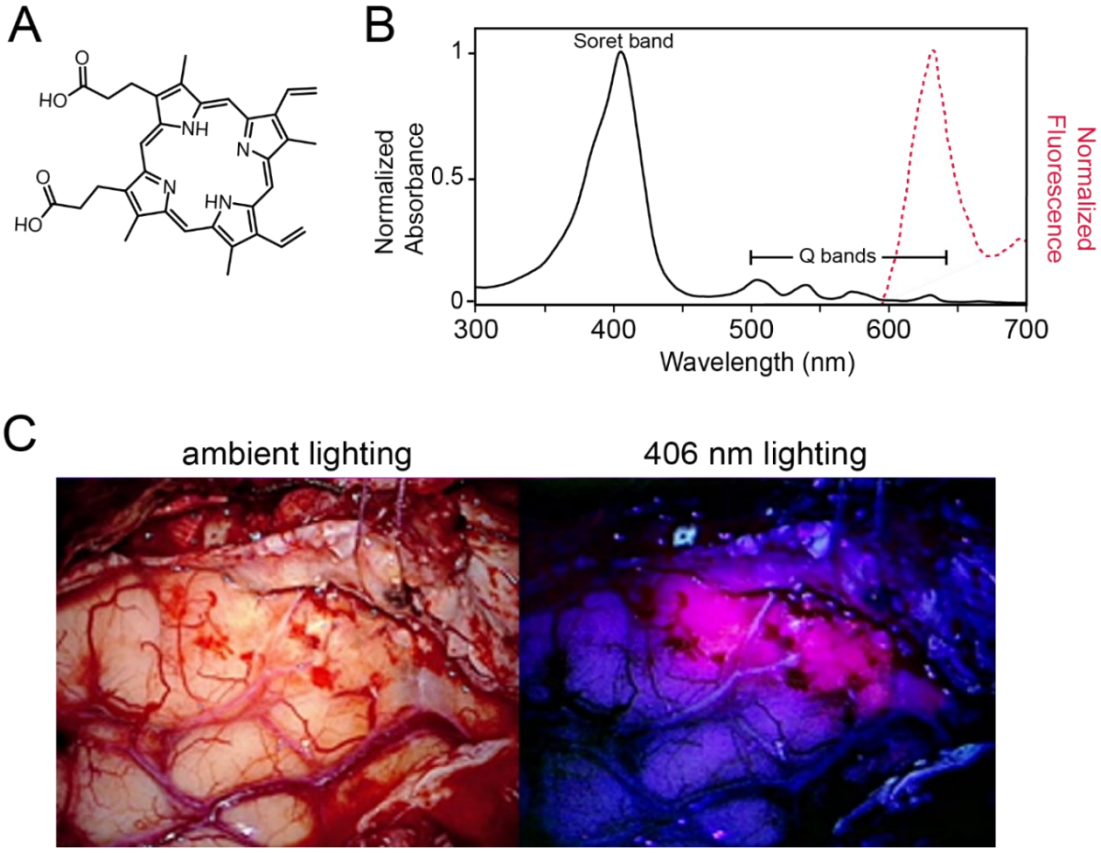

Figure 9. A) Chemical structure of PPIX, B) Normalized absorption and emission spectra of PPIX with the Soret and Q bands labelled, C) Photographs of a glioblastoma tumor before fluorescence-guided resection using Gleolan® under ambient lighting and 406 nm lighting. Healthy tissue fluoresces blue while malignant tissue fluoresces red-violet due to high levels of PPIX accumulated in the cancer cells. Photographs reproduced with permission from CHI Health St. Francis and KSNB Local4 newsroom.

tumors.[193] Importantly, 5-ALA is able to cross the blood-brain barrier, which is essential for its ability to demarcate glioblastoma.

PPIX is a hydrophobic, aromatic organic molecule as shown in Figure 9A. The absorbance and fluorescence spectra of PPIX are shown in Figure 9B. PPIX can be excited into the strongly-absorbing Soret band, at 406 nm, or into the weaker Q bands in the visible region. PPIX exhibits strong red-violet fluorescence upon excitation, as shown in Figure 9C. According to the FDA-approved regimen for fluorescence guided surgery, PPIX reaches maximum plasma levels at an average of 4 hours after oral administration of 5-ALA (Gleolan®).[194] *In vitro* studies also commonly report PPIX concentration maxima at 4 hours[195–198], though maxima at longer times have also been reported.[199]

3.2.2.2.1 The heme biosynthesis pathway

As shown in Figure 10, the first step begins with importing exogenous 5-ALA into the cell via membrane transporters. Once 5-ALA reaches the cytoplasm, the first 5 steps of the heme biosynthesis pathway are carried out, generating coproporphyrinogen III. The ATP-binding cassette super-family B member 6 (ABCB6) transporter then imports coproporphyrinogen III into the mitochondria, where it is transformed into protoporphyrinogen IX, the precursor to PPIX (our target molecule). The ferrochelatase enzyme then inserts an iron atom into the porphyrin core of PPIX, forming heme. Alternatively, PPIX can be shuttled out of the mitochondria into the cytosol by ABCG2 membrane transporters.[200]

The reason for the preferential accumulation of PPIX in cancer cells is not fully understood, but is likely due to a combination of changes in the expression of molecular transporters and dysregulation of enzymes involved in heme biosynthesis.[193,200–202] The ABCB6 transporter, responsible for shuttling coproporphyrinogen III from the cytosol to the mitochondria, is known to have higher expression levels in glioma patients with grade III and IV (glioblastoma) tumors.[202] Further, the enzymes coproporphyrinogen oxidase (CPO) and protoporphyrinogen oxidase (PPO) are known to be overexpressed, along with porphobilinogen deaminase (PBDG), causing increased PPIX synthesis. [200,203] Combined, these changes in physiology are thought to aid in production of PPIX in gliomas. Additionally, reduced expression of ATP-binding cassette super-family G member 2 (ABCG2), a transporter responsible for PPIX efflux, is known, along with changes in

the expression of ferrochelatase, the enzyme that converts PPIX to heme.[191,193,204,205] These two components are thought to be responsible for the preferential accumulation of PPIX in these cells. However, there is some conflicting data that also suggests ferrochelatase is upregulated, which would mean the overall heme biosynthetic pathway is upregulated. This data suggests it is the decrease in ABCG2 that is the overriding factor in the high PPIX concentrations in malignant cells.[200] Understandably, it is difficult to determine what processes are most important, especially given that most gliomas are heterogenous in their protein expression as described earlier.

Based on knowledge of the heme biosynthetic pathway, researchers are looking at these targets for improving PPIX accumulation in hopes of making it even easier to distinguish healthy and diseased tissue, and also for maximizing the effects of 5-ALA mediated photodynamic therapy, described in Section 3.5.4.

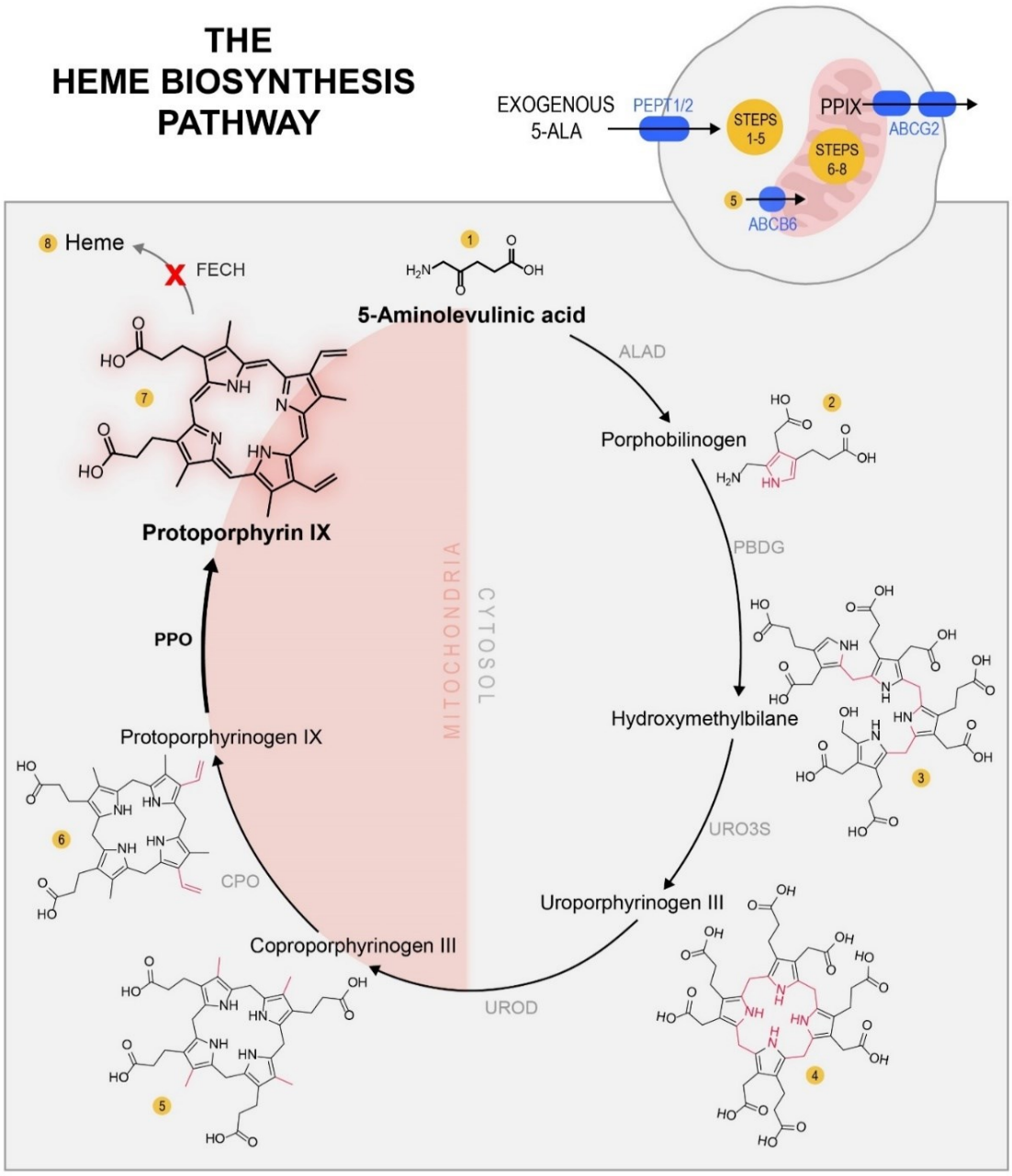

Figure 10. The heme biosynthesis pathway upon administration of exogenous 5-aminolevulinic acid. 1) 5-ALA is converted into 2) porphobilinogen by aminolevulinic acid dehydrogenase (ALAD). Porphobilinogen is converted into 3) hydroxymethylbilane by porphobilinogen deaminase (PBDG), followed by conversion to 4) uroporphyrinogen III by uroporphyrinogen III synthase (URO3S). Uroporphyrinogen III is then converted into 5) coproporphyrinogen III by uroporphyrinogen III decarboxylase (UROD). Coproporphyrinogen III is then shuttled into the mitochondria from the cytosol and converted into 6) protoporphyrinogen III by coproporphyrinogen III oxidase (CPO). Protoporphyrinogen III is then converted into 7) protoporphyrin IX by protoporphyrin III oxidase (PPO) which is upregulated in glioblastoma cells. Protoporphyrin IX is then converted into 8) heme by ferrochelatase (FECH), which is downregulated in glioblastoma cells, leading to the accumulation of fluorescent protoporphyrin IX.

3.2.3. Radiotherapy: principles of radiobiology

With respect to all cancers, radiotherapy is estimated to benefit approximately half of all cancer patients worldwide.[206] In many cases it is performed before surgical resection or in the absence of it, however, for glioblastoma radiotherapy is performed after surgical resection as discussed in Section 3.2.1 and Appendix 3. For brain cancer, it is an essential means of extending the lifespan of patients: median survival for patients receiving resection alone is 3-6 months, while the addition of radiotherapy extends survival to one year.[207] Adjuvant chemotherapy with temozolomide alongside radiotherapy (ie. the Stupp protocol[185]) extends the median survival to 14 months. As such, radiotherapy is a first-line treatment for glioblastoma, and approximately 80% of glioblastoma patients receive it.[208] There are several different types of radiotherapy used in glioblastoma, which range in terms of the radiation source, radiation dosage, and localization of the treatment. The biological basis for all of these techniques, however, is the same.

3.2.3.1. Biological basis for radiotherapy

The most basic role of ionizing radiation as a treatment modality is in inducing irreparable damage to DNA, thus preventing malignant cells from proliferating. In reality, the role of ionizing radiation in treating cancer is more complex, and involves more than just DNA damage *via* direct interaction of ionizing radiation and the DNA itself. As mentioned in Section 2.1, there are three different modes of interaction of ionizing radiation with matter. For the sake of our discussion, we will again restrict ourselves to photon-based interactions that occur *via* the photoelectric effect in the keV range.

The interaction of ionizing radiation with tissues changes as a function of photon energy, as described by the linear attenuation coefficient (equation 1 in Section 2.1). Importantly, the depth of dose maximum increases with photon energy.[7] It is this relationship which allows oncologists and medical physicists to precisely deliver the correct radiation dose to tumors at a specific depth, while (mostly) sparing the skin. X-rays induce biological damage *via* a two-step process: first, photons are absorbed by tissues (ie. mostly by water), producing secondary electrons, which can then continue to interact with biomolecules and organelles and deposit energy to cause breaks in chemical bonds or additional ionizations (Figure 11).[7,208]

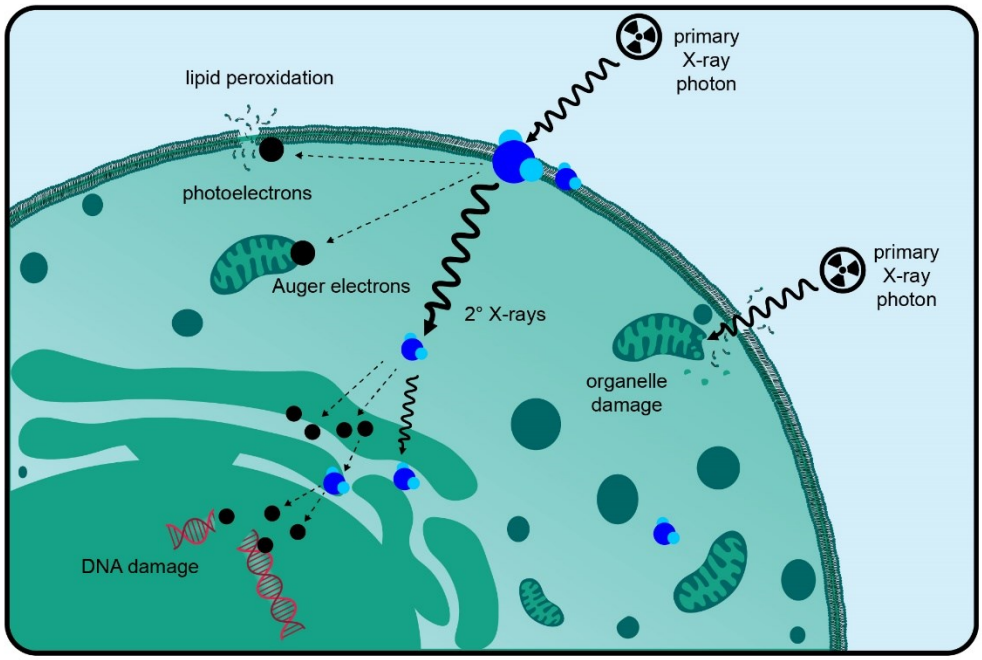

Figure 11. Graphical depiction of the interaction of X-rays with tissues during radiotherapy. An incoming primary X-ray photon can interact with water to produce secondary electrons (photoelectrons and Auger electrons) or secondary X-rays, causing a cascade of secondary ionization events. Alternatively, the primary photon can interact directly with a biological target such as a mitochondria as depicted here. The ejected electrons can also damage the lipid bilayer, DNA and other targets.

These initial interactions occur extremely quickly, at sub-femtosecond timescales. It is estimated that the high-speed electrons produced can traverse an entire mammalian cell in 100 fs.[208] The secondary electrons and ionization events are what give rise to the majority of damage to cells. 1 Gy of radiation produces on average 10^5 ionizations in a cell with a diameter of 10 μm. Much of the primary ionizations occur upon interaction of the photons with water, since it constitutes 80% of a cell.[209] The radiolysis of water primarily results in the formation of water radical cations and ejected solvated electrons, which can further react to produce hydroxyl radicals. These are all highly reactive and have sub-nanosecond lifetimes, limiting their diffusion to tens of nanometers across a cell. Radicals can induce damage to a variety of targets, but since DNA is the largest molecule in a cell, it constitutes the largest target. Notably, the hydroxyl radicals produced *via* the radiolysis of water are estimated to generate two-thirds of the DNA damage caused by X-ray radiation. Other targets of the radiolysis products of water are proteins, lipids and carbohydrates, all of which disrupt homeostasis and can trigger cell stress and cell death (see Section 3.2.3.3).[210] In 1970, this was proven using polonium-tipped microneedles precisely aimed

at the cytoplasm or nucleus of Chinese hamster fibroblast cells.[211] Large doses of radiation delivered to the cytoplasm of the cells did not cause any loss of proliferative capacity, while the delivery of only a few alpha particles to the nucleus of the cells caused almost immediate reproductive arrest.

As ionizing radiation traverses a medium, the energy deposition tracks are not uniform. Instead, the dose is deposited in the form of clusters of varying sizes.[212] When the ionization clusters occur in the proximity of DNA, they either directly ionize DNA or produce additional hydroxyl radicals that can then interact and cause damage. There are four main types of DNA damage (Figure 12) – double strand breaks (DSBs), single strand breaks, base damage/loss, and strand cross links.[208,212]

The DNA damage repair machinery can efficiently repair single strand breaks, cross-linking and base damage; DSBs are more difficult to repair and are thought to be most associated with causing cell death.[212] However, because of the formation of ionization clusters, there tends to be multiple lesions induced within a small region of the DNA strand, thus the non-DSB modes of damage can also become lethal because of the difficulties associated with repairing many lesions in close proximity.[208] The mutations found in cancer cells are often associated with the DNA

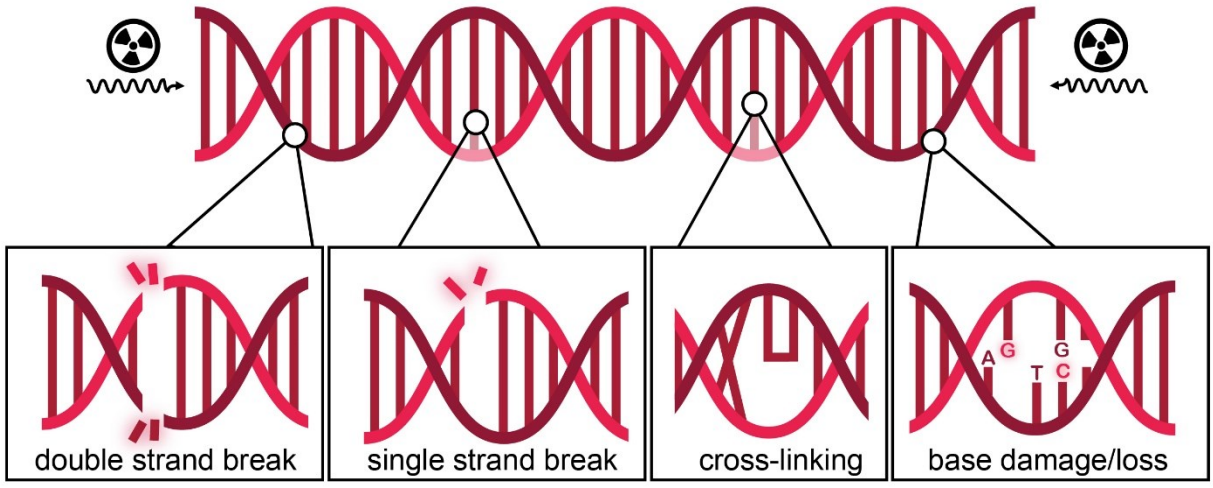

Figure 12. The four types of DNA damage caused by ionizing radiation: double strand breaks, single strand breaks, cross-links and nucleobase damage and loss.

damage repair mechanism, allowing for increased damage repair capability, or the ability to evade cell death despite the presence of DNA lesions.

3.2.3.2. The DNA Damage Response Pathway

When DNA is damaged by ionizing radiation (or any other cause), a series of steps occur that either lead to repair or death. By understanding the pathway, we are better equipped to evaluate how a cell is responding to the damage, and consequently we are better able to predict its fate. The pathway is briefly summarized in Figure 13, with attention paid to biomolecules discussed in this work. For extensive explanations of all components of the DNA damage response pathway, the reader is referred to several publications.[208,213,214]

First, the damage must be detected by sensor proteins, which are each designated with sensing a certain type of damage.[208] The ataxia telangiectasia mutated (ATM) protein is activated by a group of proteins (MRE11, RAD50 and NBS1) called the MRN complex, which detect DSBs. The DNA-dependent protein kinases (DNA-PK) are activated by the Ku70 and Ku80 sensor proteins, also in response to DSBs. The ataxia telangiectasia and Rad3-related protein (ATR) does not sense DSBs, rather, it senses the single strand breaks and other damage types.

Once the sensor proteins have been activated, a cascade of events occurs. Of major importance, many copies of the histone h2a family member X (H2AX) protein are phosphorylated at the site of a DSB, in both directions along the DNA strand. The phosphorylated form of H2AX is known as γH2AX, and is phosphorylated by all three major sensor proteins (ATM, ATR and DNA-PK).[214] The large regions of γH2AX, known as foci, act as a signal to the repair proteins that DNA damage has occurred, and keep the broken strands in place.[214] For context, γH2AX foci are so large that they can be stained and detected by light microscopy. Thus, detection of elevated γH2AX levels or of these foci are a straightforward means of confirming DNA DSBs have occurred. Poly-ADP-ribosylation-polymerase 1 and 2 (PARP1 and PARP2) also play an important role in signaling for all types of DNA damage, not just DSBs. However, PARP1 not only acts to signal DNA damage has occurred, the cleavage of this protein also indicates apoptosis has been initiated (Appendix 2).[208,215]

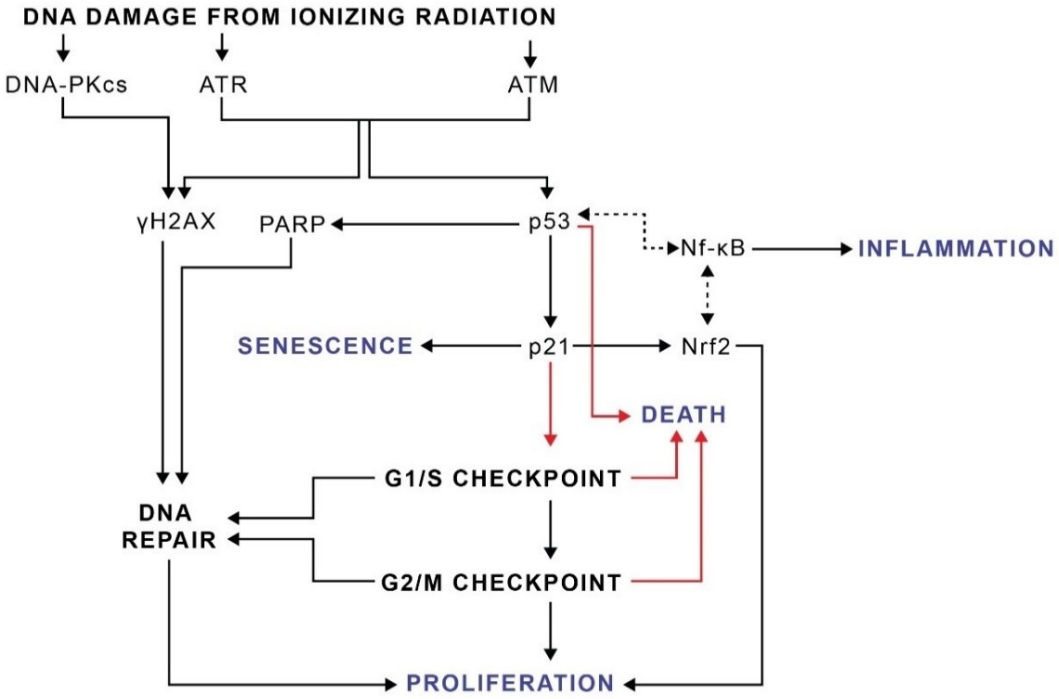

Figure 13. Simplified schematic of the DNA damage response pathway and other relevant proteins that lead to cell death, senescence, inflammation, or proliferation.

In addition to H2AX, the ATM and ATR proteins also activate p53, which is at the center of a wide variety of signalling events. The p53 protein is known as the "guardian of the genome" and controls the fate of the cell, ie. whether or not apoptosis should be activated.[208,210,216] To this end, p53 plays a role in activating the G1/S cell cycle checkpoint (Appendix 2), and in activating several downstream proteins that can activate apoptosis directly, or proteins that mediate other cell responses such as nuclear factor kappa-light-chain enhancer of activated B cells (NfκB) which mediates inflammation[217,218], and p21 which can initiate senescence[219], for example. Relevant to the PDT effect, p53 and p21 are also activated in response to oxidative stress/ROS, and p21 contributes to activation of Nrf2, a powerful regulator of oxidative stress.[220]

3.2.3.3. Cell death

The Nomenclature Committee on Cell Death defines cell death as cells which permanently cease the ability to function and exhibit irreversible loss of membrane integrity.[221,222] With respect to radiotherapy, however, it also encompasses the fate of cells which are alive but unable to

reproduce; this is known as senescence (discussed below).[208] Cell death can either be programmed or spontaneous, depending on the degree of injury. There are several types of cell death, and new modes are being discovered as advances in technology and molecular biology are made. These include the most commonly-encountered modes: necrosis, apoptosis, autophagy, and senescence. A detailed explanation of each of these types of cell death is provided in Appendix 2. Additional modes of programmed cell death have also been discovered within the past two decades, suggesting cell death is considerably more complex than our current understanding of it.[222–224]

3.2.3.4. The timescale of cell death

Unprogrammed (accidental) cell death, such as primary necrosis, is virtually instantaneous, owing to severe trauma.[221] In contrast, apoptosis and other forms of programmed cell death occur on significantly longer timescales. Mentioned in Appendix 2, there are 3 stages of apoptosis. From the initial treatment to complete dissolution of the cell, the physical process of apoptosis takes about 2 hours, but may occur days after treatment.[225] Treatment with ionizing radiation causes cell cycle arrest, and the cycle during which the cells are irradiated can drastically affect how long it takes for apoptosis to be completed.[226] Sometimes it may even take two or more cycles of cell division for a cell to commit to dying, depending on the degree and mode of damage. These modes of death are known as mitotic catastrophe, delayed mitotic death, and post-mitotic apoptosis and are commonly observed in radiotherapy treatments.

Mitotic catastrophe is the failure of a cell to complete mitosis.[208,221] This occurs due to the accumulation of mutations or lesions to DNA during successive rounds of cell division result in a dysfunctional cell. As such, one of the programmed forms of cell death are initiated either during mitosis or immediately after in the daughter cells to kill them. This is a primary reason why the full effects of a treatment involving ionizing radiation likely cannot be measured on a 24 hour timescale, or after a single round of cell division, as is often used in viability assays for chemotherapeutics, for example.[1,227] Rather, the preferred method is to measure proliferative capacity *via* the clonogenic assay, as described in Section 7.11.

3.3. Radiotherapy: clinical methods

Remarkably, within one year of Roentgen's discovery of X-rays in 1895, X-rays were

applied in the treatment of cancer on two separate occasions.[228] In 1896, both Victor Despeignes and Èmil Grubbé described treating cancer patients with X-rays; it is disputed which one was technically first to do so, though Grubbé is often credited as the first.[228,229] X-ray radiation from an external source delivered to the body is known as external beam radiotherapy. This was the first type of radiotherapy utilized and is the main type that is in use today. The discovery of radium in 1897, by Marie and Pierre Curie, led to the advent of radium therapy soon after the initial developments of external beam radiotherapy. Radium therapy formed the basis for brachytherapy, which is the use of radioisotopes internally placed inside or near malignant tissues for delivery of ionizing radiation. Today, the use of brachytherapy is in decline, but still constitutes an important treatment modality for many cancers.[230] Relevant to this work, external beam radiotherapy involves X-rays and will be discussed in more detail.

3.3.1. Fractionated external-beam radiotherapy

For decades, fractionated radiotherapy has been the standard protocol for a variety of cancers. The general goal of fractionated radiotherapy is to kill a small portion of the tumor one fraction at a time, without letting it repopulate, until most or all of the tumor has been killed.[208,210,231] As mentioned in Section 3.2.1, the standard radiotherapy treatment for glioblastoma is external-beam radiotherapy totaling to a dose of 60 Gy, administered in 2 Gy fractions 5 days per week for 6 weeks. This has been the standard treatment schedule since the 1970's.[169,232,233] The basis for fractionated radiotherapy is known as the 4 R's: repair, redistribution, regeneration and reoxygenation as first described by Withers in 1975.[231] More recently, there has been the addition of a fifth R: *radiosensitization.*[234] Details on the 4 R's and a discussion on the standard practice of fractionated radiotherapy is provided in Appendix 3.

3.3.2. Intraoperative radiotherapy

Intraoperative radiotherapy (IORT) allows for a surgeon to physically move healthy tissue that would otherwise be in the radiation path, shield it, and perform radiotherapy while the patient is on the operating table.[235] The major advantage of intraoperative radiotherapy is that it allows for the delivery of ionizing radiation immediately after reSection, bypassing the 3-4 week waiting period for fractionated radiotherapy known as the time to initiation (TTI).[236] By eliminating the TTI, the opportunity for malignant cells to proliferate prior to treatment is also eliminated.

Additionally, a major difference between IORT and fractionated therapy is that IORT must obviously be administered in a single dose while the resection cavity is open. As such, much larger radiation doses are administered during IORT, which is feasible because there is no risk to healthy tissue that would have otherwise been in the radiation path. However, IORT is often administered in conjunction with the standard post-operative Stupp protocol, rather than on its own.[237–240] IORT encompasses all of the techniques in which ionizing radiation is administered to a patient in the same session where the tumor has been operated on. This includes high dose rate brachytherapy where radioactive seeds are inserted into the cavity, electron beam radiotherapy, and low-energy photon radiotherapy using X-rays (LEX-IORT).[235,236] Henceforth, all mentions of IORT unless otherwise stated are referring to LEX-IORT. In contrast to the MV beams used in conformal radiotherapy, all of these ionizing radiation sources have relatively shallow tissue penetration depths, since the radiation source is placed directly in contact with the malignant tissue.

3.3.2.1. Fundamentals of intraoperative radiotherapy for glioblastoma

As mentioned in Section 2.1, the interaction of photons of ionizing radiation with matter is a two-step process, whereby photons generate ionization tracks composed of secondary electrons which then interact with matter. When MV X-ray energies are used in fractionated radiotherapy, relatively long tracks are generated, and DNA is damaged through direct interaction with the electron tracks. In contrast, the kV X-rays used in IORT produce relatively short tracks and high amounts of hydroxyl radicals and other ROS, which go on to damage biological targets. Although it may seem like for the same radiation dose, higher-energy X-rays would cause a greater effect, it is actually the reverse. Because low energy X-rays have short ionization tracks, they produce a higher proportion of ionizations at the end of their tracks than the MV photons do. The clusters of electrons at the end of ionization tracks give rise to DNA DSBs and other types of complex lesions, as discussed in Section 3.2.3.2. For this reason, low energy X-rays give rise to a higher proportion of lethal ionizations than high energy X-rays do.[241]

To achieve intraoperative radiotherapy using low-energy X-rays, a device called the INTRABEAM® is used. The INTRABEAM® consists of a probe that can be outfitted with a variety of applicators of different sizes and shapes. A gold target at the end tip of the instrument provides unfiltered 50 kVp X-rays, and depending on the applicator used, dose rates range from 2

Gy/min to 0.45 Gy/min.[234,242] The use of low-energy X-rays (≥ 50 kV) provides localized radiation doses up to a depth of no more than 4.5 cm.[241] The radiation applicator is inserted into the resection cavity, delivering a 20-30 Gy dose[237–239,243–245] to the surface of the tumor bed. More information on the clinical trials for IORT of glioblastoma can be found in Appendix 4.

The high single-shot radiation doses given in IORT exhibit different effects than those from sub-10 Gy radiation doses, or from fractionated doses which are commonly 2 Gy each.[233,235] On an *in vivo* scale, the large doses are thought to induce an immune response (due to inflammation and the high degree of trauma) that may contribute to cell killing and progression-free survival. Moreover, the large doses may cause vascular damage and starve the residual tumor cells of nutrients.[246] On the cellular level, there is ample evidence in multiple human cell lines across different cancers that high single-shot doses of radiation induce different effects than conventional fractionated doses.[241,246] As such, the 5 R's discussed above differ in their importance for large single doses.

The number of DNA lesions is related to the radiation dose, thus at high radiation doses DNA repair machinery can become overwhelmed. This is known as repair saturation, and is thought to contribute substantially to the differences in clonogenicity observed *in vitro* at high single-shot radiation doses.[234] When repair saturation occurs, chromosomal instability can arise, such that cells which manage to survive and proliferate have genetic alterations relative to their unirradiated malignant counterparts. Moreover, irradiated cells can interact and cause additional changes to cell survival, this is called the "cohort effect" and is known to occur under irradiation with the INTRABEAM® device.[246] Additionally, damage to proteins is thought to contribute to the differences in cells treated with high radiation doses.[247] Inflammatory and immunogenic responses occur at the tissue-scale, mediated by the upregulation of NfκB, potentially leading to immune response-mediated cell death.[234]

3.4. Radiosensitizers

Since radiotherapy is such an important treatment modality, there are many drugs on the market and under development that act to potentiate its effects in cancer cells, while sparing healthy ones as much as possible.[248] These drugs are known as radiosensitizers, and some of the traditional chemotherapeutics approved for glioblastoma act in this manner (Appendix 4). A

radiosensitizer is generally any molecule or material which can act to increase the effectiveness of ionizing radiation.

There are several mechanisms of radiosensitization, and all can be broadly categorized as either chemical or physical. Chemical radiosensitizers act in a variety of ways to affect the biology of the cells to make them more susceptible to death under standard radiation doses. This is achieved through preventing DNA damage sensing/repair[213], mimicking molecular oxygen[249], arresting cells at radiosensitive cell cycles[250], and derailed redox cycling[251], among others. Physical radiosensitizers act to attenuate ionizing radiation and multiply it, providing a local dose enhancement.[10] Radiation dose enhancement is achieved through the use of high *Z* atoms, such as platinum, bromine, and iodine.[10,252,253] Of relevance here, inorganic nanoparticles have risen to the forefront as strong candidates for achieving physical radiosensitization.[11,254–257]

3.4.1. Radiosensitization *via* the dose enhancement effect

As described in Section 2.1, the interaction of ionizing radiation with matter is strongly dependent on the properties of the absorber. Specifically, its density and effective atomic number play a crucial role in the degree of radiation attenuation.[7] High density, high Z_{eff} materials will attenuate ionizing radiation much more efficiently than tissues do, especially at the keV energies relevant for IORT. More specifically, these materials have a higher radiation interaction cross-section, and are known to interact more efficiently, but also fundamentally have a higher probability for interaction with ionizing radiation than tissues do.[258] Not only does this increase the radiation dose, it is a means of potentially improving discrimination between the irradiation of healthy and malignant tissues.[259] The goal of physical radiosensitization is to introduce these types of materials to the malignant tissues and produce a greater number of ionizations than would be achieved by interaction of X-rays with tissues directly. Specifically, the goal is to induce an enhancement *via* the Auger effect.[10]

The Auger effect is depicted in Figure 1B in Section 2.1. When a photon of ionizing radiation interacts with the orbital electrons of an atom *via* the photoelectric effect, the excited atom can relax by two main mechanisms. The outer-orbital electrons reorganize to fill the vacancy left by the core electron and either 1) eject an X-ray photon corresponding to the difference in energy, or 2) eject an outer-shell electron corresponding to that energy without the accompaniment

of radiation. These ejected electrons are called Auger electrons and were first discovered by Lise Meitner in 1922, but widespread credit was given to Pierre Auger who independently reported it in 1925.[7,260–262]

As mentioned earlier, the electron tracks generated by low energy X-rays provide more lethal damage for the same radiation dose compared to high energy X-rays. Auger electrons with a 1 keV energy range are able to travel around 50 nm, thus their ejection from a nanoparticle occurs in the form of a localized electron shower.[10,263] This results in clustered damage to DNA, proteins, or organelles that are in the vicinity of the radiosensitizer.

3.4.1.1. Nanoradiosensitizers

Nanoparticles are particularly attractive as radiosensitizers because, unlike small molecules, they can be made with high densities and thus will inherently have larger linear attenuation coefficients (described in Section 2.1). Their ability to produce an Auger cascade has been well-established in a variety of nanomaterials, particularly in gold and hafnium oxide. Gold nanoparticles were considered an obvious choice due to their high X-ray attenuation coefficients and research as candidates for contrast agents for X-ray imaging, and were the first nanoparticles demonstrated to have a radiosensitizing effect.[264,265] Notably, despite the large body of research on gold nanoparticles as nanoradiosensitizers[11,256,258,259,266], they have not yet been approved for clinical trials. There are two nanoparticle formulations currently in clinical trials for radiosensitization of cancer: AGuIX® and NBTXR3. Their modes of action are discussed below, but an in-depth discussion on the clinical trials can be found in Appendix 4. An important limitation of AGuIX® and NBTXR3® (and gold nanoparticles) is that they are not luminescent, thus they cannot act directly to stimulate photodynamic therapy as described for nanoparticle-mediated PDT (see Section 3.6).

3.4.1.1.1 NBTXR3®: An inorganic crystalline nanoparticle radiosensitizer

First published in 2012, NBTXR3® is a HfO_2 crystalline nanoparticle that is 50 nm in size and coated with a proprietary (undisclosed) coating.[267,268] NBTXR3® is a physical radiosensitizer, its mode of action is through the Auger effect as described above. It is injected intratumorally, and remains present in tumor tissue for the duration of the radiotherapy treatments. Thus, there is

clinical evidence that long-term residence of nanoparticles in tissues is not necessarily deleterious if no adverse effects are observed. Moreover, this enables repeated radiosensitization using only one dose of the nanoparticles, which is likely to be cost and time efficient. Notably, transmission electron microscopy of NBTXR3 inside cells shows their localization is restricted to lysosomes[269], confirming the Auger effect and subsequent DNA damage can be achieved with nanoparticles localized outside of the nucleus, as demonstrated also with AGuIX® discussed below.

3.4.1.1.2 AGuIX®: An inorganic-organic hybrid nanoparticle radiosensitizer

First introduced in 2011, Activation and Guidance of irradiation by X-ray (AGuIX®) is a nanoparticle consisting of 15 atoms of Gd^{3+} chelated by 10 DOTA (1,4,7,10-tetra-azacyclododecane-1-glutaric anhydride-4,7,10-triacetic acid) ligands, and wrapped with polysiloxane.[270,271] AGuIX® is very different from NBTXR3® from a physicochemical perspective, despite having the same mode of action. Each nanoparticle is approximately 5 nm in size, and was first developed with the intention of being used as a contrast agent. For this reason, AGuIX® is administered intravenously and relies on the enhanced permeability and retention effect to accumulate in malignant tissue with disrupted vasculature.[28] The high Gd^{3+} content of AGuIX does enable its successful use as a contrast agent, but also enables its ability to act as a high-Z radiosensitizer. This is a particularly useful combination in the context of image-guided therapy when magnetic resonance imaging (MRI) can be performed *in situ* during radiotherapy. Interestingly, hybrid formulations of AGuIX® have been studied for achieving interstitial photodynamic therapy (iPDT) of glioblastoma[272] and for achieving X-ray mediated PDT by replacing Gd^{3+} with Tb^{3+} ions (Section 3.6.2).[273]

3.5. Photodynamic therapy

"Water is good, air is better, but light is best." – Arnold Rikli, Swiss naturopath

3.5.1. History of PDT

The connection between light and health has existed for many millennia; the ancient Egyptians worshipped the sun and are thought to have demonstrated knowledge of a relationship between health and sunlight.[274–276] The ancient Egyptians used the *Ammi majus* plant regularly, it is now known to contain psoralen derivatives, which are photosensitizers used in modern

medicine.[277] Similarly, ancient Indian medical texts describe the use of a plant called Bavachee to cure skin ailments, which was later identified as containing psoralens as well.[278] Hippocrates, the Father of medicine, introduced the concept of heliotherapy. The ancient Chinese Daoists described phototherapy as early as the first century BC during the Han dynasty, and again during the Tang dynasty.[274,277] The use of sunlight in medicine was widely accepted worldwide, until the advent of Christianity, when sun-worship and heliotherapy became regarded as heretical pagan practice.[279]

A revival in the use of sunlight for therapeutic purposes began around the mid-19th century. Arnold Rikli, a Swiss naturopath, is credited with reintroducing the practice of using sunlight for healing.[280] Shortly thereafter, Niels Finsen established the basis for modern phototherapy, using artificial UV light to treat lupus vulgaris; he received the 1903 Nobel prize in medicine for this work.[278,280,281] The end of the 19th century also saw the first hypothesis on the mechanism of action of light therapies, when Oscar Raab described being able to kill paramecia with acridine dye on sunny days but not as effectively on cloudy ones.[282] The work of Raab is widely considered to be the basis for modern photodynamic therapy.[276,283,284] Raab hypothesized the fluorescence from acridine was responsible for killing the paramecia *via* energy transfer in a similar manner to photosynthesis. His supervisor, Herman von Tappeiner, performed extensive research on the subject after Raab's discovery. Von Tappeiner determined in 1904 that oxygen was a requirement for the therapeutic effect, eventually coined the term photodynamic therapy and demonstrated its use for the treatment of skin cancer.[285,286]

Porphyrins have a rich history in PDT and are perhaps the most encountered type of photosensitizer. In 1913, the photosensitizing effects of hematoporphyrin were described when Friedrich Meyer Betz injected himself with it and experienced severe pain when exposed to light; this lasted for over two months.[276] This early work established the importance of porphyrins in PDT. Notably, in 1924, the accumulation porphyrins and fluorescence of tumors was described by Policard in France[287], and again in 1942 by Auler and Banzer in Germany[288]. Thereafter, the first generation of photosensitizers was introduced, starting with the production and clinical approval of hematoporphyrin derivative (HpD), known by the brand name Photofrin®. The first clinical trial in 1978 by T.J. Dougherty demonstrated a clear clinical benefit of PDT for skin cancer using HpD.[278] From then onward, many photosensitizers have been developed and new modes of PDT have been studied.

3.5.2. Mechanism of PDT

As mentioned earlier, von Tappeiner determined that three components are necessary for PDT: light, a photosensitizer, and oxygen. A schematic of the process is shown in Figure 14. When light of the appropriate wavelength is absorbed by a photosensitizer, it is promoted to an excited singlet state. It can then undergo radiative relaxation (fluorescence) or it can undergo intersystem crossing from an excited singlet state to an excited triplet state. Electrons in the triplet state can then relax radiatively to the singlet ground state (phosphorescence), or the photosensitizer can react *via* two mechanisms that lead to the photodynamic effect. These are known as the type I and type II PDT mechanisms; both mechanisms usually occur simultaneously, and the proportion of each is dependent on the properties of the photosensitizer, and the oxygen content of the environment.[289]

A wide variety of ROS can be generated by the type I PDT reaction, the most important of which are superoxide ($O_2^{\bullet-}$) and hydroxyl ($OH^{\bullet-}$) radicals because of the cascades of ROS they can generate, as well as their ability to generate $^1O_2$ in some instances.[290] Superoxide anions can react with themselves to generate H_2O_2 and O_2, catalyzed by superoxide dismutase. H_2O_2 can participate in the Fenton reaction, resulting in the formation of $OH^{\bullet-}$, which can subsequently generate a variety of other ROS *via* reaction with oxygen or biomolecules.[290–292] Notably, type I reactions are either one- or two-electron redox reactions, and thus cationic and anionic radicals are always generated by this process, including the generation of a radical form of the photosensitizer. Thus, the photosensitizer usually degrades during this process, and it is important that the photoproducts do not cause toxicity upon their clearance.

The type II reaction exclusively leads to the formation of $^1O_2$ *via* nonradiative energy transfer from the excited triplet state of the photosensitizer to molecular oxygen. $^1O_2$ is often credited as the most important player in the PDT effect, owing to its high reactivity with a wide variety of substrates.[290,292,293] For a particularly thorough and exciting review about singlet oxygen, the reader is referred to the work of Callaghan *et al.*[294] Importantly, the type II reaction is obviously dependent on the oxygen content of the cell. As such, the contribution of $^1O_2$ to hypoxic tumors is highly variable, and there is mounting evidence that the type I reactions contribute to the PDT

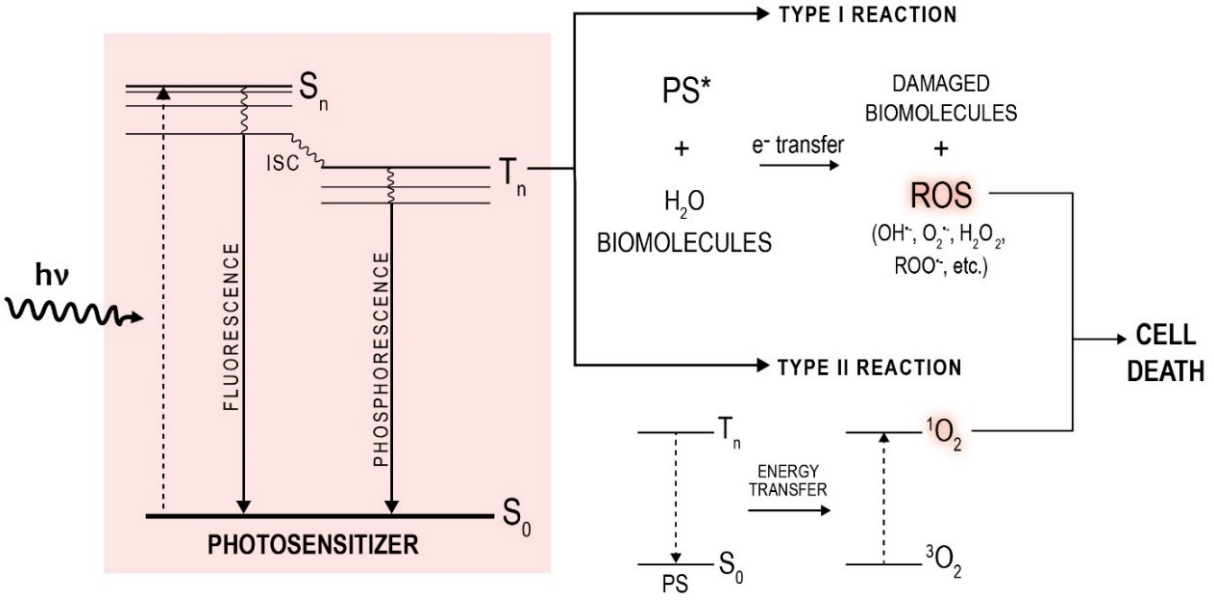

Figure 14. Graphical depiction of the mechanism of PDT leading to ROS production. Incoming light is absorbed by a photosensitizer and promotes it to an excited singlet state. The excited electrons can then relax radiatively to produce fluorescence or undergo intersystem crossing (ISC) to the triplet state. From the triplet state, the photosensitizer can relax radiatively *via* phosphorescence, or can interact with nearby substrates *via* a type I reaction in which a redox process leads to the damage of biomolecules and formation of ROS, or via a type II reaction with molecular oxygen *via* energy transfer, producing reactive singlet oxygen molecules. Singlet oxygen and other ROS can then induce oxidative damage leading to cell death.

effect more than was previously thought.[295] Unlike the type I reactions, the type II reaction is expected to be catalytic, since the process occurs through energy transfer.[296] While this is an advantage in that more ROS can be produced per photosensitizer molecule, it also prolongs the photosensitivity of the tissue. The rapid photobleaching of PPIX (as described below) is thought to be an advantage in that it reduces the time a patient is rendered photosensitive, and interestingly, the photoproduct of PPIX is a better photosensitizer than PPIX itself.[290] Photobleaching is also useful as a dosimetry metric, as described in Section 3.5.5.

Its important to note that radiotherapy and PDT both produce ROS to initiate cell death, but they fundamentally do not act *via* the same mechanisms. As mentioned earlier, radiotherapy primarily causes DNA damage to achieve cell death. In contrast, PDT invokes cell death by lethal damage to the rest of the cell, ie. the membranes and organelles.[289] $^1O_2$ is only able to interact with guanine in DNA, and most of the base damage caused by either mechanism does not appear to be

lethal.[289,292] The main modes of lethal damage are *via* reactions with proteins, and lipids. It has been demonstrated that up to 40% of $^1O_2$ reactions in cells are with proteins.[293] With respect to lipids, cascades of radical-mediated lipid peroxidation occur upon reaction with hydroxyl radicals and H_2O_2, generating a large number of ROS and causing extensive damage to lipid membranes.[290] Depending on the subcellular localization of the photosensitizer, significant organelle damage can be caused, thereby initiating different modes of cell death.[297] Specifically, the critical PDT targets are the mitochondria, lysosomes and endoplasmic reticulum, initiating any of the cell death mechanisms described in Appendix 2.[297]

Importantly, within the past decade, it has become understood that there is a significant immunological component to the PDT effect.[298] Notably, because of this, there has even been a move towards developing PDT vaccines for cancer.[299] Immunogenic cell death is a form of cell death characterized by the orchestrated release of biomolecules from the dying cell that induce the innate and adaptive immune responses.[203,298,300,301] These molecules, known as damage associated molecular patterns (DAMPs) are released in response to the oxidative damage caused by the cell. They are the key recruiters of immune cells and are able to recognize neoplastic cells and initiate apoptosis in them for a prolonged period after the PDT treatment.[302] With regard to glioblastoma, the sustained local immune response generated by PDT is attractive because it may provide the opportunity to prevent neoplastic cell growth, thereby suppressing tumor recurrence.[303]

3.5.3. Photosensitizers and Light: Inducing the PDT effect

Unlike ionizing radiation, which can penetrate tissues many centimeters, the UV and visible wavelengths used for photodynamic therapy only penetrate a few millimeters (Figure 15A). Under normal circumstances, skin acts as a barrier, preventing DNA-damaging UV rays from interacting with our organs and causing cancer. As such, UV wavelengths barely penetrate the stratum corneum and epidermis, where there are no blood vessels.[304] Blue-green wavelengths penetrate into the dermis, approximately 2-2.5 mm deep; capillaries begin to appear in this layer of the skin. Finally, red light penetrates into the subcutaneous tissue, with 600 nm light penetrating around 3-4 mm deep and 750 nm light penetrating 4-5 mm deep.

As shown in Figure 15B, the absorption properties of a variety of biomolecules are responsible for the attenuation of the different wavelengths. Unfortunately, melanin is one of the

main attenuators of UV-visible light and is meant to protect the skin from harm. However, because melanin contributes substantially to the attenuation of light, it affects the efficacy of PDT for cutaneous disease (such as melanoma) in different ethnic populations.[305,306] This is much less of an issue when considering PDT for deeper tumors, however other chromophores become more of an issue. With respect to glioblastoma, there is an estimated therapeutic depth of approximately 0.75–1.5 cm from the excitation source.[203] Hemoglobin (deoxygenated and oxygenated) and proteins are also major contributors to the attenuation and scattering of light by tissues in the sub-650 nm range, whereas fat is the major attenuator in the 750-1000 nm range. The strongly-absorbing nature of blood is a particular hurdle in intraoperative PDT, as free-flowing blood can diminish the optical clarity of the resection site.[307] Absorption minima for several biomolecules are found around the red-NIR range, thus red light is currently considered to be optimal for achieving the PDT effect using the most efficient photosensitizers developed at this time, as discussed below.[283,297,308] Importantly, photosensitizers capable of absorbing light > 800 nm may not be useful because of the inability of these wavelengths to provide enough energy to excite molecular oxygen into the singlet state.[290] Thus, direct NIR excitation could overcome the tissue depth penetration, but at the expense of generating a photodynamic response.

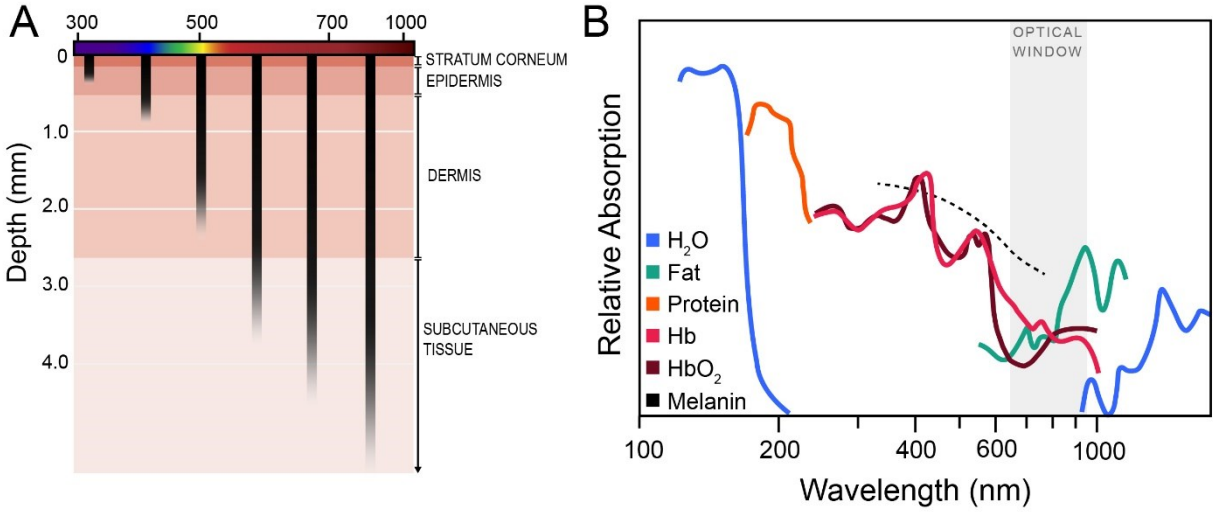

Figure 15. A) penetration depth of light through different layers of skin as a function of wavelength.[304,583,584] B) Absorption spectra of different biomolecules and the first optical biological window at which an absorption minimum is observed for multiple molecules.[388,585–588]

Mentioned earlier, the first photosensitizer approved for clinical use and made commercially available was Photofrin®, which is a mixture of hematoporphyrin oligomers. It's exact composition is not actually known, which is one of its major disadvantages, as described in Appendix 5.[308] Porphyrin-based photosensitizers such as Photofrin® represent the first and second generation of photosensitizers, along with the chlorin-based molecules which are structurally similar. To our knowledge, there are seven clinically-approved photosensitizers specifically indicated for cancer treatments as of 2023 (Appendix 5).[283,309]

Levulan® and Metvix® are regarded as the photosensitizers of choice for PDT worldwide[193,203,283,299,309,310]; Levulan® is the brand name for the PDT formulation of 5-ALA, and Metvix® is a methyl ester derivative of 5-ALA. 5-ALA meets the vast majority of requirements for a successful photosensitizer; the main contraindication is pain during treatment, which can be mediated with anesthesia.[299]

3.5.4. 5-ALA for PDT

As mentioned in Section 3.2.2.2, 5-ALA is a pro-drug of PPIX that is preferentially accumulated in malignant cells due to dysregulation of the heme biosynthesis pathway. In this section, 5-ALA and PPIX are referred to interchangeably as the photosensitizer, but it is PPIX that specifically exhibits the PDT effect. Notably, PPIX is the only endogenous photosensitizer that has achieved clinical success.

In 1956, while participating in a study on porphyrin metabolism, four volunteers who ingested relatively high amounts of 5-ALA experienced photosensitization of the skin, suggesting that it was possible to modulate PPIX expression by administering exogenous 5-ALA.[311] This observation led to the first preclinical and clinical studies of 5-ALA as a PDT agent, along with the previous demonstrations of accumulations of porphyrins in tumors by Policard, Auler and Banzer in the 1920's and 30's as discussed earlier. The initial study demonstrated complete treatment of actinic keratoses (pre-cancerous skin lesions), and strong outcomes for basal and squamous cell carcinoma in a preliminary clinical report published in 1990 by the National Cancer Institute of Canada.[311] 5-ALA was administered topically in this study, but can be used both topically and orally.

Topical administration of 5-ALA allows for highly localized accumulation of PPIX, thereby preventing any possibility of systemic photosensitivity.[308] For this reason, it is highly regarded for skin diseases, since its visible red fluorescence allows for simultaneous detection and treatment of malignant cells. Topical administration of Levulan® results in accumulation up to 1 mm, and up to 2 mm for Metvix® owing to its increased lipophilicity that allows for more efficient penetration through the stratum corneum (Figure 15A).[309] However, topical administration is not useful for fluorescence-guided surgery, or PDT of deep tumors. Oral administration of 5-ALA is indicated for subcutaneous tumors, and for fluorescence guided surgery of glioblastoma.

Currently, 5-ALA is approved for PDT of actinic keratoses and basal cell carcinoma.[312] As of 2023, there are 49 active clinical trials for the use of 5-ALA PDT, including studies for the treatment of glioblastoma (NCT04469699, NCT04391062, NCT03048240) owing to the recent FDA approval of Gleolan® in 2018 for fluorescence guided resection as described in section 3.2.2.1. Prominent neurosurgeons have described the outcome of PDT for glioblastoma as modest thus far, but note that augmenting the effect might be achieved through a greater stimulation of the immune response, or through the use of nanoparticles.[203]

3.5.5. Drawbacks of current PDT regimens

Photodynamic therapy is a unique treatment because the types of mutations in cells that give rise to acquired chemo- and radioresistance do not seem to cause resistance to the photodynamic effect.[289] Moreover, its main side-effects, pain during treatment and prolonged photosensitivity, can be addressed with relative ease using anesthesia and the more recent photosensitizers, respectively. The now-understood ability to induce an immune response *via* immunogenic cell death has given PDT even more prominence as a cancer treatment technique. Yet, it is still mainly indicated for skin cancer at this time. The main obstacles of PDT are the inherent lack of tissue penetration of non-ionizing radiation, and our limited understanding of dosimetry of these wavelengths.

With regard to tissue penetration, interstitial PDT (iPDT) has been developed, in which one or more fiber lasers are inserted into the tumor in order to deliver light to the region.[313] Compared to IORT, iPDT is more commonly performed in the absence of resection.[313–315] While this is certainly an attractive means to achieve PDT in a variety of cancers, the invasive nature of the

fibers can cause repercussions in delicate organs like the brain, whereas insertion into breast or prostate tissue is less of a risk.[316] Intraoperative PDT has also been explored, however, as mentioned earlier, a major drawback is the attenuation of light by blood. In intraoperative PDT, the resection cavity has to be continually irrigated to maintain optical clarity, which comes with its own set of complications as the light source has to be repeatedly moved.[307] Another option proposed for PDT of glioblastoma is the insertion of LED implants at the resection site after surgery, which again is sub-optimal and reduces the minimally-invasive nature of PDT. The implants and fiber lasers mentioned both pose a significant risk for uncontrolled cerebral swelling; this has caused the death of multiple patients in different clinical trials.[303] The Intraoperative photodynamic therapy of GliOblastoma (INDYGO) trial (NCT03048240) attempted intraoperative PDT using PPIX after fluorescence guided resection, and were cautiously optimistic about the results, but noted that very few patients had been enrolled in the trial thus the results had limited meaning.[317] Given the poor prognosis of glioblastoma patients, however, these early attempts at using PDT for glioblastoma do show promise if the safety concerns can be addressed and enough patients can be enrolled.

With regard to dosimetry, there is still a severe lack of understanding that permeates the field.[299] To contextualize this, the concept of dosimetry has been publicly described as "alien" to clinicians as recently as 2014.[283,318,319] There are many variables in PDT: the oxygen concentration, photosensitizer concentration, light fluence, power density, and blood flow are all critical variables that can vary patient to patient as well as vary during the treatment.[320] PDT dosimetry is therefore a combination of determining the dose of photosensitizer, dose of oxygen, and dose of light that provide the most clinical benefit. Currently there is a lack of a straightforward, reliable, and easy method to measure all of these parameters in patients. This has resulted in precise dosimetry being largely avoided and thus contributing to some safety concerns associated with PDT overdose, as was the case with Foscan® (see Appendix 5).[299,320]

The attenuation of non-ionizing photons with tissues is governed by absorption and scattering, which change between patients due to the proportion of chromophores such as melanin in the tissue, and during the treatment depending on the amount of blood present, how oxygenated the blood is, and how much of the photosensitizer has been bleached over the course of the treatment.[316] Clinically, there is a move towards establishing which of these parameters are

outcome-limiting, and which are the most important for establishing a safe treatment. Interestingly, photobleaching of PPIX during PDT has been used as a metric to determine when to stop the treatment, representing a potentially simple way to prevent PDT overdose.[320] While this is far from quantitative, there have been several studies on 5-ALA PDT to measure outcomes based on photobleaching as the dose metric.[320–322]

Relative to ionizing radiation dosimetry in radiotherapy, the understanding of non-ionizing radiation interactions with tissues lag decades behind in comparison.[319] The use of ionizing radiation to stimulate the PDT effect would therefore potentially aid in overcoming this hurdle in PDT dosimetry. Moreover, it would enable two treatment modalities (radiotherapy and PDT) using a single radiation source.

3.6. X-ray mediated photodynamic therapy

In 2008, Wei Chen and colleagues demonstrated for the first time that radioluminescent nanoparticles (RLNPs) could be used to activate a photosensitizer.[323] This proof-of-concept demonstration formed the basis for X-PDT. In X-PDT, RLNPs are excited with ionizing radiation and can radiatively or non-radiatively transfer energy to a photosensitizer, thereby stimulating the production of ROS *via* excitation with X-rays, rather than the visible and NIR wavelengths used in conventional PDT. Not only does this overcome the tissue depth penetration and dosimetry issues of PDT, it enables the use of photosensitizers which are excited outside of the optical biological window discussed previously (Figure 15B). The promise of X-PDT was initially greeted with skepticism[324,325], but it has nonetheless shown great promise in a wide variety of cancers at the *in vitro* and *in vivo* levels (Table 22 Appendix 7).[1–3]

3.6.1. Designing an X-PDT system: energy transfer

The ability to use nanoparticles as mediators of the PDT effect relies on the potential for energy transfer between the nanoparticle (donor) and the photosensitizer (acceptor). Energy transfer between two species is fundamentally dependent upon the distance between them, and their spectral overlap.[326] Spectral overlap refers to the degree to which the donor's emission spectrum "matches" with the acceptor's absorption spectrum; this is mathematically determined by taking the integral of the regions where the spectra overlap. As such, the spectral overlap is

dependent on the shape of the spectra, as well as their extinction coefficients.

Energy transfer can occur *via* radiative and non-radiative mechanisms; the probability of each mechanism is largely dependent on the distance for the same donor-acceptor pair (ie. the spectral overlap does not change).[327] The most common non-radiative energy transfer mechanism was first comprehensively described in 1946 by Theodor Förster, from which the name Förster resonance energy transfer (FRET) comes.[328,329] Simplistically, FRET occurs *via* the coupling of resonant oscillating electric fields of two distinct species. This process has a distance dependency of R^6, as such FRET is only efficient at very short distances. Realistically, it is highly unlikely to achieve efficient FRET between lanthanides and photosensitizers at distances longer than 10 nm.[326,327,330–332] More often, the critical distance (R_0) is between 5 and 20 Å when a lanthanide is a component of the donor-acceptor pair, as is the case between a lanthanide ion and a ligand in a metal complex.[51]

In contrast, in a simple radiative mechanism, photons are emitted by the donor and absorbed by the acceptor. As such, the energy transfer is limited by the distance the emitted photon travels before encountering a species able to absorb it, and therefore can occur on much longer distances than FRET. However, FRET is a directional process whereas radiative energy transfer is not. With radiative energy transfer, if the photon is not emitted in the direction of the absorber, the desired energy transfer will not occur.

With respect to X-PDT, the choice of photosensitizer can be made based on the luminescent properties of the nanoparticle, or vice versa. The wide range of emissions from the lanthanides has been particularly beneficial to X-PDT because they enable the possibility to use photosensitizers that absorb wavelengths other than those within the first optical biological window (Section 3.5); ie. other than those in the 600-800 nm region. For example, a popular combination in X-PDT is that of Tb^{3+} and Rose Bengal; the $^5D_4 \rightarrow {}^7F_J$ transitions of Tb^{3+} have good spectral overlap with the absorbance band of Rose Bengal.[41,47,333–336] Rose Bengal is excited with green light, which precludes its use in traditional PDT, despite it having one of the highest singlet oxygen yields ever reported ($\phi \approx 0.8$).[337] As such, the principle of energy transfer greatly extends the potential for photosensitizers that were previously regarded as powerful but clinically irrelevant.

3.6.2. State of the field

The rich history of lanthanide scintillators has inspired the development of these materials at the nanoscale, bringing about entirely new avenues of using their radioluminescent properties. Coming full circle, lanthanide-doped radioluminescent materials have been at the forefront of X-PDT research. For the sake of brevity, our discussion will be restricted to the X-PDT systems that employ lanthanide ions, as they compose the majority of reported systems and are related to the work herein. However, the interested reader is referred to several reports of noteworthy systems based on other luminescent species.[338–341] For additional in-depth discussions on X-PDT and the state of the field, the reader is referred to several particularly insightful reviews.[1–3,342]

Theoretical models for X-PDT suggested the potential for RLNPs to induce efficient ROS production was dismal at best. Morgan, Capala and colleagues used theoretical modelling to study the potential for singlet oxygen generation using LuI_3 and LaF_3 nanoparticles with an imaginary photosensitizer.[324] They determined it was unlikely X-PDT could produce the singlet oxygen quantities necessary to achieve the Niedre killing dose at clinically-relevant doses, and indicated X-ray energies in the < 300 keV range would be most efficient. The Niedre killing dose is the number of $^1O_2$ molecules per cell required to achieve a 1/*e* survival fraction, which is on the order of 10^7 $^1O_2$ molecules per cell, but will vary somewhat with the cell type.[343] Bulin, Dujardin and colleagues further explored this theory, suggesting the previous model underestimated the contribution of secondary dose deposition effects from the surrounding medium.[35] By modelling 10 nm Gd_2O_3 nanoparticles in water, irradiated with 500 keV photons and having a light yield of 15000 photons/MeV, they estimated 44 $^1O_2$ molecules would be produced per photon, further confirming there would not be enough $^1O_2$ produced to achieve a lethal effect without using high photon fluences. Moreover, this model demonstrated that 92% of the energy deposited in the nanoparticles was from secondary ionizations of water molecules that absorbed the incident photon. Thus it was determined that in solution, the primary mode of RLNP excitation is *via* these secondary interactions. Kudinov and colleagues also modelled this scenario using $LaF_3:Ce^{3+}$ RLNPs and estimated 6300 $^1O_2$ molecules/cell would be obtained. Thus, the same conclusions have been drawn by different researchers using different models over the past 15 years[1]: the likelihood of producing enough $^1O_2$ to achieve a lethal PDT effect is small under clinical radiotherapy conditions. So why is there experimental evidence that X-PDT works? The combined

evidence from studies on RLNPs in the presence and absence of photosensitizers at the *ex vivo, in vitro* and *in vivo* levels has provided us with the understanding that $^1O_2$ generation is only one component of the X-PDT effect.

The early reports of the X-PDT effect set the foundation for more complex studies of the effect biological models, and were largely based on Ce^{3+} and Tb^{3+}-doped RLNPs to excite Rose Bengal, and exogenous porphyrins.[323,344–349] Around this time, AGuIX® was also introduced (see Section 3.4.1.1.2), which seems to have spurred interest in the field. In 2016, Xie and colleagues reached a milestone in the field, demonstrating that X-PDT exhibited a therapeutic effect characteristic of both radiotherapy and PDT by observing biomarkers associated with PDT-mediated lipid peroxidation and RT-mediated DNA damage.[350] As such, they demonstrated that X-PDT does not simply act by stimulating PDT, providing an explanation for why X-PDT works despite the predicted poor $^1O_2$ yields. Thereafter, more reports demonstrating X-PDT were published, with the vast majority demonstrating excitation of Merocyanine 540 and Rose Bengal using Tb^{3+} emissions.[334–336,351–354]

Notably, there were also several reports during this time of what can be described as self-sensitized X-PDT, where the nanoparticle itself produced the ROS, rather than a discrete organic photosensitizer molecule. Purschke and colleagues published several reports using $LuPO_4:Pr^{3+}$ nanoparticles to induce direct DNA damage using the UV-C emissions from the radiative 5d-4f transitions of Pr^{3+} in that host.[355–359] In $LuPO_4$, the $^1S_0$ state is situated above the lowest $4f^15d^1$ levels of Pr^{3+} in contrast to the positioning of the Pr^{3+} states in the RLNPs used herein ($NaLuF_4:Pr^{3+}$). $LuPO_4:Pr^{3+}$ produces strong UV-C emissions, but weak or no emissions at 406 nm and beyond. These UV-C emissions are unable to excite most photosensitizers, thus precluding the use of these nanoparticles in combination with most photosensitizers. Hf-based metal-organic frameworks (MOFs) using porphyrins as linkers were also demonstrated to provide a promising effect, generating ROS directly from the porphyrin scaffold of the MOF structure.[341,360]

In 2020, Bulin and colleagues demonstrated concrete evidence that lanthanide doped fluoride nanoparticles provide a significant radiation dose enhancement effect, in line with what is observed in NBTXR3® and AGuIX®.[263] $LaF_3:Ce^{3+}$ nanoparticles were used because the UV emissions from Ce^{3+} in this host do not cause DNA damage, thus the authors considered it a good

control system for investigating radiosensitization. Excitation with 50 keV X-rays provided the highest radiation dose enhancement, generating a cascade of photoelectrons and Auger electrons that were predicted to travel up to 100 μm in the surrounding tissue. This not only confirmed Xie's supposition that X-PDT is a combination of radiotherapy and PDT[350], it demonstrated that radiosensitization was a component as well. As such, the high density and high *Z* properties of RLNPs that are essential for providing strong radioluminescence emissions also act to provide a radiation dose enhancement effect. In line with this, a Tb^{3+} analogue of AGuIX® was also developed, introducing the capability for X-PDT at the expense of the MRI contrast provided by Gd^{3+} in the original formulation (see Section 3.4.1.1.2).[273]

Chapter 4. Statement of the Problem

Patients with glioblastoma have an incredibly dismal prognosis, despite decades of research into treatments. It is now understood that the treatment resistant and highly invasive nature of glioblastoma cells results in tumor recurrence, in most cases within 2 cm of the original resected tumor. The recurrence of the tumor occurs due to incomplete resection, which is often the case due to the need to spare as much healthy brain tissue as possible. Preservation of eloquent regions of the brain is regarded as essential for ensuring good patient quality of life. Thus, there is a need to develop treatments which can eradicate the malignant cells remaining at the margin of the resection site and thereby prevent their infiltration into nearby healthy tissue. To date, there has been little progress in extending the survival of patients with glioblastoma and there is a need to address treatment of this disease through entirely new means.

Nanoparticle-based X-PDT has been demonstrated on multiple occasions as a viable means to achieve a greater therapeutic effect in radioresistant cancers. However, the systems have been largely based on RLNP compositions and photosensitizer choices exhibiting good spectral overlap for energy transfer and high $^1O_2$ yields, but with little emphasis on clinical implementation of the system. To this end, we aimed to develop an X-PDT system that could be incorporated into existing clinical workflows that already have FDA approval. In this way, the introduction of the nanoparticles does not interrupt protocols that are currently optimized and therefore a realistic route to their use in the clinic may be realized from the inception of the technique. Herein, we aimed to develop an X-PDT system with the intent of harnessing two currently-implemented, state-of-the-art clinical techniques used in surgical resection of glioblastoma: fluorescence-guided resection using endogenous PPIX upon 5-ALA administration, and low X-ray energy intraoperative radiotherapy (LEX-IORT).

As mentioned earlier, 5-ALA is conveniently the only FDA-approved drug for fluorescence guided resection of gliobastoma, and is also the most popular photosensitizer in clinical use to date. Unfortunately, PPIX is not efficiently excited *via* X-rays, and the use of visible light to stimulate PDT is particularly inefficient in an intraoperative context, where blood is constantly attenuating the light before it reaches the malignant issue. Thus, we aimed to develop a radioluminescent nanoparticle composition and specifically optimize its luminescence properties

for activation of PPIX upon excitation with X-rays, thereby inducing the X-PDT effect using endogenously produced PPIX that is present in malignant cells after fluorescence guided resection. The use of endogenous PPIX therefore restricts the PDT effect to malignant cells, enabling a more selective treatment and potentially stimulating immunogenic responses from the X-PDT-treated malignant cells.

When doped into an appropriate host, the intraconfigurational 4f emissions of Pr^{3+} exhibit remarkable spectral overlap with PPIX (Figure 16). Specifically, the $^1S_0 \rightarrow {}^1I_6$ transition of Pr^{3+} overlaps with the strongly-absorbing Soret band of PPIX, while the LOL transitions provide emissions that overlap well with the Q bands of PPIX. In addition, the $^1S_0 \rightarrow {}^1I_6$ transition of Pr^{3+} can only be obtained using high-energy excitation, such as X-rays. As such, the efficient spectral overlap between Pr^{3+} and PPIX is enabled under conditions relevant for X-PDT. Moreover, the spectral overlap enables excitation of the Soret band with X-rays, which cannot currently be used for excitation due to the poor tissue depth penetration of this wavelength. As such, increased ROS production may be enabled using this excitation band.

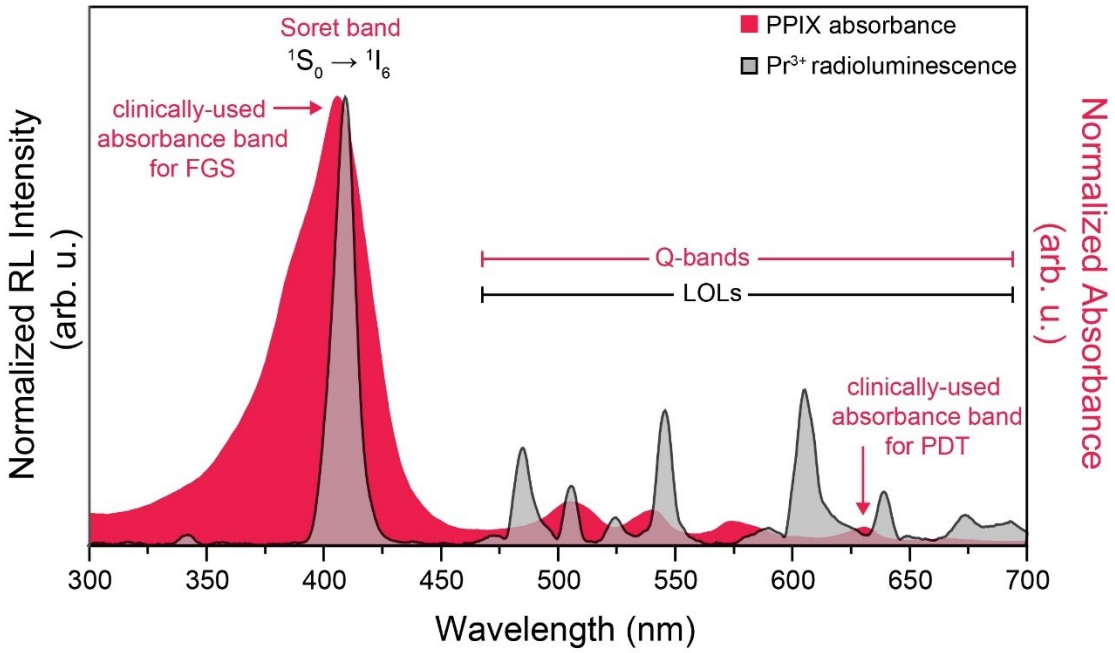

Figure 16. Normalized radioluminescence emission from Pr^{3+} and normalized absorbance from PPIX. The different spectral features of Pr^{3+} and PPIX are labelled in black and pink, respectively. (FGS: Fluorescence Guided Surgery)

We aimed to develop a robust synthesis for $NaLuF_4:Pr^{3+}$ that could be used to obtain a wide range of Pr^{3+} compositions to ensure the emissions were optimized for use in an X-PDT system. We also aimed to thoroughly characterize the luminescence properties of these nanoparticles such that there was a strong understanding from the materials aspect about their behavior. In certain instances, this meant performing in-depth studies on their newly-discovered persistent luminescence properties to elucidate the mechanism of this phenomenon. The RLNP system was spectroscopically evaluated under X-ray excitation parameters matching those used in LEX-IORT (Au target, 50 kV, 0.6 Gy/min) as well as under harsher radiation dose rates (30 Gy/min) to evaluate their radiation hardness. The parameters used for investigating the RLNP system *in vitro* in human glioblastoma cells were restricted to those that match the LEX-IORT protocol, representing a proof-of-concept demonstration that takes into consideration parameters reported for clinical IORT at all stages of development.

Since high-Z inorganic nanoparticles are known to act as radiosensitizers, we evaluated the effects of the nanoparticles with and without the addition of 5-ALA to establish how much of an effect could be generated from the nanoparticles alone. To our knowledge, no nanoparticle X-PDT system has reported outcomes at the high doses that are applied in IORT or is designed under the IORT framework to treat the residual tumor bed, rather than the tumor itself. We also considered multiple concentrations of nanoparticles, and evaluated all RLNP concentrations and X-ray doses in the absence and presence of 5-ALA, as we postulate there is no single set of treatment parameters that would be universally optimal; rather, it is more realistic that different doses and RLNP concentrations would be more relevant depending on the patient's situation (margin of tumor volume, area of the brain, etc). We therefore aimed to produce data that spans a broad range of possible scenarios, in hopes that this allows for a) a better overview of the effects this treatment has and b) provides a range of outcomes under different combinations that can be compared to existing literature reports. To this end, we also report a variety of different enhancement factors that are either encouraged by the ICRU or widely reported for clinical, pre-clinical and proof-of-concept radiosensitizer reports and made relevant comparisons to these systems.

Chapter 5. Materials and Methods

5.1. Reagents

Lu_2O_3 (99.999%) and $PrCl_3$ (99.99%) were purchased from Chemicals 101 Corp. (Toronto, ON). Sodium oleate (95%), ammonium fluoride (99.99%), oleic acid (90%), 1-octadecene (90% purity, technical grade, #O806), sodium citrate tribasic dihydrate (≥99.0%, #S4641), poly-L-lysine (0.1 % w/v in H_2O; #P8920), protoporphyrin IX (≥95% purity, P8293), HNO_3 (70%, #225711), H_2O_2 (50 wt. % in H_2O, stabilized), Mowiol® 4-88 (#81381), Trizma® hydrochloride (T3253), glycerol (≥99%; #G5516), DABCO (#D27802) were obtained from MilliporeSigma. The ICP-MS multielement standard solution (CLMS-1, 10 mg/L; Ce, Dy, Er, Eu, Gd, Ho, La, Lu, Nd, Pr, Sc, Sm, Tb, Th, Tm, Y, Yb) was purchased from Spex CertiPrep. The resazurin assay kit (#TOX8), paraformaldehyde (95% purity, #158127), 2',7'-Dichlorofluorescein diacetate (≥97% purity, #D6883), and methylene blue (M9140) were purchased from MilliporeSigma. NucBlue™ (DAPI, R37606) and HCl (TraceMetal Grade, A508-P500) were obtained from Thermo Fisher Scientific. 5-Aminolevulinate hydrochloride (≥99% purity) and the Annexin V/Propidium iodide kit (sc-4252 AK) were purchased from Santa Cruz Biotechnology. DMEM (#319-005-CS), FBS (#080-450), trypsin-EDTA (#325-542) were from Wisent Bioproducts (St-Bruno, QC). The mycoplasma detection kit was obtained from Applied Biological Materials Inc. (abm, #G238).

Primary antibodies used for Western blotting and their dilution are listed in Table 1. Affinity-purified HRP-conjugated secondary antibodies were purchased from Jackson ImmunoResearch Laboratories, Inc. (USA); they were diluted 1:2,000.

Table 1. List of antibodies used for the Western blot assays and their corresponding dilutions.

Antigen	Supplier	Catalog number	Dilution
γH2AX	Millipore Sigma	05-636	1:2,000
Cleaved lamin A	Cell Signaling Technology	#2031	1:500
PARP1	Santa Cruz Biotechnology	sc-25780	1:1,000
NFκB	Santa Cruz Biotechnology	sc-372	1:1,000

Nrf2	Santa Cruz Biotechnology	sc-365949	1:500
p53	Cell Signaling Technology	#2524	1:1,000
Grp78	Santa Cruz Biotechnology	sc-13539	1:1,000
Grp94	Santa Cruz Biotechnology	sc-393402	1:1,000
p16	My BioSource	MBS821415	1:500
Lamin B	Santa Cruz Biotechnology	sc-6216	1:1,000
Actin	Chemicon	MAB1501	1:100,000

5.2. Instrumentation

5.2.1. Persistent luminescence spectroscopy

Persistent luminescence spectroscopy was performed using the same experimental setup used for radioluminescence spectroscopy using powdered samples. No emission slit was used during the acquisition of radioluminescence and persistent luminescence signals for the time dependent experiments. Upon excitation with a certain radiation dose, persistent luminescence spectra were acquired at 30 s intervals until luminescence could no longer be detected. The persistent luminescence duration was determined to be the amount of time it took for the luminescence signal to decrease to 5% of the original persistent luminescence intensity for the dose-dependent persistent luminescence studies in Section 7.5.7, and 100 counts above baseline for the persistent luminescence studies in Section 7.5.1. Results are representative of the persistent luminescence properties of a minimum of two independent nanoparticle batches studied in duplicate.

5.2.2. Radioluminescence spectroscopy

Unless otherwise stated, radioluminescence emission spectroscopy was performed by exciting powdered or colloidal nanoparticle samples using an Amptek MINI-X X-ray source (4W, Au target, unfiltered and uncollimated beam operating at 50 kVp and 80 μA). The output spectrum can be found in Figure 68, Appendix 6. Emissions were collected using an optical fiber from Ocean

Optics Inc (600 μm diameter) coupled to a Princeton Instruments FERGIE BRX-VR UV-NIR spectrograph fitted with a 1200 grooves/mm grating blazed at 290 nm with a 50 μm slit. Persistent luminescence kinetics studies in Section 7.5.1 were performed using the same conditions but with an approximate dose rate of 30 Gy/min at the position of the sample and the 50 μm slit was removed. Cell irradiation experiments were performed using the same Amptek MINI-X X-ray source used for radioluminescence spectroscopy (4W, Au target, unfiltered and uncollimated beam operating at 50 kVp and 80 μA with a dose rate of 0.6 Gy/min). Persistent luminescence studies in Section 7.5.7 were performed with a dose rate of 0.6 Gy/min at the position of the sample and the 50 μm slit was removed; experimental parameters were identical to those used in the cell irradiation experiments.

As stated in the figure captions, in some cases radioluminescence spectra were collected using a 150 kVp X-ray source. In those instances the following applies: Samples were irradiated inside a cabinet irradiator (SmART X-RAD 225Cx from Precision X-ray) operating at 150 kVp, 20 mA with a 0.3 mm Cu beam hardening filter. Emissions were collected by an optical fiber coupled to an Andor Shamrock 193i-A spectrograph with Al/MgF_2 optics, using a 300 grooves/mm grating blazed at 500 nm, and detected by an Andor Newton DU970P-BV EMCCD.

The intensity corrected radioluminescence spectrum (Figure 69 of Appendix 6) was obtained by generating a correction factor for all wavelengths using an Ocean Optics halogen/deuterium lamp (DT-MINI-2-GS) and a calibrated output spectrum provided by the manufacturer.

5.2.3. Powder X-ray diffraction

All $NaLuF_4$:20% Pr^{3+} PXRD data was obtained on a Scintag XDS-2000 diffractometer equipped with an unfiltered Cu k-alpha source operating at 45 kV and 40 mA, with a Si(Li) peltier-cooled solid state detector. All scans were performed in the 10 – 90° 2θ range with a step size of 0.02° and count times of 0.5 – 2 seconds. Samples were prepared by depositing a few drops of saturated nanoparticle dispersions in hexanes onto a quartz zero background disk and let dry to form thin, flat, uniform powders.

All other PXRD data was obtained using a Bruker AXS D2 Phaser at a step size of 0.02 °

over a range of 10-70° 2θ. The spectrometer was equipped with a Cu-Kα source (λ = 1.54178 Å) operating at 30 kV and 10 mA for excitation and a Bruker LYNXEYE detector operating in θ/2θ scanning geometry.

5.2.4. Thermoluminescence

Thermoluminescence measurements were performed by the research group supervised by Philippe Smet at the University of Gent in Belgium. The thermoluminescence glow curves were measured in a home-built setup inside a Siemens D5000 X-ray diffractometer (Cu anode, not filtered, operated at 40 kV, 40 mA) yielding an estimated air kerma rate of 15 Gy min^{-1} at the position of the sample. The heating was performed by a resistive heating element at a rate of 1 °C /s, with temperature feedback using a USB-6002 DAQ device (National Instruments). The emission spectra were measured by means of a QE65000 spectrometer (Ocean Optics).

The diffuse reflectance measurements were performed on powder covered with a quartz slide. The spectra were recorded using a Perkin Elmer Lambda 1050 S UV/VIS/NIR spectrophotometer, equipped with a Spectralon-coated integrating sphere (150 mm InGaAs Int. Sphere from PerkinElmer) and using Spectralon as reference.

5.2.5. Transmission electron microscopy

Transmission electron microscopy of $NaLuF_4$:20 mol% Pr^{3+} nanoparticles in shown in Sections 6.1, 6.2, and 7.3 were performed using a JEOL-JEM-2100F microscope operating at 200 kV equipped with a charge-coupled device (CCD) camera by Gatan. TEM sample preparation was done by depositing a 1 wt % solution of nanoparticles dispersed in toluene or hexanes onto a 3 mm, 300-mesh copper grid coated with formvar/carbon film from Electron Microscopy Sciences. The same microscope is used in the STEM mode (Scanning Transmission Electron Microscopy) to acquire HAADF (High Angle Annular Dark Field) images by collecting high angle scattered electrons, which gives rise to images with a Z contrast. The STEM mode is then combined with an Oxford EDS detector (model Xplore) to acquire elemental mappings of the scanned areas. Intensity of each element is extracted from a selected peak corresponding to that element to create elemental mappings. Jean-Phillipe Masse of the Centre for Characterization and Microscopy of Materials (CM^2) at Polytechnique Montréal acquired the EDS elemental maps.

All other transmission electron microscopy was performed using a ThermoScientific Talos L120C scanning transmission electron microscope operating at an accelerating voltage of 120 kV. Nanoparticles were deposited onto 300 mesh copper grids coated with a formvar/carbon film from Electron Microscopy Sciences Inc by dipping the grid into a 1 mg/mL colloidal dispersion of the nanoparticles in hexanes and allowing it to dry in ambient conditions.

5.2.6. UV-Visible Absorption Spectroscopy

All absorption spectroscopy experiments were performed on a Varian Cary 100 Bio UV-Vis spectrophotometer using a 1 cm path length quartz cuvette at 20 °C in a single front-cell configuration. Absorption spectroscopy of protoporphyrin IX (5 nM in 50/50 v/v DMSO/H_2O) was carried out with an Agilent Technologies Cary 60 UV-Vis spectrophotometer at a resolution of 1 nm and scanning speed of 600 nm/min in a 1 cm path-length quartz cuvette from Thorlabs.

5.2.7. Effective Atomic Number Calculations

Z_{eff} values were calculated using the Auto-Z_{eff} software developed by the Medical Radiation Physics Research Group at RMIT University.[1] Spectrum-weighted Z_{eff} values were calculated using the pre-set parameters for the INTRABEAM source (50 kVp, Au target).

5.2.8. Zeta potential and Dynamic light scattering measurements

Zeta potentials were acquired on a Malvern Zetasizer Nano ZSP at 20°C using colloidal dispersions of each type of nanoparticle at a concentration of 1 mg/mL in deionized water. Zeta potential values are reported as the average of 5 independent batches of each type of nanoparticle coating, except for 5-ALA coated nanoparticles which were made in duplicate. Dynamic light scattering (DLS) measurements were performed on the same instrument using the same settings.

5.2.9. Fourier transform attenuated total reflectance infrared spectroscopy

FT-IR-ATR was performed using powder samples on a ThermoScientific Nicolet iS5 FT-IR-ATR spectrometer equipped with an iD5 ATR accessory with a diamond-laminate crystal window. Data were collected at a resolution of 0.4 cm^{-1} with a minimum of 256 scans per sample using a DTGS KBr detector set to a gain of 1 with an optical velocity of 0.4747 cm s^{-1} and an aperture setting of 100.

5.2.10. Inductively coupled plasma mass spectrometry

ICP-MS was performed with a 7500ce inductively coupled plasma mass spectrometer from Agilent Technologies equipped with a quartz Scott-type spray chamber, off-axis Omega lens ion focusing and an octupole reaction system with a quadrupole mass spectrometer analyzer operating at 3 MHz. Calibration curves were established using ion concentrations of 0, 0.05, 0.1, 1 and 5 mg/L for Lu^{3+} and Pr^{3+}.

5.2.11. Photoluminescence spectroscopy of $NaLuF_4:Pr^{3+}$ nanoparticles

Photoluminescence measurements under 457.5 nm excitation were performed using a Sabre Innova Argon Ion Laser operating at a power density of 2 W/cm^2. A long-pass filter with a cut off of 475 nm was used to remove the laser line during spectroscopy and photography of the emissions.

5.2.12. Epifluorescence microscopy

Fixed cells were imaged with a Nikon Inverted Microscope Eclipse Ti-E, equipped with 60x objective (NA 1.45) and a Photometrics Evolve 512 EMCCD camera. Protoporphyrin IX and Pr^{3+} were excited with 405 nm and 488 nm LEDs, respectively. The LEDs were installed in a Heliophor Light engine. A quad band filter (445/30, 525/50, 595/40,695/90 nm emission bands) was used to restrict emission to appropriate wavelengths. All images were acquired with NIS-elements software version 1.4.6. Images for each data set were processed identically with ImageJ version 1.53n.

5.3. Experimental Methods

5.3.1. Synthesis of $LuCl_3$ precursors

$LuCl_3$ was prepared from Lu_2O_3 precursors by reaction with concentrated trace metal grade HCl. 10 g of Lu_2O_3 were dissolved in 20 mL 50/50 v/v% aqueous HCl (diluted in ultra-pure water). The mixture was stirred at 200 RPM under reflux at 80 °C until the solution was colorless and clear. The solvent was evaporated at 90 °C and the resulting white crystalline $LuCl_3$ was collected and used without further purification.

5.3.2. Synthesis of $NaLuF_4:Pr^{3+}$ (Method 1)

This method was developed based on the protocol reported by Cooper *et al.*[48] All compositions were synthesized on a 1 mmol scale of lanthanides. 311.5 mg of $LuCl_3 \cdot x\ H_2O$ and 71.1 mg of $PrCl_3 \cdot x\ H_2O$ were added to 6 mL oleic acid and 15 mL 1-octadecene in a 250 mL three-neck round bottom flask. The mixture was stirred at 700 rotations per minute (RPM) and degassed at 120 °C for 30 minutes to remove all traces of water. After 30 minutes, the solution was cooled to 50 °C, brought to ambient pressure, and 10 mL of a methanolic solution containing 2.5 mmol NaF and 4 mmol NH_4F was injected at a rate of 1 mL/minute. The solution is left to stir for 30 minutes at 50 °C. A vacuum distillation trap is then introduced to the center opening of the round bottom flask and the solution is then slowly heated to 90 °C, during which the methanol is slowly evaporated and condenses into the trap; most of the methanol evaporates between 70 and 90 °C and the entire process can take upwards of 30 minutes. At 90 °C, a steady flow of argon is then introduced into the flask and the solution is heated to 120 °C, the argon is removed and the solution is again degassed for 30 minutes to remove any residual methanol or water introduced during the injection. The solution is then brought back to ambient pressure, the argon flow is reintroduced and the reaction is heated to 310 °C for 2 hours. The reaction is then cooled to room temperature under argon. To isolate and purify the nanoparticles, the reaction mixture is centrifuged for 15 minutes at 4000 RPM. The supernatant is removed and the pellet is dispersed in 5 mL hexanes and precipitated by the addition of 30 mL 99% ethanol and 10 mL of 99% methanol. The resulting mixture is centrifuged for an additional 15 minutes at 4000 RPM. This process is repeated twice more to yield the purified oleate-coated nanoparticles. Nanoparticles were stored as a pellet covered in ethanol at room temperature.

5.3.3. Synthesis of $NaLuF_4:Pr^{3+}$ nanoparticles (Method 2)

All compositions of $NaLuF_4$: x% Pr^{3+} (x = 1, 10, 15, 20, 25, 30, 35, 40 mol% Pr^{3+}) were prepared using a co-precipitation technique. The quantities of reagents corresponding to each composition can be found in Table 2. This is the final optimized protocol, changes to this method are discussed in Chapter 6. All compositions were synthesized on a 1 mmol scale of lanthanides. $LuCl_3 \cdot 6\ H_2O$ and $PrCl_3 \cdot 6\ H_2O$ were added to 6 mL oleic acid and 15 mL 1-octadecene in a 250 mL three-neck round bottom flask. The solution was stirred at 500 RPM for the duration of the reaction. The solution containing the lanthanide salts was first heated to 120 °C under 10 mbar

pressure and left to stir for 30 min at this temperature. The solution was then brought to ambient pressure and a steady stream of argon gas was introduced to prevent interaction of the solution with air. The solution was cooled to 90 °C and 6 mmol of solid sodium oleate and 11 mmol of solid sodium fluoride were added directly to the flask. The solution was stirred for 45 min at 90 °C under argon. The argon flow was removed, the temperature was raised to 125 °C, and the mixture was degassed at 10 mbar for an additional 30 min once reaching the set temperature. The pressure was brought back to ambient conditions and argon was again introduced into the reaction. The solution was then heated to 325 °C at a rate of 10 °C/min and kept at this temperature for 1.5 h to grow the nanoparticles. Still under argon, the solution was then cooled to 100 °C and the temperature was ramped back up to 325 °C for an additional 30 min to ensure complete conversion to the hexagonal crystal phase. The nanoparticle mixture was then cooled to room temperature and purified. Purification was achieved by first centrifuging the mixture at 4,500 RPM for 10 min. The supernatant was discarded and the pellet was dispersed in 10 mL hexanes, followed by the addition of 40 mL 99% ethanol to precipitate the nanoparticles. A nanoparticle pellet was again collected by centrifugation at 4,500 RPM for 10 min and this process was repeated 3 times to yield a large white pellet. To remove all traces of sodium oleate, the large white pellet was dispersed in 10 mL of pure oleic acid and left overnight to yield a smaller, light green pellet. The pellet was then purified via the same precipitation/centrifugation technique to yield the isolated $NaLuF_4:Pr^{3+}$ nanoparticles which were stored as a pellet in ethanol at room temperature.

Table 2. $NaLuF_4:Pr^{3+}$ nanoparticle compositions synthesized by method 2 and the corresponding masses of lanthanide chloride salts used in their synthesis.

Nanoparticle composition	**Mass $LuCl_3 \cdot 6\ H_2O$ (mg)**	**Mass $PrCl_3 \cdot 6\ H_2O$ (mg)**
$NaLuF_4$: 1 mol% Pr^{3+}	385.5	3.6
$NaLuF_4$: 10 mol% Pr^{3+}	350.5	35.5
$NaLuF_4$: 15 mol% Pr^{3+}	331.0	53.3
$NaLuF_4$: 20 mol% Pr^{3+}	311.5	71.1
$NaLuF_4$: 25 mol% Pr^{3+}	292.0	88.8
$NaLuF_4$: 30 mol% Pr^{3+}	272.6	106.7
$NaLuF_4$: 35 mol% Pr^{3+}	253.1	124.4
$NaLuF_4$: 40 mol% Pr^{3+}	233.7	142.1

5.3.4. Preparation of $NaLuF_4$: Pr^{3+} coated with citrate or citrate/poly-L-lysine

This protocol was adapted from a previous report.[2] 100 mg (wet mass) of oleate-capped $NaLuF_4$:Pr^{3+} nanoparticles was dispersed in 10 mL hexanes and sonicated for 10 min. The dispersion was then set to stir at 1000 RPM and 10 mL of pH 2 H_2O (adjusted with HCl) was added all at once. The mixture was stirred for 1 h, after which the nanoparticles visibly transferred from the hexanes layer to the aqueous layer. The aqueous layer was then harvested and centrifuged at 17,500 xg for 5 min. The supernatant was discarded; the pellet was dispersed in 1 mL deionized water, and re-centrifuged. A small aliquot of nanoparticles was taken and dispersed in water to evaluate the zeta potential, confirming the removal of the oleate capping ligand. An average zeta potential of +33.3 mV was obtained. Approximately 30% of the nanoparticle mass was lost during this process. Oleate-free nanoparticles were isolated at this stage.

To obtain citrate coated nanoparticles, 70 mg (wet mass) of oleate-free nanoparticles were then dispersed in 2 mL of 0.1 M sodium citrate and stirred at 1,000 RPM for 2 h. The particles were then centrifuged at 17,500 xg for 5 min, the supernatant discarded, and the pellet was dispersed in 1 mL deionized water and re-centrifuged to remove excess citrate. This process was repeated twice (for a total of 3 centrifuging steps) to yield citrate-capped nanoparticles, yielding approximately 50 mg (wet mass) of citrate-capped nanoparticles. A small aliquot was taken and analyzed by zeta potential to confirm the presence of the citrate ligand. An average zeta potential of -34.5 mV was recorded. Citrate coated nanoparticles were isolated at this stage.

To coat the citrate-capped particles with poly-L-lysine (PLL), the citrate-capped pellet was then dispersed in 0.5 mL of deionized water and 1 mL of 0.1 % PLL solution was added. The pH was then adjusted to 10 with NaOH and the mixture was sonicated in an ultrasonic bath for 30 min. The citrate-PLL capped nanoparticles were isolated by centrifugation (17500 xg for 5 min) and purified by centrifugation in deionized water to remove any unbound PLL. The zeta potential was determined to be an average value of +35.8 mV, confirming the presence of PLL as the outer layer of the nanoparticles.Approximately 30 mg (wet mass) of nanoparticles were isolated. A stock concentration of 25 mg/mL citrate-PLL coated nanoparticles in sterile deionized water was stored at 4 °C. The zeta potential of nanoparticles was determined at weekly intervals and was constant for at least one month (see Section 8.1.1). However, stock dispersions of nanoparticles were

typically used within 2-3 weeks of preparation.

5.3.5. Preparation of $NaLuF_4$: Pr^{3+} coated with 5-ALA

50 mg (wet mass) of oleate-free nanoparticles were dispersed in 5 mL pH 8 H_2O (adjusted with NaOH) by sonicating the dispersion for 10 minutes. 5-ALA hydrochloride was defrosted and weighed immediately before preparation of the following solution. In a separate vial, 5 mg 5-ALA was dissolved in 0.5 mL pH 8 H_2O. The nanoparticle dispersion was set to stir at 700 RPM and the 5-ALA solution was added dropwise to it. After 4 hours of stirring, the dispersion was centrifuged (17500 xg, 5 min) to isolate the 5-ALA capped nanoparticles. The nanoparticles were re-dispersed in deionized water and centrifuged again to remove any unbound 5-ALA. The pellet was then dispersed in sterile deionized water and stored at 4 °C. The stock dispersion was used for *in vitro* experiments immediately after confirming the zeta potential, which was on average -2.4 mV.

5.3.6. Quantification of nanoparticle compositions using ICP-MS

To digest the nanoparticles into their constituent ions, 100 µL of a 1 mg/mL suspension of $NaLuF_4$:Pr^{3+} nanoparticles in hexanes were added to a 20x150 mm test tube, followed by the addition of 1 mL concentrated ultra-trace metal grade HCl, 1 mL concentrated ultra-trace metal grade HNO_3, and 100 µL of ultra-trace metal grade H_2O_2. The mixture was heated under reflux to 120 °C for 24 hours, upon which a clear, colorless solution was obtained indicating the nanoparticles had been completely digested. The solvent was then evaporated at 100 °C to yield a solid white precipitate. The precipitate was dissolved in 1 mL 5% v/v aqueous HNO_3 (trace-metal grade) by vortexing for 1 minute. A 100 µL aliquot was then taken and diluted to a total volume of 1 mL. Samples were sealed with parafilm and stored at 4 °C until they could be analyzed. Duplicate measurements were carried out for each nanoparticle sample. Samples were analyzed and prepared by Freesia Vettier.

5.3.7. Cell culture

U251 human glioblastoma cells were kindly provided by Dr. Maysinger at McGill University. Cells were cultured in DMEM (Wisent Bioproducts Inc., Ca^{2+}/Mg^{+} free, phenol-red, sodium pyruvate) supplemented with 10 % v/v fetal bovine serum (Wisent Bioproducts Inc., heat-

inactivated, US origin), without antibiotics, at 37 °C and 5 % CO_2. Testing for mycoplasma contamination was routinely performed *via* PCR and DAPI staining; experiments were performed using cells that routinely scored negative for mycoplasma contamination. Cells were routinely seeded at 60% confluency and passaged at regular intervals, not exceeding 14 passages from the time of defrosting the cells for growth. All treatments, irradiations and incubations were performed in the dark to avoid accidental ROS generation or photobleaching of other light-sensitive species. HeLa cells were kindly provided by Dr. Piekny at Concordia University and cultured in an identical fashion.

The amounts of cells, nanoparticles and 5-ALA were scaled approximately according to the surface area of the treatment flasks and/or cell seeding density as shown in Table 3.

Table 3. Types of cell culture plasticware used for the in vitro experiments and their corresponding surface areas. The number of cells plated and the volume of RLNPs and 5-ALA were scaled for each assay based on the dish used.

Plate type	Growth area (cm^2)	Number of cells plated	Volume of RLNPs (mL)	Volume of 1 mM 5-ALA solution (mL)
35 mm Petri dish (Western blots, clonogenic assays)	9.4	1.2×10^5	2.5	3.0
35 mm Petri dish (ICP-MS)	9.4	1.7×10^5	3.5	4.2
24 well plate	1.82	1.6×10^4	0.5	1.0
96 well plate	0.29	6×10^3	0.125	0.25

5.3.8. Preparation of 5-ALA solution for cell culture

1 mM solutions of 5-ALA were prepared in serum-free DMEM. 5-ALA solutions were freshly prepared prior to each treatment. Solid 5-ALA was defrosted and weighed immediately before preparation of the solutions. Solutions of 5-ALA were added to the cells within 2 hours of preparation. Solutions were incubated at 37 °C prior to their introduction to the cells.

5.3.9. Preparation of nanoparticle suspensions for cell culture

25 mg/mL stock nanoparticle suspensions were prepared in sterile deionized water and vortexed for 5 minutes prior to preparing the sample suspensions. Concentrations of 50, 100 and 200 µg/mL were prepared by diluting the stock with an appropriate volume of serum-free DMEM.

Small volumes of sterile deionized water were added to the lower concentrations of nanoparticles in order such that all suspensions were equally diluted with water. Suspensions were prepared such that 5% or less of the total volume of DMEM was diluted with water. Suspensions were incubated at 37 °C and then vortexed for 2 minutes prior to their introduction to the cells.

5.3.10. *In vitro* fluorescence assays

A BMG Labtech ClarioSTAR® monochromator microplate reader was used to measure fluorescence of resorufin at $\lambda_{ex} = 550$ nm and $\lambda_{em} = 590$ nm at 37 °C. Fluorescence excitation at 405 nm and emission at 620 nm at 37 °C were used for the detection of protoporphyrin IX. Gain and focal height were optimized by the ClarioSTAR® software before each experiment.

5.3.11. Metabolic activity assays of cells without X-ray irradiation

All nanoparticle toxicity and 5-ALA toxicity assays in the absence of X-ray irradiation were performed in 96 well plates. Cells were seeded at 6,000 cells per well and incubated for 24 hours prior to treatment. On the day of treatment, media was aspirated from each well, cells were rinsed with 100 μL of PBS followed by the addition of 250 μL of 1 mM 5-ALA in serum-free DMEM were to each well. Cells were incubated for 4 hours. The 5-ALA solution was then removed and, without washing, replaced with 100 μL of nanoparticle suspension at each desired concentration. The cells were again left to incubate for 1 hour, after which the media was aspirated and replaced with DMEM. The cells were then left to incubate for 24 hours under standard conditions. The media was then aspirated and a solution of 10% v/v TOX8 resazurin assay kit in DMEM (see below) was added to each well without rinsing with PBS; each well received 100 μL of resazurin solution. After 4 hours, the plates were then assessed for metabolic activity in a plate reader. All experiments were performed in triplicate for each assay and as a minimum of 3 independent experiments using different cell passage numbers.

5.3.11.1. Preparation of resazurin solution

The resazurin solution was prepared in the dark and kept in the dark throughout the experiment. The concentrated TOX8 resazurin stock was brought to room temperature and then diluted to 10% v/v in DMEM. It is essential to mix thoroughly to incorporate the resazurin homogenously into the DMEM. The solution was incubated at 37 °C until its introduction to the

cells.

5.3.12. Metabolic activity assay after X-PDT treatment

All X-PDT viability assays were performed in 24 well plates, using a minimum of 4 independent experiments at different cell passage numbers, each independent experiment was performed in triplicate. Cells were seeded at 16,000 cells per well and incubated for 24 hours prior to treatment. On the day of treatment, media was aspirated from each well, cells were rinsed with 100 µL of PBS, and 1.0 mL of 1 mM 5-ALA in serum-free DMEM was added to each well and incubated for 4 hours. For viability without 5-ALA treatment, the cells were incubated with serum-free DMEM for 4 hours. The 5-ALA solution was then removed and, without washing, replaced with 500 µL of nanoparticle suspension at each desired concentration. The cells were again left to incubate for 1 hour, after which the media was aspirated and replaced with 200 µL of DMEM. The cells were then irradiated with the desired dose of X-rays (controls were sham-irradiated under identical conditions). After irradiation, an additional 0.8 mL of complete DMEM was added to the cells. After incubation for 24 or 48 hours, media was then aspirated and a solution of 10% Resazurin in complete DMEM (see 5.3.11.1) was added to each well without rinsing with PBS. Cells were incubated at 37°C for 4 hours, and then assessed for metabolic activity in a plate reader.

5.3.13. Fixed-cell microscopy of cells treated with 5-ALA and/or RLNPs

Poly-lysine coated coverslips (circular, 12 mm diameter) were placed in a 24-well plate and seeded with 16,000 cells per well. After 24 hours, cells were washed with PBS and incubated in serum-free DMEM or treated with 1 mM 5-ALA solution in serum-free DMEM for 4 hours. The media was aspirated and nanoparticle suspensions in DMEM were added for 1 hour. The cells were rinsed with PBS and fixed on ice in 4 % paraformaldehyde solution for 15 minutes**.** Coverslips were rinsed twice with PBS, once with deionized water, and mounted on glass slides in Mowiol mounting medium. Slides were stored at 4 °C. Technical triplicates were assessed for each experiment; at least two independent experiments were performed for each condition. All compiled microscopy figures depict representative images of the results.

5.3.14. Quantification of PPIX production by fluorescence spectroscopy

A 24-well plate was seeded with 16,000 cells/well and left to incubate for 24 hours. Cells

were washed with PBS and 1 mM 5-ALA solution in serum-free DMEM was added to the cells and left to incubate for 1, 2 or 4 h. At the end of each incubation time, the 5-ALA containing medium was aspirated and cells were rinsed with PBS three times. A 50/50 v/v% solution of serum-free, phenol-red free DMEM and DMSO were added to the cells and left to incubate at room temperature for 15 minutes in order to solubilize the PPIX produced by the cells and dissolve it into the supernatant. Phenol-red free media was used to eliminate the fluorescence of phenol red as a variable in the measurement. Prior to performing fluorescence spectroscopy, the supernatant in each well for each sample was mixed thoroughly by pipetting. A BMG Labtech ClarioSTAR® monochromator microplate reader was used to measure fluorescence of protoporphyrin IX at $\lambda_{ex} = 405$ nm and $\lambda_{em} = 620$ nm at 25 °C. Gain and focal height were optimized by the ClarioSTAR® software before each experiment. Each parameter was evaluated in triplicate, and results are based on a minimum of two independent experiments.

5.3.15. Quantification of RLNP-cell interactions monitored by ICP-MS

For each experiment, technical triplicates were digested and analyzed by inductively coupled plasma mass spectrometry (ICP-MS). Data shown here represent the results of three independent experiments performed on different cell passages. In brief, 35 mm dishes were seeded with 170,000 cells and incubated for 24 h. Each dish was washed once with PBS and incubated with serum-free media or 1 mM 5-ALA in serum-free media for 4 h. The cell media was aspirated, and nanoparticle suspensions in serum-free DMEM were added. After 1 h, cells were trypsinized (250 µL of trypsin-EDTA for 2 minutes) and the digestion was stopped by adding 250 µL of DMEM. The cell suspension was then collected in a 5 mL microcentrifuge tube. The dish was then rinsed with 100 µL of PBS and this was added to the previously-isolated cell suspension to ensure all cells were collected. Clumps of cells were removed by gently pipetting the suspension. Cell numbers from the trypsinized cell suspension were then counted with a hemocytometer in duplicate.

For ICP-MS analysis, the cell suspensions were sonicated for 5 min to lyse the cells. Each cell suspension was then analyzed in duplicate by taking two 100 µL aliquots of the suspension and then proceeding with the following protocol for each aliquot. In a 20x150 mm glass test tube containing the 100 µL aliquot, 1 mL of concentrated trace-metal grade HCl, 1 mL of concentrated

trace-metal grade HNO_3 and 200 µL of trace-metal grade H_2O_2 were added. After reflux at 115 °C for 24 h, an additional 200 µL of H_2O_2 was added. When colorless, the solution was dried at 125 °C. The remaining white residue was dissolved in 1 mL 5 % v/v aqueous HNO_3, and 100 µL aliquots were further diluted with 900 µL 5% v/v aqueous HNO_3. The concentrations of Lu^{3+} and Pr^{3+} were then determined by ICP-MS.

To assess the number of nanoparticles associated with cells, the mass of a single nanoparticle was derived from its volume based on average static TEM dimensions assuming a hexagonal prism morphology. The *a* and *c* parameters of the individual unit cells were calculated using the (100) and (002) reflections from the PXRD diffractograms, which then provides the volume of a single unit cell. The number of unit cells was then calculated to obtain the number of Lu^{3+} or Pr^{3+} ions per nanoparticle. The number of nanoparticles per cell was then determined based on the ICP-MS data for ion concentrations and the number of cells counted during preparation of the ICP-MS samples.

5.3.16. Detection of reactive oxygen species

Intracellular reactive oxygen species (ROS) were detected with 2',7'-Dichlorofluorescein diacetate (DCFH-DA). Cells were seeded in 24-well plates at 16,000 cells/well, grown for 24 h, and treated with 5-ALA and nanoparticles as described for the viability assays. Upon 30 min incubation with nanoparticles, a freshly prepared 10 mM DCFH-DA stock solution in sterile DMSO was added to the cells to obtain a final concentration of 50 µM. After 30 min incubation, the solution was replaced with 200 µL of DMEM, and cells were irradiated. Following irradiation, samples were immediately assessed for ROS production by fluorescence spectroscopy in a plate reader. Fluorescence excitation at 500 nm and emission at 525 nm at 37 °C were used for the detection of dichlorofluorescein (DCF). Gain and focal height were optimized by the ClarioSTAR® software before each experiment.

5.3.17. Preparation of crude cell extracts and Western blotting

Cells were seeded in 35 mm dishes and treated as described for the toxicity assays. In brief, 1.5 mL of DMEM was added to the cells after irradiation, and incubation was continued for 24 h. Cells were collected in 2 mL microcentrifuge tubes and centrifuged at 750 xg for 5 min. The pellet was

then gently resuspended in PBS and centrifuged again at 750 xg for 5 min. The supernatants were aspirated and pellets stored at -80 °C. The preparation of crude extracts and Western blotting followed our published protocols.[361] Enhanced chemiluminescence signals for Western blots were acquired with a Bio-Rad ChemiDoc™ MP Imaging System. For each antigen, all lanes were on the same filter, exposed for the same time, and processed identically in Photoshop CS4 extended, version 11.0. For graphical depiction and statistical evaluation electrochemiluminescence signals were normalized to the actin loading control.

5.3.18. Apoptosis/necrosis assay using Fluorescence Activated Cell Sorting analysis

Each 35 mm petri dish was seeded with 170,000 cells and incubated for 24 h prior to the treatments specified for the toxicity assays. 24 h after irradiation, the Annexin V-FITC and propidium iodide staining was performed as recommended by the supplier. Live cells were analyzed by fluorescence-activated cell sorting (FACS) with a BD Accuri^{TM} C6 Plus flow cytometer. To this end, 1x10^6 cells in 200 µL cell sorting buffer (1% fetal bovine serum in PBS (Ca^{2+}/Mg^{2+}free) supplemented with 25 mM HEPES and 1 mM EDTA). Cells were stained with Annexin V-FITC and propidium iodide according to the supplier's instructions. Cells were rinsed with binding buffer, passed through a 70 µM filter and analyzed by FACS. A minimum of 3x10^5 events were recorded per sample with flow rate set to medium. Gating strategy consisted of cells being gated on a forward scatter (FSC) versus side scatter (SSC) plot to exclude cell debris and doublets. Annexin V-FITC and propidium iodide fluorescence were visualized using FL1 (emission filter 533/30) versus FL2 (emission filter 585/45) on log-scale density plots with quadrants to quantify percentages of apoptotic and necrotic cells. Data shown in the flow cytograms are representative of three independent experiments.

5.3.19. Clonogenic assays

Prior to the full X-PDT assays, the number of cells seeded for colony formation was established *via* the protocol developed by Brix *et al.*[362] Of great importance, cooperative growth can vastly alter the calculated survival fractions from a clonogenic assay, as it results in higher plating efficiencies for higher cell seeding densities.[363] Cooperative growth is a phenomenon that occurs when cells are stimulated to grow by being in proximity of other cells.[362] Cellular

cooperation was observed for U251 cells and corresponding average plating efficiencies were calculated using equation 7. Sample plating efficiencies are listed in Table 4.

$$\textbf{\textit{Plating efficiency}} = \frac{\textbf{\textit{\# colonies counted}}}{\textbf{\textit{\# cells seeded initially}}} \quad (7)$$

Table 4. Sample plating efficiencies calculated for untreated, unirradiated controls in the absence and presence of 5-ALA.

0 Gy, 0 µg/mL RLNPs		
Seeding Density (cells/well)	**Plating Efficiency**	
	(-) 5-ALA	**(+) 5-ALA**
125	0.0480	0.044
250	0.1315	0.215
500	0.3120	0.4745
1000	0.3321	0.5575

Clonogenic assays were carried out *via* the protocol developed by Brix *et al.*[3] 35 mm dishes were seeded at a density of 170,000 cells/dish. The treatment was as described for the toxicity assays, with all volumes adjusted to 35 mm dishes. Samples were exposed to X-rays, trypsinized and cell numbers were counted in duplicate. Based on the cell count, the culture was serially diluted according to the values in Table 5, and triplicates of the dilutions were plated in 6-well plates. A minimum of 4 seeding densities were used per experiment (ranging from 100 cells/well to 20k cells/well). The samples were incubated for 7 days and stained with methylene blue (0.5 v/v% in 70% ethanol) for 30 minutes. Colonies of ≥ 50 cells were counted manually under a stereomicroscope (Amscope, SM-2T-V331). The number of cells in each colony were counted manually to ensure there were ≥ 50 cells per colony. Colonies were counted for at least four different seeding densities. A minimum of four independent replicates were performed for each treatment condition. Survival fractions were calculated using the power regression-based analysis Excel spreadsheet template published by Brix *et al.*[364]

Table 5. Seeding densities used to obtain survival data using power regression analysis to generate dose-response curves across all NP concentrations and radiation doses with and without incubation with 5-ALA.

0 µg/mL RLNPs		
Radiation Dose (Gy)	**(-) 5-ALA**	**(+) 5-ALA**
	Seeding Densities (cells/well)	**Seeding Densities (cells/well)**
0	125, 250, 500, 1000	125, 250, 500, 1000, 2000
2	125, 250, 500, 1000	125, 250, 500, 1000
5	125, 250, 500, 1000	125, 250, 500, 1000
10	250, 500, 1000, 2000, 5000	250, 500, 1000, 2000, 5000
20	500, 1000, 2000, 5000, 10000	1000, 2000, 5000, 10000

50 µg/mL RLNPs		
Radiation Dose (Gy)	**(-) 5-ALA**	**(+) 5-ALA**
	Seeding Densities (cells/well)	**Seeding Densities (cells/well)**
0	125, 250, 500, 1000	125, 250, 500, 1000
2	125, 250, 500, 1000	250, 500, 1000, 2000
5	125, 250, 500, 1000, 2000, 5000	125, 250, 500, 1000, 2000, 4000
10	250, 500, 1000, 2000, 5000	500, 1000, 2000, 4000
20	500, 1000, 2000, 5000, 10000	500, 1000, 2000, 4000

100 µg/mL RLNPs		
Radiation Dose (Gy)	**(-) 5-ALA**	**(+) 5-ALA**
	Seeding Densities (cells/well)	**Seeding Densities (cells/well)**
0	125, 250, 500, 1000	125, 250, 500, 1000
2	100, 200, 400, 600, 800, 1000	100, 200, 400, 600, 800, 1000, 2000, 4000

5	100, 200, 400, 600, 800, 1000, 2000	400, 800, 1000, 2000, 4000
10	500, 1000, 2000, 5000, 10000	500, 1000, 2000, 5000, 10000
20	500, 1000, 2000, 5000, 10000	5000, 10000, 20000

200 µg/mL RLNPs		
Radiation Dose (Gy)	**(-) 5-ALA**	**(+) 5-ALA**
	Seeding Densities (cells/well)	**Seeding Densities (cells/well)**
0	125, 250, 500, 1000	125, 250, 500, 1000
2	100, 200, 400, 600, 800, 1000	100, 200, 400, 600, 800, 1000, 5000, 10000
5	100, 200, 400, 600, 800, 1000, 2000	500, 1000, 2000, 5000, 10000
10	500, 1000, 2000, 5000, 10000	1000, 2000, 5000, 10000
20	500, 1000, 2000, 5000, 10000	5000, 10000, 20000

Chapter 6. Synthesis of $NaLuF_4:Pr^{3+}$ nanoparticles

6.1. Crystallographic properties of $NaLuF_4:Pr^{3+}$

In 1966, Thoma *et al*. reported the phase diagrams for the entire series of $NaREF_4$ systems.[365] Of particular relevance to this work, these results highlight the major role of cation size (and consequently, polarizability) in determining the crystal phase of $NaREF_4$ materials. The ionic radii of the cations in the nanomaterial of interest vary significantly, with Na^+, Pr^{3+} and Lu^{3+} having ionic radii of 1.24, 1.18 and 1.03 pm, respectively.[366] As such, it proved challenging to produce $NaLuF_4:Pr^{3+}$ nanoparticles with a high degree of phase purity, size and morphological uniformity. Of importance, throughout this work, the primary goal was to obtain $NaLuF_4:Pr^{3+}$ nanoparticles that were sub-100 nm in size, highly uniform, and highly reproducible. Each of these criteria are relevant for efficient cell uptake[367], and thus are important for achieving successful biological use.

$NaREF_4$ crystallizes in three phases: cubic, hexagonal, and orthorhombic.[365] The cubic (α) and the hexagonal (β) crystal phases are of practical relevance as they are relatively stable at room temperature.[368] The α phase crystallizes in space group $Fm\bar{3}m$, where the RE^{3+} ions are 8-fold coordinated and occupy a single site of O_h symmetry (Figure 17A). Several possible space groups have been proposed for β-$NaREF_4$, but the two most commonly accepted are $P\bar{6}$ and $P6_3/m$.[368]

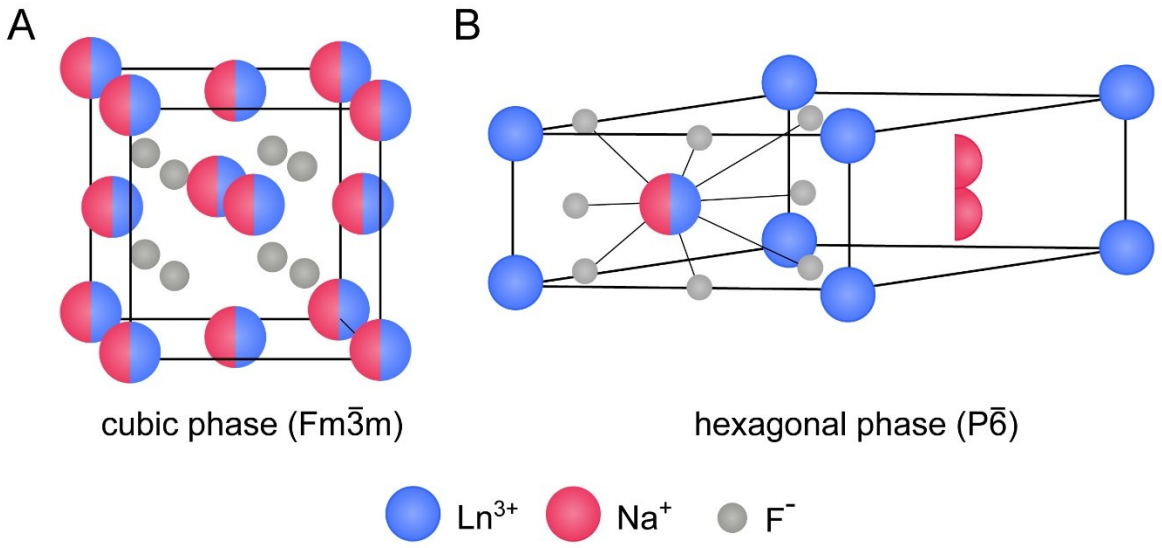

Figure 17. Graphical representation of the unit cells of cubic and hexagonal $NaLuF_4$. Lanthanide ions are depicted in blue, sodium ions in pink, and fluoride ions in gray.

While the space group of β-$NaLuF_4$ is still contested[368], β-$NaPrF_4$ is known to crystallize in a $P\bar{6}$ space group.[369] In the hexagonal phase for both space groups, the RE^{3+} ions are 9-fold coordinated and occupy sites with C_{3h} symmetry. One site is fully occupied by RE^{3+} and the other is 1:1 occupied by Na^+ and RE^{3+} ions (Figure 17B).

6.2. Optimization of the synthesis of β-$NaLuF_4$:Pr^{3+}

Similar to what has been observed for upconverting nanoparticles based on the $NaREF_4$ host, early results obtained from a sample of α-$NaLuF_4$:20% Pr^{3+} showed drastically-reduced radioluminescence relative to their hexagonal-phase counterparts (see Section 7.2).[37,38,368] Thus, obtaining β-$NaLuF_4$:Pr^{3+} nanoparticles was the focus of all further studies. β-$NaLuF_4$ is notoriously difficult to obtain through direct nucleation.[365] Rather, it is obtained *via* a cubic to hexagonal phase transition, of which the energy barriers are significant.[38] The propensity for $NaREF_4$ to crystallize in the cubic or hexagonal phase is a consequence of the size of the RE^{3+} ion, where the disparity in size between Na^+ and RE^{3+} dictates the preferred phase. As the size disparity increases, it becomes more difficult to form the hexagonal phase.[365] Na^+ and Pr^{3+} only differ in ionic radii by 5%, thus formation of β-$NaPrF_4$ is relatively easy. In contrast, Na^+ and Lu^{3+} differ in ionic radii by 17%, and β-$NaLuF_4$, and β-$NaLuF_4$ notoriously difficult to isolate.[365]

Initial attempts to synthesize β-$NaLuF_4$:Pr^{3+} focused on achieving uniform nanoparticles at a concentration of 20% Pr^{3+}, as this concentration had been reported to yield strong $^1S_0$ emissions under VUV excitation.[370] A more detailed discussion on the reasoning behind the dopant concentrations chosen for study can be found in Chapter 7. We first began using a classic co-precipitation technique[38,48] involving a methanolic injection of NaOH (see Section 5.3.2), herein referred to as method 1. This method has previously yielded uniform β-$NaLuF_4$ nanoparticles with high reproducibility.[48] Under standard conditions known to yield uniform β-$NaLuF_4$:Gd^{3+},Tb^{3+} nanoparticles around 30 nm in size (entry 0, Table 6), β-$NaLuF_4$:20% Pr^{3+} nanoparticles that were hexagonal phase (Figure 18A) and 403 ± 15 nm in size were obtained (Figure 18B). Notably, the nanoparticles are remarkably uniform in size and morphology. Nanoparticle size is related to the ease of nucleation at the supersaturation stage during synthesis.[37,38] Given the vastly different energy barriers to forming $NaLuF_4$ and $NaPrF_4$ as described by Mai[38], along with the varying ionic radii of the cations, it is unsurprising that nucleation was inefficient and large nanoparticles

were obtained.

Subsequent attempts using method 1 were focused on size reduction while maintaining uniformity. Size reduction is often achieved by reducing the amount of energy introduced into the system; ie. by reducing the temperature of the reaction and/or the time. Unfortunately, the same conditions that favor smaller particles generally also favor the formation of nanoparticles with the cubic crystal phase. Several routes have been reported for achieving the α-to-β phase conversion.[38,371,372] The most commonly-used route is doping the lattice with RE^{3+} ions which have lower phase transition energy barriers, or preferentially nucleate directly in the hexagonal phase in $NaREF_4$, such as Gd^{3+}.[38] Unfortunately, $Pr^{3+} \rightarrow Gd^{3+}$ energy transfer is known to be efficient due to resonance between the 5d levels of Pr^{3+} and different transitions of Gd^{3+} depending on the host, resulting in drastically-reduced radioluminescence yields from Pr^{3+}.[373–375] Rather, this combination is used to enhance Gd^{3+} emissions.[376,377] Thus this strategy is not viable for developing radioluminescent β-$NaLuF_4$:Pr^{3+}.[373] Other strategies include altering the source and/or ratio of precursors, increasing the reaction temperature and/or heating rate, or changing the synthesis route.[37,38,372,378,379] All of these avenues were explored, as described below.

Table 6. Summary of synthetic parameters investigated using method 1 to synthesize $NaLuF_4$:20 mol% Pr^{3+} nanoparticles. Method described in Section 5.3.2.

Entry	Ramp (°C/min)	Stir rate (RPM)	Temp. (°C)	Time (h)	Na^+:Ln^{3+}:F^- ratio	Phase	Size (nm)
0[a]	10	-	310	2	2.5 : 1 : 4	β	403 ± 15 nm
1	10	700	315	2	2.5 : 1 : 4	α	Mixed
2	10	700	320	2	2.5 : 1 : 4	β	289 ± 13 nm
3[b]	10	700	320	2	2.5 : 1 : 4	Mix	--
4	10	700	320	3	2.5 : 1 : 4	α	475 nm[c]
5	15	700	320	3	2.5 : 1 : 4	β	984 nm[c]
6	15	700	320	2	2.5 : 1 : 4	β	Mixed
7	15	700	320	2	2.5 : 1 : 4	β	Mixed
8	15	700	320	2	2.5 : 1 : 4	β	Mixed
9	15	700	310	2	2.5:1:11	Mix	4, 36, 87 nm
10	15	500	310	2	2.5:1:11	β	92 ± 21

[a]This synthesis was performed by Daniel R. Cooper.
[b]Oleic acid:1-octadecene ratio was changed to 1:1
[c]Size obtained by DLS.

Table 6 contains a summary of highlighted conditions explored to optimize the

nanoparticle synthesis using method 1. The corresponding PXRD and TEM results are shown in Figure 18. First, a reaction at 315 °C for 2 hours (entry 1) yielded nanoparticles with two distinct size distributions, which were sub-100 nm in size, but an α crystal phase. As previously mentioned, based on the results presented in Section 7.2, the cubic phase is not desirable for generating strong radioluminescence from Pr^{3+} in this host. An increase to 320 °C for 2 hours yielded uniform β phase nanoparticles 285 ± 13 nm in size, thus some degree of size reduction was achieved relative to entry 0. These results suggested that 320 °C was near the threshold for the energy required to achieve the phase transition.

Changes in the oleic acid:1-octadecene (OA:ODE) ratio were investigated, as the ratio of coordinating and non-coordinating solvents is known to have an effect on the uniformity of the nanoparticles.[37] A range of ratios were investigated, from a 1:3 ratio to a 3:1 ratio of OA:ODE. None produced significant improvements toward achieving smaller hexagonal-phase nanoparticles, with results similar to entry 3, where a 1:1 ratio of OA:ODE was used, producing large nanoparticles with a mixed crystal phase. Thus, the commonly-reported 1:2.5 OA:ODE ratio (15 mL OA, 6 mL ODE)[48,380–383] was maintained throughout the remaining syntheses, in order to reduce the number of variables under investigation.

Since octadecene boils at 315 °C (though this is elevated in the presence of oleic acid), we explored other routes to introducing more energy to the reaction, as increasing the temperature further would cause more octadecene evaporation. Thus, rather than further increasing the temperature, we tried increasing the reaction time to 3 hours (entries 4 and 5), however this resulted in pure α-phase nanoparticles, indicating the energy barrier for the phase transition could not be overcome with time alone. The temperature is typically increased at a rate of 10 °C/min to achieve the final reaction temperature (>300°C), thus we postulated that a higher temperature ramping rate may provide sufficient energy to induce the phase transition. Indeed, increasing the ramping rate to 15 °C/min successfully generated β-$NaLuF_4$ on multiple tries (entries 5-8). Unfortunately, this yielded nanoparticles of nearly 1000 nm when 3 hours was used (entry 5). Interestingly, with a 2 hour reaction time, the nanoparticles exhibited a poor overall size distribution, but the majority of nanoparticles were around 150-200 nm in size and a pure hexagonal phase was obtained (entries 6-8).

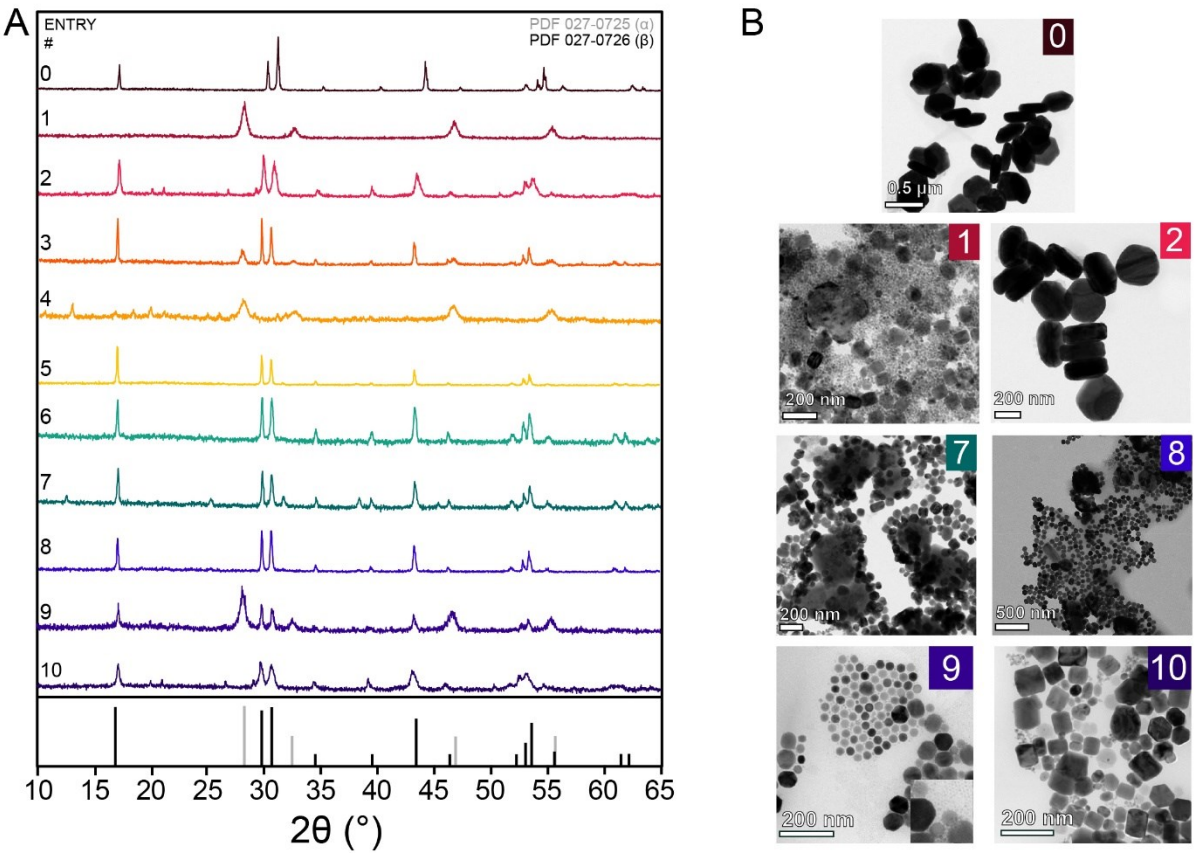

Figure 18. A) PXRD diffractograms and B) selected TEM images of $NaLuF_4$:20% Pr^{3+} nanoparticles. Numbers 0-10 corresponding to the entries in Table 6. The PXRD patterns of cubic and hexagonal $NaLuF_4$ are shown at the bottom of panel A, corresponding to PDF 00-027-0725 (gray) and PDF 00-027-0726 (black), respectively.

Several more attempts were made to reduce the size of the nanoparticles using method 1, to no avail. Changes in degassing time, degassing temperature, $NaOH/NH_4F$ injection rate and evaporation temperature, and other parameters were also explored, all resulting in results similar to those obtained in entries 7, 8 and 9 in Figure 18. The thermal decomposition synthesis from trifluoroacetate precursors and from rare-earth oleates was also attempted, with constant cubic phase, large particles obtained.

Since the discrepancy in cationic radii is known to affect the synthesis of the $NaREF_4$ hosts, the ratio of Na^+ and Ln^{3+} ions available during the nucleation and growth phases were hypothesized to affect the outcome of the synthesis. In line with this hypothesis, size control has been demonstrated through modification of the ratio of Na^+, Ln^{3+} and F^- ions in solution during synthesis.[372,379] Interestingly, increasing the ratio of Na^+ and F^- to Ln^{3+} is also known to favor the

formation of hexagonal-phase nanoparticles, as previously mentioned. Increasing the ratio of NH_4F (entry 9) generated much smaller nanoparticles, but with a mixed crystal phase and multiple size distributions. We repeated the reaction with a reduced stirring speed to try and reduce turbulence in the reaction during stirring. This resulted in nanoparticles with a pure hexagonal crystal phase that were 92 ± 21 nm in size (entry 10). Thus, particles of sub-100 nm size had been achieved, but with high polydispersity. Increasing the Na^+:Ln^{3+} ratio using method 1 required a large volume of NaOH/NH_4F in MeOH to be injected, which was impractical to evaporate in the next step of the synthesis, and caused oxidation of oleic acid. Multiple attempts were made to use method 1 with a 6:1:11 Na^+:Ln^{3+}:F^- ratio, however, nanoparticles were not isolated in any of these attempts because the oxidized oleic acid and high salt contents formed a thick black mixture that could not be purified. This prompted us to change our sodium source to solid sodium oleate, which could be added directly as a powder to the reaction along with solid NH_4F (referred to as method 2, Section 5.3.3). PXRD and TEM results for highlighted examples are shown in Table 7 and Figure 19.

Table 7. Summary of parameters used to optimize the synthesis of $NaLuF_4$:20% Pr^{3+} nanoparticle using synthesis method 2. Method described in Section 5.3.3.

Entry	Ramp (°C/min)	Stir rate (RPM)	Temp. (°C)	Time (h)	Na^+:Ln^{3+}:F^- ratio	Phase	Size (nm)
11	15	500	320	2	6:1:11	Mix	74 ± 12
12	15	500	325	2	6:1:11	Mix	63.7 ± 8.8
13	15	500	325	2+0.5	6:1:11	β	67.6 ± 6.7
14	15	500	325	2+0.5	6:1:11	β	90.1 ± 6.0
15	15	500	325	2+0.5	6:1:11	β	85.3 ± 7.0
16	15	500	325	2+0.5	6:1:11	β	70.1 ± 5.7

The use of a hydroxide-free sodium source proved beneficial for multiple reasons. It enabled the ability to drastically change the Na^+:Ln^{3+}:F^- ratio without introducing large amounts of strong base and methanol to the reaction, the reaction time was reduced since the methanol removal was no longer a step. Finally, syntheses using minimal OH-containing reagents are known to yield lanthanide-doped nanoparticles with less OH defects in the lattice, reducing luminescence

quenching from susceptible energy levels.[384,385] Increasing the Na^+:Ln^{3+}:F^- ratio to 6:1:11 reduced the size and improved the polydispersity significantly (entry 11), as did increasing the temperature by 5 °C (entry 12), however a crystal phase mix was repeatedly observed. As discussed by Haase *et al.*, β-phase nanoparticles could be obtained by re-heating their α-phase counterparts through Ostwald ripening.[372] As such, we redispersed the nanoparticles from entry 12 in oleic acid and octadecene, and heated the mixture to 325 °C for 30 minutes under argon. The nanoparticles were completely converted to the β-phase and the size distribution was slightly narrowed. We postulated that the re-heating step could be done immediately after the initial synthesis, thus saving time and reducing solvent waste. As shown in entries 14-16, a two-stage heating method successfully produced monodisperse, sub-100 nm nanoparticles with uniform morphology and hexagonal crystal phase in a reproducible fashion (Figure 19). Notably, the nanoparticles are in line with the 70-100 nm sizes purported to be ideal for achieving optimal radioluminescence (see section 2.2.1).

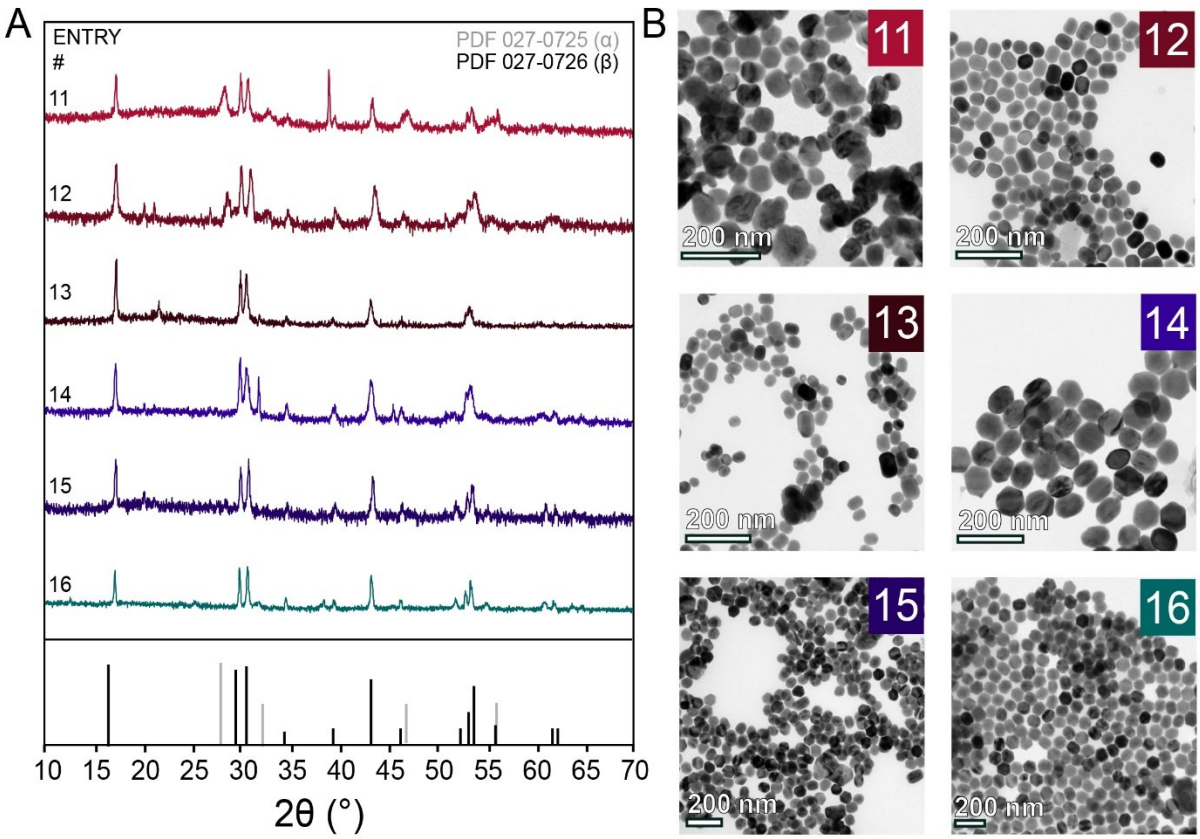

Figure 19. A) PXRD and B) selected TEM results for $NaLuF_4$:20% Pr^{3+} nanoparticles listed as entries 11-16 in Table 7. The PXRD patterns of cubic and hexagonal $NaLuF_4$ are shown at the bottom of panel A, corresponding to PDF 00-027-0725 (gray) and PDF 00-027-0726 (black), respectively.

This technique was used to synthesize β-$NaLuF_4$:Pr^{3+} nanoparticles ranging from 0-40 mol% Pr^{3+} (Table 8), illustrating the robustness of the established parameters toward relatively large changes in the composition. As described in Chapter 7, this range of Pr^{3+} concentrations were evaluated to optimize the radioluminescence intensity of the $^1S_0 \rightarrow {}^1I_6$ transition. The corresponding PXRD and TEM images are shown in Figure 24 along with their spectroscopic properties.

Table 8. Synthetic parameters used to produce $NaLuF_4$: x% Pr^{3+} nanoparticles (x = 0-40 mol%) using method 2 and the corresponding crystal phase and static size of the nanoparticles.

Entry	Mol % Pr^{3+}	Ramp (°C/min)	Stir rate (RPM)	Temp. (°C)	Time (h)	Na^+:Ln^{3+}:F^- ratio	Phase	Size (nm)
17	0	15	500	325	2+0.5	6:1:11	β	57.38 ± 4.7
18	1	15	500	325	2+0.5	6:1:11	β	79.1 ± 6.7
19	10	15	500	325	2+0.5	6:1:11	β	75.7 ± 6.1
20	15	15	500	325	2+0.5	6:1:11	β	77.6 ± 3.9
21	20	15	500	325	2+0.5	6:1:11	β	68.4 ± 5.2
22	25	15	500	325	2+0.5	6:1:11	β	87.1 ± 5.9
23	30	15	500	325	2+0.5	6:1:11	β	80.9 ± 5.7
24	35	15	500	325	2+0.5	6:1:11	β	69.0 ± 3.7
25	40	15	500	325	2+0.5	6:1:11	β	88.3 ± 6.1

Chapter 7. Spectroscopy of $NaLuF_4:Pr^{3+}$ nanoparticles

7.1. Spectroscopic properties of β-$NaLuF_4:Pr^{3+}$

As mentioned in Section 2.3.1, luminescence from Pr^{3+} arises from two main routes: UV emissions arise from transitions from the $^1S_0$ excited state at 46500 cm^{-1}, and visible and NIR emissions arise from the transitions from the LOLs at 25,000 cm^{-1} or lower (Figure 20A). For Pr^{3+}, the $^1S_0$ state is close in energy to the $4f^15d^1$ states; in the case of $NaLuF_4$ the $^1S_0$ state is below the $4f^15d^1$ levels. The position of the lowest $4f^15d^1$ state in our material is much higher than the $^1S_0$ state, at 52829 cm^{-1} (see Section 7.5.3). When there is a sufficient gap between the $4f^15d^1$ state and the $^1S_0$ state, intraconfigurational $4f^2 \rightarrow 4f^2$ transitions occur. In contrast, when the $4f^15d^1$ states and the $^1S_0$ states are close in energy, the gap between them can be easily bridged, resulting in interconfigurational $4f^15d^1 \rightarrow 4f^2$ transitions in the UV region, and/or the expected intraconfigurational $4f^2 \rightarrow 4f^2$transitions.

Herden *et al.* have investigated the properties of Pr^{3+} doped $NaREF_4$ materials in-depth under VUV excitation.[369,370,386] In particular, their studies on $NaLaF_4:Pr^{3+}$ microparticles motivated us to begin our investigation using 20% Pr^{3+}, as they report the strongest $^1S_0 \rightarrow {}^1I_6$ emissions were obtained for this concentration in that host.[369] Of note, VUV excitation directly excites Pr^{3+}, whereas the studies herein are focused on excitation with X-rays, where the excitation of the host lattice plays a prominent role.

As shown in Figure 20B, $NaLuF_4$:20% Pr^{3+} exhibited the characteristic 4f emissions from Pr^{3+}; the band positions are listed in Table 9. Of note, the emission spectra presented throughout this thesis are not corrected for the spectral sensitivity of the detector, thus the intensity of the UV emissions below 350 nm appear less intense than they actually are. A version of the spectrum presented in Figure 20B that has been corrected for the sensitivity of the detector is presented in Figure 68 (Appendix 6) to give an idea of the real emission intensities. Similar to what was reported for $NaLaF_4$:20% Pr^{3+}, the emission from the $^1S_0 \rightarrow {}^1I_6$ transition at 407 nm is the most intense band in the radioluminescence spectrum, followed by less intense LOL emissions spanning the visible spectral region.

As discussed in Section 7.4, the positions of the transitions observed in β-$NaLuF_4$:20% Pr^{3+}

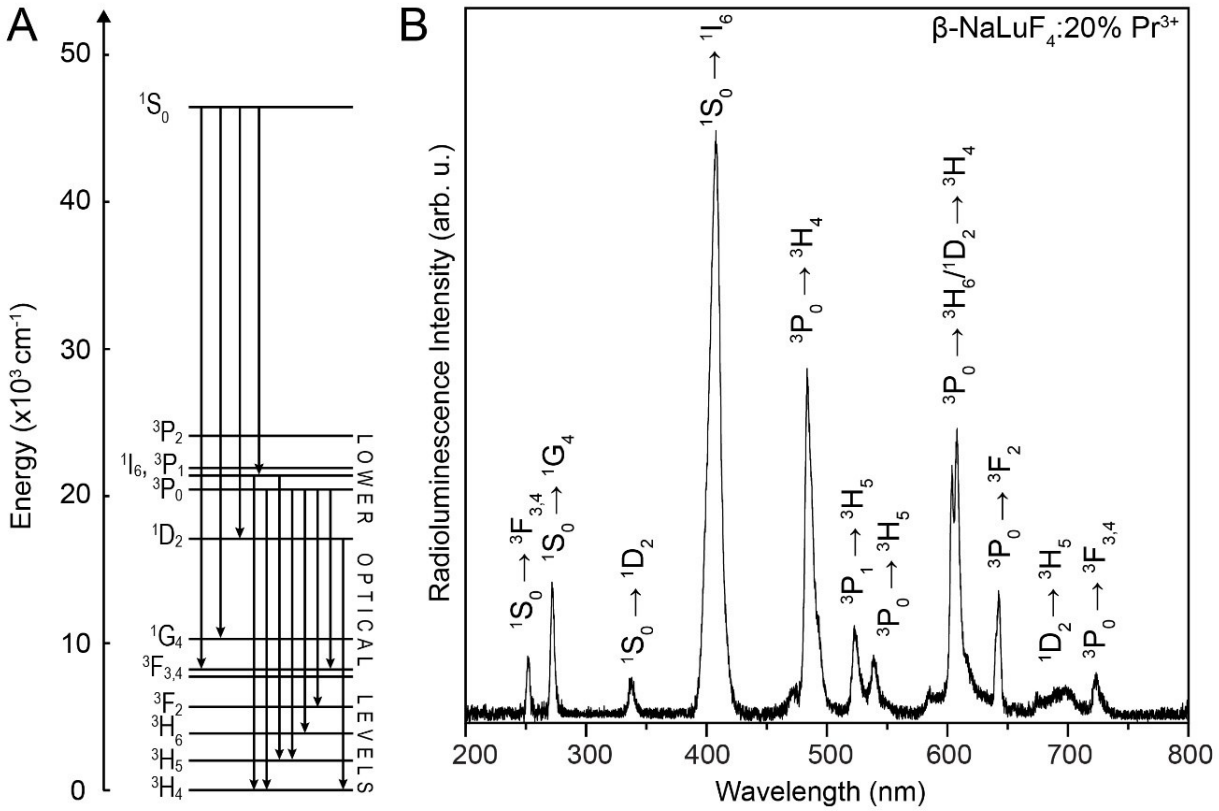

Figure 20. A) Energy level diagram of Pr^{3+} and corresponding transitions observed in β-$NaLuF_4$:20% Pr^{3+}, B) Radioluminescence emission spectrum of β-$NaLuF_4$:20% Pr^{3+}nanoparticles under excitation with X-rays (50 kVp, 80 μA, Au target, unfiltered, uncollimated beam)

are the same in all other compositions studied, though their intensities varied significantly. Notably, UV emission bands from the $^1S_0 \rightarrow {}^3F_{3,4}$, $^1G_4$, and $^1D_2$ transitions were observed with maxima at 251, 272 and 336 nm, respectively. These emissions are particularly interesting, as many biomolecules absorb these wavelengths, including DNA, cytochrome C, FAD, tryptophan, NAD, and hemoglobin, among others.[387,388] A few reports on Pr^{3+}-doped materials aim to take advantage of UV emissions for cancer therapies by damaging the aforementioned biological targets.[355–358]

Mentioned in Section 2.3.1, Pr^{3+} is able to undergo PCE, generating one photon from the $^1S_0 \rightarrow {}^1I_6$ transition, followed by a subsequent emission from the LOLs due to the population of the $^1I_6$ state, which can non-radiatively decay to the emissive ^3P_J states. Notably, PCE does not always yield a quantum efficiency greater than unity, thus quantum efficiency measurements are not the decisive factor for observing PCE in a material. Rather, it is the concurrent emission from the

$^1S_0 \rightarrow {}^1I_6$ transition and the LOLs that is the hallmark of the process[389,390], as observed in the nanoparticles synthesized here. Thus, the emission spectra herein suggest PCE is occurring in this material, in line with the observation of this phenomenon as reported for other Pr^{3+}-doped fluoride materials.[65,69,70,369,391,392]

Table 9. Summary of the observed transitions in β-$NaLuF_4$ and their corresponding wavelengths (nm), wavenumbers (cm^{-1}) and energies (eV).

Transition	Wavelength (nm)	Wavenumber (cm^{-1})	Energy (eV)
$^1S_0 \rightarrow {}^3F_{3,4}$	251	39841	4.94
$^1S_0 \rightarrow {}^1G_4$	272	36765	4.56
$^1S_0 \rightarrow {}^1D_2$	336	29762	3.69
$^1S_0 \rightarrow {}^1I_6$	407	24570	3.05
$^3P_0 \rightarrow {}^3H_4$	483	20704	2.57
$^3P_1 \rightarrow {}^3H_5$	522	19157	2.38
$^3P_0 \rightarrow {}^3H_5$	538	18588	2.30
$^3P_0 \rightarrow {}^3H_6$ and $^1D_2 \rightarrow {}^3H_4$	608/611	16448	2.04
$^3P_0 \rightarrow {}^3F_2$	642	15576	1.93
$^1D_2 \rightarrow {}^3H_5$	697	14347	1.78
$^3P_0 \rightarrow {}^3F_{3,4}$	722	13851	1.72

7.2. Radioluminescence and nanoparticle crystal phase

Radioluminescence from $NaLuF_4$:20% Pr^{3+} was observed to vary substantially with crystal phase (Figure 21). [65] This is expected, as the separation of the $4f^15d^1$ states relative to the $^1S_0$ state also changes with the crystal phase of the $NaREF_4$ host; the $^1S_0$ state of Pr^{3+} is closer in energy to the $4f^15d^1$ states in α-$NaLuF_4$ than it is in β-$NaLuF_4$.[370] β-$NaLuF_4$:20% Pr^{3+} exhibited all of the expected $4f^2 \rightarrow 4f^2$ emissions upon excitation with ionizing radiation, while α-$NaLuF_4$:20% Pr^{3+} exhibited extremely weak radioluminescence from the LOLs.

The weak radioluminescence observed from α-$NaLuF_4$:20% Pr^{3+} is attributed to the relatively high concentration of Pr^{3+} in this composition. Materials developed for Pr^{3+} luminescence are rarely doped with more than 1% Pr^{3+}, as Pr^{3+} luminescence is highly dependent on concentration and most materials are optimized for maximal emissions from the

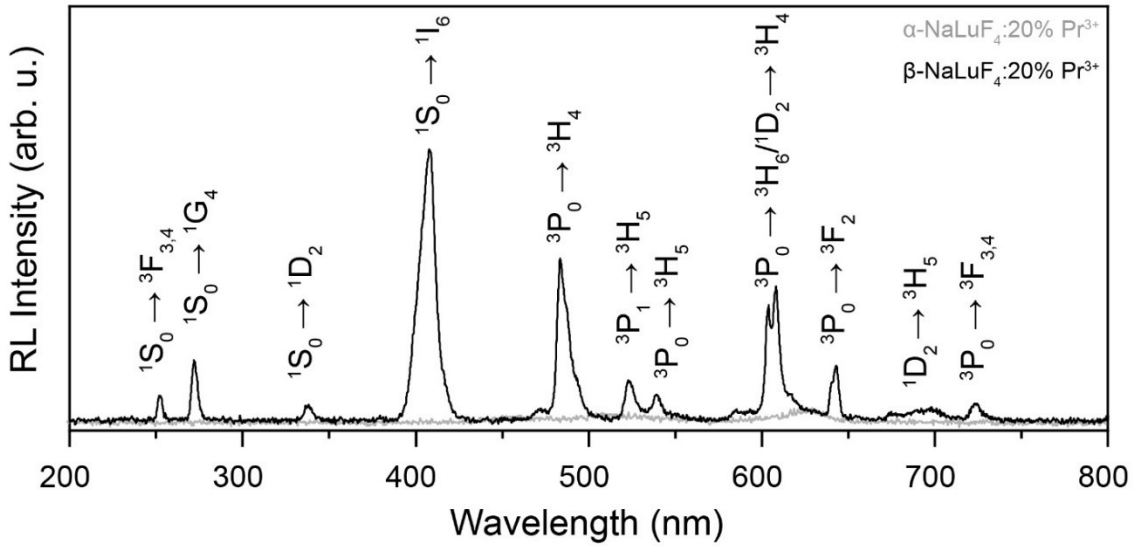

Figure 21. Radioluminescence emission spectra of powder samples of α-$NaLuF_4$:20% Pr^{3+} (gray trace) and β-$NaLuF_4$:20% Pr^{3+} (black trace). X-ray source: 150 kVp, 20 mA, 0.3 mm Cu filter.

LOLs.[20,66,390,393] Concentration quenching has been reported in several Pr^{3+}-based scintillator materials, with significant quenching reported at concentrations of 0.7 mol% Pr^{3+} or higher.[358,390,394,395] Moreover, in materials where the proximity of the $^1S_0$ state to the $4f^15d^1$ levels is sufficient to allow both intra- and interconfigurational transitions, it has been reported that concentration quenching manifests as a decrease in the $^1S_0$ emissions and increase in LOL emissions.[394] This is commonly attributed to energy migration *via* the $^1S_0$ to defects in the lattice[389], since there is no potential for cross-relaxation involving the $^1S_0$ state, and a large number of phonons would be required to bridge the 26500 cm^{-1} gap between the $^1S_0$ and the LOLs. The obvious improvement in radioluminescence from β-$NaLuF_4$:20% Pr^{3+} prompted us to evaluate the spectroscopic properties of the hexagonal phase for all remaining studies.

7.3. Radioluminescence and nanoparticle size

The effect of nanoparticle size on radioluminescence intensity was investigated to establish the effect of RLNP size on the luminescence. As shown in Figure 22A, the four sizes investigated (403 ± 15, 285 ± 13, 79 ± 3 and 72 ± 22 nm) were characterized by TEM (Figure 22B) and PXRD, and all had a hexagonal crystal phase (Figure 22C). Of note, different reaction times and temperatures were used to achieve size control. Since differences in crystallinity may arise due to changes in the reaction parameters, it is possible that this contributes to the observed differences.

Elemental mapping was also performed on the samples using energy dispersive spectroscopy (EDS), and no major differences in the distribution of Pr^{3+} ions could be observed *via* this method (Figure 22D). Inductively-coupled plasma mass spectrometry was also used to confirm the nanoparticles exhibited Pr^{3+} concentrations close to the nominal 20 mol% (Table 10). Inductively-coupled plasma mass spectrometry (ICP-MS) was used to further confirm the nanoparticles contained near-equal concentrations of Pr^{3+}.

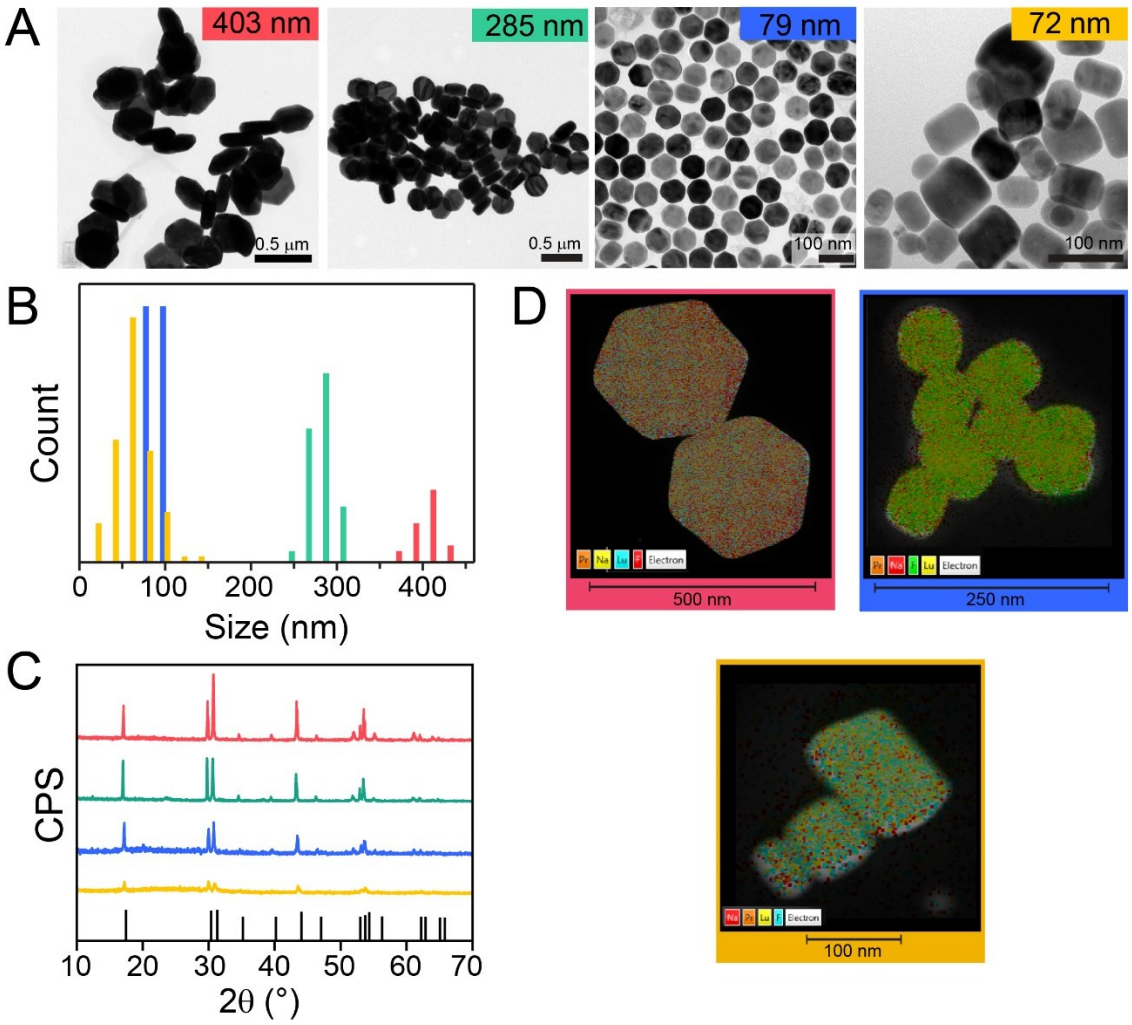

Figure 22. Physical characterization of $NaLuF_4$:20% Pr^{3+} nanoparticles of different sizes. For all panels, red corresponds to the largest nanoparticles (403 nm), green to 285 nm particles, blue to 79 nm particles, and yellow to 72 nm particles. A) Transmission electron microscopy images, B) corresponding static size distributions obtained from the TEM images obtained by measuring a minimum of 300 nanoparticles C) powder X-ray diffractograms of the four samples along with the corresponding hexagonal phase diffraction pattern for $NaLuF_4$ (PDF 00-027-0726). D) Energy dispersive spectroscopy elemental mapping images for the nanoparticle samples.

All of the samples exhibited the expected emissions from β-$NaLuF_4$:20% Pr^{3+} as described previously. Indeed, as the particles became larger, the overall radioluminescence intensity increased. Since radioluminescence is dependent upon attenuation of ionizing radiation by the host material, it was expected that an increase in size would lead to higher emission intensity. Additionally, larger nanoparticles have less surface defects relative to their volume, and are known to exhibit more intense luminescence.[396]

Interestingly, however, the ratio of the $^1S_0 \rightarrow {}^1I_6$ emission and the LOL emissions changed significantly with size as well (Figure 23). The relative increase in the LOL emissions is counterintuitive, since a higher surface defect density at the surface of the smaller nanoparticles should facilitate quenching of these lower-energy states. Mentioned before, ICP-MS confirms the change in the LOL intensities with size is not due to a variation in dopant concentration. As will be substantiated in the following sections, the same properties responsible for the persistent luminescence can explain the observed size dependency of the $^1S_0$ and LOL emission ratios.

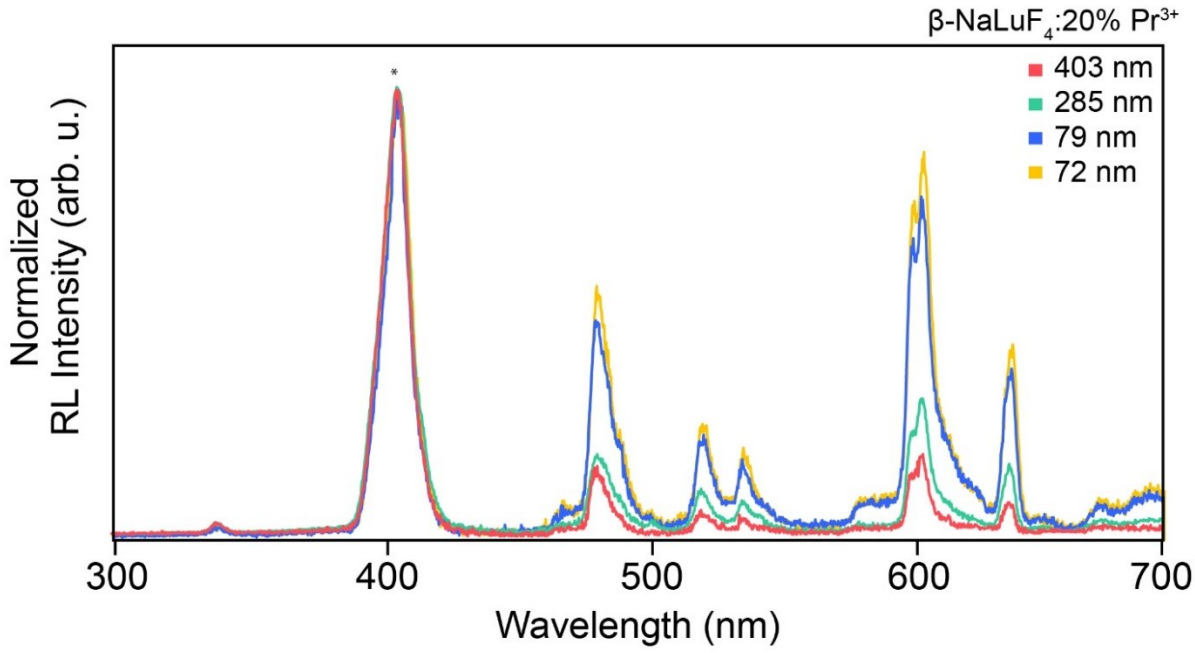

Figure 23. Normalized radioluminescence emission spectra of powder $NaLuF_4$:20% Pr^{3+} nanoparticles as a function of nanoparticle size, normalized to the intensity of the $^1S_0 \rightarrow {}^1I_6$ transition as denoted by the asterisk (*). (X-ray excitation, Au target, unfiltered, uncollimated beam, 50 kVp, 80 μA).

Table 10. Raw ICP-MS data and corresponding calculated Pr^{3+} concentration in each RLNP sample. Sample 1 corresponds to the 400 nm RLNPs, sample 2 the 280 nm particles, sample 3 the 79 nm particles, sample 4 the 70 nm particles, and sample 5 is undoped $NaLuF_4$ nanoparticles. ICP-MS was performed in duplicates and values were averaged. Error in the values is limited by the accuracy of the instrument, which is 5% of the raw data values. Sample 3A could not be analyzed due to human error.

Sample	Pr^{3+} (ppm)	Lu^{3+} (ppm)	mol% Pr^{3+}	Average mol% Pr^{3+}
1A	0.926	4.354	20.88	20.90
1B	0.689	3.235	20.91	
2A	0.520	2.325	21.73	21.71
2B	0.504	2.258	21.68	
3A	--	--	--	18.90
3B	0.1559	0.6689	18.90	
4A	0.349	1.748	19.86	19.94
4B	0.196	0.973	20.02	
5A	0.00010	1.843	0.0058	0.0039
5B	0.00002	1.026	0.002	

7.4. Radioluminescence and Pr^{3+} concentration

The overarching objective of the research was to optimize the composition to yield the maximum emission from the $^1S_0 \rightarrow {}^1I_6$ transition. To our knowledge, there are no reports of Pr^{3+} compositions specifically optimized to yield maximal emissions from this transition, thus we investigated a wide range of Pr^{3+} concentrations to ensure the maximal emissions would be achieved. The spectroscopic properties of β-$NaLuF_4$:x% Pr^{3+} were evaluated ranging from 1 to 40% Pr^{3+}. The concentration study was performed at least three times with different samples to ensure the trends were reproducible. Nanoparticle compositions used for this study exhibited similar morphologies (Figure 24A), a hexagonal crystal phase (Figure 24B), and overlapping size distributions, as shown in Figure 24C for a representative set of samples. The average nanoparticle size across all compositions was 78.3 ± 7.3 nm (Table 11).

Table 11. Average static sizes and corresponding standard deviations of $NaLuF_4$: x mol% Pr^{3+} (x = 1-40) RLNPs measured from the TEM images presented in Figure 24A.

Composition	Average size (nm)
$NaLuF_4$: 1% Pr^{3+}	79.1 ± 4.7
$NaLuF_4$: 10% Pr^{3+}	75.7 ± 6.1
$NaLuF_4$: 15% Pr^{3+}	77.6 ± 3.9
$NaLuF_4$: 20% Pr^{3+}	68.4 ± 5.2
$NaLuF_4$: 25% Pr^{3+}	87.1 ± 5.9
$NaLuF_4$: 30% Pr^{3+}	80.9 ± 5.7
$NaLuF_4$: 35% Pr^{3+}	69.0 ± 3.7
$NaLuF_4$: 40% Pr^{3+}	88.3 ± 6.1
Average size of all compositions	**78.3 ± 7.3**

As previously mentioned, the emissions from Pr^{3+} arise from two main avenues; the $^1S_0$ state which produces UV emissions, and the LOLs, which produce visible and NIR emissions. The population of the LOLs is affected by the population of the $^1S_0$ state, and these states are also highly susceptible to cross-relaxation. In contrast, the $^1S_0$ state is well-separated from the other 4f states (26500 cm^{-1} from the $^1S_0$ to the $^3P_2$ level) and quenching processes involving the $^1S_0 \rightarrow {}^1I_6$ transition are prevented by the absence of resonant transitions and are resistant to phonon-mediated

relaxation as well. As such, emissions from the LOLs should be favored at low Pr^{3+} concentrations, whereas emissions from the $^1S_0$ state should become more intense at higher concentrations. As shown in Figure 25, this is precisely what is observed.

β-$NaLuF_4$:1% Pr^{3+} exhibits the strongest LOL emissions, which decrease substantially with increasing Pr^{3+} concentration. It also exhibits the lowest $^1S_0 \rightarrow {}^1I_6$ emission intensity of all studied compositions. As mentioned above, the LOLs are highly susceptible to cross-relaxation. LOL

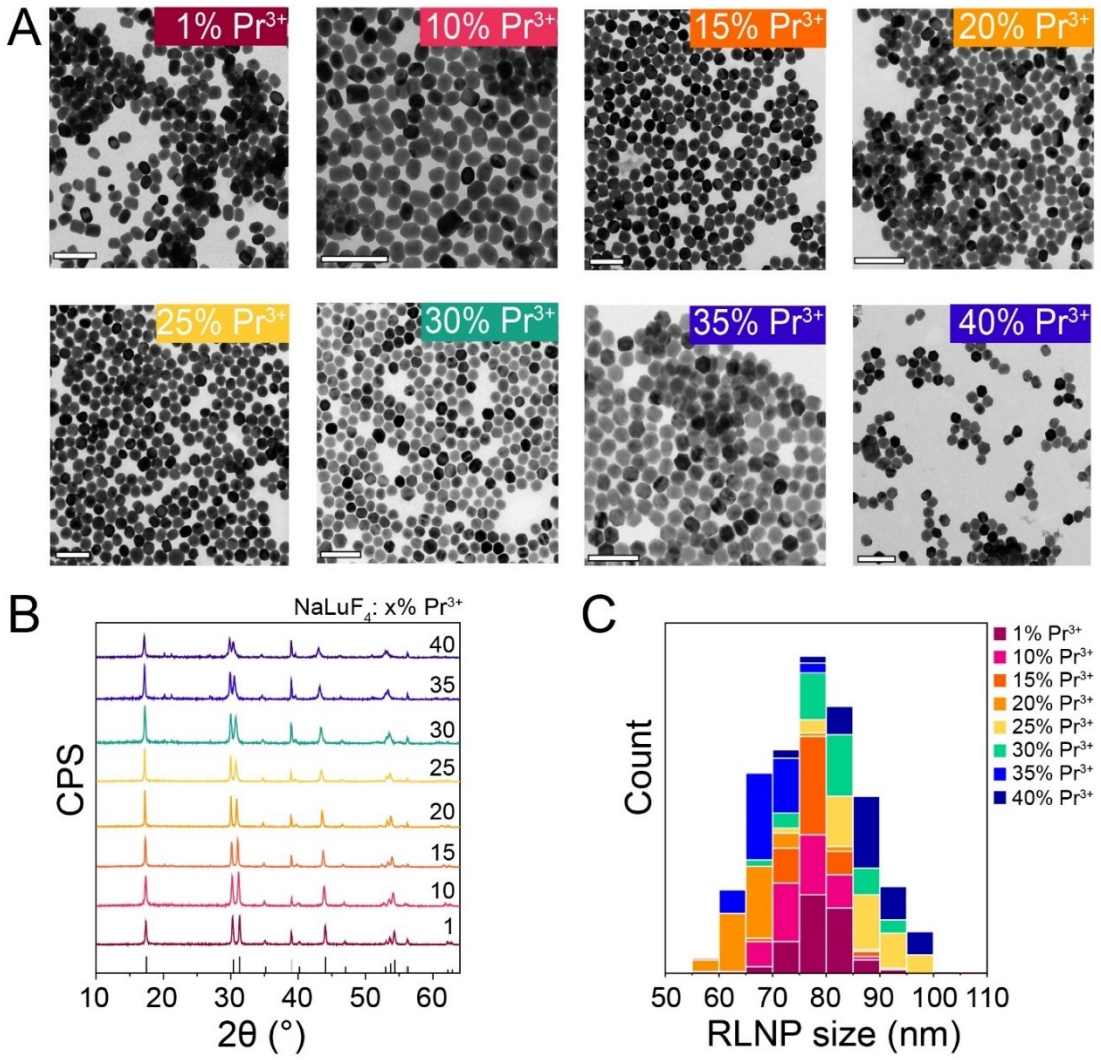

Figure 24. A) TEM images of NaLuF4:1-40% Pr^{3+} nanoparticles, B) P-XRD diffractograms of the nanoparticles shown in panel A, the corresponding diffraction pattern (PDF 00-027-0726) is shown at the bottom in black. The diffraction pattern in gray corresponds to sodium fluoride (PDF 00-001-1181). C) Static size distributions of the nanoparticles shown in panel A measured from the TEM images using a minimum of 300 nanoparticles.

emissions could be observed at all studied Pr^{3+} concentrations, despite the likelihood of efficient cross-relaxation at such high Pr^{3+} concentrations. As described in section 7.5.4, the same properties which give rise to persistent luminescence may also contribute to the higher-than-expected LOL emissions, in line with what is also observed as a function of size described in Section 7.3.

In contrast, the $^1S_0 \rightarrow {}^1I_6$ emission band increases with increasing Pr^{3+} concentration, up to 25% Pr^{3+}, and less dramatic differences in emission intensity are observed as a function of concentration. This is in line with the resistance of the $^1S_0$ transitions to concentration quenching, as mentioned above. The decrease in the $^1S_0 \rightarrow {}^1I_6$ emission intensity beyond 25% was attributed to increased lattice distortions and the generation of a greater number of defects in the lattice, thus facilitating energy migration to quenching centers. Similar results were observed for $NaLaF_4:Pr^{3+}$ under VUV excitation, however the maximum intensity was described to be 20% Pr^{3+}; this may be because of the larger increments in Pr^{3+} concentrations studied in that work wherein the $^1S_0 \rightarrow {}^1I_6$ emission may not have been fully optimized.[369] Based on these results, we used β-$NaLuF_4$:25% Pr^{3+} for the *in vitro* X-PDT studies discussed in Chapter 8.

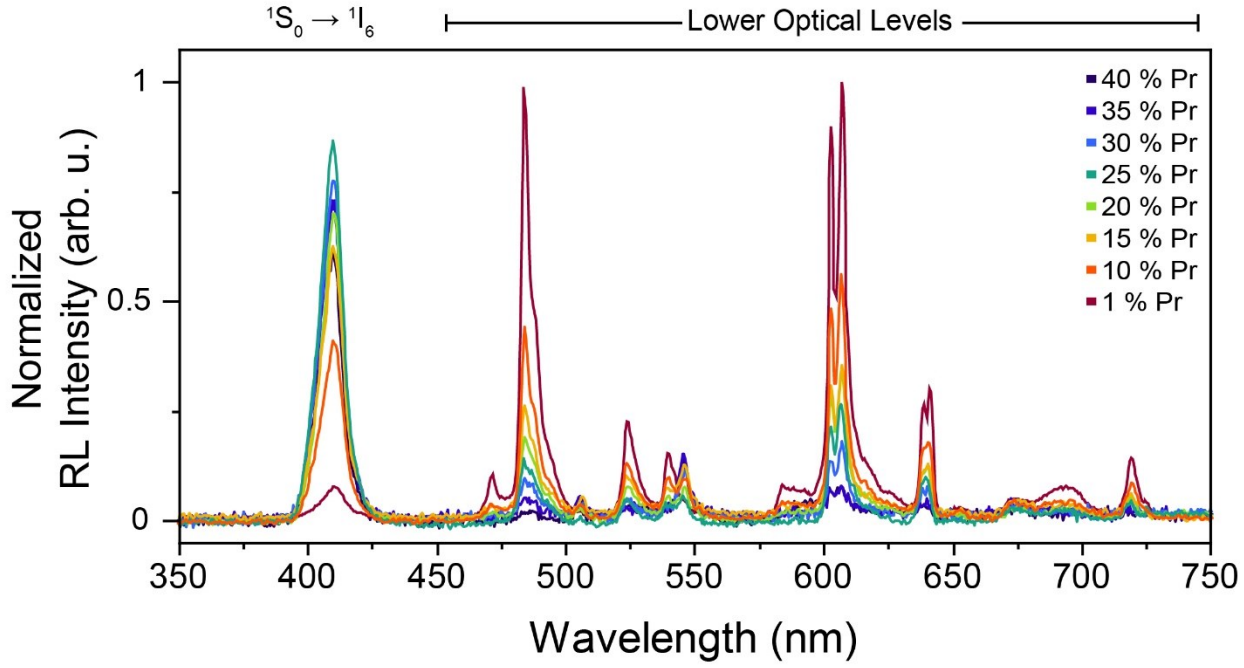

Figure 25. Normalized radioluminescence emission spectra of β-NaLuF4:x% Pr^{3+} (x = 1-40 mol%) under excitation with X-rays (50 kVp, 80 μA, Au target, uncollimated, unfiltered beam).

7.4.1. Density and Z_{eff} of $NaLuF_4$:1-40% Pr^{3+}

Of relevance to the results presented in Chapter 8, the theoretical effective atomic number and density of each composition was calculated, providing an idea of how the interaction of the RLNPs with ionizing radiation may change as a function of Pr^{3+} concentration (Table 12). Notably, the density decreases with increasing Pr^{3+} concentration, but the $^1S_0$ emissions improve in intensity; thus the change in density is not large enough to cause a major decrease in X-ray attenuation. The Z_{eff} of each composition was calculated with and without spectrum weighting (see Section 2.1). Spectrum-weighted Z_{eff} values take into account the energies of a specific radiation source and apply a weighting factor to account for what the perceived effective atomic number is for that source. Here, we applied spectrum-weighting using a 50 kVp INTRABEAM® source, which has an output profile identical to the X-ray source used in this work. The spectrum-weighted values are higher than the mean Z_{eff} values because the attenuation of low energy X-rays improves as a function of effective atomic number and density, in accordance with the linear attenuation coefficient of X-rays as discussed in Section 2.1.

Table 12. Density and effective atomic number of $NaLuF_4$: x% Pr^{3+}. Densities calculated by Steven L. Maurizio. Spectrum-weighted values were calculated using the INTRABEAM® 50 kVp X-ray source parameters in the Auto-Z_{eff} software (Section 5.2.7).

Composition	Density (g/cm^3)	Mean Z_{eff}	Spectrum-weighted Z_{eff}
$NaLuF_4$	6.57	30.6378	35.5648
$NaLuF_4$: 1% Pr^{3+}	6.55	30.6027	35.5150
$NaLuF_4$: 10% Pr^{3+}	6.40	30.3703	35.1534
$NaLuF_4$: 15% Pr^{3+}	6.32	30.2304	34.9438
$NaLuF_4$: 20% Pr^{3+}	6.24	30.0908	34.7376
$NaLuF_4$: 25% Pr^{3+}	6.15	29.9452	34.5244
$NaLuF_4$: 30% Pr^{3+}	6.07	29.8650	34.3290
$NaLuF_4$: 35% Pr^{3+}	5.99	29.6944	34.1075
$NaLuF_4$: 40% Pr^{3+}	5.90	29.5215	33.8835

7.5. Persistent Luminescence

Beyond the basic radioluminescent properties of β-$NaLuF_4$: Pr^{3+}, persistent luminescence was observed from the compositions containing 20 and 25% Pr^{3+}. The longest persistent luminescence duration was observed in β-$NaLuF_4$:20% Pr^{3+}, thus the persistent luminescence properties of this composition were studied in-depth for this composition.

As shown in Figure 26A, changes in the radioluminescence intensities of the $^1S_0 \rightarrow {}^1I_6$ and LOL transitions were observed as a function of irradiation time, which is a hallmark of persistent luminescence as described in Section 2.4.1. Interestingly, the $^1S_0$ emission intensities decrease with irradiation time, while the LOL emission intensities increase. An increase in emission intensity with time is classically due to charge trapping, which forms the basis for the persistent luminescence phenomenon (see Section 2.4 for more information).[109] However, this does not explain the cause of the decrease in the $^1S_0$ emissions with irradiation time.

Interestingly, the persistent luminescence emissions from this material are different from their radioluminescence emissions (Figure 26B); only the LOL emissions are observed. This is somewhat unique, as usually the emissions observed during excitation are usually identical to those observed during persistent luminescence.[101] As such, we were interested in determining the mechanism responsible for persistent luminescence from this material, as well as understanding the reason behind the decrease in the $^1S_0$ emission intensities and if they were related to the persistent luminescence mechanism.

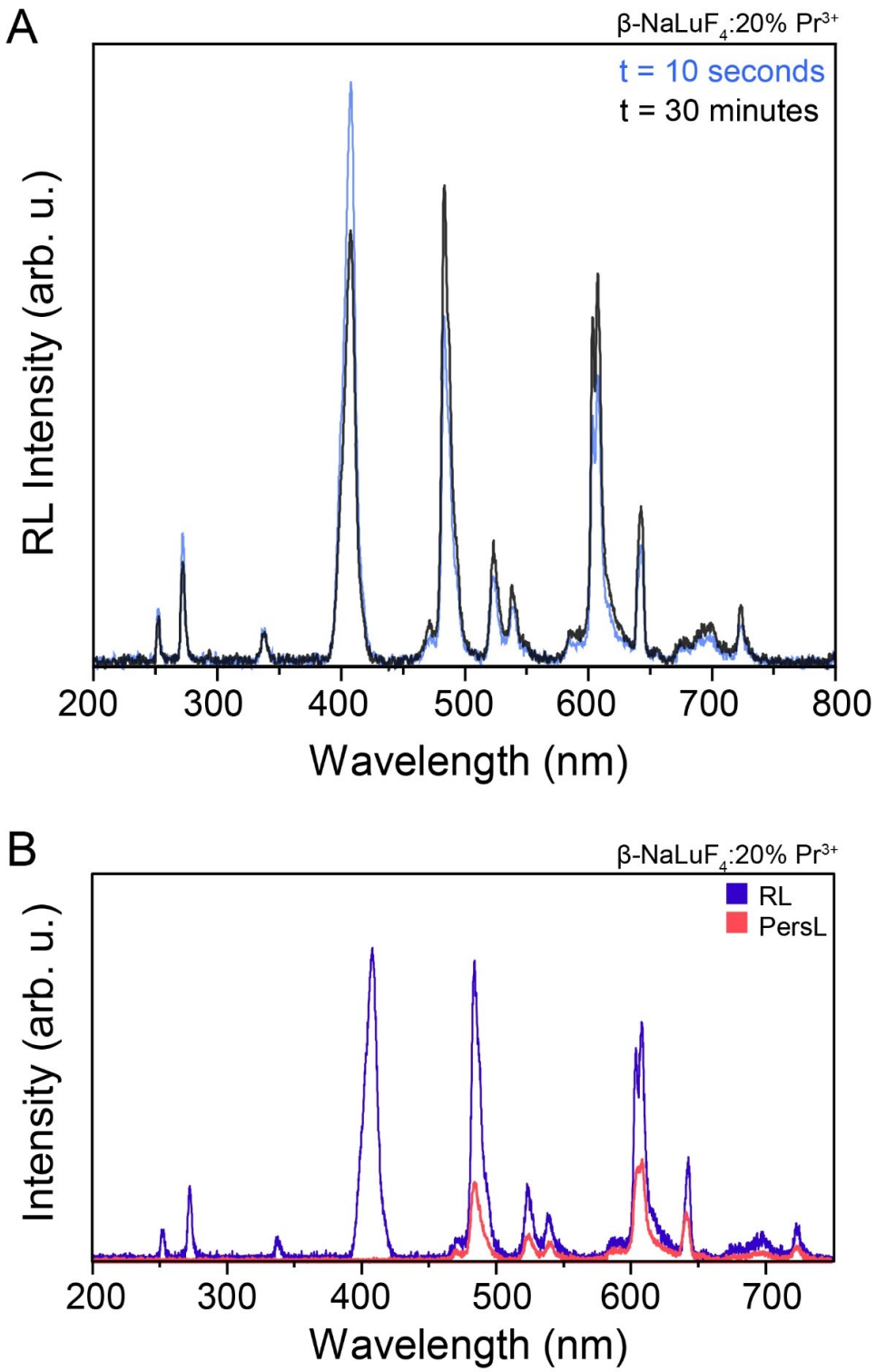

Figure 26. Radioluminescence (RL) emission spectrum of β-$NaLuF_4$:20%Pr^{3+}after 10 seconds (blue) and 30 minutes (black) of X-ray irradiation. B) Radioluminescence (blue) and persistent luminescence (red) spectra compared. (50 kVp, 80 μA, Au target, unfiltered, uncollimated beam)

7.5.1. Kinetic studies on $NaLuF_4$:20%Pr^{3+}

The change in radioluminescence intensity as a function of time was monitored for all transitions, along with the persistent luminescence intensity as a function of time after excitation was ceased (Figure 27). Samples were irradiated at a dose rate of 30 Gy/min, and their radioluminescence intensities reached a near-plateau after approximately 30 minutes of irradiation. The plateau signifies the trapping states are filled, or have reached an equilibrium between trapping and de-trapping processes.

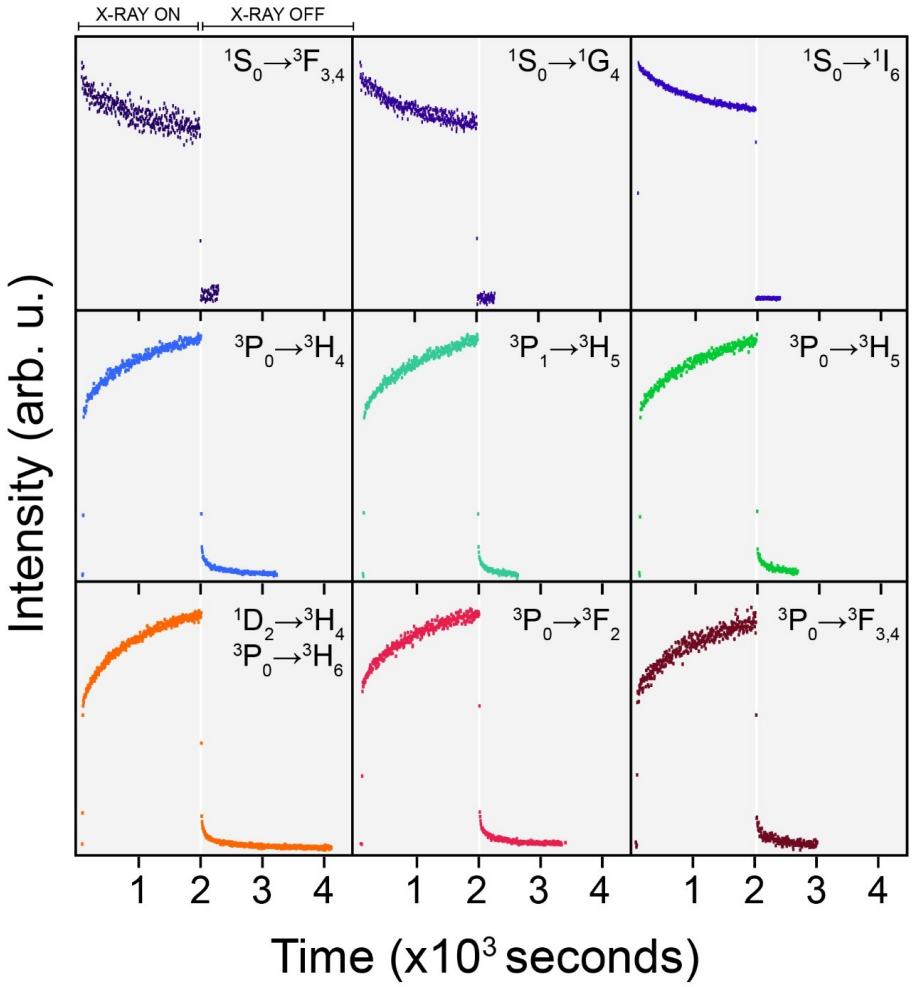

Figure 27. Time-dependent radioluminescence and persistent luminescence intensity of each Pr^{3+} transition from $NaLuF_4$:20% Pr^{3+} nanoparticles during X-ray irradiation and after the excitation has ceased. (50 kVp, 80 μA, Au target, unfiltered, uncollimated beam)

The persistent luminescence duration was determined to be the length of time it took to reach 100 counts above baseline after excitation ceased. As mentioned in Section 2.4.4, the lack of a standard means of determining the persistent luminescence duration that applies to all persistent luminescence materials (including those developed for applications in biology) makes it difficult to compare our results with the literature, and often the method used to determine the duration is not stated. The method used herein allows for clear comparison between the samples studied in this work. Persistent luminescence from the $^3P_0 \rightarrow {}^3H_6/{}^1D_2 \rightarrow {}^3H_4$ transitions at 608 nm were observed for 36 minutes; since this was the most intense LOL emission, it makes sense that this transition could be observed for the longest amount of time. The persistent luminescence decay rate was similar for all the LOL emissions, in agreement with the conclusion that the most intense transition was simply observable for the longest amount of time. While the duration is far shorter than what is considered useful for safety signage, persistent luminescence from the LOLs may provide an opportunity to achieve an added therapeutic effect, since it exhibits spectral overlap with the Q bands of PPIX and could potentially also be used for bioimaging, since red persistent luminescent materials are attractive for this purpose.[397]

The persistent luminescence duration was also found to increase with decreasing particle size, as shown in Figure 28. As mentioned in Section 6.2, the reaction parameters differed in order

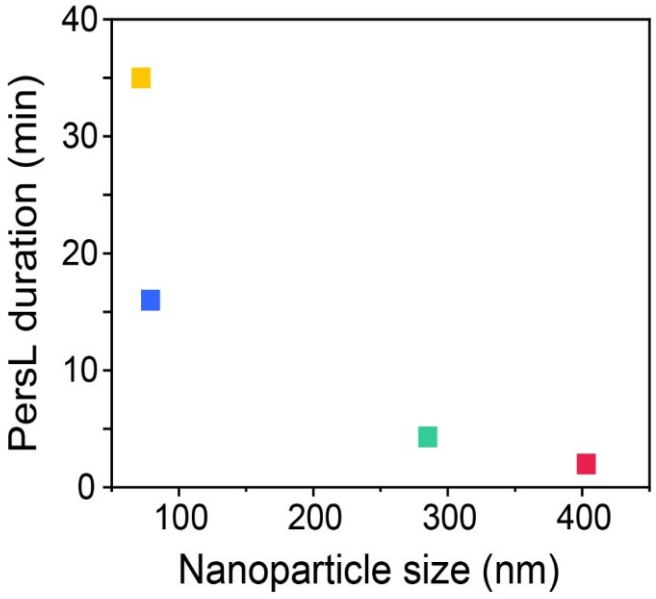

Figure 28. Persistent luminescence duration from the LOLs of $NaLuF_4$:20% Pr^{3+} nanoparticles as a function of nanoparticle size.

to obtain the different sizes, which could affect their crystallinity. The improvement in persistent luminescence duration with smaller nanoparticles suggests that the trapping states responsible for persistent luminescence arise due to the formation of surface defects. Since smaller nanoparticles have a higher defect density, and defects are known to form trapping states, the greater number of defects at the surface of smaller nanoparticles allows for more charge to be trapped. Therefore, more trapped charge is available to be liberated after excitation is ceased, resulting in a longer persistent luminescence duration. Similar results have been reported for $CaTiO_3:Pr^{3+}$ at the bulk and nanoscale (section 2.4.3), CaO defects in the lattice were found to act as electron traps, facilitating longer persistent luminescence with decreasing size.[85,94,398]

Notably, the radioluminescence intensities did not return to their original ratios upon re-excitation after the persistent luminescence was allowed to decay fully (Figure 29). Upon re-excitation of the nanoparticles, the same intensity ratios (higher LOL and lower $^1S_0$ emission intensities) at the end of trap charging were obtained, even after 3 months of storage in ambient

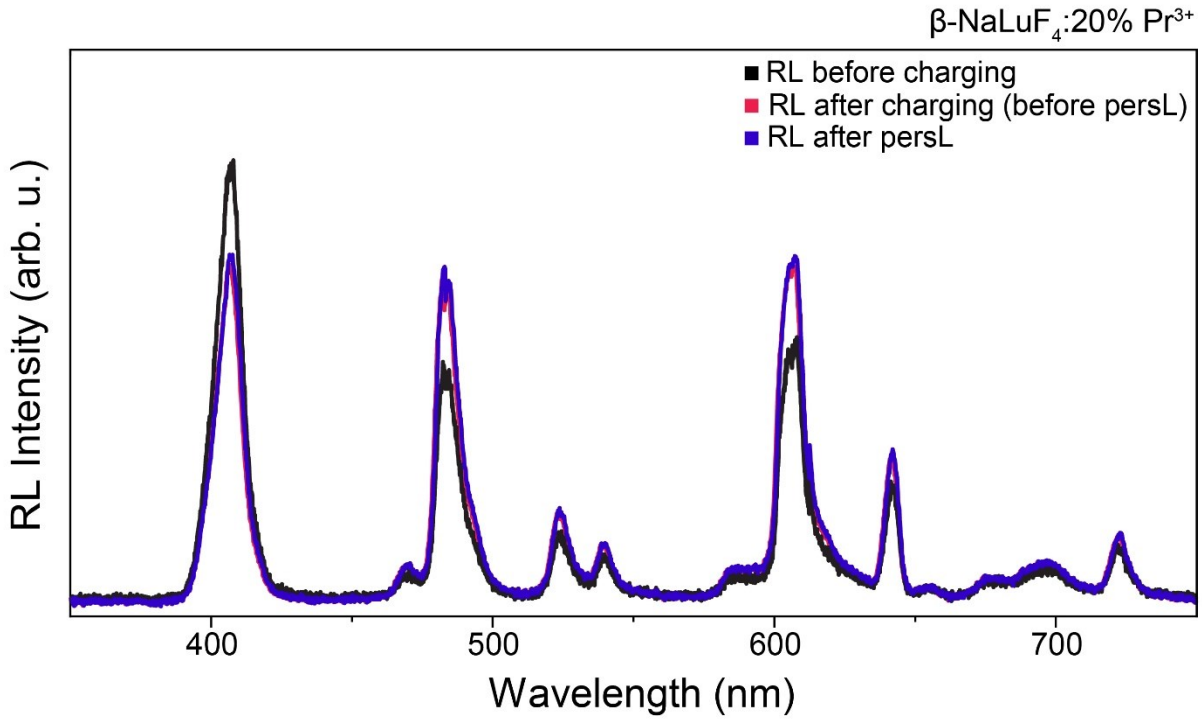

Figure 29. Radioluminescence of $NaLuF_4:20\%Pr^{3+}$ nanoparticles immediately upon X-ray excitation (black), after 30 minutes of X-ray excitation (red), and upon X-ray excitation after persistent luminescence has fully decayed (blue).

conditions. This is known as a "memory effect" and suggests the presence of deep traps that allow for stable charge storage at room temperature, in addition to the trapping states that give rise to persistent luminescence.[86,157,399,400] Thermoluminescence spectroscopy was performed to gain a better understanding of the trap states in our material that gave rise to the properties observed thus far.

7.5.2. Thermoluminescence spectroscopy of $NaLuF_4$:20%Pr^{3+}

Our collaborators at Lumilab at the University of Gent in Belgium (Philippe Smet, David Van der Heggen and Jonas Joos) performed a comprehensive evaluation of the thermoluminescent and radioluminescent properties of the material over four heating cycles. The experiment was performed as follows: a radioluminescence spectrum was taken (labelled "before") and then the sample was irradiated for 45 minutes with X-rays. Another radioluminescence spectrum was taken (labelled "after") and then the sample was heated and the thermoluminescence glow curve was obtained from 300-550 K (Figure 30A). The cycle was repeated a total of 4 times (Figure 30B). This allowed for monitoring of the change in the radioluminescence emission intensities as a function of irradiation time (Figure 30C), thereby corroborating the results obtained in our lab, and then evaluating the positions of the trapping states that gave rise to persistent luminescence.

The thermoluminescence glow curve was a broad band with a maximum intensity of 368 K (Figure 30A). The broad nature of the glow curve suggests that there is a continuous distribution of traps, rather than a set of discrete trapping levels. In 1930, Urbach described a facile method of approximating the trap depth.[114] The Urbach equation (equation 6, Section 2.4.2) gives a value of 0.8 eV for the trap depth of our material; trap depths between 0.6-0.7 eV have previously been stated as ideal for generating persistent phosphors.[107] The trap depth is most commonly ascribed as the energy gap between the trap state and the conduction band.[104,109,112] As mentioned earlier, the nanoparticles exhibit a "memory effect" whereby they retain the emission intensity obtained after trap charging. As shown in Figure 30B and 30C, the emission intensities could be recovered to their original ratios after each thermoluminescence cycle. This confirms the presence of deeper traps relative to the position of the LOL states, and that significant energy is required to liberate these traps. In some materials, charges can be liberated from deep traps using light of an appropriate energy; this is known as optically-stimulated luminescence (OSL). These materials are

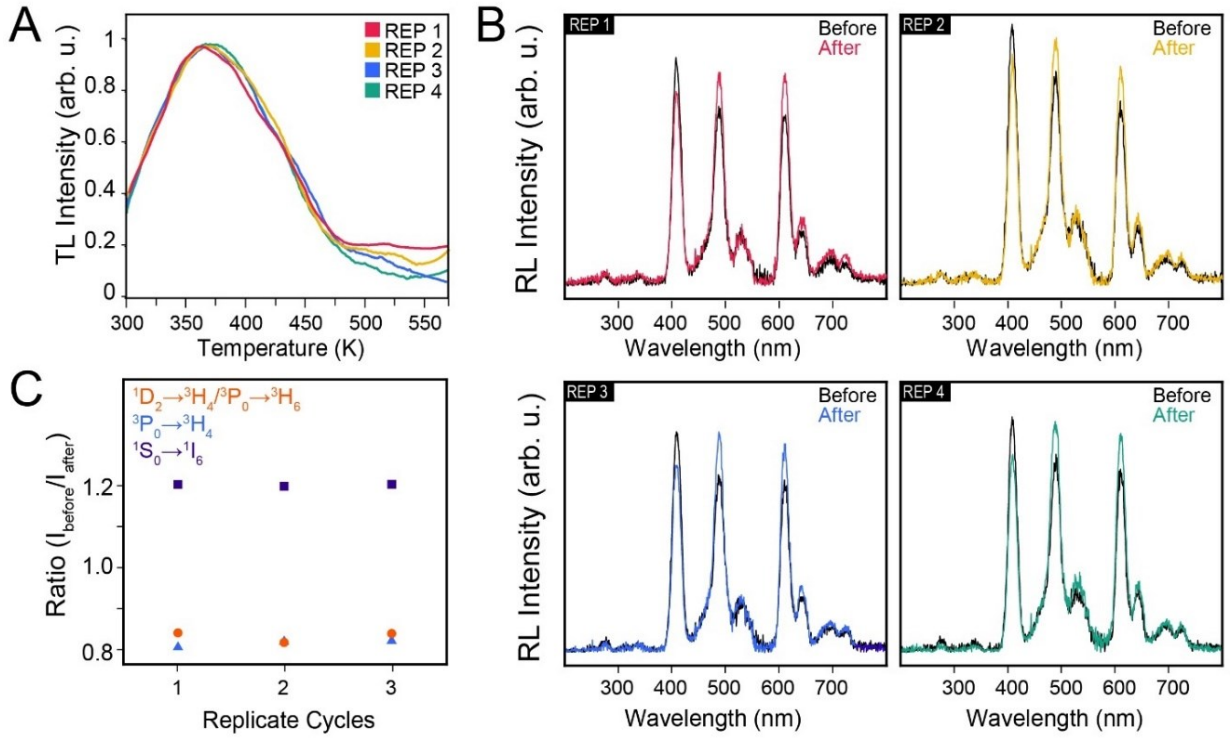

Figure 30. A) Thermoluminescence glow curves of $NaLuF_4$:20%Pr^{3+} nanoparticles corresponding to each heating cycle and radioluminescence spectrum in panel B. C) Ratio of the intensity of the $^3P_0 \rightarrow {}^3H_6/{}^1D_2 \rightarrow {}^3H_4$, $^3P_0 \rightarrow {}^3H_4$ and $^1S_0 \rightarrow {}^1I_6$ transitions before and after each heating cycle as depicted in panels A and B.

highly sought after for radiography[401] and dosimetry[402,403] applications. Unfortunately, this material does not produce OSL to our knowledge, as several excitation wavelengths were used to try and induce it to no avail. Regardless, the ability to restore the luminescence intensities to their original ratios confirms the presence of a trap distribution consisting of shallow traps that give rise to persistent luminescence and deep traps that enable charge storage at room temperature.

As mentioned in Section 2.4.3, persistent luminescence can either occur through a global trapping mechanism involving the conduction band, or *via* a local model, where de-trapping directly to a luminescent center occurs. In the latter case, the trap depth describes the energy gap between the trap state and the excited state of the luminescent center from which persistent luminescence is observed. In the local model, the trap depth is relative to the states of the luminescent centre and not the conduction or valence bands.[107] As such, the obtained 0.8 eV trap depth may either place the trap states at similar energies to the $4f^15d^1$ states of Pr^{3+}, or it may correspond to the energy required to initiate direct recombination between the trap and a nearby

Pr^{3+} ion. In order to ascertain which mechanism is more likely, we must first consider the band gap energy of β-$NaLuF_4$.

7.5.3. Band gap modelling

The electronic band gap of β-$NaLuF_4$ has never been experimentally reported, to our knowledge. The only band gap value for this material was reported by Huang in 2016, at 8.8 eV using density functional theory (DFT) to model it.[404] In the same article, Huang reports theoretical values of 8.5 and 7.4 eV for β-$NaYF_4$ and β-$NaGdF_4$, respectively (which also have not been experimentally determined to our knowledge). However, the experimentally-reported band gaps of $NaLaF_4$ and $LiREF_4$ (RE = Y, Gd and Lu) are all higher than 10.9 eV.[89,405–407] Finally, it is a known weakness of the DFT+*U* model used by Huang *et al.* that band gap values are often underestimated by the techniques used in their calculations, despite attempts to use correction factors to mediate the underestimations.[408–411] Taken together, this prompted us to further our collaboration with the Lumilab research group, where Jonas Joos determined the band gap energy of $NaLuF_4$ using reported experimental values of other wide-gap materials.

As shown in Figure 31 (values reported in Table 13), a band gap of 13.8 ± 0.9 eV was obtained for $NaLuF_4$ using Vegard's law.[412] Vegard's law states a linear relationship exists between the chemical composition of an alloy and its lattice constant. Deviations are common, and it is more of an approximation rather than a law, but the relationship is useful in instances where experimental data is unavailable.[413,414] Many rare-earth binary and ternary compounds (including fluorides) are known to follow Vegard's law[415–418], which can also be extended to a linear relationship between the ionic radius and band gap[419,420], as evidenced below. To do so, the experimentally-reported band gaps of $NaLaF_4$[89], $LiREF_4$[406,421] and $REAlO_3$[407,422] (RE = La, Y, Gd, Lu) and the theoretical band gaps from Huang for $NaREF_4$[404] (RE = Y, Gd, Lu) were graphed as a function of ionic radius and the value for $NaLuF_4$ was extrapolated.

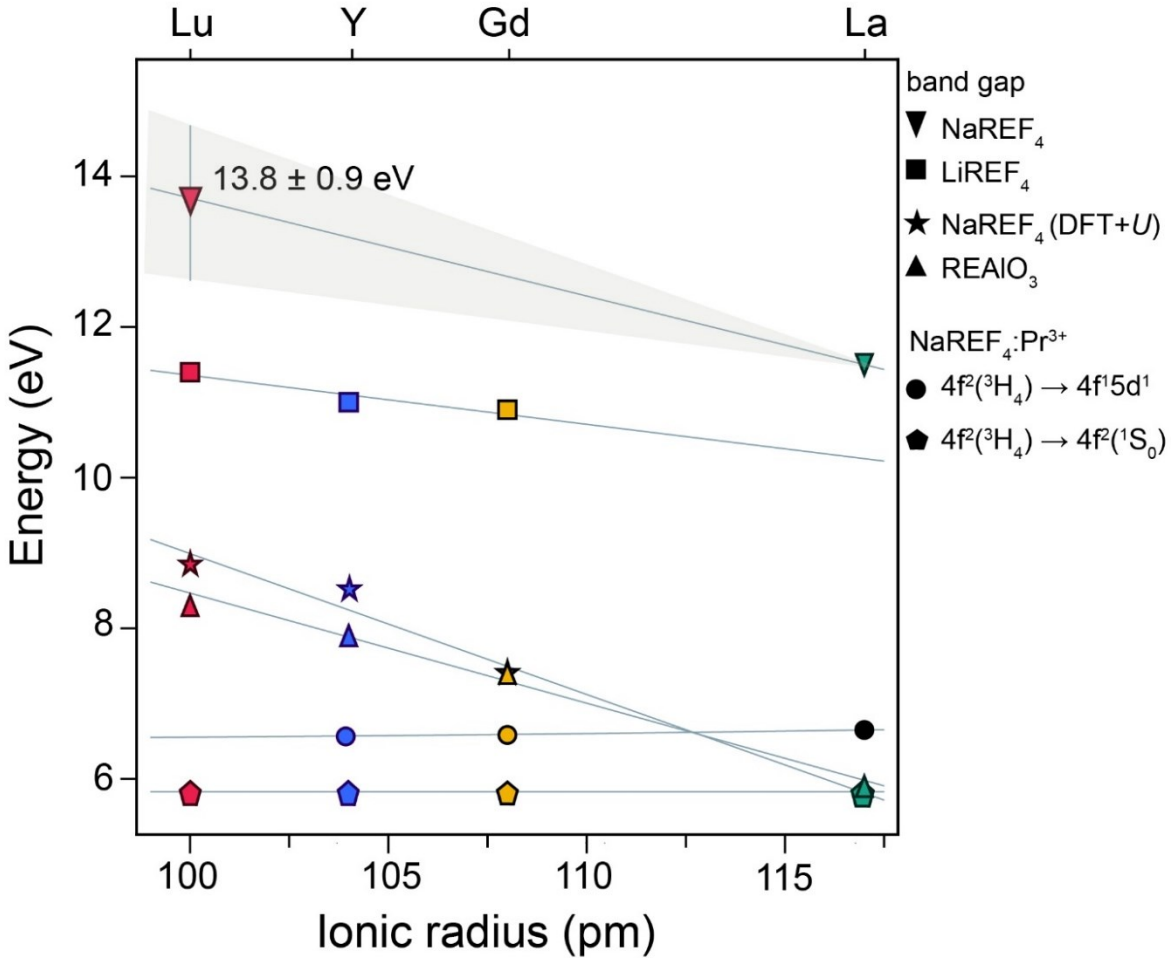

Figure 31. Extrapolated energy as a function of ionic radius for $NaREF_4$, $LiREF_4$ and $REAlO_3$ (RE = Lu, Y, Gd, La). (▲,▼,■,★) are band gap energies, (⬟) is the $^3H_4 \rightarrow {}^1S_0$ transition energy and (●) is the $^3H_4 \rightarrow 4f^15d^1$ transition energy of Pr^{3+} in $NaREF_4$ as a function of RE size.

In addition, the energies of the lowest $4f^15d^1$ states of Pr^{3+} in $NaREF_4$ (RE = La, Y, Gd, Lu) were extrapolated using the known experimental values[90] for the $4f^05d^1$ transition of Ce^{3+} in the same hosts, based on the red shift model (Section 2.3.2). The lowest $4f^15d^1$ state in $NaLuF_4$ was calculated to be 6.55 eV (52829 cm^{-1}) above the $^3H_4$ ground state; thus the energy of the entire Pr^{3+} radiative electronic manifold is far smaller than the calculated band gap energy. The position of the lowest $4f^15d^1$ state at 52829 cm^{-1} is among the highest energies reported, in line with what is observed for some of the similar binary and ternary fluoride hosts.[423] Moreover, the position of this state further corroborates that the $NaLuF_4$ host satisfies the criteria for observing PCE from Pr^{3+} as described in Section 2.3.1.

Table 13. Experimental, calculated, and extrapolated band gap energies of several Ln^{3+} containing crystals (Ln=Y, La, Gd, Lu) and lowest level of the $4f^N$-$5d^1$ configuration of Ce^{3+} (N=1) and Pr^{3+} (N=2), with respect to the electronic ground state, in $NaLnF_4$. Table made by and calculations performed by Jonas Joos.

	Ionic radius	**Band gap energy**					**Lowest $4f^{N-1}5d^1$ level**	
							Ce^{3+}	**Pr^{3+}**
Ln		**$LnAlO_3$**	**$LiLnF_4$**	**$NaLnF_4$**			**$NaLnF_4$**	
		Exp.	**Exp.**	**Exp.**	**Calc.**	**Extrapol.**	**Exp.**	**Extrapol.**
Lu	100	8.3[405]	11.4[406]	-	8.85[404]	13.8	-	6.55
Y	104	7.9[424]	11.0[406]	-	8.50[404]	13.2	5.06[90]	6.57
Gd	108	7.4[407]	10.9[421]	-	7.41[404]	12.7	5.08[90]	6.59
La	117	5.9[422]	-	11.5[89]	-	11.5	5.15[425]	6.65

7.5.4. Determination of the persistent luminescence mechanism

At this stage, several models were proposed to account for the results obtained, as depicted in Figure 32. Importantly, while the figure is drawn to scale, we are unable to determine exactly at what energy the $^3H_4$ state of Pr^{3+} lies in relation to the valence band. Thus, the Pr^{3+} 4f manifold may lie closer to the valence band or closer to the conduction band. A myriad of errors introduced at different stages of modelling the level locations make it difficult to accurately determine the position of the Pr^{3+} 4f manifold relative to the band edges.[411] Moreover, the lack of luminescence

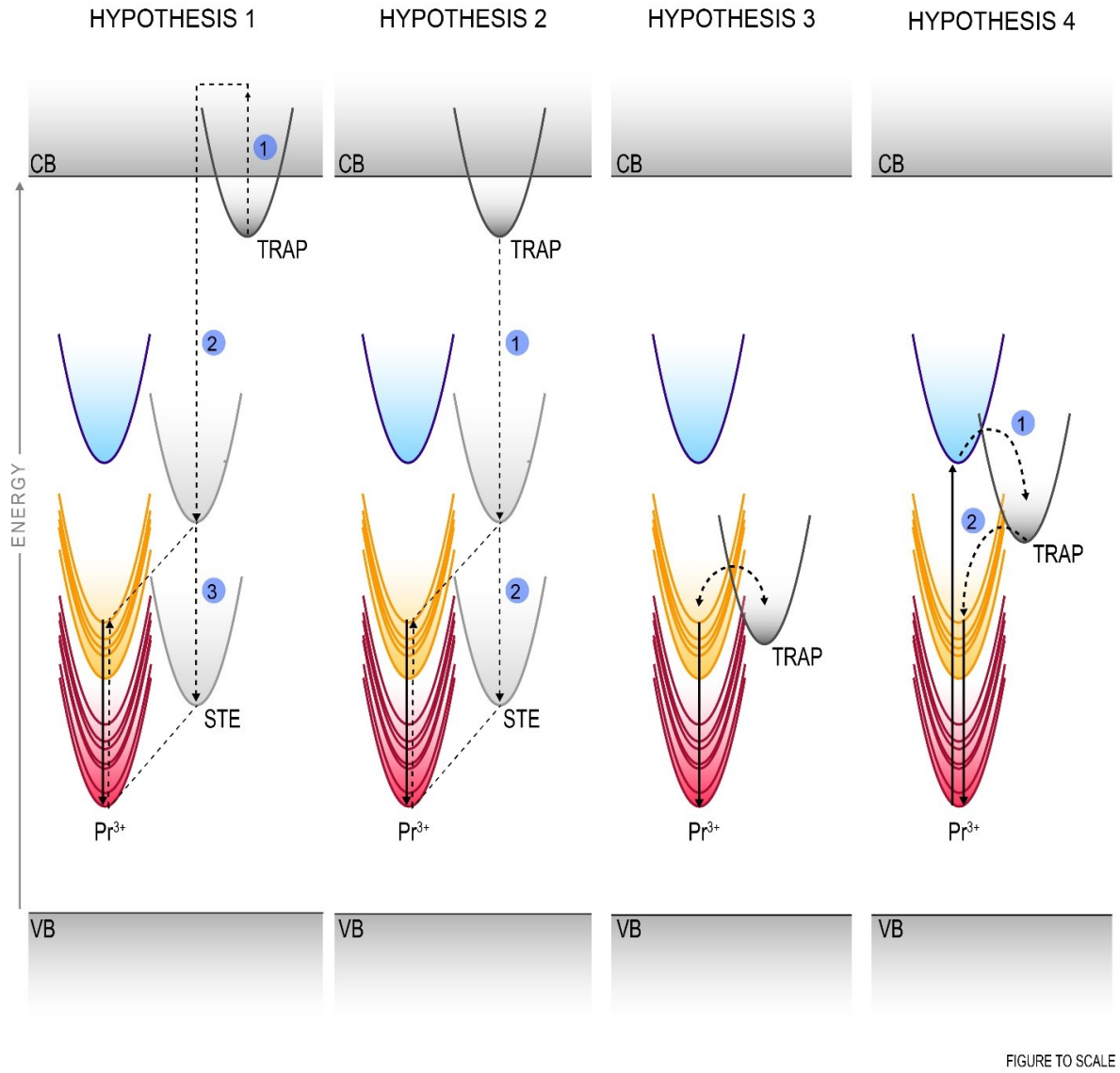

Figure 32. Proposed mechanisms for persistent luminescence in $NaLuF_4:Pr^{3+}$. Only the de-trapping process is numbered for clarity. STE: self-trapped exciton, CB: conduction band, VB: valence band. Configuration coordinates are qualitative.

data for $NaLuF_4$ materials precludes the construction of an HRBE/VRBE diagram at this time (Section 2.3.2). Construction of HRBE/VRBE schemes for fluoride hosts are notoriously difficult because the charge transfer bands are so high in energy that conventional spectroscopy equipment cannot detect them, but that information is needed to build the diagram.[426] A configuration coordinate energy level diagram was used for this Figure, as it allows for a more facile means of understanding the possible interactions. As is common in the field[427,428], the configuration coordinate parabolas presented here are qualitative in nature.

7.5.4.1. Hypotheses 1 and 2: Self-trapped exciton-mediated mechanisms

Hypothesis 1 follows a mechanism that is common in X-ray storage phosphors, such as $BaFBr:Eu^{2+}$.[401,429] X-ray storage phosphors are slightly different than persistent luminescence materials, in that they accumulate trapped charge upon excitation with ionizing radiation only. In the case of alkali halide materials, the process is mediated by the formation of self-trapped excitons (STE) during excitation with ionizing radiation. These radiation-induced STEs are composed of F^- centers that act as electron traps, and V_k centers that act as hole traps.[430] In our model, we hypothesize that the STE levels are resonant with the LOLs and populate them through energy transfer, resulting in increased LOL emissions as more STEs are formed during irradiation. Simultaneously, population of the LOLs by the STEs would prevent radiative relaxation from the $^1S_0$ state since the LOLs would already be occupied. Thus, the $^1S_0$ emissions would decrease with increased STE formation. Once excitation is ceased, de-trapping of electrons *via* the conduction band would cause STE recombination and stimulate persistent luminescence from Pr^{3+}. STE-mediated changes in Pr^{3+} luminescence have been documented in $BaF_2:Pr^{3+}$, $CaTiO_3:Pr^{3+}$, and $Lu_2Si_2O_7:Pr^{3+}$, among others.[146,157,431] Hypothesis 1 accounts for all of the observations, however, if de-trapping occurred through the conduction band, persistent luminescence from the $^1S_0$ state of Pr^{3+} would be expected. Thus, hypothesis 2 is a modified version of hypothesis 1, where de-trapping is a local process and occurs directly from an electron trap to the STE, bypassing the conduction band entirely. This would account for persistent luminescence only being observed from the LOLs.

With respect to both of these models, the presence of an STE emission band would signify the likelihood that one of these hypotheses are correct. β-$NaLuF_4:Ce^{3+}$ and β-$NaLuF_4:Gd^{3+},Ce^{3+}$

were previously reported by our lab to exhibit STE emission, with a broad, intense band centered at 440 nm.[48] However, this band was not observed in β-$NaLuF_4$:Gd^{3+}, Tb^{3+} or β-$NaLuF_4$:Gd^{3+}, Eu^{3+} in the same report. No STE emission is observed in the radioluminescence spectra of β-$NaLuF_4$:Pr^{3+}, but given that the $^1S_0 \rightarrow {}^1I_6$ transition overlaps with the region STE emission was observed in this host, we chose to synthesize undoped β-$NaLuF_4$ to see if perhaps the STE emission was being overshadowed by the Pr^{3+} emissions. No STE emission was observed, thus these two hypotheses were ruled out since there was no evidence that STEs were forming in this material.

7.5.4.2. Hypothesis 3: An equilibrium scenario

Hypothesis 3 is a local model which does not involve the formation of STEs. In it, we consider a local trapping scenario in which the LOLs interact directly with the trap states. In this case, the trap states are positioned slightly below the LOLs. It is easiest to envision the proposed mechanism as an equilibrium situation described by Le Chatelier's principle.

Prior to irradiation, at room temperature and in the dark, the LOLs and trap states exist in equilibrium. When irradiation begins, the equilibrium is shifted toward trap filling. When the traps are empty, the luminescence dynamics of Pr^{3+} are such that the LOLs have a low radiative probability because the probability of filling a trap is higher. This, in turn, causes a high radiative probability of the $^1S_0$ state, since the LOLs are continually depopulated during the trap filling process, which facilitates depopulation of the $^1S_0$ state. With time, as the traps become filled, the probability to continue filling them decreases, thus the radiative relaxation probability of the LOLs increases, as observed in the spectra. Concurrently, the radiative relaxation probability of the $^1S_0$ decreases since the LOLs are no longer being depopulated *via* two routes. Once excitation ceases, the equilibrium shifts toward Pr^{3+}, and the traps populate the LOLs, resulting in persistent luminescence until an equilibrium is reached between them. In this mechanism, only excitation into the LOLs is necessary to induce trap filling. Therefore, we excited β-$NaLuF_4$:Pr^{3+} at 457.5 nm into the ^3P_J levels. The photoluminescence emission spectrum is shown in Figure 33A, confirming population of the LOLs can be achieved with this excitation wavelength; a colloidal sample of nanoparticles excited at this wavelength is dominated by red emissions (Figure 33B).

After 5 minutes of continuous irradiation, no change in emission intensity was observed, and no persistent luminescence was observed. Thus, this mechanism was also ruled out.

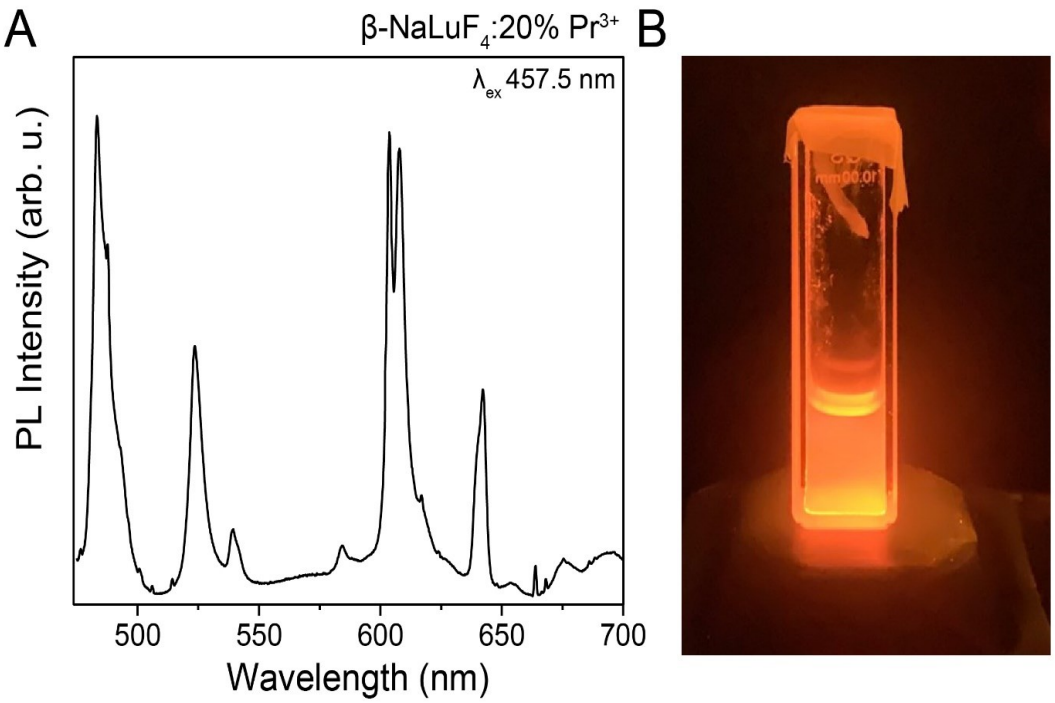

Figure 33. A) Photoluminescence (PL) emission spectrum of NaLuF4:20%Pr^{3+} upon excitation with 457.5 nm light. B) Photograph of a colloidal dispersion of $NaLuF_4$:Pr^{3+} in hexanes excited at 457.5 nm (viewed through a 515 nm long pass filter to cut the excitation light). Photoluminescence spectrum obtained by Steven L. Maurizio.

7.5.4.3. Hypothesis 4: The Goldilocks zone

Failure of the previous hypotheses led us to conclude that the trap states must lie below the $^1S_0$ state, but at higher energies than the LOLs. Since the wide band gap of $NaLuF_4$ precludes efficient charge separation, a local trapping mechanism is most likely at play. Thus, the positioning of the trap states below the $^1S_0$ level would account for the lack of persistent luminescence from this state, and would facilitate population of the LOLs upon de-trapping.

In hypothesis 4, there is an overlap of the energy wells of trapping states with both the $^1S_0$ state and the LOLs of Pr^{3+}. During excitation/charging, the $^1S_0$ state populates the traps, and the traps populate the LOLs, resulting in increased LOL emissions during the charging process. Persistent luminescence would then occur from the LOLs *via* release of the trapped charge. Thus, we postulate it would be specifically excitation of Pr^{3+} into the $^1S_0$ state that causes trap filling. Our collaborators at LumiLab performed persistent luminescence excitation spectroscopy in order

to determine exactly what wavelengths would induce persistent luminescence under deep UV excitation (which populates the $^1S_0$ state), if any. Indeed, an excitation band at 215 nm was observed, as shown in Figure 34. This confirms that trap filling is a direct consequence of population of the $^1S_0$ state situated at 46511 cm^{-1}. Notably, in this model, one would expect that the $^1S_0$ states increase in intensity with time, in line with what is traditionally observed for the states involved in the trap filling process (see Section 2.4.1 for more information).[432]

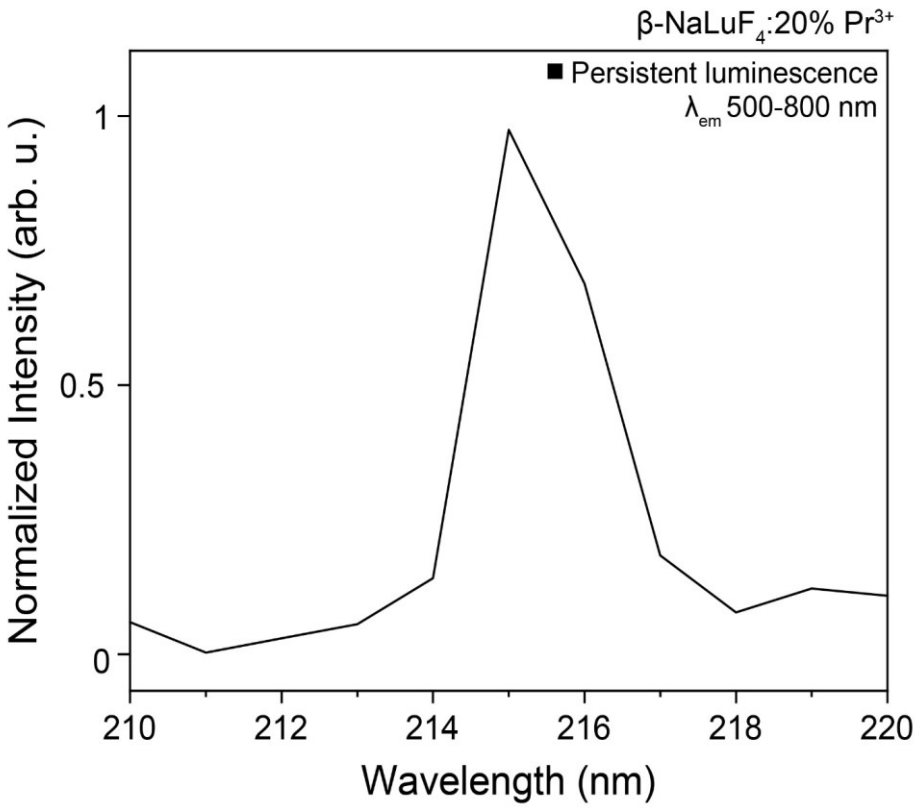

Figure 34. Persistent luminescence excitation spectrum of β-$NaLuF_4$:20% Pr^{3+} nanoparticles. Excitation performed using a Xe lamp (λ_{em} 500-800 nm).

7.5.5. Defect formation analysis

Since the most likely persistent luminescence model could not account for the decrease in the $^1S_0$ intensity, we postulated that a separate phenomenon such as defect formation could be responsible. Powder X-ray diffraction was performed on $NaLuF_4$:20% Pr^{3+} before and after irradiation for 45 minutes at 40 Gy/min (Figure 35). No changes in crystal structure were observed, thus confirming the change in intensity was not due to degradation or changes in the crystal phase

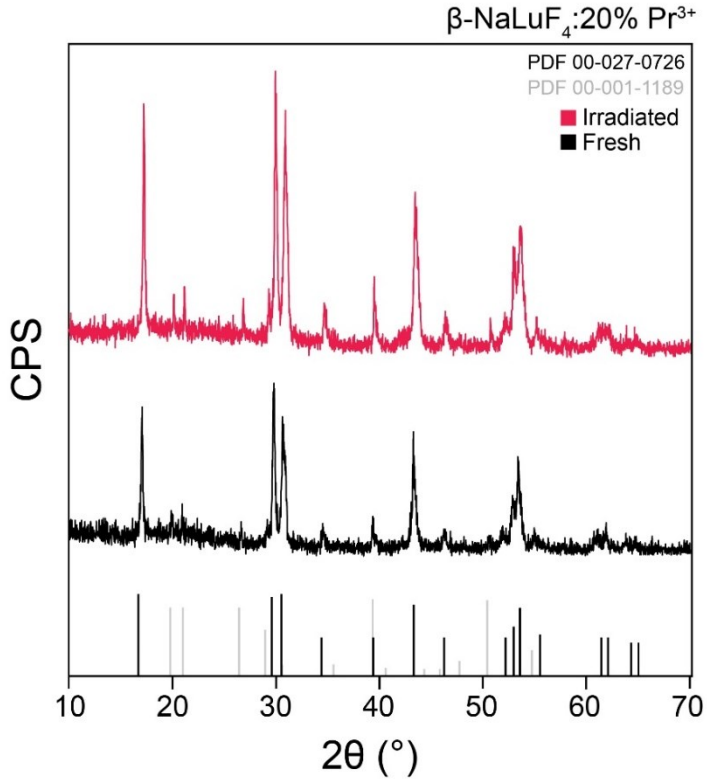

Figure 35. Powder X-ray diffraction of $NaLuF_4$:Pr before (black) and after (pink) irradiation. Diffraction pattern in gray corresponds to Na_2SiF_6 PDF 00-001-1189, and β-$NaLuF_4$ PDF 00-027-0726 in black.

of the nanoparticles. This is an important consideration for the therapeutic use of the nanoparticles, as this is conclusive evidence that radiation doses far greater than necessary for a therapeutic effect (Section 3.2) would be required to cause the material to degrade.

Since optically active defects like F centers are difficult to prove by X-ray diffraction, we used diffuse reflectance spectroscopy to investigate their potential formation. Undoped $NaLuF_4$ was studied rather than $NaLuF_4:Pr^{3+}$, since Pr^{3+} has strong absorbance in the visible region. As shown in Figure 36A, the irradiated sample exhibits a change in reflectance, and the ratio of the diffuse reflectance spectra before and after irradiation confirm the formation of a broad band centered at 340 nm, which overlaps well with all of the $^1S_0$ emissions (Figure 36B). Defects that absorb in the UV and blue spectral regions are known to alter the emission spectrum of many persistent luminescent materials.[433,434] These types of defects give rise to a phenomenon known as photochromism, or tenebrescence (which is specific to inorganic materials).[435] However, in this case, no color change of the powder was evident by eye, though the emission spectrum changed

considerably. While the precise nature of the defect is not known at this time, its formation certainly accounts for the observed decrease in luminescence from the $^1S_0$ states during irradiation.

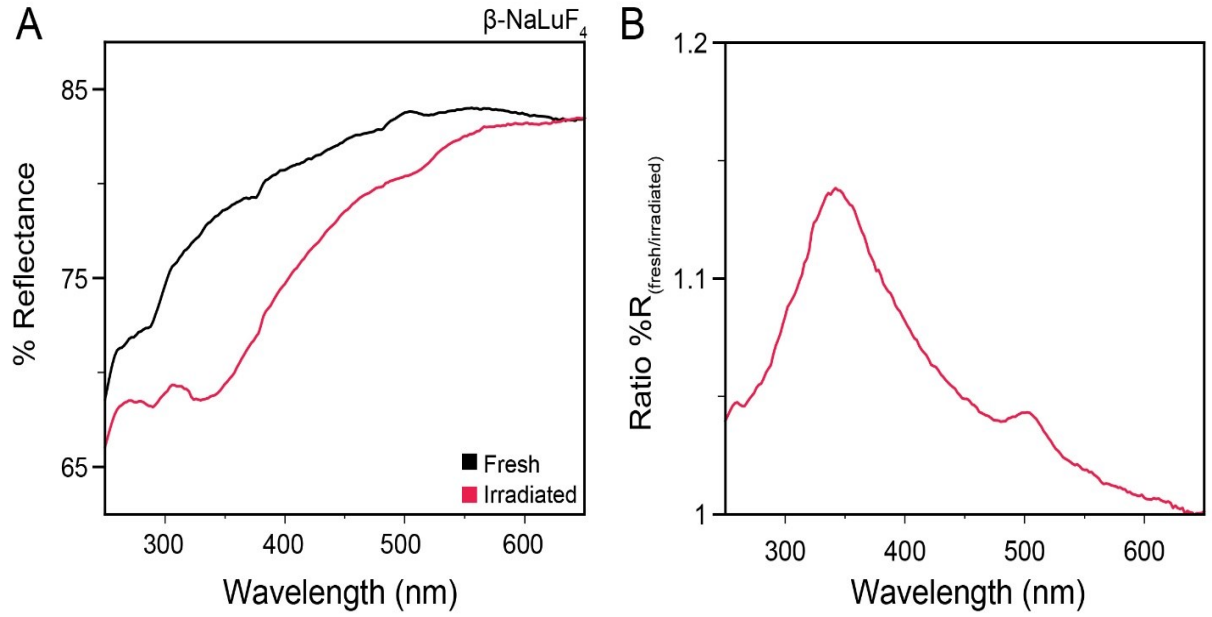

Figure 36. A) Diffuse reflectance spectra before (black) and after (pink) X-ray irradiation of $NaLuF_4$:20% Pr^{3+}, B) ratio of the diffuse reflectance spectra in panel A which exhibit the absorbance profile of the generated defect.

7.5.6. Summary of the mechanism

In summary, two distinct processes give rise to the change in radioluminescence intensities from the $^1S_0$ state and the LOLs, as well as persistent luminescence. The presence of a continuous trap distribution centered between the $^1S_0$ state and the LOLs gives rise to persistent luminescence through a local (de-)trapping model, in which persistent luminescence is observed only from the LOLs. The process of trap charging results in an increase in the LOL emissions during the charging process. Concurrently, during the charging process, an optically-active defect is formed, having a broad absorbance centered in the UV region. This defect thus absorbs the emissions from the $^1S_0$ state, causing a decrease in the radioluminescence intensities from this state as a function of irradiation time. Understanding of the fundamental luminescence processes occurring in this nanomaterial during irradiation with X-rays not only sheds new light on persistent luminescence in nanomaterials, it provides a solid basis for translation of these materials to biological applications.

7.5.7. Persistent luminescence as a function of radiation dose

As discussed in Section 7.4, the $NaLuF_4$:25 mol% Pr^{3+} nanoparticles were the optimal composition for use in our *in vitro* studies. Notably, they also exhibited persistent luminescence, which is assumed to occur *via* the mechanism described above. We investigated their persistent luminescence properties under the same radiation doses and the same dose rate used in the *in vitro* studies in Chapter 8. Persistent luminescence was not observed upon 2 Gy of dose applied to the particles, however upon delivering radiation doses of 5 Gy or more, persistent luminescence became detectable from the LOLs as expected (Figure 37A). The initial persistent luminescence intensity ranged between 15 and 25% of the radioluminescence intensity, as shown in Figure 37B. Notably, the persistent luminescence duration was roughly proportional to the radiation dose delivered; a 5 Gy dose resulted in 10 minutes of persistent luminescence, 10 Gy resulted in slightly over 15 minutes of persistent luminescence and 20 Gy resulted in nearly 30 minutes of additional emission. Persistent luminescence PDT has been demonstrated on a multiple occasions using either X-rays or UV excitation to charge the traps in the material prior to their introduction in cells or *in situ* after the materials are uptaken by the cells.[106] Although significantly weaker than the radioluminescence emissions, it is conceivable that the persistent luminescence from the LOLs

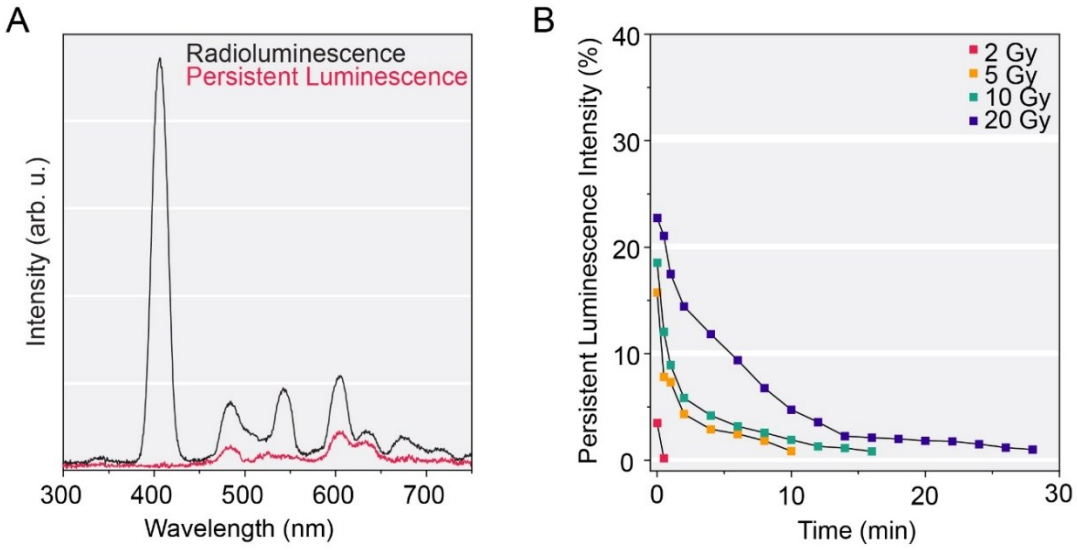

Figure 37. A) Radioluminescence spectrum (black) of $NaLuF_4$:25% Pr^{3+} and corresponding persistent luminescence spectrum (pink) taken 10 seconds after X-ray excitation ceased (5 Gy was delivered to the nanoparticles). B) Persistent luminescence intensity as a percent of the initial radioluminescence intensity of the LOLs as a function of time after X-ray excitation ceased. Each radiation dose delivered to the nanoparticles is depicted where a 2 Gy dose is in red, 5 Gy in yellow, 10 Gy in green, and 20 Gy in blue. (50 kVp, 80 μA, unfiltered, uncollimated beam. No slit was placed at the entrance of the spectrometer).

could induce photodynamic activation of PPIX through excitation into the Q bands. While this is likely to give a minimal contribution to the overall therapeutic effect, any additional ROS production obtained without additional external irradiation would be desirable.

Chapter 8. *In vitro* evaluation of X-PDT in U251 cells

8.1. Preliminary evaluation of β-$NaLuF_4$: 25% Pr^{3+} nanoparticles for activation of protoporphyrin IX

The spectral overlap between the emissions from β-$NaLuF_4$:Pr^{3+} and the absorbance of PPIX is a near-perfect match; this forms the basis for using this combination in X-PDT (see Section 3.6). The Soret band of PPIX has a maximum at 406 nm, which overlaps with the $^1S_0 \rightarrow {}^1I_6$ transition of Pr^{3+}, while the Q-bands from PPIX overlap with the LOL emissions from Pr^{3+}. Since the Soret band has a much higher absorption cross-section than the Q-bands, it is most important to maximize the emissions from the $^1S_0 \rightarrow {}^1I_6$ transition of Pr^{3+} rather than the visible emissions from the LOLs. Thus, based on the concentration study outlined in Section 7.4, β-$NaLuF_4$: 25% Pr^{3+} was chosen as the optimal composition for *in vitro* studies since it provides the strongest $^1S_0 \rightarrow {}^1I_6$ emissions. Overlap of the radioluminescence spectrum of β-$NaLuF_4$: 25% Pr^{3+} and the PPIX absorption spectrum are shown in Figure 38.

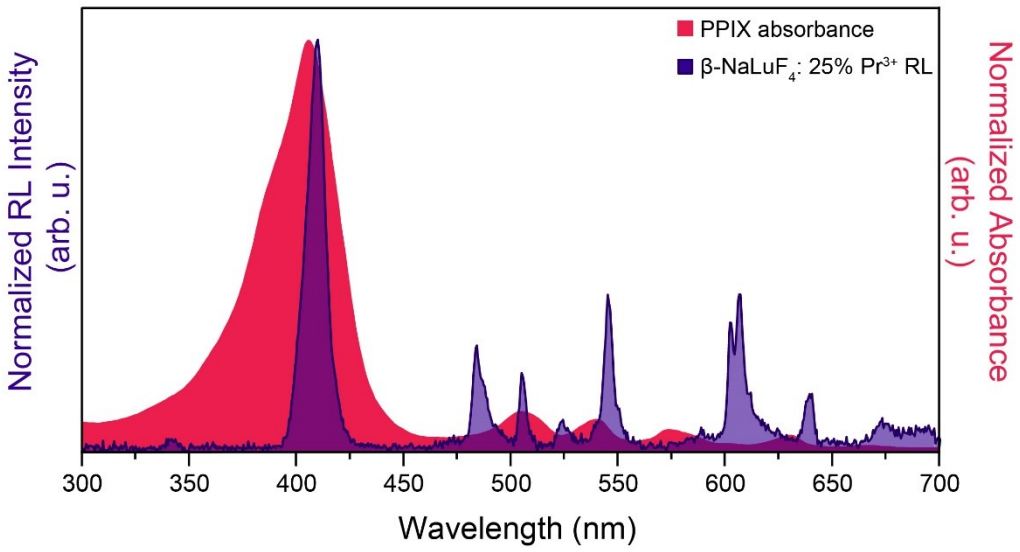

Figure 38. Normalized absorbance spectrum (red) of protoporphyrin IX and radioluminescence emission spectrum (blue) of $NaLuF_4$:25% Pr^{3+}. Both spectra were recorded in 50/50 v/v DMSO/H_2O. (50 kVp, 80 μA, Au target, unfiltered, uncollimated beam).

8.1.1. Surface coating of β-$NaLuF_4$: 25% Pr^{3+}

In order to obtain nanoparticles suitable for biological applications, they must first be rendered hydrophilic, as the oleate capping ligand used during the synthesis imparts the nanoparticles with a hydrophobic surface. For biological applications, the nanoparticles must not only be hydrophilic, they must have a surface coating that prevents aggregation, as large clumps of nanoparticles are less likely to enter cells. The surface charge can affect RLNP-cell interactions, and also can affect the stability of the nanoparticles in colloidal dispersion.[367,436,437] We tested three surface coatings that rendered the nanoparticles to have a highly negative, approximately neutral, or highly positive surface charge. First, citrate was chosen because it is a well-established coating for nanoparticles due to its non-toxic, small-molecule nature and ability to impart a highly negative surface charge.[438,439] 5-ALA was used as a neutral surface coating since it is a small, zwitterionic molecule that was already being introduced into the cells to generate PPIX and has appropriate functional groups to electrostatically coordinate to the RLNP surface, and is known to be non-toxic. Finally, since the surface of as-synthesized $NaLuF_4$ is positively charged, we used a layer-by-layer approach to generate stable highly-positively charged nanoparticles. Oleate-free (bare) $NaREF_4$ nanoparticles are known to aggregate in aqueous media, precluding their use in biological applications.[45] In this case, we used citrate as the base layer to impart a negative charge and then coated the citrate layer with poly-L-lysine *via* electrostatic interaction. Poly-L-lysine (PLL) is an amino acid-derived polymer and is used in cell culture plastics manufacturing to enhance adhesion of cells to plastic dishes.[440] It is a well-established surface coating for nanoparticles to achieve a high positive charge, and the combined citrate/PLL coating has been previously demonstrated on $NaREF_4$ nanoparticles for biological applications.[41,440–442]

Nanoparticles with each surface coating were evaluated by FT-IR-ATR and zeta potential to confirm the coating was performed successfully (Figure 39). Average zeta potential values of -34.5 mV, -2.4 mV, +35.8 mV, and +33.3 mV were obtained for nanoparticles coated with citrate, 5-ALA, citrate/PLL, and uncoated (oleate-free), respectively (Figure 39A). As shown in Figure 39B, the coating could be monitored by changes in the FT-IR-ATR spectrum, with the loss of C-H and C-O vibrations from the FT-IR-ATR spectrum of the oleate-free nanoparticles, concurrent with the appearance of an O-H stretch due to water molecules coordinating to the surface. The addition of the citrate/PLL coating and 5-ALA coatings are also evidenced by the appearance of

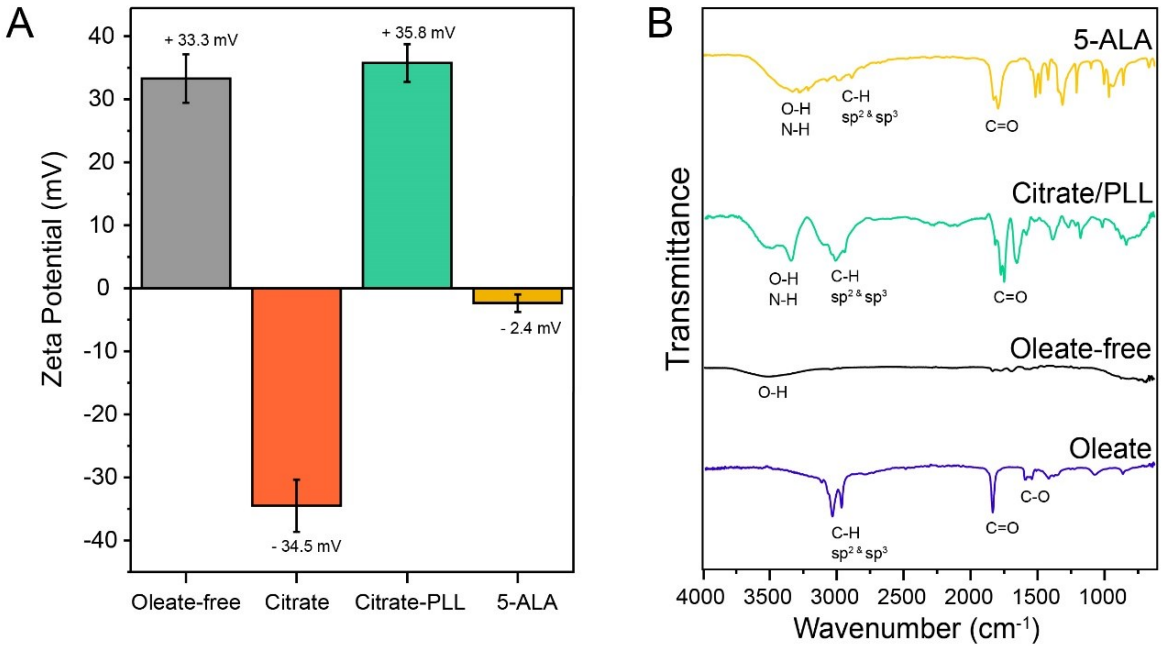

Figure 39. A) Zeta potential measurements of 1 mg/mL dispersions of oleate-free (gray), citrate (orange), citrate/PLL (green), and 5-ALA (yellow) coated $NaLuF_4$:25% Pr^{3+} nanoparticles in deionized water. B) FT-IR-ATR spectra of the corresponding powder samples analyzed in panel A along with oleate-capped nanoparticles (blue).

vibrations corresponding to their structures after coating the oleate-free nanoparticles with each. Notably, citrate/PLL coated nanoparticles exhibit two overlapping bands in the 3000-4000 cm^{-1} region, in line with the presence of two different species (ie. the O-H stretch from the small molecule citrate and N-H stretch from the poly-L-lysine polymer).

The stability of the nanoparticles with time was evaluated *via* zeta potential at regular intervals to determine how long the stock dispersions could be stored (Figure 40). Citrate and citrate/PLL nanoparticles maintained the same zeta potential for over 1 month. In contrast, 5-ALA coated nanoparticles lost their surface coating after 48 hours, as evidenced by a change in colloidal stability and an increase in zeta potential. Since bare $NaLuF_4$ nanoparticles have an average charge of +33.3 mV, the increased zeta potential was likely due to the degradation of 5-ALA and exposure of the bare nanoparticle surface. 5-ALA is known not to be stable in solution at physiological pH, thus it was not unexpected that degradation occurred.[443–445] *In vitro* studies using 5-ALA coated nanoparticles were therefore performed using fresh nanoparticle samples on the same day of their preparation.

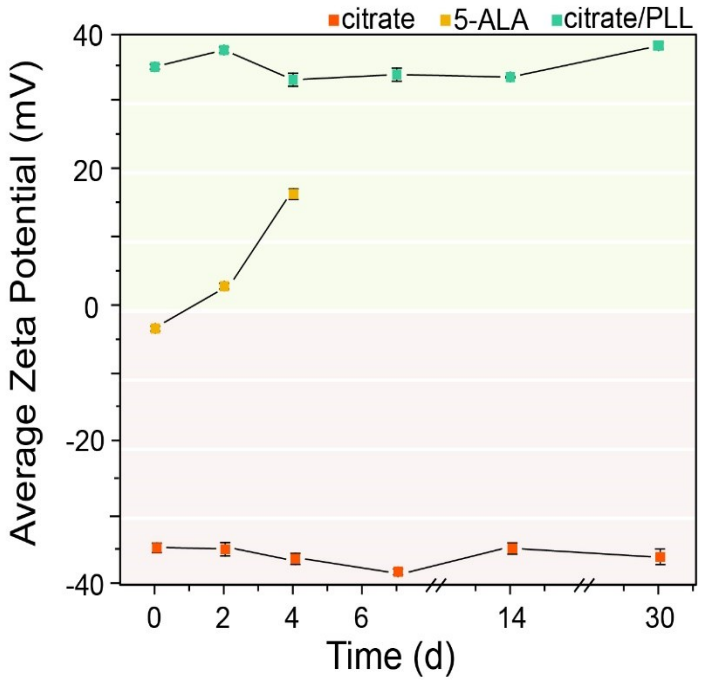

Figure 40. Average zeta potential values for $NaLuF_4$:25% Pr^{3+} nanoparticles coated with citrate (orange), 5-ALA (yellow), or citrate/PLL (green) as a function of storage time. At each time point, an aliquot of the stock solution was taken and diluted to 1 mg/mL in deionized water and analyzed.

8.1.2. *In vitro* investigation of surface coatings

Prior to treatment with ionizing radiation, cell viability was analyzed utilizing several different parameters during the investigation of the surface coating (Figure 41). First, each coating was studied at 10, 100 and 500 μg/mL nanoparticle concentrations to ascertain if there was a concentration-dependent effect on the viability for the nanoparticles with each coating. Second, the viability was evaluated in cell medium supplemented with sodium pyruvate and without sodium pyruvate. Sodium pyruvate is a hydrogen peroxide scavenger and is known to play a role in mitigating oxidative stress on cells.[446] Moreover, the presence or absence of it in cell culture medium can significantly alter the outcomes of treatments that are related to oxidative damage, such as PDT.[446] Generally, the presence of sodium pyruvate aids in the health of the cells, thus it was worth investigating at a pre-irradiation stage whether a significant difference could be observed if it was incorporated in the medium. Finally, we were interested in the immediate effects of the nanoparticles and their coatings versus the effect after a round of cell division. Thus, we performed viability assays immediately after incubation with the nanoparticles, and 24 hours post-

incubation.

At this stage, we decided to investigate the viability of the cells using a single incubation time for each coating. Once the coating was chosen, we then examined the uptake as a function of time. Four hours was chosen as the incubation time, as this is a very common incubation time

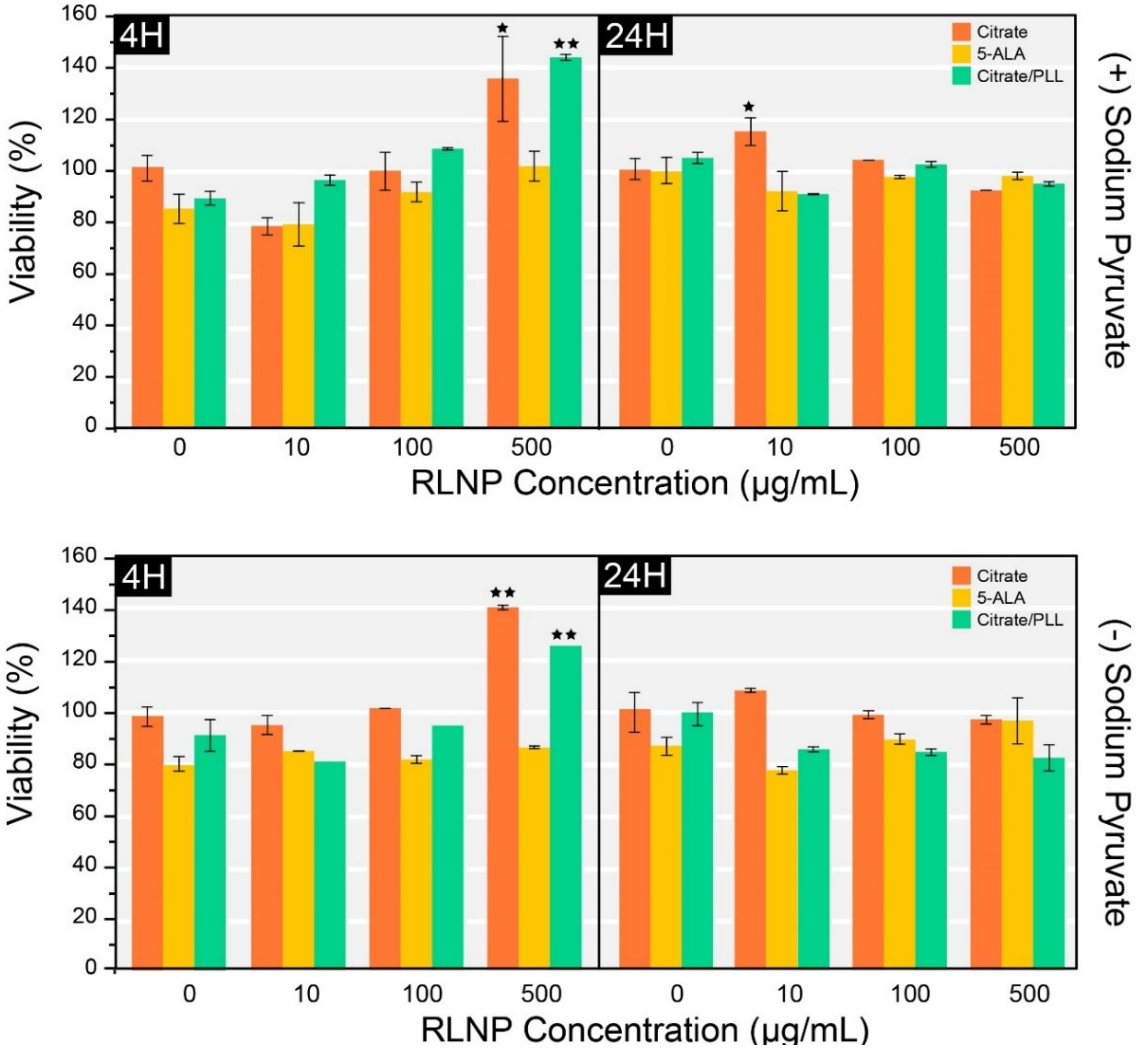

Figure 41. Viability assays of U251 cells 4 hours and 24 hours post-treatment with $NaLuF_4$:25%Pr^{3+} nanoparticles coated with citrate, 5-ALA or citrate and poly-L-lysine at 0, 10, 100 and 500 μg/mL concentrations. The top panel is the result of the experiment performed in cell culture medium containing sodium pyruvate, and the bottom panel is the result of the experiment performed in cell culture medium in the absence of sodium pyruvate. Both experiments were performed in an identical fashion. Statistical significance is relative to the untreated controls in each panel (0 μg/mL RLNPs) and was determined using Student's t-test (one symbol = $p < 0.05$, two symbols = $p < 0.01$).

across different nanoparticle compositions, coatings, sizes, and across different cell lines (including those used herein).[40,46,447–451]

After treatment with nanoparticles, it takes an additional 4 hours for the viability assay used herein to yield results, as the assay measures the metabolic activity of the cells. This is achieved by measuring the ability of cells to uptake non-fluorescent resazurin and for NADH and NADPH in metabolically-active cells to reduce it to the fluorescent resorufin analyte.[452] Thus, the earliest timepoint that could be measured after the nanoparticle treatment is the minimum assay incubation time of 4 hours required to yield the conversion to resorufin. In keeping with the standards set forth by the International Organization for Standardization in 2009[453], viabilities above 80% were considered non-cytotoxic. As shown in Figure 41, none of the conditions tested yielded viabilities below 80%, thus all nanoparticle coatings and concentrations were not acutely toxic up to 24 hours after introduction of the nanoparticles. Of note, 4 hours post-treatment with 500 μg/mL of citrate and citrate/PLL nanoparticles, a sharp increase in viability was observed (up to 145%). The resazurin assay used throughout this thesis to determine viability is a metabolic activity-based assay. Thus, increases in viability above 100% corresponds to increased metabolic activity. This is likely indicative of cellular stress due to the high nanoparticle concentrations used, however, since viability returned to nearly 100% at the 24-hour timepoint for these treatment scenarios, the increased metabolic activity was only temporary, and clearly not lethal. Viabilities with and without sodium pyruvate were similar for all conditions in that no toxicity was observed. Since the viabilities of the cells treated with sodium pyruvate-containing media were close to 100%, we decided to use sodium pyruvate-supplemented media throughout the studies. Interestingly, this is not recommended for *in vitro* PDT treatments, since it makes cells less apt to ROS damage; however, it is a more realistic scenario for sodium pyruvate to be present, as it is a native species present in tissues.[446] Thus, the results obtained herein for the PDT effect are not augmented by an omission of sodium pyruvate.

Our interest in feasibility for clinical translation necessitates that the nanoparticle formulation developed be stable enough for industrial production and distribution, both of which require significant amounts of time. Thus, since the 5-ALA-coated nanoparticles exhibited similar viabilities to the other varieties of nanoparticles but were only stable in storage for less than 48 hours, we excluded this as an option for the sake of practicality. For the choice between citrate and

citrate/PLL coatings, very little difference in viability was observed between the two, and the same can be said for their storage stability. Thus, since its known that positively-charged nanoparticles generally exhibit more efficient uptake than their negative counterparts[367,437,454,455], the citrate/PLL coating was chosen. Hereafter, all mentions of nanoparticles or RLNPs in this chapter are β-$NaLuF_4$: 25% Pr^{3+} coated with citrate and PLL.

8.1.3. Energy transfer studies in solution

After the coating was chosen, spectroscopy was carried out on colloidal dispersions of nanoparticles in 50/50 v/v% DMSO/H_2O in the presence and absence of PPIX. A 5 nM concentration of PPIX was used in this study, as it is known that intracellular PPIX concentrations are in this range after 5-ALA administration.[456,457] Since the PPIX concentration in solution will have some impact on the distance between PPIX molecules and nanoparticles, the scenario studied here is reasonable for simulating the interactions of the nanoparticles with intracellular PPIX. Energy transfer (ET) was evaluated by the decrease in radioluminescence intensity from the nanoparticles integrated across the entire emission spectrum and calculated according to

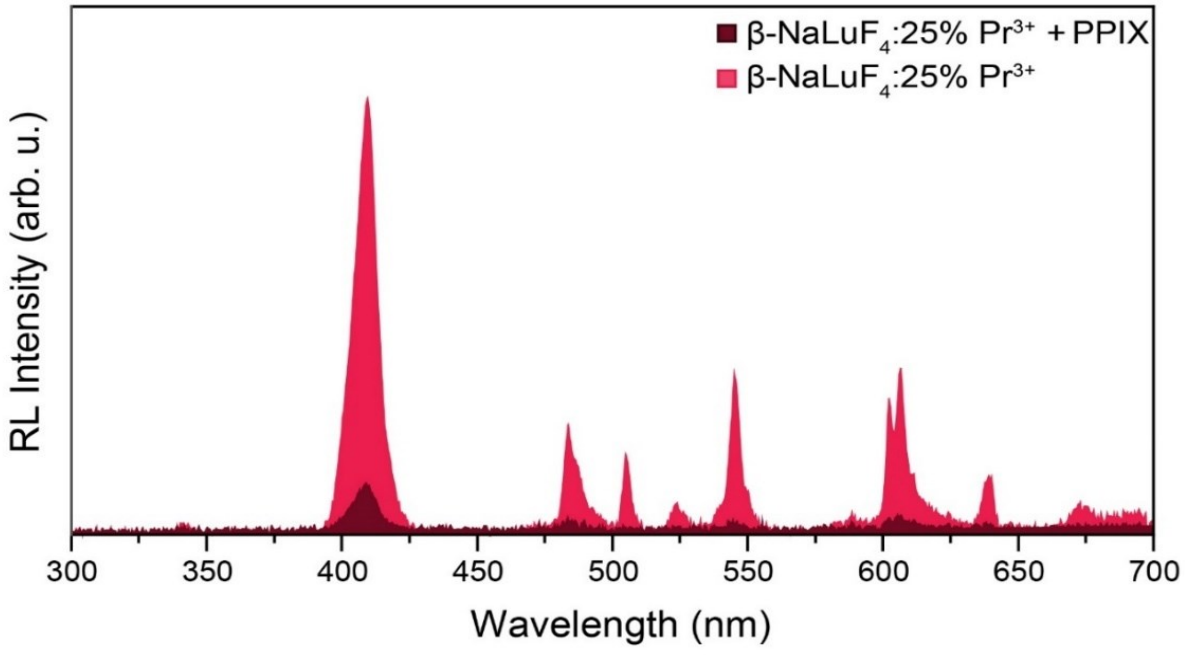

Figure 42. Radioluminescence emission spectra of colloidal $NaLuF_4$: 25% Pr^{3+} nanoparticles coated with citrate/poly-L-lysine alone (light red trace) and in the presence of 5 nM PPIX (dark red trace). Both spectra were obtained from colloidal nanoparticle dispersions in 50/50 v/v DMSO/H_2O at 15 mg/mL concentrations each.

equation 8:

$$\mathbf{ET = 1 - \frac{I_{(RLNPs+PPIX)}}{I_{(RLNPs)}}} \quad (8)$$

As shown in Figure 42, a major decrease in all of the transitions from Pr^{3+} was observed, in line with what is expected given the spectral overlap with PPIX across the entire emission spectrum of Pr^{3+}. An energy transfer of 78% was calculated using equation 8, indicating sufficient activation of PPIX was occurring.

8.2. Nanoparticle incubation time optimization

The overarching goal of incorporating these nanoparticles into an intraoperative workflow means it is essential to use the shortest incubation times possible to minimize the time a patient would be on an operating table. Thus, nanoparticle incubation was studied at times ranging from 0.5 to 6 hours at concentrations of 10, 50, 100, 200 and 500 μg/mL. All treatments were non-cytotoxic at 24 hours after incubation with the nanoparticles, as shown in Figure 43 (≥ 80% viability).

Since no significant changes in viability were observed, we postulated that this could be due to a lack of interaction of the nanoparticles with the cells, rather than a lack of toxicity. Thus, fluorescence microscopy was performed to confirm interaction of the nanoparticles with the cells at each timepoint. Conveniently, Pr^{3+} can be excited into the ^3P_J states using conventional excitation wavelengths available on a standard epifluorescence microscope (a wide-band blue LED), producing LOL emissions as shown in the photoluminescence spectrum of the $NaLuF_4$:Pr^{3+} nanoparticles excited into the ^3P_J states in Section 7.5.4. As such, the RLNPs can be used as an *in situ* luminescence probe. Prior to imaging the samples, several control experiments were performed to ensure the excitation and emission filters in the microscope were appropriate to isolate emissions from the RLNPs upon blue light excitation without detecting them in the channel used to visualize the red emissions from PPIX upon 405 nm excitation (see Section 5.2.12 for microscope parameters). We also confirmed the 405 nm excitation source used for PPIX did not excite the nanoparticles.

Imaging experiments were carried out in both HeLa cells and U251 cells for a few reasons.

First, HeLa cells are thicker than U251 cells, and therefore it is easier to visualize RLNP distribution as a function of cell depth. Second, confirmation of the uptake in two very different cell lines (cervical epithelial and brain astrocyte) provides an additional level of confidence of the method.

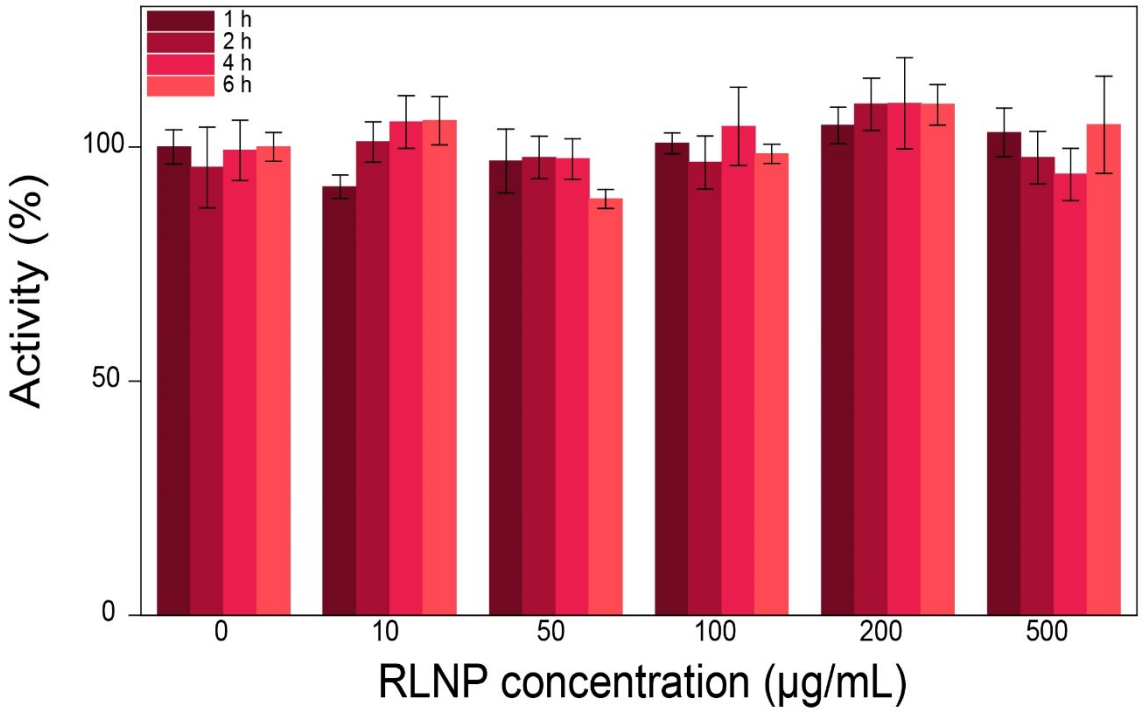

Figure 43. Viability of U251 cells treated with 0, 10, 50, 100, 200 and 500 µg/mL $NaLuF_4:Pr^{3+}$ nanoparticles for 1, 2, 4, or 6 h. Cell viability was measured at 24 hours after the end of the nanoparticle incubation time. Statistical significance was assessed with One-way ANOVA combined with Bonferroni post-hoc analysis. No statistically significant differences were observed.

As observed in Figure 44, nanoparticle emissions could be detected after only 30 minutes of incubation and increased as a function of time thereafter. However, generally across both cell lines and all nanoparticle concentrations, at 1 hour there was sufficient luminescence detected from the particles, thus this was chosen as the incubation time moving forward. Given the intraoperative workflow envisioned for this X-PDT system, it is important that the shortest possible incubation time is used such that the patient is not in the operating room for a prohibitive amount of time.

Z-stack projections of the cells as a function of nanoparticle concentration were also generated

to obtain further evidence that nanoparticles had been internalized in the cells. As shown in Figure 45, the luminescence from the nanoparticles is observed throughout the image stack. This is indicative of nanoparticle uptake and internalization and provided early confirmation that RLNP-cell interactions were taking place.

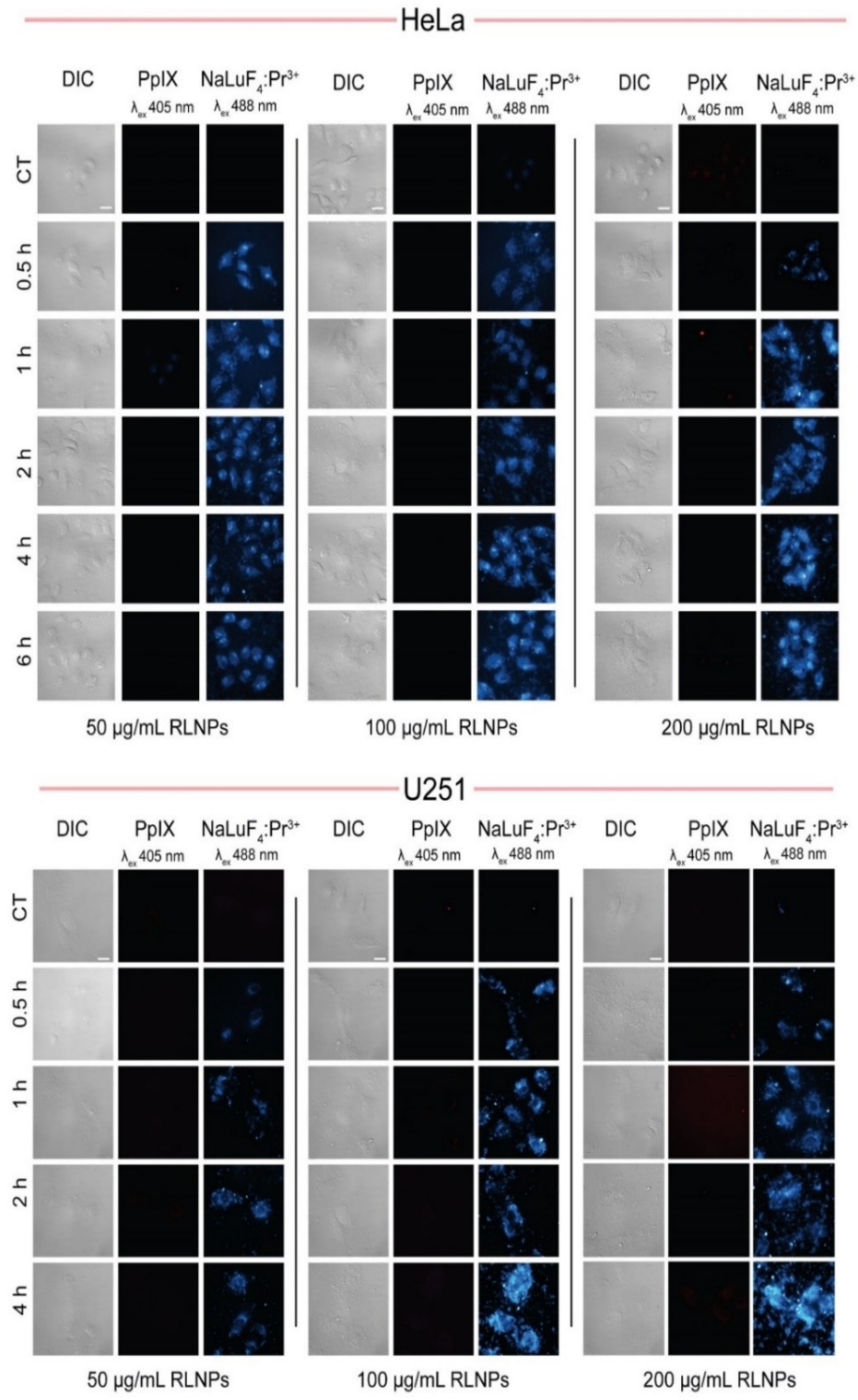

Figure 44. DIC and fluorescence microscopy of fixed HeLa (top) and U251 (bottom) cells incubated with 50, 100 or 200 µg/mL $NaLuF_4:Pr^{3+}$ RLNPs for 0.5, 1, 2 and 4 hours. The PPIX channel (λ_{ex} 406 nm) is shown to confirm no luminescence from the RLNPs (λ_{ex} 488 nm) is observed in the channel used to excite PPIX. Scale bar is 20 µm.

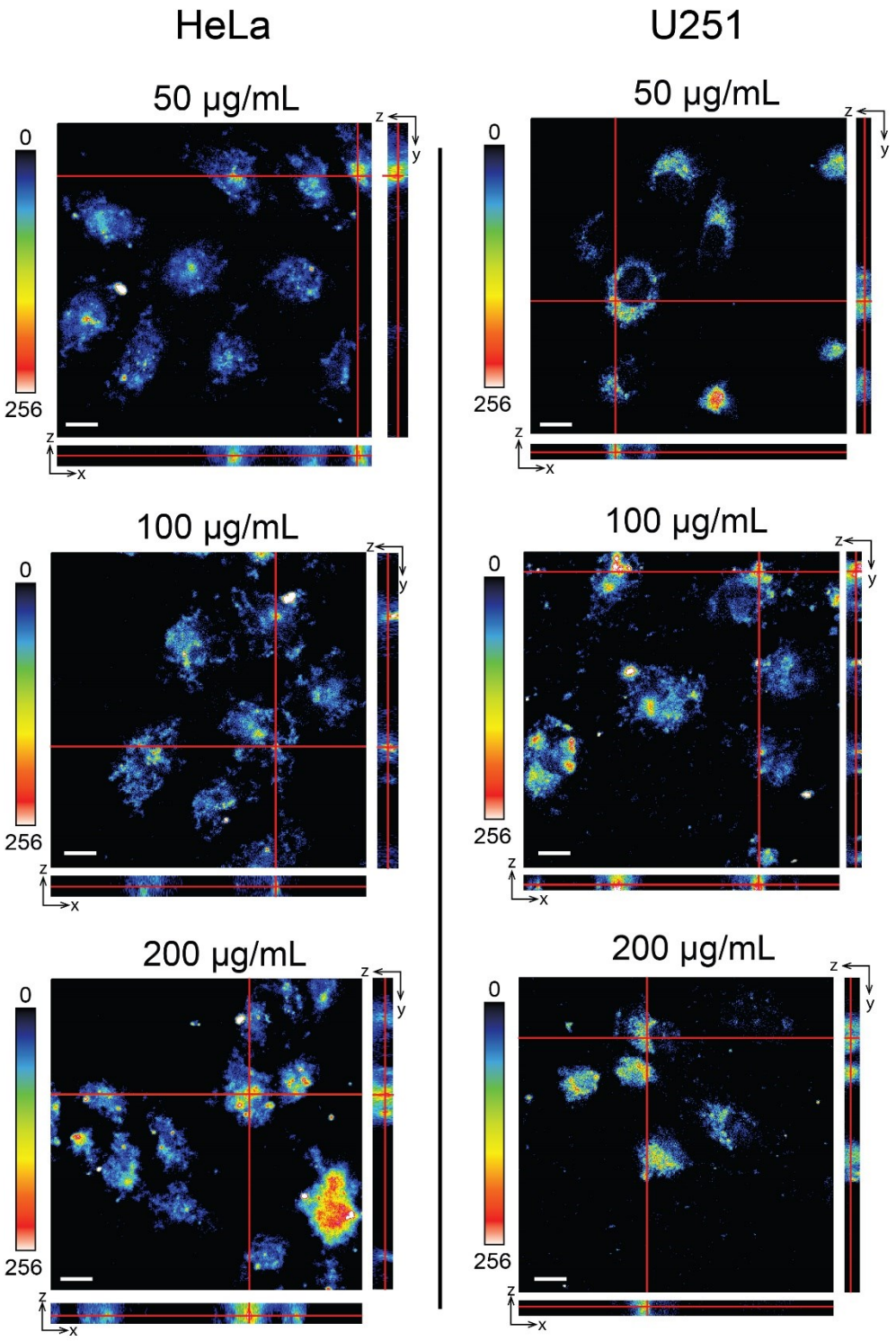

Figure 45. Fluorescence microscopy as a function of cell depth (z) of HeLa (left) and U251 (right) cells incubated for 1 hour with 50, 100 or 200 µg/mL $NaLuF_4:Pr^{3+}$ nanoparticles. (λ_{ex} 488 nm) Red lines correspond to the xz and yz positions in the image stacks.

8.3. 5-ALA uptake and PPIX accumulation

As mentioned in Section 3.2.2.2, 5-ALA stimulated PPIX accumulation occurs in cancer cells due to abnormalities in the heme biosynthesis pathway. Prior to performing X-PDT, we set out to establish the parameters sufficient to induce strong PPIX production and accumulation for our studies. *In vitro* 5-ALA PDT studies are most often performed using 1 mM 5-ALA and incubation for 4 hours in human cancer cells.[196,198,204,458–460] In addition to the concentration of 5-ALA and incubation time, the presence of serum proteins *in vitro* can drastically reduce intracellular accumulation of PPIX due to increased efflux rates.[204,205,461,462] PPIX is exported from cells *via* the ABC transporter pathway, and higher levels of the ABCG2 protein that is responsible for shuttling PPIX out of cells are observed in many human tumors; this is known to interfere with PDT.[204] Thus, in addition to studying PPIX production and accumulation with time, we evaluated the effect of serum as well.

As shown in the fluorescence microscopy images (Figure 46), upon excitation with 405 nm light, strong red fluorescence was observed upon administration of 1 mM 5-ALA that increased as a function of time, with 4 hours yielding the highest intensities. Notably, the distribution of protoporphyrin IX within a single cell is not homogeneous, and some cells produce more protoporphyrin IX than others; this is well-known.[195,196] Indeed, cells treated with 5-ALA in fetal bovine serum-free media (labelled as (-) FBS) exhibited significantly brighter fluorescence, confirming the need to use serum-free media during the experiments. With regard to clinical translation, there are much smaller amounts of serum proteins in extracellular fluid than what is typically used during *in vitro* cell experiments[204]; hence the presence of serum proteins affecting PPIX accumulation is a problem restricted to the *in vitro* scenario. Notably, it is recommended that *in vitro* 5-ALA experiments are performed in a serum-free environment.[312]

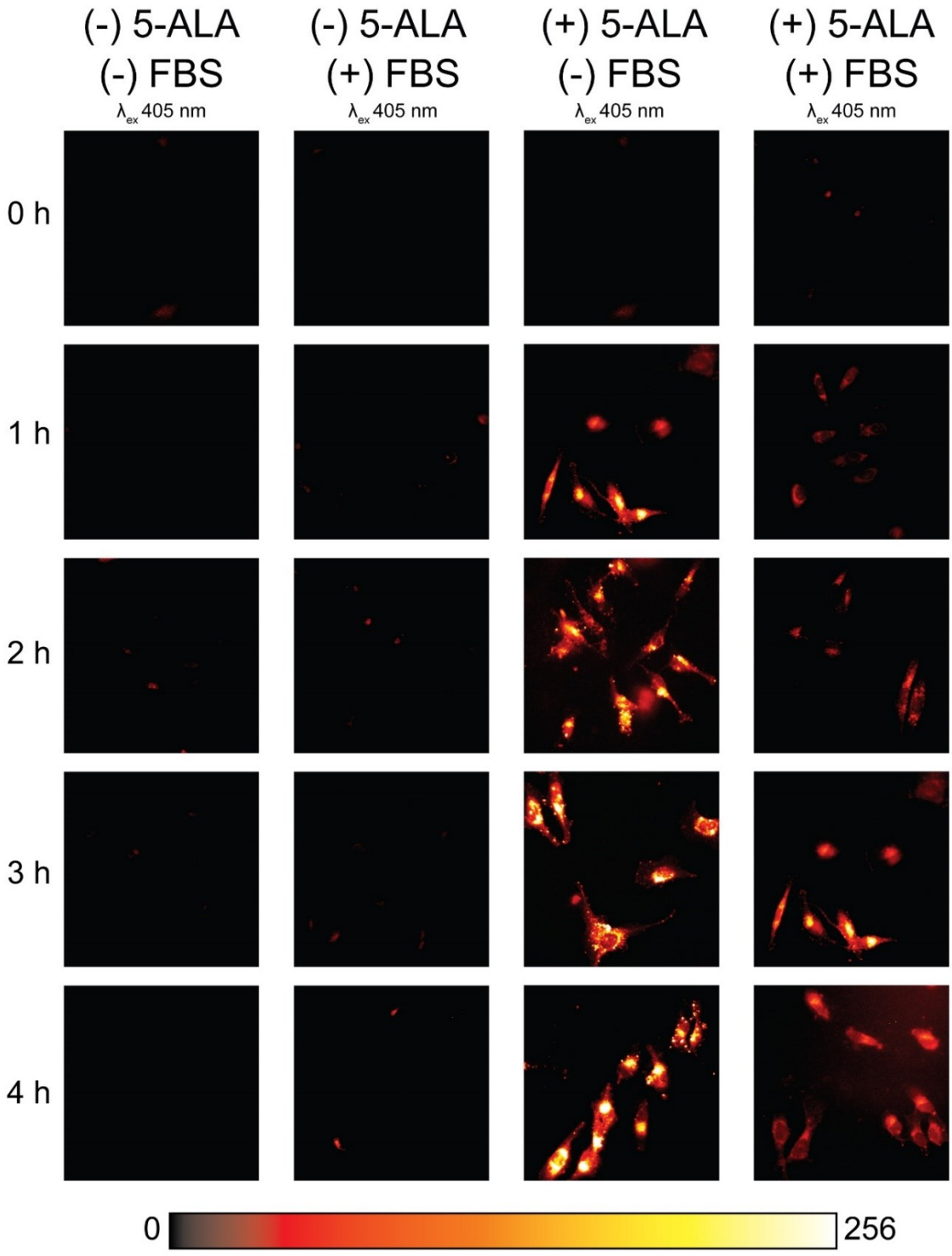

Figure 46. Fluorescence microscopy of U251 cells treated with 5-ALA for 1, 2, 3 and 4 hours, using fetal bovine serum-free medium ((-)FBS) or medium supplemented with 10% fetal bovine serum ((+)FBS). Excitation was performed at 405 nm to visualize PPIX emission.

Fluorescence spectroscopy was also performed to corroborate the microscopy results, and to quantify the accumulation of PPIX. As shown in Figure 47, after 4 hours, a nearly 20 times increase in PPIX fluorescence intensity was observed relative to untreated cells. The percentage increase in fluorescence is similar to what has been observed in 5-ALA-treated human breast cancer cells and murine glioma cells.[195,463] Taken together, we have provided independent means of confirming the parameters used (1 mM 5-ALA, serum-free medium, 4 hour incubation) are sufficient for generating large amounts of accumulated PPIX in U251 cells. Thus, parameters were established for both the 5-ALA incubation (4 hours) and the RLNP incubation (1 hour), which could then be merged.

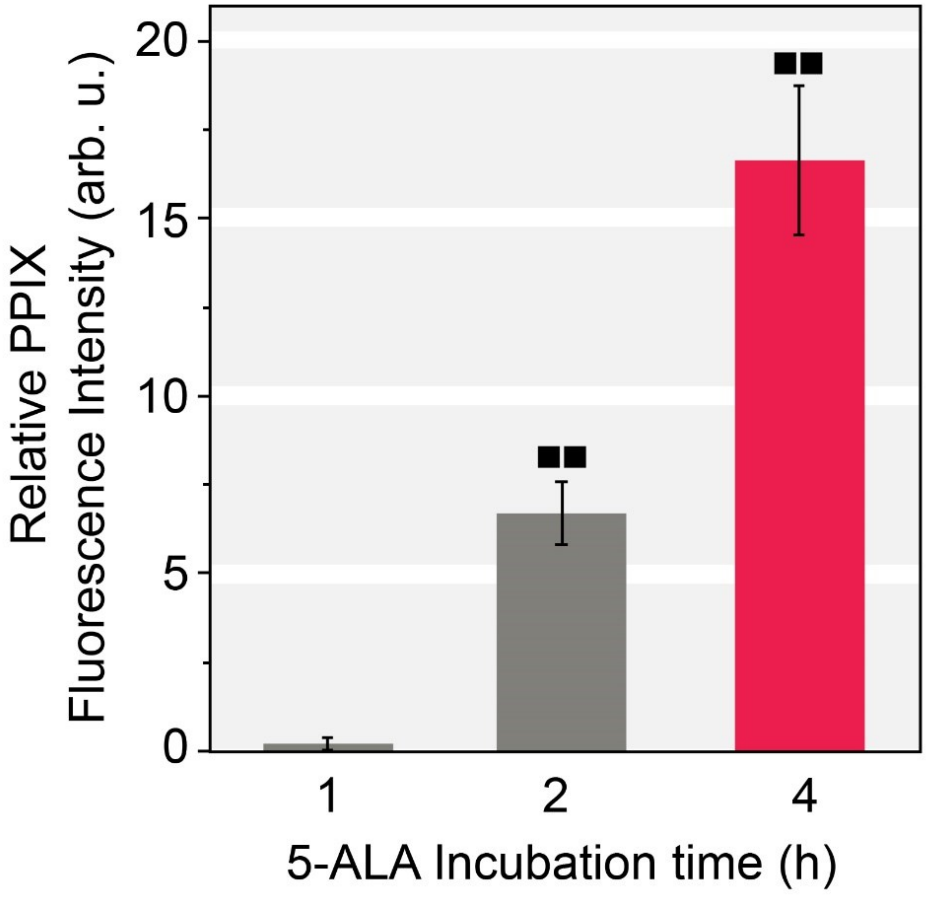

Figure 46. Relative fluorescence intensity of U251 cells treated with 1 mM 5-ALA for 1, 2 and 4 hours normalized to untreated control samples. Statistical significance is relative to the untreated controls in each panel (0 μg/mL RLNPs) and was determined using Student's t-test (one symbol = $p < 0.05$, two symbols = $p < 0.01$).

8.4. Combining RLNPs and 5-ALA: Order of introduction

Most nanoparticle-PDT systems combine the nanoparticle and photosensitizer into a single unit to be delivered to the cells, since these systems employ synthetic photosensitizers.[40,41,334,464,465] Thus, incubation of the PDT agent (ie. the nanoparticle/photosensitizer) occurs in a single step. In contrast, the work herein requires the photosensitizer pro-drug 5-ALA to be added separately from the nanoparticles since we are relying on the cells to produce the PPIX photosensitizer. This enables a more selective X-PDT effect, since only the malignant cells will be able to produce PPIX-generated ROS. We postulated that the order of addition of the two agents may strongly affect their cellular interactions. In other words, if 5-ALA is administered first, does it affect the uptake of the nanoparticles? Or if the nanoparticles are administered first, do they affect the degree of PPIX accumulation? To answer these questions, we used a combination of cell viability, fluorescence microscopy, fluorescence spectroscopy, and inductively coupled plasma mass spectrometry (ICP-MS) to ascertain if the order had an effect, and to determine which order to move forward with.

8.4.1. Viability assays

Viability assays were carried out 24 hours post-treatment for both scenarios in U251 cells across a wide RLNP concentration range (10, 50, 100, 200 and 500 ug/mL) to ensure if there was a difference as a function of nanoparticle concentration that it would be observed. As shown in Figure 48, none of the treatments were significantly different, and there was no observable trend in either case. Importantly, none of the treatments showed a significant loss in viability at any nanoparticle concentration, confirming that the combination of RLNPs and 5-ALA is not acutely cytotoxic, even up to relatively high nanoparticle concentrations. Further experiments were carried out at longer timepoints to confirm a lack of long-term toxicity as well, as discussed in Sections 8.8-8.9. Based on viability alone, there was no obvious reason to choose one order of administration over the other.

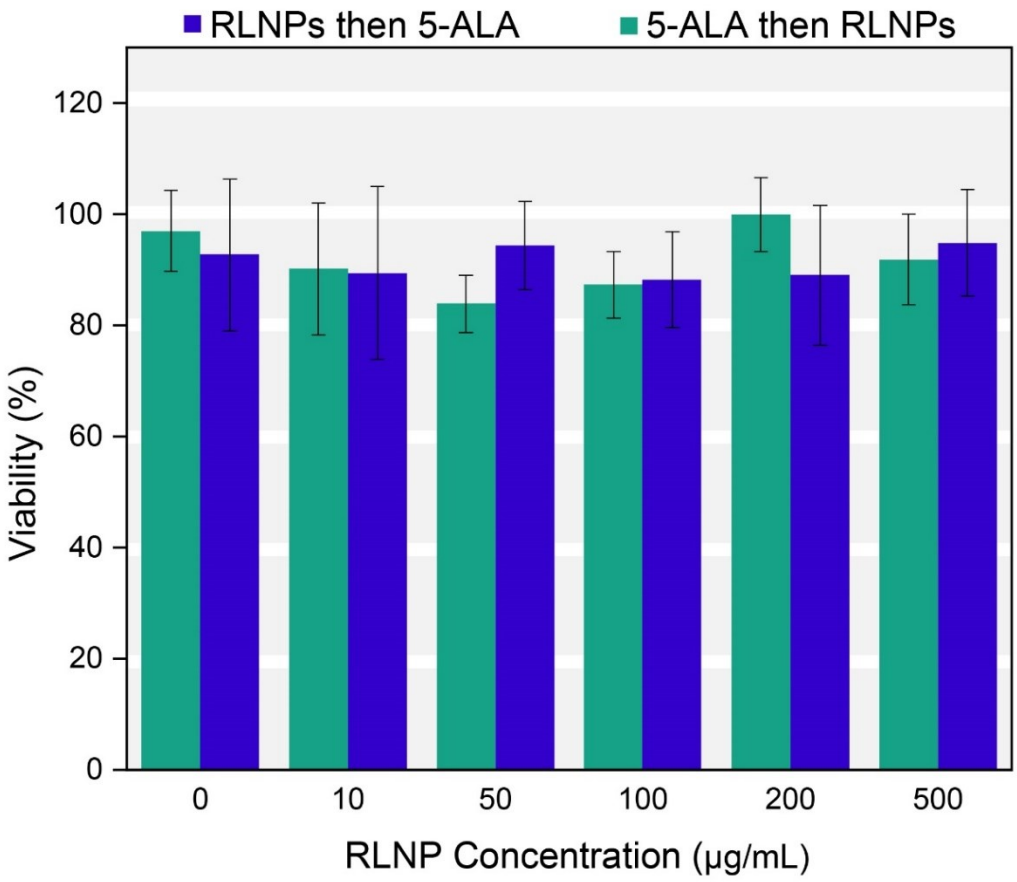

Figure 47. Cell viability of U251 cells treated with 1 mM 5-ALA for 4 h followed by a 1 hour incubation with 10, 50, 100, 200 and 500 ug/mL $NaLuF_4:Pr^{3+}$ RLNPs (green) or with RLNPs first followed by 5-ALA (blue). Statistical significance is relative to the untreated controls (0 µg/mL RLNPs, no 5-ALA) and was determined using Student's t-test (one symbol = $p < 0.05$, two symbols = $p < 0.01$). No statistically significant differences were observed.

8.4.2. Fluorescence microscopy

Fluorescence microscopy was then used to potentially obtain visual indications of differences in the order of addition, since no changes in viability were observed. Microscopy was performed again on both HeLa and U251 cell lines to ensure the results were robust. As shown in Figure 49 and 50, no obvious effects due to differences in the order of addition were observed at any nanoparticle concentration or in either cell line, corroborating the viability results.

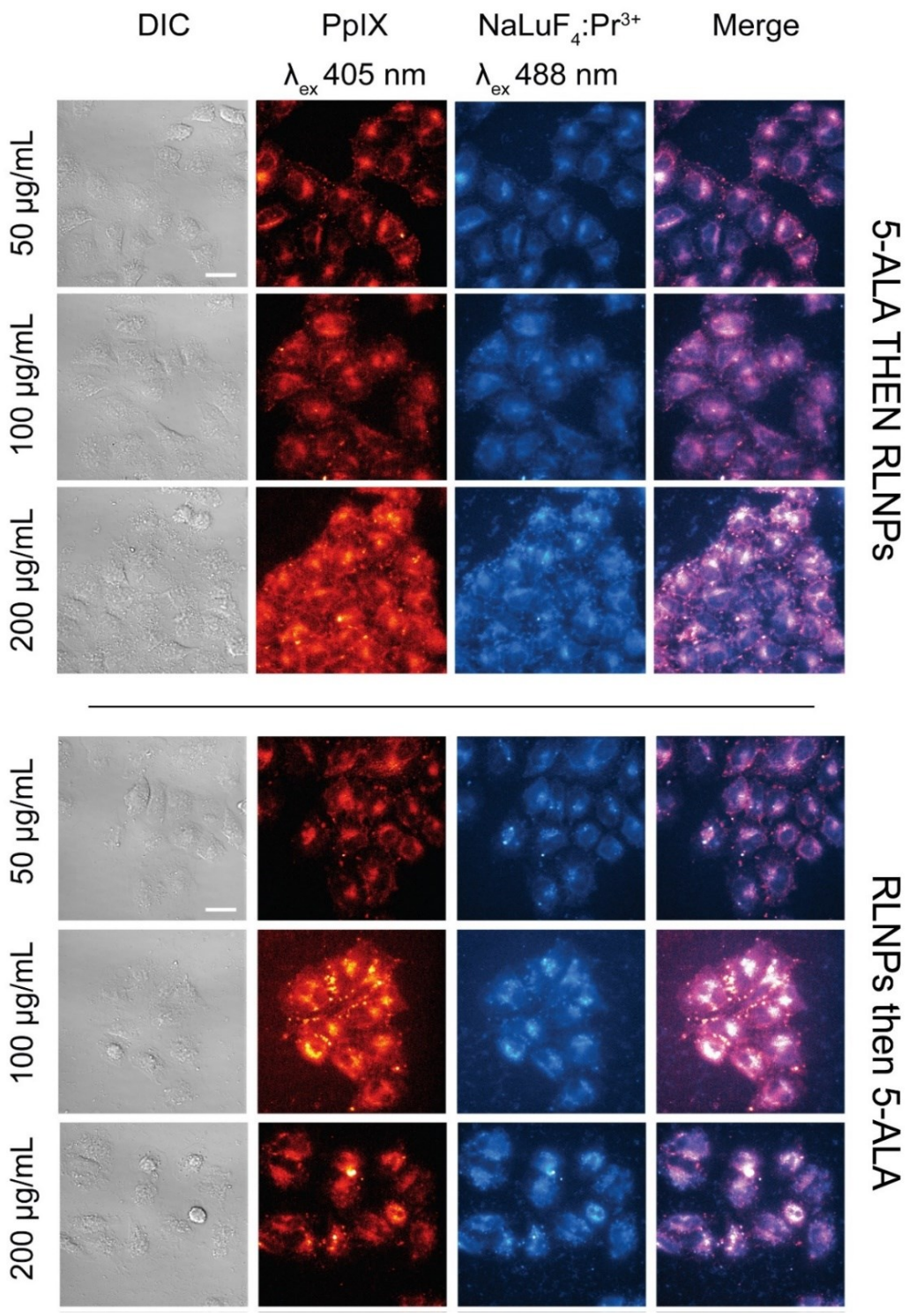

Figure 48. Fluorescence microscopy of HeLa cells upon administration of 5-ALA and 50, 100, or 200 µg/mL RLNPs. The top panel corresponds to the addition of 5-ALA then RLNPs, the bottom corresponds to the addition of RLNPs then 5-ALA. From left to right the columns represent differential imaging contrast (DIC) images, excitation with 405 nm light, excitation with 488 nm light, and the merged image. Scale bar is 20 µm.

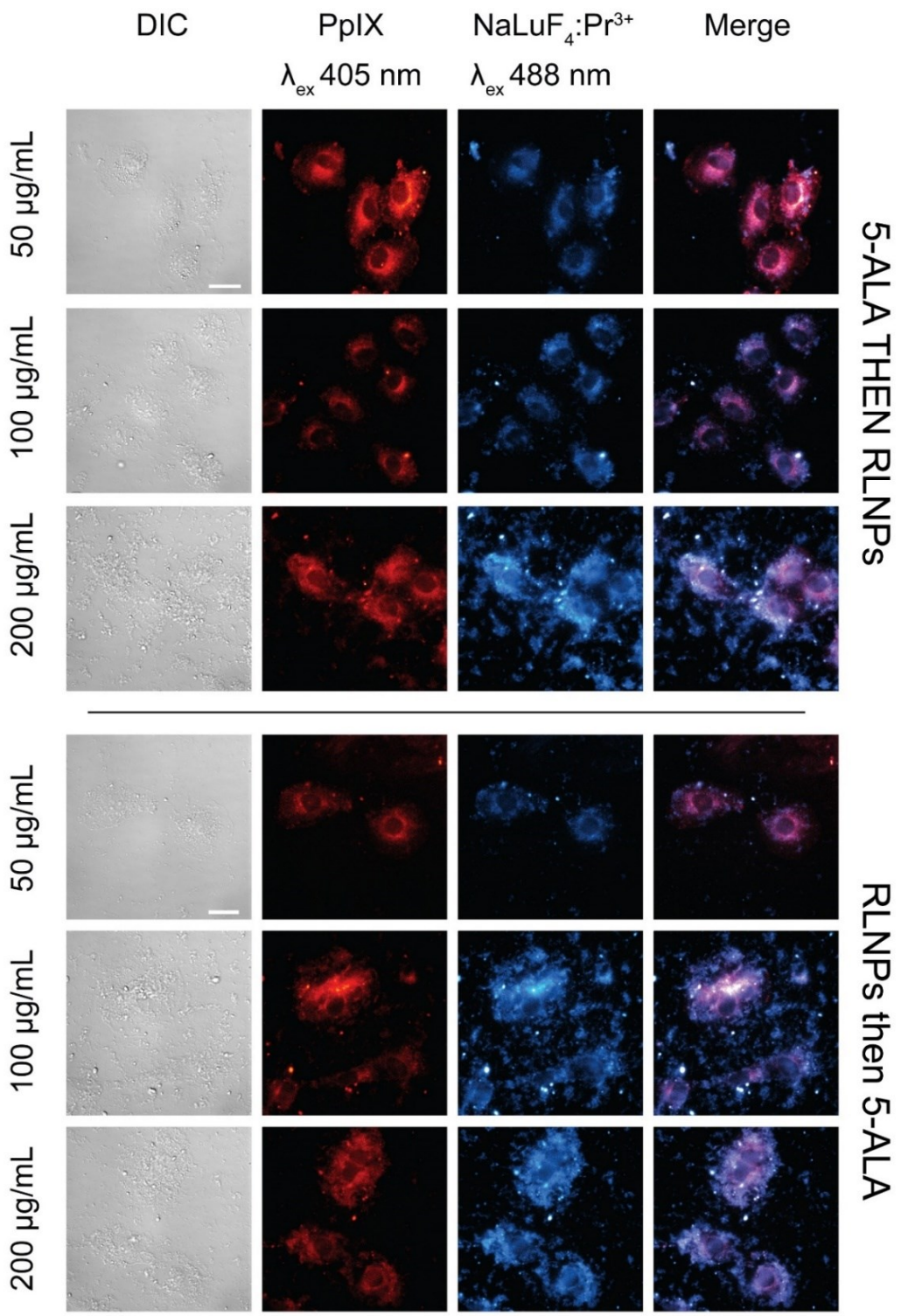

Figure 49. Fluorescence microscopy of U251 cells upon administration of 5-ALA and 50, 100, or 200 µg/mL RLNPs. The top panel corresponds to the addition of 5-ALA then RLNPs, the bottom corresponds to the addition of RLNPs then 5-ALA. From left to right the columns represent differential imaging contrast (DIC) images, excitation with 405 nm light, excitation with 488 nm light, and the merged image. Scale bar is 20 µm.

8.4.3. Quantification of RLNP-cell interactions

To further independently ensure incubation with 5-ALA did not affect nanoparticle-cell interaction and vice-versa, we performed ICP-MS to quantify the association of nanoparticles with cells in the presence and absence of 5-ALA incubation at 50, 100 and 200 µg/mL RLNP concentrations (Figure 51). It is imperative that the number of nanoparticles per cell is the same in the presence and absence of 5-ALA incubation, as this makes it possible to study the effect of the nanoparticles as radiosensitizing agents their own. Ultimately, this allows us to determine the contribution of the PDT effect to the treatment and the contribution of the nanoparticles to the treatment.

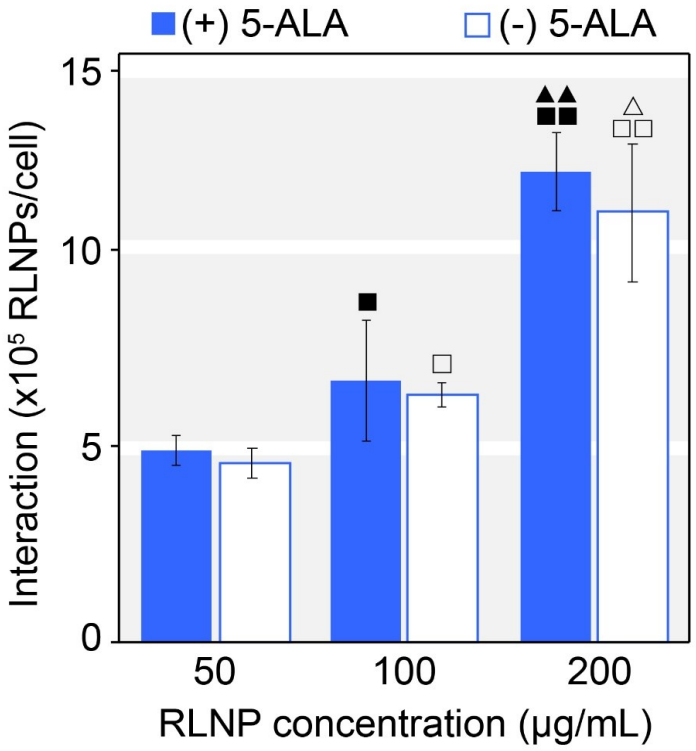

Figure 50. Nanoparticle-cell interactions quantified by ICP-MS for nanoparticle concentrations of 50, 100 and 200 µg/mL in the absence (blue filled bars) and presence (outlined blue bars) of 5-ALA. Error bars represent the standard deviation. Statistical significance was determined using one-way ANOVA for the significance relative to the untreated control, and Students t-test was used to evaluate signficance with and without 5-ALA within the same nanoparticle concentration (one symbol corresponds to $p < 0.05$, two symbols correspond to $p < 0.01$). Square symbols (■) represent significance relative to cells treated with 50 µg/mL RLNPs. Triangles (▲) represent significance relative to cells treated with 100 µg/mL RLNPs. Filled and outlined symbols correspond to the incubation without and with 5-ALA, respectively.

As shown in Figure 51, the number of RLNP interactions per cell increased in a statistically significant fashion as a function of concentration, and no statistically significant differences in RLNP-cell interactions were found with and without 5-ALA. Importantly, though the cells were rinsed thoroughly prior to harvesting for analysis, which removes any nanoparticles that were not strongly interacting with the cells, we cannot describe the results herein as the degree of RLNP uptake. Cells which are associated with the membrane but not yet internalized would be retained during the rinsing procedure, thus some percentage of the nanoparticle-cell interactions are due to nanoparticles that were not yet uptaken by the cell. Nonetheless, nanoparticles that are associated with the cell membrane can still elicit direct damage to the membrane *via* lipid oxidation (see section 3.2.3).[466]

Since the order of addition did not have any consequences in favor of either method, we chose to use the order that made the most sense in the context of a clinical workflow. Logistically, when considering the intraoperative scenario, it makes far more sense to treat with 5-ALA first, then resect the tumor and treat with nanoparticles for one hour prior to performing IORT. This was the paramount reason that the 5-ALA-then-RLNP workflow was chosen for further study. All studies after this were performed using the 4 hour 5-ALA incubation followed by 1 hour of RLNP incubation method.

8.5. *In vitro* reactive oxygen species formation

Prior to evaluating the X-PDT response, it was imperative to confirm the generation of reactive oxygen species (ROS) was occurring. ROS generation is an essential component of both radiotherapy and PDT.[257,283,467] In the case of radiotherapy, DNA is the primary target of ROS, while in PDT, the oxidative stress to multiple cellular targets forms the basis for treatment. Thus, both types of ROS (types I and II, as discussed in Section 3.5.2) are useful and there is no preference in X-PDT for the formation of one over the other. *In vitro* ROS production assays are most commonly performed using 2',7'-dichlorodihydrofluorescein diacetate (DCFH-DA), which detects both type I and type II ROS in cells, as shown in Figure 52A. The DCHF-DA assay was performed for RLNP only and RLNP/5-ALA treated cells using multiple radiation doses from 2 to 20 Gy (Figure 52B). We studied this range because 2 Gy is the established radiation dose used in fractionated EBRT, while 20 Gy is the most common dose used for single-shot IORT of

glioblastoma (see Section 3.3.2 or Appendix 3 for more information).[236,237,239,468]

DCF fluorescence was normalized to the signal obtained in control samples treated with 5-ALA, RLNPs or RLNPs/5-ALA but no X-ray irradiation. As expected, ROS were generated across all radiation doses for all conditions tested, and increased in a dose-dependent fashion. ROS were detected in cells treated with X-rays alone for all radiation doses, which is attributed to the detection of the radiolysis products of water. 5-ALA treated cells also exhibited some ROS production; PPIX is a known weak radiosensitizer, thus it is expected that elevated levels of ROS are produced (relative to X-rays only) after 5-ALA treatment.[458,469] RLNPs alone (no 5-ALA) induced significantly elevated levels of ROS, confirming the nanoparticles are able to act as radiosensitizers in the absence of 5-ALA. This was encouraging, as it establishes a preliminary basis that a therapeutic effect can be induced *via* dose enhancement as described by Bulin.[263] Finally, as expected, the combination of 5-ALA and RLNPs induced the highest levels of ROS

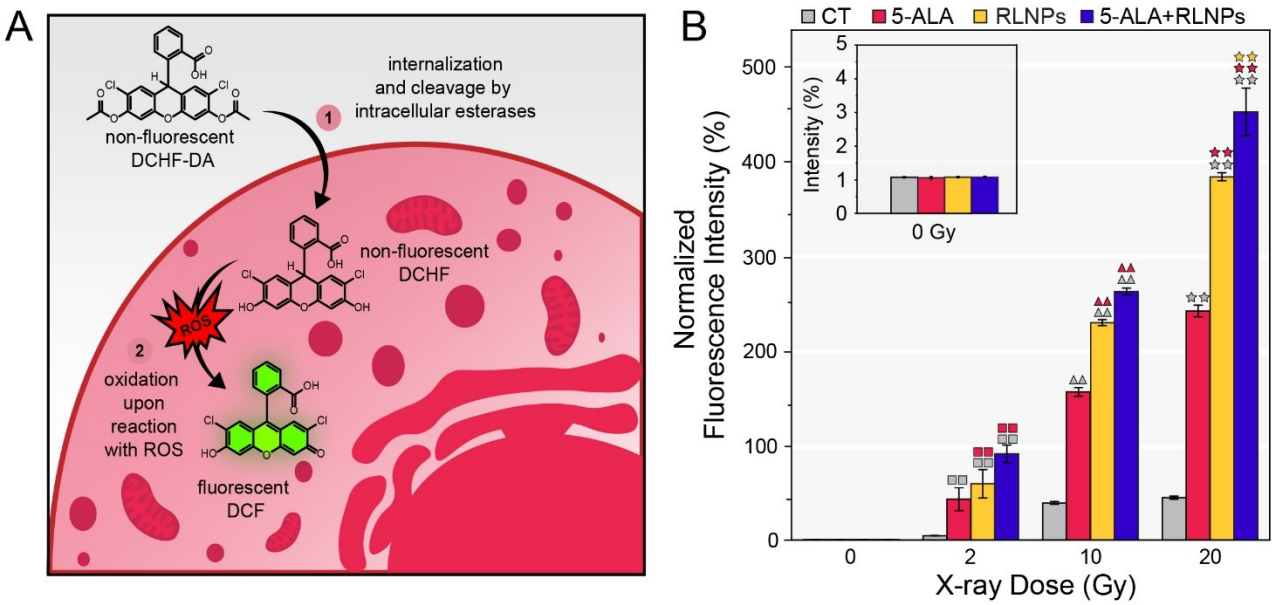

Figure 51. A) Schematic of the DCHF-DA assay mechanism. B) DCHF-DA assay of U251 cells treated with 100 µg/mL RLNPs with and without 5-ALA and 0, 2, 10 or 20 Gy of X-rays. DCF fluorescence intensity is normalized to the unirradiated control for each scenario. Gray: no RLNPs, no 5-ALA, red: 5-ALA only, yellow: RLNPs only, and blue RLNPs and 5-ALA. Statistical significance was tested using the Student's t-test (two symbols indicate $p < 0.01$). Symbols represent comparisons relative to unirradiated controls for each treatment at each radiation dose, where (■) is 2 Gy, (▲) is 10 Gy and (★) is 20 Gy.

formation and was significantly higher than treatment with RLNPs alone at each radiation dose studied.

Notably, the effects are not additive; the DCF intensity exhibited upon treatment with 5-ALA and RLNPs is not greater than the sum of the intensities of RLNPs or 5-ALA alone. This is because the attenuation of ionizing radiation in the cells changes substantially in the presence of the nanoparticles in comparison to the scenario of PPIX alone. Since PPIX has a substantially lower Z_{eff} than the RLNPs (4.82 vs. 34.52, respectively (spectrum-weighted for INTRABEAM® 50 kVp)) there is a much higher probability for RLNPs to attenuate and/or scatter incoming radiation. As mentioned in Section 3.4, this is the basis of the radiation dose enhancement effect. Additionally, it is likely that the RLNPs and PPIX produce different proportions of the different types of ROS. RLNPs will induce the formation of hydroxyl radicals *via* the interaction of ejected secondary electrons with water, but won't produce $^1O_2$ directly, whereas PPIX can produce $^1O_2$ in addition to other ROS. Together, these factors may account for the differences in observed ROS production. Regardless, more ROS were clearly produced when RLNPs were introduced, and thus a potential therapeutic effect could be studied.

8.6. Short-term *in vitro* studies

After determining the optimal treatment parameters and workflow and confirming the system produces ROS, we moved on to studying the therapeutic outcome 24 hours post-treatment. We studied three RLNP concentrations (50, 100 and 200 μg/mL) in the presence and absence of 5-ALA at four different radiation doses (2, 5, 10 and 20 Gy). As mentioned previously, this range of radiation doses has clinical relevance for both fractionated and intraoperative radiotherapy.

Ionizing radiation was administered to the cells using an X-ray source with similar properties to the source used in IORT of glioblastoma, the Zeiss INTRABEAM®. Specifically, cells were irradiated with an X-ray source that had a gold target, an unfiltered and uncollimated beam, operating at 50 kVp and 80 μA. The beam was positioned such that a dose rate of 0.6 Gy/min was delivered to the cells. The INTRABEAM® also has a gold target and operates at 50 kVp, usually at dose rates of 0.45 Gy/min to 2 Gy/min as mentioned in Section 3.3.2.[9,244,468,470] The output spectrum of the X-ray source used herein can be found in Appendix 6. As will be discussed in Section 8.9, the therapeutic response to ionizing radiation is often not linear, thus studying a

wide range of radiation doses provides good insight into how the treatment response unfolds. Moreover, by evaluating each radiation dose with different nanoparticle concentrations, we are able to understand more about the relationship between radiation dose and nanoparticle concentration. We postulate there is likely not a one-size-fits-all approach to X-PDT, especially in an organ as delicate as the brain. For example, if a tumor is located close to a particularly eloquent region of the brain, it may be beneficial to introduce a higher concentration of nanoparticles but use a lower radiation dose to salvage the nearby healthy tissue. Contrarily, there may be a dose-response scenario in which a lower concentration of nanoparticles can be used to elicit a localized PDT effect for a smaller resection site that could handle higher radiation doses.

8.6.1. Cell viability

Cell viability was assessed 24 hours post-treatment for all combinations, as shown in Figure 53. Control groups receiving only X-rays or X-rays and 5-ALA exhibited only small decreases in viability after 24 hours, even with a 20 Gy radiation dose. Thus, radiotherapy alone and with 5-ALA was not sufficient to cause acute cell death, in line with the expected radioresistant nature of the U251 cell line (see Section 3.1.2). Specifically, here acute cell death refers to necrosis, or a rapid induction of apoptosis. After 24 hours, cells will have only undergone one round of mitosis, at most. Thus, death *via* mitotic catastrophe would not be included in this timepoint, nor would death after prolonged cell cycle arrest (see Appendix 2). For the control groups, a statistically significant difference with and without 5-ALA treatment was only observed upon 2 Gy irradiation, presumably because the viabilities at 2 Gy exceeded 100%. Viabilities are ascertained through metabolic activity assays, thus a value above 100% represents increased metabolic activity relative to untreated cells. Presumably, the increased activity is due to cell stress, which was likely sub-lethal, given the high degree of radioresistance of glioblastoma cells[471], and the lack of death even up to 20 Gy. As mentioned in Section 8.7, this may also be indicative of the induction of cellular senescence.

While there was a trend of decreasing viability with increasing radiation dose, few statistically significant differences were observed relative to control groups receiving radiation only, except for at 20 Gy. Additionally, there were few statistically significant differences between outcomes with and without 5-ALA treatment. Thus, at this timepoint, it was not possible to

determine if the combination of nanoparticles and 5-ALA for the X-PDT effect provided a better outcome than the radiosensitization effect from the nanoparticles alone, but it was clear that there was a trend in which the nanoparticle treatments provided a better outcome than X-rays alone at

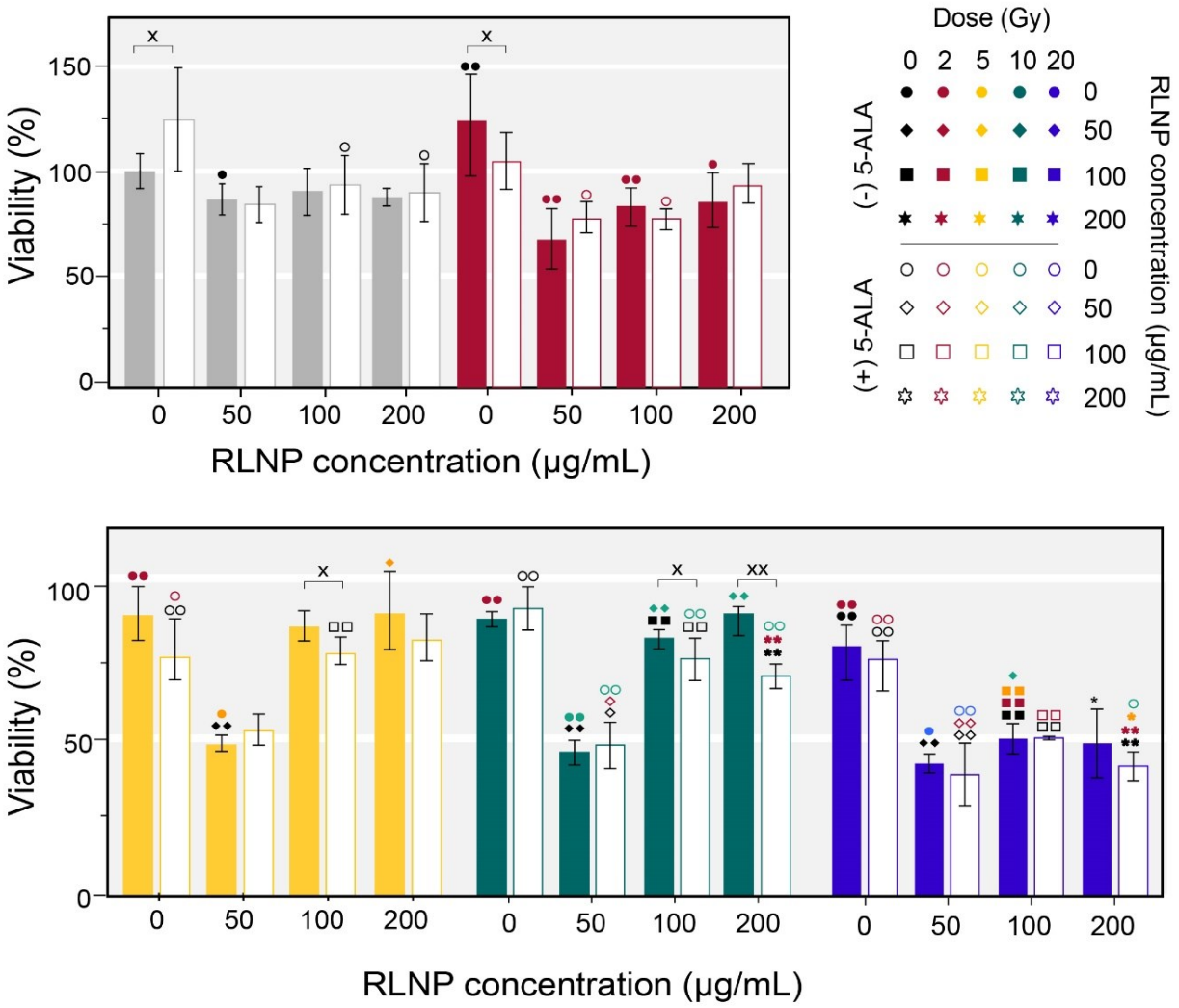

Figure 52. Viability assays of U251 cells 24 hours post-treatment with 50, 100, or 200 µg/mL $NaLuF_4:Pr^{3+}$ RLNPs without (filled) and with (outlined) 5-ALA incubation and irradiation with 0 (gray), 2 (red), 5 (yellow), 10 (green), or 20 (blue) Gy irradiation. Statistical significance was evaluated by one-way ANOVA or Student's t-test (one symbol corresponds to $p < 0.05$, two symbols correspond to $p < 0.01$). Circles correspond to significance relative to controls receiving 0 µg/mL RLNPs, 0 Gy, diamonds to 50 µg/mL RLNPs, squares to 100 µg/mL RLNPs, and stars to 200 µg/mL RLNPs. X represents statistical significance between with and without 5-ALA treatment. Filled symbols correspond to significance relative to the controls without 5-ALA treatment, outlined symbols to controls treated with 5-ALA.

each radiation dose, and that viability was reduced with increasing radiation dose.

Notably, several reports indicate that despite their ubiquity in *in vitro* cancer treatment research, viability assays are likely sub-optimal for assessing the efficacy of PDT, as well as for assessing treatments involving ionizing radiation.[297,472,473] Since viability assays provide only a small window of insight into the effects of a therapy, we undertook more in-depth investigations at the cellular level to ascertain the cell response to the treatment. This was done again at 24 hours post-treatment through fluorescence activated cell sorting (FACS) analysis and Western blot analyses, for all of the treatments under the two highest radiation doses (10 and 20 Gy).

8.6.2. Fluorescence activated cell sorting analysis

FACS is an analytical technique that takes advantage of microfluidic technology to facilitate single cell analysis. In this case, we used FACS to distinguish between live, dead, early and late apoptotic and necrotic cell populations. A discussion on the types of cell death can be found in Appendix 2. Cells were stained with fluorescent probes that allow for differentiation of these populations. Namely, propidium iodide was used to stain necrotic cells, and annexin V-fluorescein isothiocyanate (FITC) was used to stain apoptotic populations. Propidium iodide (PI) is a molecule that becomes highly fluorescent upon intercalation of DNA.[474] Since necrotic cells are characterized by a permeable membrane and DNA fragmentation, PI is able to infiltrate necrotic cells and bind to cytoplasmic and nuclear DNA, thus labelling the cell as necrotic. Annexin V is a molecule which is able to bind to phosphatidylserine, which normally exists in the inner leaflet of the cell membrane.[475,476] When cells initiate apoptosis, the cell membrane rearranges and phosphatidylserine is translocated to the outer leaflet where annexin V can then bind to it, labelling the cell as apoptotic.[475] A fluorescent molecule such as fluorescein isothiocyanate FITC is typically conjugated to Annexin V to endow it with fluorescent properties, as was the case here. Importantly, in later stages of apoptosis, the cell membrane becomes permeable; thus, PI can stain these cells as well. A similar scenario exists for necrotic cells, as the permeable membrane allows for annexin V to bind to phosphatidylserine on the inner leaflet even though the cell is not apoptotic. Thus, annexin V/PI staining is only able to differentiate between cells which are viable (annexin V negative, PI negative), in the early stages of apoptosis (annexin V positive, PI negative), necrotic and/or late-apoptotic (annexin V positive, PI positive), and dead

(annexin V negative, PI positive – this scenario typically is not observed). Each of these populations is observed as a quadrant in a FACS flow cytogram, as shown in Figure 54.

Cytograms were obtained for all treatment scenarios at 100 μg/mL RLNPs with and without 5-ALA treatment at 0, 10 and 20 Gy radiation doses. 100 μg/mL was chosen as the RLNP concentration for further study because it was the middle concentration studied, and it showed statistically significant differences with and without 5-ALA in some of the viability assays (Figure 54). Forward and side scattering was observed for all populations treated with 10 and 20 Gy relative to their counterparts that did not receive any radiation. Higher levels of forward and side scattering (ie. a higher percentage of apoptotic and necrotic cells) were observed for cells treated with RLNPs only, and even more so for cells treated with RLNPs and 5-ALA. In fact, statistically significant differences were observed during FACS analyses that could not be obtained *via* the viability assays (Figure 55). A significant loss in viable cells was observed in the presence of RLNPs with and without 5-ALA treatment for all radiation doses, which confirms that the high metabolic activities observed in the viability assays (Section 8.4.1) do not provide the full picture. However, in agreement with the viability assays, there were still high percentages of live cells for all treatment scenarios. Moreover the small percentage of cells in the early stages of apoptosis for all treatments clearly shows the cells are either resistant to radiation and surviving the treatment, or they are potentially prone to a different type of death besides apoptosis or necrosis (see Appendix 2). U251 cells are known to have mutations in p16, p21, pTEN and p53 genes all of which play a role in the response to ionizing radiation.[176,208,477,478] Of major importance, p53 is a crucial regulator of apoptosis[208]; thus the lack of apoptosis initiation is not unexpected, but does not rule out a favorable outcome based on a different cell death mechanism.

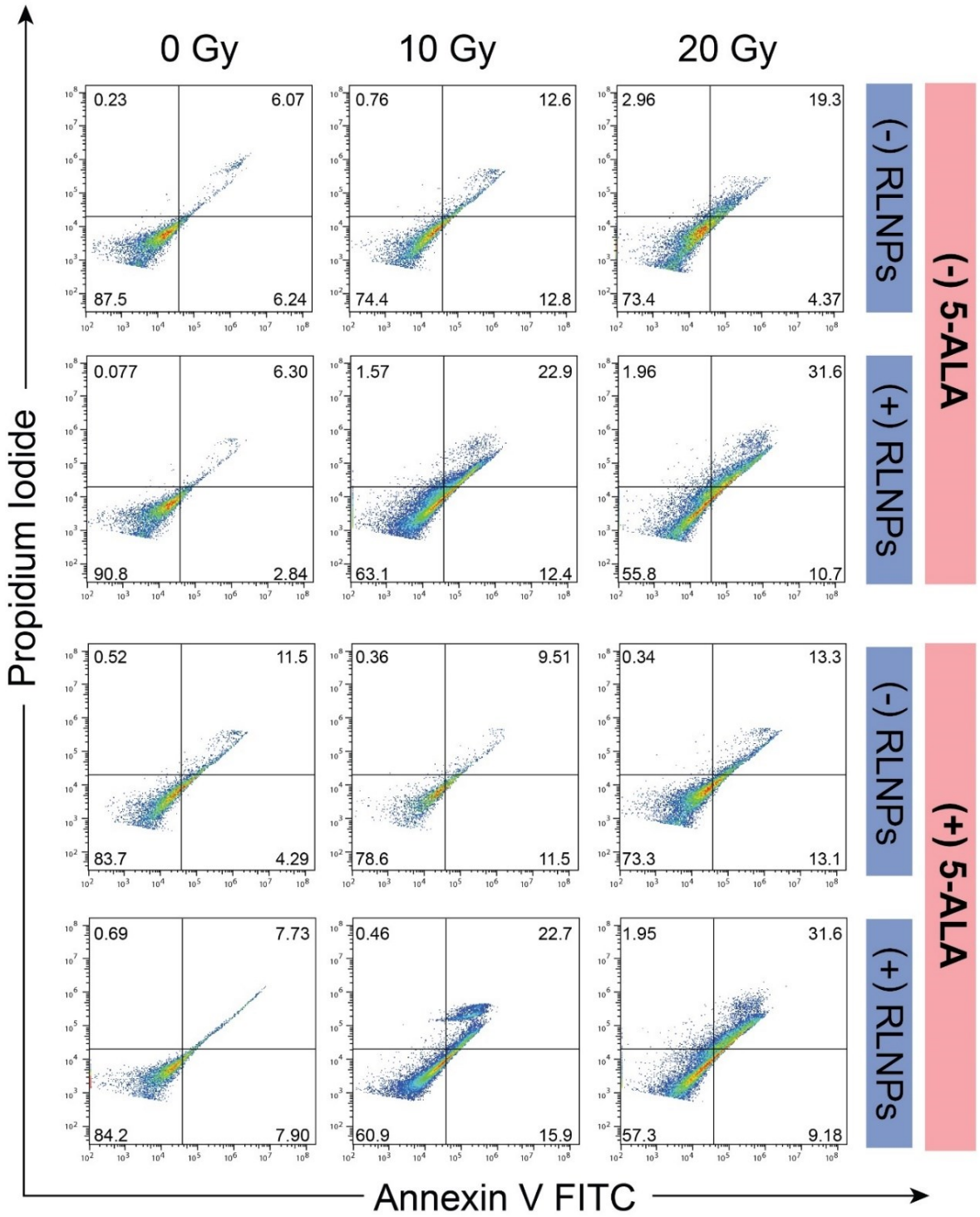

Figure 53. FACS cytograms of cells 24 hours post-treatment stained with Annexin V FITC (AxV) and propidium iodide (PI). Cells were treated with 0 or 100 µg/mL RLNPs with or without 5-ALA, and with or without 10 or 20 Gy of X-ray radiation. Bottom left quadrant represents live cells (-/- AxV/PI), bottom right early apoptotic cells (+/- AxV/PI), top right late apoptotic and necrotic cells (+/+ AxV/PI), top left dead cells (-/+ AxV/PI).

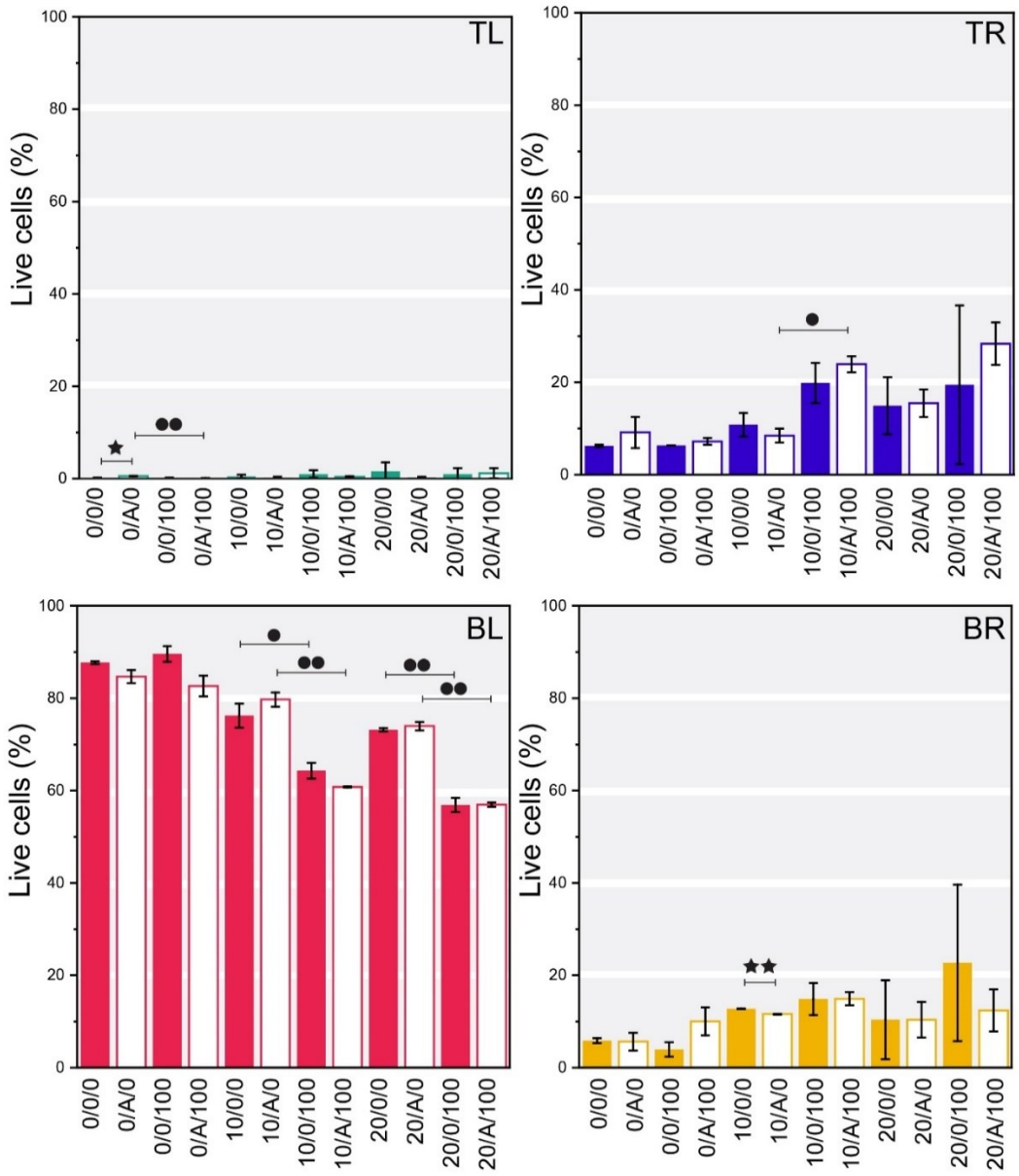

Figure 54. Statistical analysis of the FACS cytogram depicted in Figure 54 above. Statistical significance was determined using Student's t-test (one symbol = $p < 0.05$, two symbols = $p < 0.01$). Stars represent statistical significance with and without 5-ALA treatment, circles represent statistical significance with and without RLNPs. Bottom left (BL) represents annexin/PI -/- (live), BR represents early apoptotic (+/-), top right (TR) (+/+) late apoptotic and necrotic, and TL represents dead cells (-/+). Labels correspond to radiation dose/5-ALA/RLNP concentration (ex. 0/0/0 represents 0 Gy, no 5-ALA, no RLNPs).

8.7. Western Blot assays

As mentioned previously, we wanted to obtain a more complete picture of the treatment outcomes beyond simple metabolic activity assays. This prompted us to collaborate with Ursula Stochaj in the Department of Physiology at McGill University to investigate intracellular biomarkers related to cell stress, damage, death and senescence at this timepoint to try and gain a better understanding of the cellular response to the treatments. Specifically, we evaluated nine proteins through Western blotting: γH2AX, PARP1, cleaved lamin A, p53, Nrf2, NfκB, lamin B, Grp78 and Grp94 levels were studied 24 hours after cells were treated with 0 or 100 μg/mL RLNPs with or without 5-ALA and 0, 10, 20 Gy X-rays (Figure 56). The protein levels expressed by the cells at the 24 hour timepoint will provide a better understanding of how the cells reacted to the treatments, as well as potentially give insight into the outcomes that may be observed at later timepoints.

As discussed in Section 3.2.3, DNA damage is the main outcome of the interaction of ionizing radiation with cells.[208] Some of the proteins involved in the DNA damage response pathway can thus be used to determine if DNA damage occurred in the cells (Section 3.2.32). γH2AX is a protein at the center of the DNA damage response, and is expressed in response to DNA double strand breaks. Indeed, γH2AX expression was elevated for all samples which received treatment with ionizing radiation. Elevated γH2AX levels were also observed in cells treated with RLNPs in the absence of radiation. This is unexpected and difficult to understand, as RLNP localization in the nucleus was not observed *via* microscopy (Figure 46), and it is unlikely that the RLNPs cause DNA DSBs in the absence of irradiation, from outside of the nucleus. Additional studies should be carried out to determine the cause of this result, as other proteins that act as stress markers, such as p53, were not found at elevated levels for the RLNP treated controls. Instead, we postulate that the increase in γH2AX may be due to the increase in sodium ion content of the cells upon administration of the Na^+-containing RLNPs. This has been demonstrated to cause elevated γH2AX levels in other instances, where DSBs were not observed.[479,480]

While all irradiated groups exhibited higher γH2AX levels, RLNP-treated cells did not express significantly higher levels relative to the irradiated control cells (no RLNPs, 10 or 20 Gy X-rays, with and without 5-ALA). γH2AX is expressed within minutes after double strand breaks

occur[481], and repair of the strand breaks can occur on the scale of a few hours.[208] Thus, it is likely that after 24 hours, many of the double strand breaks had been repaired and significant differences could not be detected from this method. This is expected for radioresistant lines like U251, which are able to bypass apoptosis and initiate DNA repair despite high degrees of damage. Additionally, as mentioned in Section 3.4.2.1, the types of cluster damage induced by low energy X-rays and Auger electrons may not give rise to double strand breaks, but are still highly lethal. Alternatively, the apoptosis cascade may have been initiated in cells with large numbers of strand breaks that would've had the highest γH2AX levels, and those cells may have already died and were lost prior to the analysis at 24 hours. This is important to consider, as the Western blot analysis only provides insight into the cells that remained alive at 24 hours. Future studies may aim to evaluate γH2AX levels as a function of time after irradiation for these treatments to confirm these hypotheses. Nonetheless, the elevated γH2AX levels (relative to the unirradiated, untreated control samples) suggest that the cells sustained radiation damage that persisted 24 hours post-treatment.

The tumor suppressor protein p53 is involved in a wide variety of signalling pathways involved in cell stress responses, the DNA damage response, apoptosis activation, and senescence, among others (see 3.2.3.2 for additional details of the role of p53).[208,219,482,483] U251 cells have a mutation present in the gene encoding p53, resulting in the production of a mutant version of the protein, as mentioned in Section 3.1.2. This mutant p53 has additional pro-cancer functions, thus high levels of it are associated with a poor prognosis.[183,484,485183] Herein, the mutant p53 levels were found to be variable for the treatment conditions, though cells receiving X-ray irradiation with RLNPs (with and without 5-ALA) did exhibit reduced mutant p53 levels relative to the control groups. The reduction in mutant p53 expression suggests that treatment with the RLNPs and the RLNP/5-ALA combination may facilitate improved therapeutic outcomes by preventing the negative effects associated with high levels of this protein.

8.7.1. The Unfolded Protein Response

The Unfolded Protein Response (UPR) is a pro-survival mechanism that maintains homeostasis in the endoplasmic reticulum.[486] The UPR is activated in response to endoplasmic reticulum stress, and is often continually activated in cancer cells, including glioblastoma cells, which contributes to their ability to survive and resist treatment.[486] As described in Appendix 2,

autophagy may be initiated in response to changes in the UPR. NFκB, Nrf2, Grp78, and Grp 94 are all associated with the UPR, and with ionizing-radiation induced autophagy. As such, we studied the changes in these four proteins.

With regard to oxidative damage, which is especially relevant in PDT, we studied the expression of Nrf2. A reduction in Nrf2 levels was observed for all RLNP-treated cells relative to untreated controls, with and without irradiation. Nrf2 is a protein that is responsible for regulating oxidative stress in cells, and is typically inactive under healthy conditions; it only becomes active when ROS is detected in cells in order to neutralize them and keep the cells alive.[487] High levels of Nrf2 are therefore associated with cell repair, thereby contributing to the treatment-resistant nature of glioblastoma; this has been specifically proven in U251 cells.[487,488] As such, the reduction in Nrf2 levels observed upon treatment with the nanoparticles indicates that the cells should have a reduced ability to repair oxidative damage, thus the cells should be more prone to death by ROS production. NFκB is a protein complex that regulates gene transcription and mediates the cellular inflammation and immune responses.[217,218,485] Significant reductions in NFκB levels were observed for cells treated with RLNPs and RLNPs/5-ALA at both 10 and 20 Gy relative to the levels expressed by untreated, unirradiated controls. Abnormal activation of NFκB is known to play a role in radiation resistance of glioblastoma cells, and its inhibition was found to reduce cell invasion and promote long term toxicity in a study using U251 cells.[485] The reductions observed herein are indicative of a promising outcome from the RLNP/5-ALA treatment, though perhaps at a longer timescale than 24 hours, and potentially *via* routes other than apoptosis. In glioblastoma, glucose-related protein 78 (Grp78) is known to be upregulated in response to ionizing radiation, which results in increased radioresistance because Grp78 suppresses pro-apoptotic proteins.[486,489,490] Grp78 is involved in proteostasis, and signals for the degradation of misfolded proteins as part of the UPR.[490] Loss of Grp78 is associated with radiosensitization and an increase in the death of glioblastoma cells, since there is a reduced ability to suppress pro-apoptotic proteins, and misfolded ones are more likely to accumulate and cause cell death. Together, these results may indicate that the cells are prone to death *via* these routes, rather than through apoptosis. This may explain why the FACS data (Section 8.6) does not show indications of early apoptosis in a large proportion of the cells.

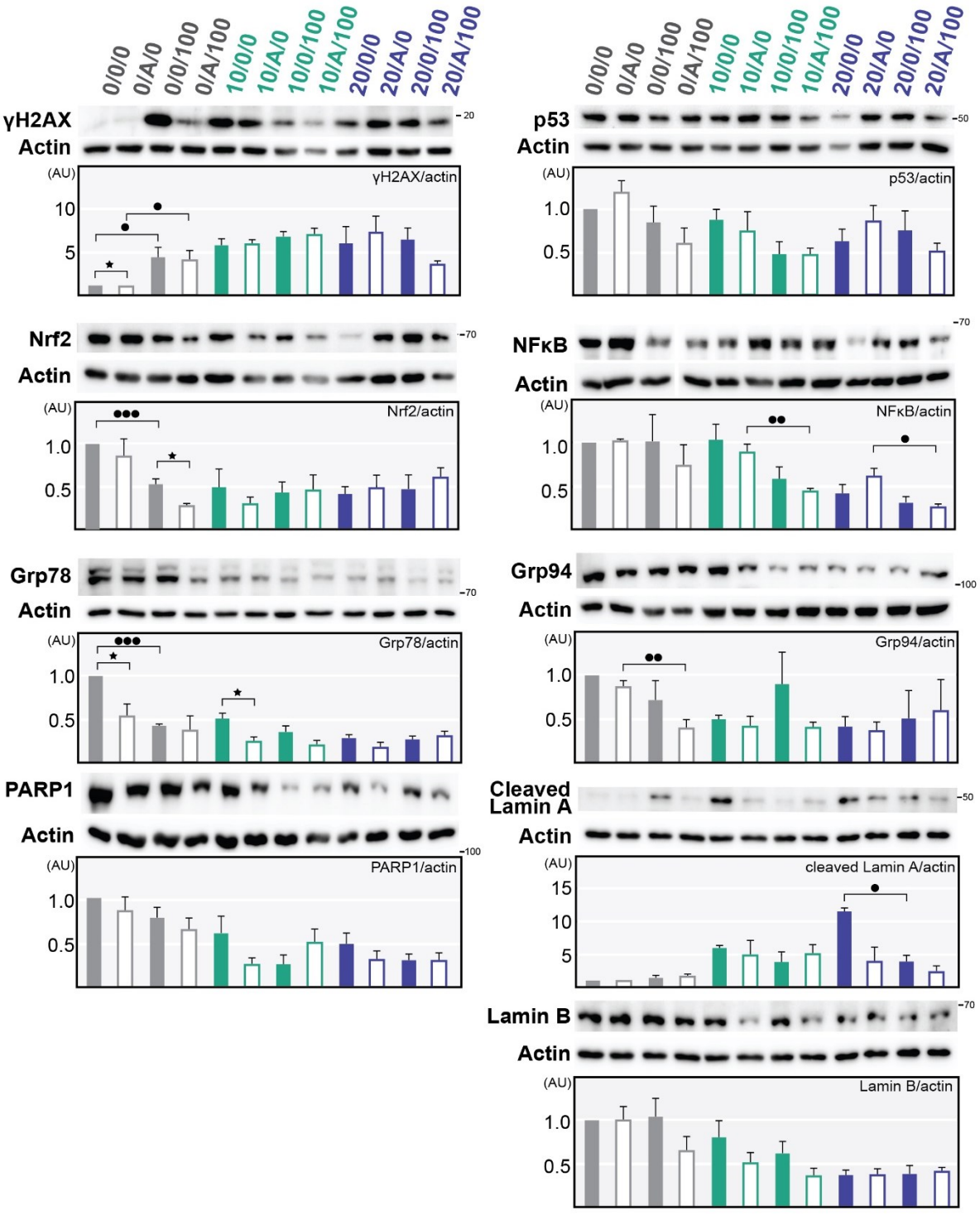

Figure 55. Western blot analysis of U251 cells 24 hours post treatment with 0 or 100 μg/mL $NaLuF_4:Pr^{3+}$ nanoparticles without (filled) and with (outlined) 5-ALA and 0 (gray), 10 (green) or 20 Gy (blue) X-ray irradiation. Significance assessed using one-way ANOVA across different radiation doses or Student's t-test within a single radiation dose (one symbol corresponds to $p < 0.05$, two symbols $p < 0.01$, three symbols $p < 0.005$). Labels for each lane are listed on top of the graphs and correspond to X-ray dose/5-ALA/RLNPs (ex. 20/0/100 = 20 Gy, no 5-ALA, 100 μg/mL). The signal for each protein was normalized to the actin signal for each condition.

In all cases, reductions in Grp78 were observed relative to the control group, with all 5-ALA treated cells showing reduced abundance relative to cells treated only with X-rays or with X-rays and RLNPs. Radiation-dose dependent reductions were also observed, including in cells treated only with X-rays. Usually, Grp78 levels increase in response to ionizing radiation. It is possible that similar to what was observed for γH2AX, the increase occurred immediately after irradiation and should be investigated at earlier timepoints in the future, or that the RLNPs and RLNPs/5-ALA treatments prevent Grp78 upregulation. Regardless, a reduction in Grp78 abundance is an encouraging outcome that suggests the cells may be succumbing to the RLNPs and RLNPs/5-ALA treatment.

Glucose related protein 94 (Grp94) is a heat shock protein that shares functions with Grp78 in the UPR pathway, but is significantly less investigated.[490,491] Of the comparatively little that is known about the role of Grp94 relative to Grp78, it has been established that Grp94 is overexpressed in glioblastoma, and higher Grp94 levels correlate with more aggressive disease and shorter overall patient survival.[490,492] Reduced Grp94 levels were observed for nearly all test groups receiving radiation, suggesting again that RLNP-treated cells should be more prone to death. Thus, all of the factors that are involved in the UPR pathway (NFκB, Nrf2, Grp78 and Grp94) displayed favorable changes in abundance that are suggestive of a response to the RLNP only and the RLNP/5-ALA treatments.

8.7.1.1. Markers for cell death and senescence

The implied outcomes of all of the biomarkers discussed above, along with the high cell viabilities and low percentage of apoptotic cells detected *via* FACS at 24 hours post-treatment prompted us to assess whether any apoptosis signalling pathways had been initiated at this timepoint. As mentioned in Appendix 2, apoptosis is the least inflammatory mode of cell death, and until recently was though to be the main type of programmed cell death. Apoptosis is initiated by the activation of caspases, which are proteins that orchestrate the programmed destruction of a cell.[208,493] Accordingly, we evaluated two markers of apoptosis that are targeted by different caspases: PARP1 loss, and lamin A cleavage. PARP1 is a protein that regulates DNA integrity, and is cleaved by caspase 3 and caspase 7 during apoptosis.[493] Lamin A is a structural protein of the nuclear envelope, and is cleaved by caspase 6.[493] If apoptosis is initiated, it is expected that

levels of PARP1 will decrease, concurrent with an increase in the abundance of cleaved lamin A. Since these events occur independently through activation of different caspases, it is expected that their profiles would not be identical.

The levels of PARP1 diminished considerably with the addition of RLNPs as a function of radiation dose, though significant differences with and without 5-ALA treatment were not detected. This may indicate that the added PDT effect stimulates other modes of cell death, in line with the different outcomes between RLNP only and RLNP/5-ALA treatments observed at later timepoints (Section 8.8-8.9). Corroborating these results, cleavage of lamin A was observed for irradiated cells, confirming that apoptosis had been initiated in some portion of the cells that appeared viable at 24 hours, and corroborating increase in proportion of cells at early and late-stage apoptosis as observed *via* FACS. Indeed, cell viability assays performed 48 hours post-treatment exhibited markedly reduced viabilities, as discussed in Section 8.8. As mentioned in Section 3.2.3.3, although the apoptosis execution process takes about 2 hours, it may take far longer for the execution process to be initiated, further explaining the observed viabilities at 24 hours.

In classic radiobiology, a cell is considered dead if it can no longer reproduce.[208] In other words, senescent cells, which are proliferatively arrested but metabolically active, are considered radiobiologically dead, in the same fashion as a cell that undergoes apoptosis or necrosis. A detailed discussion on senescence can be found in Appendix 2. Lamin B is a protein that contributes to the structural integrity of the nuclear envelope, and loss of this protein is a hallmark indicator of the senescent state.[494,495] Indeed, a decrease in lamin B was observed for all cells that received a combination of RLNPs and ionizing radiation, with a higher radiation dose corresponding to a greater loss in lamin B. This suggests senescence had been triggered in a portion of the cells, which also explains the high metabolic activities observed at 24 h post-treatment and lack of apoptosis observed in the FACS analyses. As mentioned before, senescent cells are alive but unable to reproduce, thus using these assays, they would potentially be regarded as alive/viable. Based on these results, and the changes in biomarkers associated with autophagy, it is likely that apoptosis is not the only mode of death triggered in response to the treatment developed here.

Cellular senescence is a common outcome of both chemotherapy and radiotherapy, and it

is currently still unclear whether or not it is desirable.[494,496] Notably, to our knowledge, this is the first X-PDT study to investigate senescence as a potential result. In the short term, senescence corresponds to prolonged progression-free survival, as senescent cells cannot contribute to tumor growth. Senescence is also accompanied by the secretion of pro-inflammatory factors, which are known to have deleterious effects and promote inflammation-related disease.[494,497,498] On the other hand, the secretion of pro-inflammatory factors can also stimulate an immune response, having an anti-tumorigenic effect; this is the basis of immunogenic cell death as described in Section 3.5.2.[498] U251 cells are predisposed to entering senescence rather than apoptosis.[181,499] The fate of glioblastoma cells toward senescence or apoptosis is known to be governed by their PTEN status, where PTEN deficient cells, such as U251[181,499], tend to favor senescence as a fate after exposure to ionizing radiation rather than apoptosis.[499]

Senescent cells are also known to increase in size[496], which was observed throughout the project for all experiments where cells received ionizing radiation. As an example, Figure 57 shows two sets of U251 cells: on the right are untreated cells, and on the left is a U251 cell 24 hours after treatment with 100 μg/mL RLNPs and irradiation with 5 Gy of X-rays under identical conditions to those used herein. Note that the image magnification and dimensions of the field of view are identical, illustrating the drastic change in size that occurs. Though the field of view only

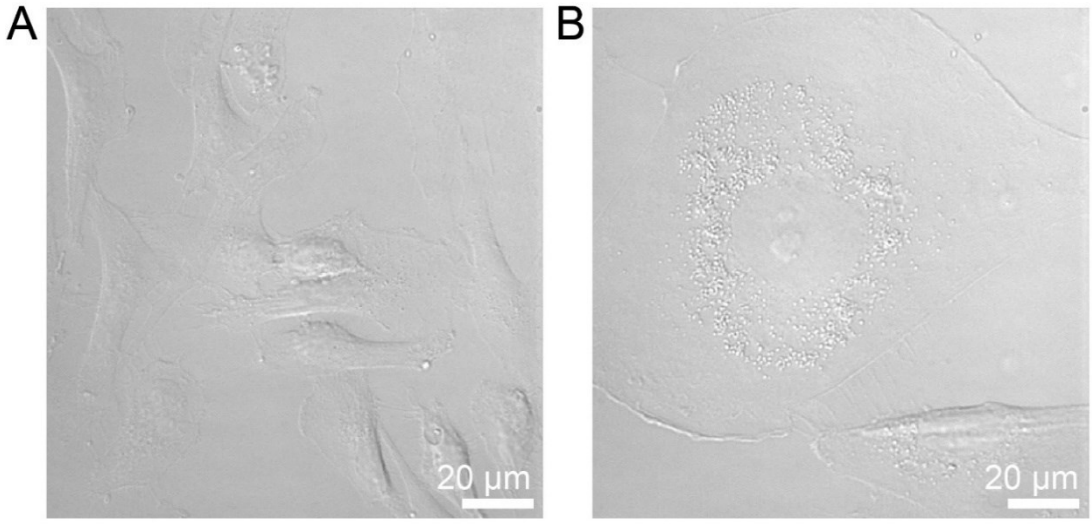

Figure 56. A) DIC microscopy images of fixed, untreated U251 cells. B) DIC images of fixed U251 cells treated with 100 μg/mL $NaLuF_4:Pr^{3+}$ RLNPs and 5 Gy of X-rays 24 hours post-treatment.

shows a single cell, the majority of the cells in the dishes exhibited this change in size; the effect was not anomalous and was highly reproducible. Together, the loss of lamin B and the increase in cell size confirm the induction of senescence in some of the treated cells.

In summary, we evaluated nine biomarkers that all suggest at 24 hours post-treatment the cells are prone to death or senescence. These results corroborate the cell viability assays and FACS analyses, and explain some of the results of those experiments. Moreover, these results confirm that it is difficult to determine the overall treatment outcomes after only 24 hours, especially with respect to the X-PDT effect versus radiosensitization (ie. with and without 5-ALA treatment). In all cases, however, the changes in the levels of these biomarkers suggest that a favorable therapeutic effect is taking place (ie. death or senescence). This prompted us to perform studies at longer timepoints, as discussed in the remainder of the chapter.

8.8. Viability assays 48 hours post-treatment

Damage induced by ionizing radiation may not manifest after a single round of cell division (ie. after 24 hours in U251 cells). Moreover, cell cycle arrest after ionizing radiation treatments may extend the cell division time (Appendix 2). Sub-lethal DNA damage may propagate through multiple rounds of cell division, until the accumulated mutations are so severe that mitosis cannot be completed, or a different type of cell death is initiated (ex. apoptosis, necroptosis, etc). This phenomenon is known as mitotic catastrophe, and is a common mechanism of cell death after treatment with ionizing radiation.[208] Since the protein expression levels observed by Western blotting indicated some proportion of the cell population was potentially near death, we evaluated viabilities at 48 hours post-treatment.

As shown in Figure 58, viabilities were reduced for control cells treated only with X-rays relative to the viabilities at 24 hours, however, even with a 20 Gy radiation dose, after 48 hours viability was only reduced to 73.4 ± 1.65 %, barely below the ISO standard for cytotoxicity, as previously discussed.[453] This further suggests that this radiation dose alone is not potent enough to eradicate the U251 cells, despite it being considered a sterilizing dose for other mammalian cell lines.[500] In contrast, all RLNP-treated populations exhibited large reductions in viability across all radiation doses, confirming a strong therapeutic effect *via* radiosensitization and X-PDT. Statistically significant differences between treatments with and without 5-ALA became more

apparent at the 48 hour timepoint as well (relative to the 24 hour one), where differences were found at 2 and 10 Gy, and for all RLNP treatments with 20 Gy radiation. This is a particularly important result, as it is common in the nanomedicine community to evaluate treatment outcomes using viability assays, only after 24 hours. As such, we hope these results encourage others to consider the effects of time in the event an immediate result is not observed. Notably, these differences become even more apparent when assessing proliferation.

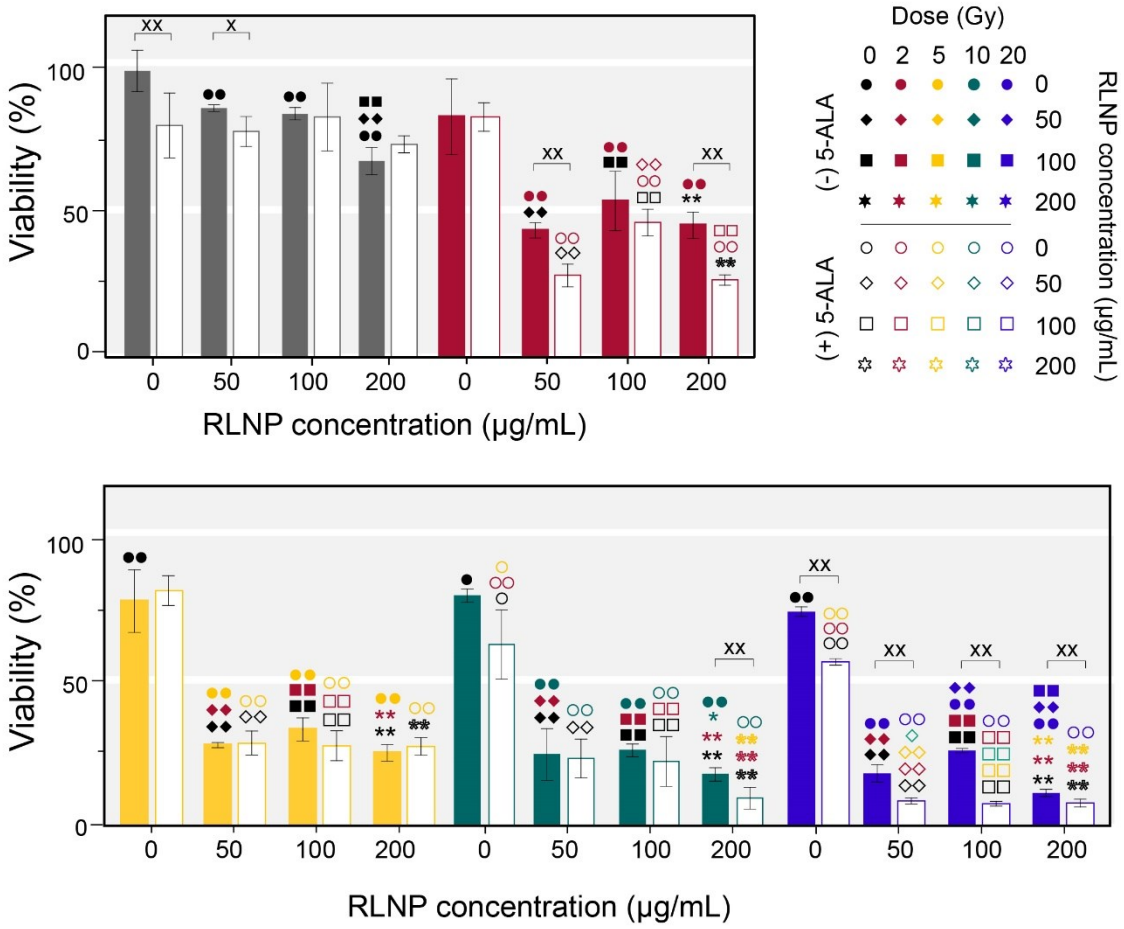

Figure 57. Viability assays of U251 cells 24 hours post-treatment with 50, 100, or 200 µg/mL $NaLuF_4:Pr^{3+}$ RLNPs with out (filled) and with (outlined) 5-ALA incubation and irradiation with 0 (gray), 2 (red), 5 (yellow), 10 (green), or 20 (blue) Gy irradiation. Statistical significance was evaluated by one-way ANOVA or Student's t-test (one symbol corresponds to $p < 0.05$, two symbols correspond to $p < 0.01$). Circles correspond to significance relative to controls receiving 0 µg/mL RLNPs, 0 Gy, diamonds to 50 µg/mL RLNPs, squares to 100 µg/mL RLNPs, and stars to 200 µg/mL RLNPs. X represents statistical significance between with and without 5-ALA treatment. Filled symbols correspond to significance relative to the controls without 5-ALA treatment, outlined symbols to controls treated with 5-ALA.

8.9. Clonogenic assays: assessing proliferation

The ultimate goal of radiotherapy in cancer is to prevent the proliferation of malignant cells. In other words, a treatment is considered successful if it results in the failure of cells to replicate, due to cell death or senescence as mentioned previously.[208] It can take multiple cycles of replication for the effects of ionizing radiation to manifest as replicative death. Thus, the gold-standard means of assessing the efficacy of radiotherapy *in vitro* is through assessing the proliferative capacity of cells after treatment.[208,266,362] Clonogenic assays are also encouraged for assessing the PDT effect, although this is a much less common practice.[297,501,502]

Proliferative capacity is assessed by observing the ability of a single cell to generate a colony of cells. This is known as a clonogenic (or colony-forming) assay. Essentially, before or after treatment, cells are seeded very sparsely (such that they are essentially single cells) in a dish and allowed to grow. Since the colony forms from a single cell, they are all effectively clones, thus the clonogenic assay evaluates clonogenicity, which is synonymous with proliferative capacity. Because mitotic catastrophe occurs within a few cycles of division, a cell is only considered reproductively viable if it is able to generate a colony of 50 cells or more, which requires at least 6 cycles of division to achieve.[208,209,362] If this is condition is satisfied, the treated cell is considered likely to be able to proliferate indefinitely, and therefore was not sufficiently damaged by the radiotherapy treatment. The more colonies that are able to form after treatment, the less successful the treatment is. Ideally, no colonies form and the treatment eradicated all of the cells.

There are several parameters that must be considered prior to performing the assay. The first is whether to adopt a pre-treatment or post-treatment plating technique. In our case, it was more feasible to use a post-treatment plating technique, in which a single dish of cells was treated and then counted and sparsely plated in dishes as described above. Within the post-treatment framework, there are the options for immediate and delayed plating.[503] Immediate plating is done immediately (hence the name) after treatment, while delayed plating is done some time after the treatment to give the cells time to die, or for potentially-lethal damage repair.[479] We used an immediate plating technique, as it includes all degrees of damage in the outcome. The next major consideration in the clonogenic assay is cooperative growth, in which the cells communicate with one another and stimulate proliferation; this can skew the results of the assay dramatically.[364] Not

all cell lines exhibit cooperative growth, thus we evaluated our cells for this before carrying out the remaining assays. To do so, untreated cells were seeded across a wide range of densities and left to grow until colonies of ≥ 50 cells were obtained. In the case of U251 cells, this was achieved after 7 days of incubation. A photograph of a sample well from a clonogenic assay is shown in Figure 59A; the blue spots correspond to colonies of cells stained with methylene blue. Importantly, not all spots correspond to countable colonies; only colonies of ≥ 50 cells where cells appear to be healthy (normal size and morphology) and colonies are not too diffuse or too dense can be counted.[362]

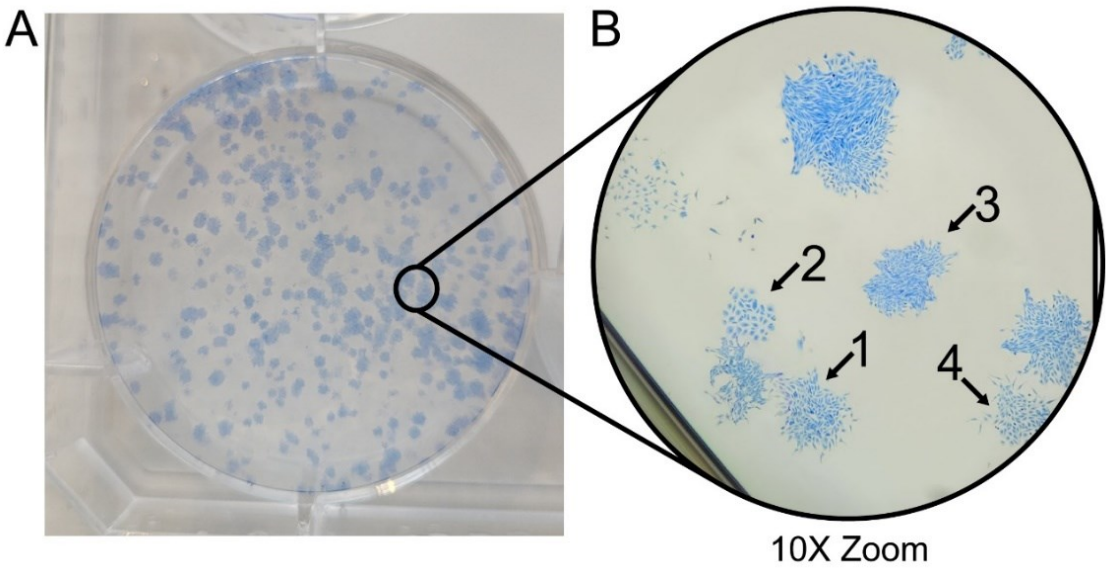

Figure 58. Photographs of a sample clonogenic assay. A) A photograph of an entire well of colonies stained with methylene blue, as seen with the naked eye. B) A photograph of the stained colonies as seen under a stereomicroscope (10X zoom) and corresponding examples of colonies that are healthy (1 and 3) or unhealthy (2 and 4).

A photograph of the sample from Figure 59A under a stereomicroscope is shown in Figure 59B, outlining examples of countable and non-countable colonies. The colony marked by arrows 1 and 3 contain ≥50 cells, all cells have a similar size and the colonies are roughly spherical with a reasonable density; thus they are healthy, countable colonies. Notably, the colony marked by arrow 2 is of a similar size as 1 and 3, but consists of large cells and there are less than 50 of them and thus are not counted; this underlines the importance of counting colonies under a microscope, as not all "blue dots" in the photograph in Figure 59A are countable colonies. Finally, the colony marked by arrow 4 also consists of ≥50 cells, but the cells are diffusely packed, of varying sizes

and morphologies and are growing irregularly; this is indicative of an unhealthy colony and is not counted toward the survival fraction. The survival fraction (SF) is the final metric that describes the treatment outcome, as discussed below.

Seeding densities and average plating efficiencies (PE) for a representative assay of untreated cells were obtained using equation 7 (Section 5.3.19) and are reported in Table 4. The plating efficiencies increased substantially with seeding density, confirming that cooperative growth was occurring in the presence and absence of 5-ALA treatment. This in agreement with the results obtained by Brix *et al.* where U251 was found to be one of the four brain cancer cell lines in their study to exhibit cellular cooperation.[363]

Because cellular cooperation can so strongly skew the results of a clonogenic assay, Brix *et al.* developed a power-regression based (PR) model that accounts for the effects of cellular cooperation to calculate a survival fraction.[362,363] To confirm this model was indeed appropriate for generating survival fractions from our data, we calculated survival fractions of cells irradiated with X-rays (no RLNP or 5-ALA treatments) using the plating efficiency (PE) method using equation 9 and using the PR model (Table 14).

$$\boldsymbol{SF = \frac{PE_{treated}}{PE_{control}}} \tag{9}$$

Indeed, the PE method yields almost nonsensical results with high uncertainties, while the PR method generates values that are in line with the expected results (higher radiation doses should give rise to lower survival fractions) and much smaller uncertainties. Thus, the PR method was used to calculate all survival fractions reported herein, as cooperative growth was observed for this cell line. Of importance, all survival data was generated using a minimum of four different cell seeding densities plated in triplicate, and each independent experiment was performed a minimum of 3 times. The use of multiple seeding densities is essential for providing the PR model with enough data to accurately account for cellular cooperation.[362,363]

Table 14. Representative survival fractions calculated with PE and PR based analyses for cells treated with 2, 5, 10 or 20 Gy.

Treatment condition	Survival fraction (%)	
	PE method	PR method
2 Gy	142.30 ± 55.3	86.82 ± 10.9
5 Gy	65.23 ± 17.9	69.79 ± 5.9
10 Gy	67.41 ± 15.6	48.88 ± 10.9
20 Gy	27.15 ± 6.8	16.61 ± 2.6

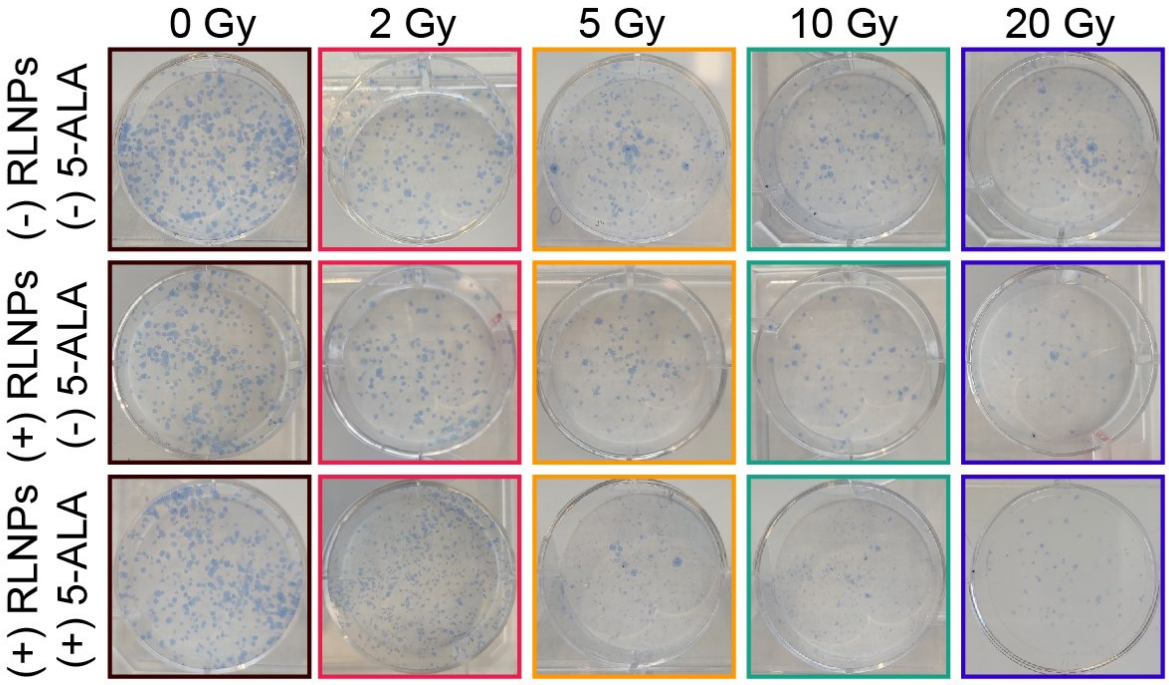

Figure 59. Photographs of sample clonogenic assays for U251 cells treated with 0 or 100 µg/mL RLNPs, with and without 5-ALA, irradiated with 0, 2, 5, 10 or 20 Gy of X-rays.

Clonogenic assays were performed for all treatment scenarios studied in the viability assays at 24 and 48 hours (50, 100 and 200 µg/mL; with and without 5-ALA; 0, 2, 5, 10 and 20 Gy). As mentioned in 3.2.3, we evaluated this range of radiation doses because of the relevance of 2 Gy in conventional fractionated RT and 20 Gy in IORT. Photographs of representative colonies of cells treated with 100 µg/mL RLNPs, with and without 5-ALA at each radiation dose are shown in Figure 60. Visual inspection of the colonies shows a clear loss in colony formation with increasing

radiation dose and when the RLNPs are used in conjunction with 5-ALA.

The survival fractions calculated for all control groups (0 Gy, treated with 5-ALA and/or 50, 100 and 200 μg/mL RLNPs) are displayed in Figure 61 and reported in Table 15. Minimal changes in survival were observed for all RLNP concentrations, with and without 5-ALA relative to the control groups (untreated and treated only with 5-ALA). These results corroborate the viability assays at 24 and 48 hours (Sections 8.6 and 8.8), confirming that the nanoparticles are not acutely toxic and do not induce losses in proliferation or viability 1-week post-treatment, at the point when the cells are considered to be indefinitely proliferating. Importantly, this also confirms that the results obtained for Western blot analysis of γH2AX (Section 8.7) that suggested the RLNPs may be genotoxic should be evaluated in further depth, as no deleterious effects were observed on a long-term scale. This is an important step toward establishing the long-term safety of the nanoparticles and the nanoparticle/5-ALA combination.

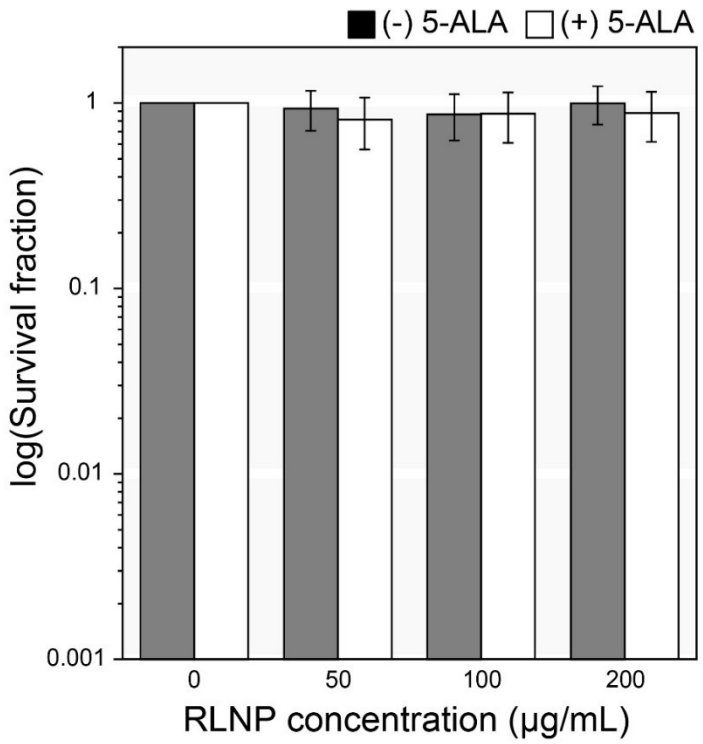

Figure 60. Clonogenic assay results for U251 cells treated with RLNPs and/or 5-ALA in the absence of X-ray irradiation.

Table 15. Survival fraction (SF) data used to generate the bar graph in Figure 61 for U251 cells treated with 50, 100, or 200 μg/mL $NaLuF_4:Pr^{3+}$ RLNPs with or without 5-ALA and the corresponding percent uncertainties in the SF calculation.

RLNP concentration (μg/mL)	(-) 5-ALA		(+) 5-ALA	
	SF (%)	% Uncertainty	SF (%)	% Uncertainty
0	100	--	100	--
50	93.55	22.8	81.45	25.2
100	86.98	24.2	87.46	26.45
200	99.64	23.2	88.19	26.45

Dose-response curves were generated from the survival fractions obtained for all the treatment scenarios (Figure 62), and the corresponding raw values are reported in Table 22 of Appendix 7. Of note, survival curves are most often reported only up to 8 Gy[208,266,353,362,363,504], while comparatively few studies have reported dose-response curves beyond 15 Gy.[360,500,503] To our knowledge, no X-PDT studies have included the 20 Gy dose in their study, despite its relevance for IORT and for radioresistant cancers like glioblastoma.

The shape of the dose-response curves obtained for U251 cells treated only with X-rays up to 20 Gy are nearly linear, with no shoulder observed at the low dose end of the curve. A shoulder is often observed on the low-dose end of the dose-response curve in radioresistant mammalian cells due to effective DNA damage response machinery, and/or due to mutations that further contribute to radioresistance.[181,208] Both of these effects contribute to high survival at low radiation doses, causing the appearance of a shoulder.[208,504,505] The lack of a shoulder in the dose response curves of glioblastoma cells have been reported elsewhere[237,353,503] despite clear evidence these lines are radioresistant. Thus, the shape of the dose-response curve for the cells treated here are in agreement with what has been observed by other researchers.

Notably, even up to 20 Gy, the survival fractions were only reduced to 14.4 and 13.1% without and with 5-ALA, respectively, further illustrating the radioresistant nature of glioblastoma. The results are in remarkable agreement with those of Cifarelli *et al.* in which a 20 Gy radiation

dose delivered to the U3035 and U3020 glioblastoma lines resulted in a survival of 19.6 and 16.9%.[500] Guardiola *et al*. also reports similar results in the U87 and F98 glioblastoma lines upon treatment with 19 Gy.[503] Moreover, little difference was observed in the dose response curves with and without 5-ALA treatment (and no RLNP treatment). In agreement with the results of Yamamoto *et al*. in rat glioma cell lines (9L and C6), only a weak radiosensitizing effect was observed, presumably due to the generation of ROS by PPIX upon X-ray irradiation.[458,469] These results are independently corroborated by the ROS detected using the DCHF-DA assay discussed in Section 8.5.

8.9.1. Treatment outcomes: radiosensitization vs X-PDT

The treatments involving RLNPs drastically reduced the survival fractions for all concentrations studied relative to treatment with X-rays only or with X-rays and 5-ALA (Figure 62). The results obtained by evaluating clonogenicity are much more promising than those achieved at the 24 and 48 hour timepoints; the lowest survival fraction obtained was 0.38 ± 0.04 % for the X-PDT treatment at 20 Gy, versus the previously mentioned 13.4% obtained for 20 Gy X-rays and 5-ALA alone. Importantly, the 20 Gy dose given in IORT is usually adjuvant with the Stupp protocol, which includes an additional 60 Gy delivered to the tumor margin. The results herein suggest a major decrease in the number of surviving cells, thus indicating the 20 Gy IORT protocol when nanoparticles are included can drastically improve outcomes given that survival is associated with the number of cancerous cells remaining after resection.

Notably, unlike the results at 24 and 48 hours, there was a distinct difference between the treatment outcomes with and without 5-ALA. The X-PDT treatment provided substantially larger reductions in survival, confirming the additional damage induced by the PDT effect provides better outcomes than what can be achieved with the nanoradiosensitizers alone. Impressively, the lowest survival fraction obtained using X-rays alone at 20 Gy (14.4%) was equivalent to the survival fraction obtained using only 2 Gy with 200 μg/mL RLNPs and 5-ALA to perform X-PDT (14.1 %). A 2 Gy radiation dose alone, typical for fractionated radiotherapy, resulted in a survival of 75.17 ± 11.09. As such, there is a clear advantage to using the RLNP/5-ALA combination to kill glioblastoma cells.

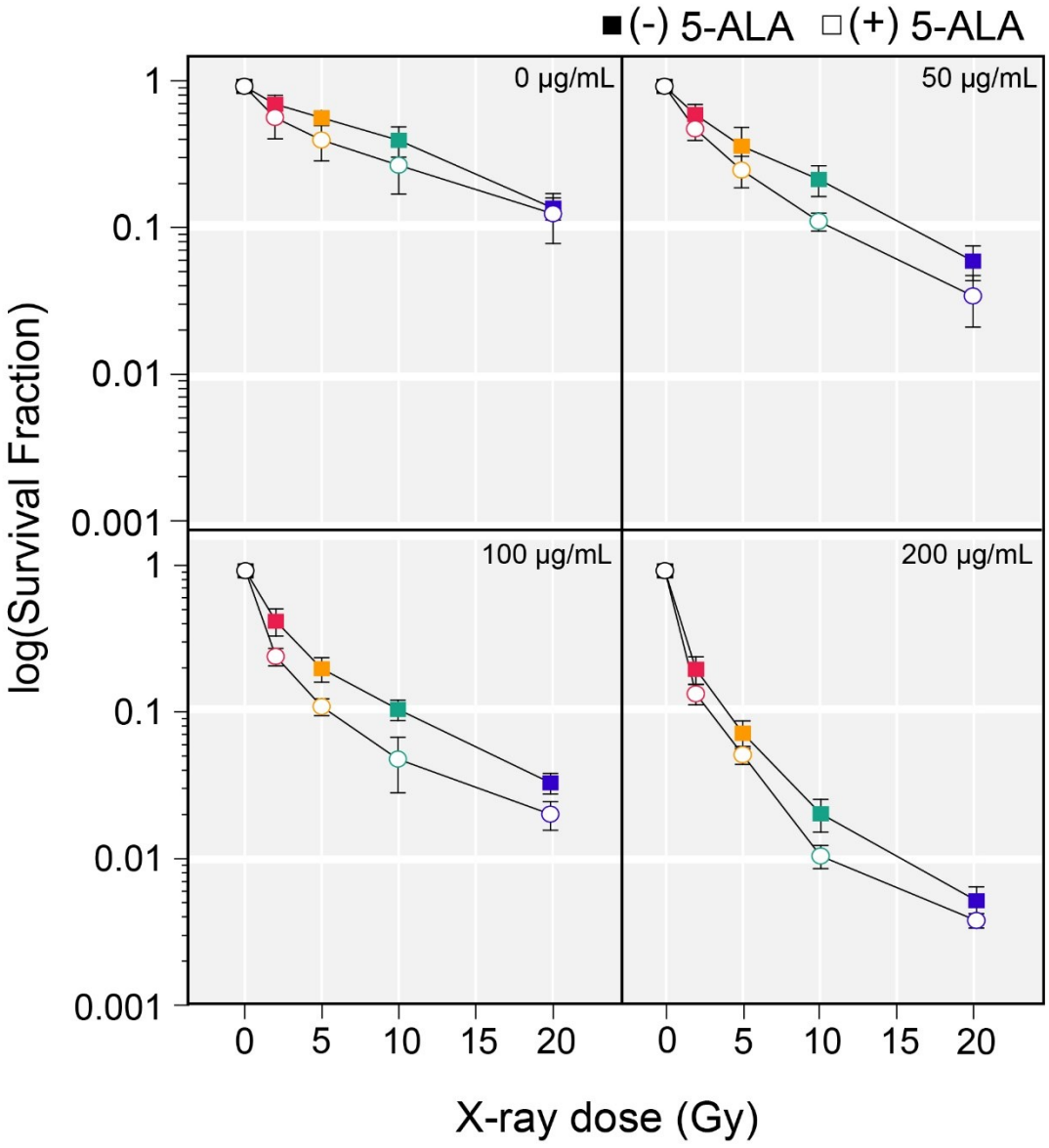

Figure 61. Dose-response curves for U251 cells generated from clonogenic assays. Survival fractions (SF) were calculated 7 days post-treatment at each radiation dose. 0 Gy (black), 2 Gy (red), 5 Gy (yellow), 10 Gy (green), and 20 Gy (blue) for 0, 50, 100, and 200 µg/mL RLNPs. Filled symbols represent cells treated with RLNPs only, outlined symbols correspond to cells treated with RLNPs and 5-ALA.

8.9.2. The Linear-Quadratic Model and Target models

The shape of the dose-response curves provide additional means of understanding of the treatment outcomes, and can be better understood by analyzing the curves using common radiotherapy models such as the Linear-Quadratic (LQ) and target models. Gabriella Tessitore

performed the fitting of the data to these models and the following results and discussions on these models stem from her ideas and contributions to this work.

Radiobiological models are based on the assumption that cell killing due to irradiation with ionizing radiation can be simplified down to the likelihood that a lethal DNA double strand break occurred upon interaction of the radiation with a cell.[208] The statistical nature of the models is best understood by using target theory, along with the LQ model, both of which are briefly described below. Thorough and particularly helpful explanations of target theory can be found in the textbook written by Joiner[208] and in a review by Bodgi *et al.*[505] It is important to note, however, that the commonly-encountered radiobiological models suffer from important limitations, and all of them were developed based on the effects of ionizing radiation alone.[208,505,506] Thus, with respect to nanoradiosensitizers and X-PDT, it is unlikely that any of the models can accurately describe the data in its entirety. Nonetheless, we felt it was important to quantify the common parameters obtained from these models as it can allow for an increased understanding of the data using classical interpretations in radiobiology.

The Linear-Quadratic model is described by equation 10. It relates the survival fraction (*SF*) of a population of cells to the number of lethal (α) and sublethal (β) hits that will be acquired upon treatment with a single dose of ionizing radiation, *D*.[507] The α and β parameters govern the shape of the dose-response curve, and their ratio is used to describe the degree of radiosensitivity of a cell population. The LQ model is based on the concept of target theory as previously mentioned; traditionally, the target in question is DNA. The parameter αD corresponds to the dose at which a single hit leads to cell death, whereas the quadratic βD^2 component represents lethal death by multiple hits simultaneously.

$$\boldsymbol{SF = e^{-\alpha D - \beta D^2}} \tag{10}$$

The single hit multi target (SHMT) model is represented by equation 11, and describes the probability of survival (*SF*) based on the number of targets (*n*) hit one time simultaneously to achieve death. D_0 represents the dose that reduces survival to 1/*e* of the previous value in the exponential portion of the dose-response curve, and *D* is the dose delivered to the cells in a single fraction.[208]

$$SF = 1 - \left(1 - e^{-\frac{D}{D_0}}\right)^n \quad (11)$$

The fitting values are reported in Table 16 along with the corresponding residual squared values. Of note, in all instances, the β parameter fits to zero. Given that the β parameter is associated with the quadratic part of the equation, it is not unexpected that the value is zero, since the survival curves are either nearly linear, or are concave. Moreover, if β = 0, then the α/β ratio is infinite; while high α/β ratios have been reported in a variety of tissues[208,508], it is more likely that the LQ model is simply not a reasonable model for this data set. This is in agreement with the report of Emami *et al.,* who conclude that the LQ model is not reasonable for high-dose, low LET combinations, such as those used in IORT and in this work.[508] Notably, concave dose-response curves (and negative β values[341], despite their lack of physical meaning) have been reported for several X-PDT systems, underscoring the steep low-dose response that can be achieved using the X-PDT technique.[336,341,353,360] It should be noted that the majority of the X-PDT systems do not achieve such a steep response, thus highlighting the efficacy of the aforementioned systems, and ours.

Table 16. Fitting results to the LQ and single hit-single target models, and corresponding residual squared values for the dose response curves shown in Figure 62.

	(-) 5-ALA			**(+) 5-ALA**		
RLNPs (μg/mL)	**α (Gy^{-1})**	**$Residual^2$**	**D_0 (Gy)**	**α (Gy^{-1})**	**$Residual^2$**	**D_0 (Gy)**
0	0.0966	0.007	10.353	0.159	0.030	6.296
50	0.180	0.009	5.544	0.286	0.008	3.497
100	0.345	0.011	2.897	0.630	0.010	1.59
200	0.752	0.003	1.330	0.959	0.002	1.043

Since the dose-response curves are plotted on a semi-log scale, the α values correspond to the slope of the curves. Indeed, the α values of the curves obtained for the X-PDT scenarios are all steeper than the curves for RLNPs only. Because α is related to the probability achieving a lethal hit, it follows that the additional modes of damage produced by the PDT effect when 5-ALA and the RLNPs are combined would cause a greater number of lethal hits. While this is not the way in

which the LQ model was intended to be interpreted (as it was developed based only on the effects of ionizing radiation), in practicality, it is a sensible conclusion in the context of a model which is actually a special case of a target model, as discussed below.

In the SHMT model (equation 11), when only a single target is involved, the equation is reduced to equation 12. Noticeably, this scenario resembles the LQ model when $\beta = 0$. Thus, the single-hit single-target scenario is related to the LQ model such that α and D_0 are inversely proportional.

$$\boldsymbol{SF = e^{-\frac{D}{D_0}}} \tag{12}$$

In our case, α and D_0 are inversely proportional, as the data is in agreement with a single hit-single target scenario. The values obtained for D_0 are listed in Table 17. The D_0 values provide a facile means of understanding the effect of dose on cell killing. For example, 10.4 Gy is necessary to achieve death by a single hit in the absence of RLNPs, whereas only 1.3 Gy is necessary to achieve the same outcome after treatment with 200 μg/mL RLNPs.

The decrease in D_0 with increasing RLNP concentration is explained by the radiation dose enhancement effect. As the number of RLNPs per cell increases, the attenuation of ionizing radiation by the RLNPs relative to the attenuation of X-rays by tissues increases. Upon interaction with X-rays (at the energies relevant here, ≥ 50 keV), a cascade of secondary electrons and X-rays are ejected from the nanoparticles *via* the photoelectric effect (see Section 2.1 and 2.2.1 for further discussion). The secondary electrons and photons can then go on to interact with proximal biological targets and manifest more sub-lethal and lethal hits. Thus, the interaction of a single incident primary photon with an RLNP can result in more target hits than what would be achieved if the incident primary photon only interacted with the cell. In essence, a greater dose is deposited to the cell when the RLNPs are present, hence the term *dose enhancement effect*. This effect has been documented by Bulin *et al.* as a major component of the therapeutic effect from lanthanide-doped fluoride nanoparticles as discussed in Section 3.6.2.[263] Moreover, the UV emissions from the $^1S_0 \rightarrow {}^1G_4$, ^3F_J, ^3H_J transitions of Pr^{3+} are appropriate for inducing DNA damage directly. This could also contribute to a higher proportion of lethal hits.

8.9.3. Mean Inactivation Dose and Sensitizer Enhancement Ratio

When considering the relative contributions of the RLNP dose enhancement effect and the PDT effect to the treatment outcomes, one can see that for all scenarios (0, 50, 100 and 200 μg/mL) the dose-response curves with and without 5-ALA treatment are not parallel. In other words, the effect of adding RLNPs or RLNPs and 5-ALA is not constant across all radiation doses. Because of this, the reported enhancements provided by a radiosensitizer or X-PDT treatment can vary drastically depending on the radiation dose studied. The mean inactivation dose, $\overline{D}$, is the dose at which there is a 50% probability of killing half of a given cell population, and it acts as a measure of the radioresistance of the cells.[506] First reported by Kellerer and Hug in 1972[509], it is calculated by integrating the entire survival curve across a range of doses, thus it considers the overall effect of the treatment across a range of scenarios. Notably, the ICRU report 30 recommends using $\overline{D}$ (and not the other factors) for characterizing dose-response curves.[266,510,511] $\overline{D}$ can be obtained from the LQ model *via* integration using the 12-point formula[510] and, interestingly, when $\beta = 0$ (as is the case for our data), $\overline{D} = \alpha^{-1}$, thus it is equivalent to D_0 from the single hit-single target model described above. It must be stressed that this is the case for the data reported herein, but $\overline{D}$ is rarely equivalent to D_0, as most survival curves are characterized as having $\beta > 0$.

The sensitizer enhancement ratio (SER) is calculated as the ratio of $\overline{D}$ in the presence and absence of a radiosensitizer.[266] SER values are reported in Table 17 and depicted graphically in Figure 63. Note that the $\overline{D}$ values are identical to the D_0 values in Table 16, but are re-reported in

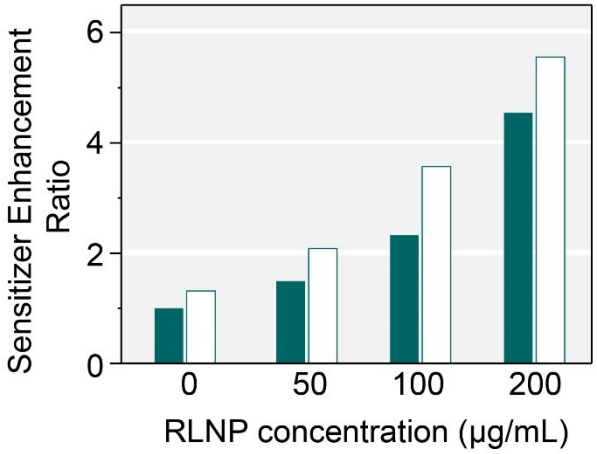

Figure 62. MID-derived sensitizer enhancement ratio as a function of nanoparticle concentration (0, 50, 100, and 200 μg/mL). Filled bars represent results for RLNPs alone, outlined bars represent treatment with RLNPs and 5-ALA.

the context of the SER calculation. The SER values are calculated relative to the untreated cells, and illustrate that PPIX (5-ALA treated cells, no RLNPs) does exhibit a radiosensitizing effect, with an SER of 1.64. As described previously, PPIX is known to be a weak radiosensitizer.[458] The 50 μg/mL RLNP dose performs slightly better than 5-ALA treated cells, with an SER of 1.87. Notably however, the combination of 50 μg/mL RLNPs and 5-ALA together generate a substantially higher SER than the RLNPs or 5-ALA alone. Table 21 in Appendix 7 summarizes all of the enhancement factors reported in the literature that are discussed here. Compared to the D_0 reported for silver and gold nanoparticles in U251 cells, which were 1.64 and 1.23, respectively, the RLNPs on their own give a higher SER, even without the 5-ALA treatment.[512] This is a particularly useful comparison, as it is in the same cell line and gold nanoparticles are well-studied radiosensitizers and are considered to be highly attractive therapeutic candidates.[266,513,514] In all cases, the SER of the X-PDT treatment provided a greater enhancement than the RLNPs alone, although the RLNPs generate an impressive enhancement on their own.

Table 17. Values obtained for the mean inactivation dose (MID) and sensitizer enhancement ratio (SER) from the dose-response curves in Figure 62.

	(-) 5-ALA		**(+) 5-ALA**	
RLNPs (μg/mL)	$\bar{D}$ **(Gy)**	**SER**	$\bar{D}$ **(Gy)**	**SER**
0	10.353	--	6.296	1.64
50	5.544	1.87	3.497	2.96
100	2.897	3.57	1.59	6.51
200	1.330	7.78	1.043	9.93

In summary, the MID-derived SER takes into account enhancements generated across the range of radiation doses studied, conclusively demonstrating that regardless of the specific radiation dose, the X-PDT treatment provides a greater enhancement than what can be achieved with RLNPs alone. MID-derived SER values have not been reported for any X-PDT systems, to our knowledge. However, they have been reported for several nanoradiosensitizers, including AGuIX®, which is in clinical trials as mentioned in Section 3.4.1.1.2; in Panc1 cells, a SER of 1.46 was reported.[515] As detailed in Table 21 in Appendix 7, the conditions under which the SER for this nanoradiosensitizer was obtained are quite different from those herein, thus it is not straightforward to make a comparison, though our values suggest greater enhancements than what

are achieved using AGuIX®. This is not surprising, as AGuIX® is a small-molecule polysiloxane-based gadolinium chelate, thus its ability to attenuate ionizing radiation is quite different from the relatively large nanoparticles studied herein. Moreover, AGuIX® is not luminescent, thus there is no potential to couple it with a photosensitizer and therefore an X-PDT effect cannot be generated.

8.9.4. Radiation Enhancement Ratio

In cases where it is not practical or feasible to obtain a full dose-response curve, the RER is a useful means of reporting an enhancement at a specific radiation dose. The RER_X is calculated using equation 13. In our case, for the RLNP only treatments, the SF_{CT} is the survival fraction of the untreated control (no RLNPs, no 5-ALA) at the specified radiation dose, and for the RLNP and 5-ALA treatments the SF_{CT} is the 5-ALA treated control at the specified radiation dose.

$$\boldsymbol{RER_X = \frac{SF_{CT}}{SF_{NP}} \; at \; X \; Gy} \tag{13}$$

Most commonly, the RER_{2Gy} is reported, since 2 Gy is a standard, clinically relevant radiation dose. However, since we have obtained survival fractions for a range of radiation doses, we have calculated the RERs for all radiation doses studied, as reported in Table 18 and depicted graphically in Figure 64.

In line with what we expect based on the shape of the survival curves, the RER values do not increase in a constant manner, thus confirming the enhancements are not constant across all doses. As expected, higher RLNP concentrations and higher radiation doses result in greater enhancements, with the X-PDT scenario generally resulting in even greater RER values. Notably, the RER_{2Gy} and RER_{5Gy} are the same for the RLNPs and RLNPs/5-ALA treatment for 50 µg/mL RLNPs, suggesting that at these doses, the X-PDT effect provides negligible improvement in treatment outcomes. This contrasts with what is concluded when calculating the SERs across the entire dose-response curve. Thus, care should be taken to investigate the differences at these doses further if they are to be used in a different cell line or *in vivo*. This is a good example of how calculating the different enhancement factors may provide additional insight that cannot be gleaned from a single metric.

Table 18. Radiation enhancement ratios for 0, 2, 5, 10, and 20 Gy radiation doses and 50, 100, and 200 μg/mL RLNPs with and without 5-ALA treatment. Values derived from clonogenic assays shown in Figure 62.

Dose (Gy)	50 μg/mL RLNPs		100 μg/mL RLNPs		200 μg/mL RLNPs	
	(-) 5-ALA	(+) 5-ALA	(-) 5-ALA	(+) 5-ALA	(-) 5-ALA	(+) 5-ALA
2	1.2	1.2	1.7	2.4	3.6	4.3
5	1.6	1.6	2.9	3.7	8.0	8.0
10	1.9	2.4	3.9	5.7	20.3	26.7
20	2.3	3.7	4.2	6.4	27.6	34.6

Values of RER at 2 and 4 Gy have been reported most often in the literature, as detailed in Table 21 in Appendix 7. Notably, the RER_{2Gy} for NBTXR3® (also in clinical trials, see Section 3.4.1.1.1) in T98G glioma cells was reported to be 1.22 for an 800 μM nanoparticle dose (the highest dose they studied). This is on par for what we obtained for an RER_{2Gy} of our RLNP only treatments at the lowest dose studied (50 μg/mL), and half of the enhancement we achieve using 100 μg/mL RLNPs and 5-ALA. Similar to AGuiX®, NBTXR3 is not luminescent and thus also cannot be used for X-PDT. Interestingly, the producers of AGuIX® realized this and developed a Tb^{3+}-based version of AGuIX® to perform X-PDT using a custom porphyrin called P1. As reported in Table 21 in Appendix 7, an RER_{2Gy} of 1.55 in U251-MG cells was obtained for this system, which further underscores the promise of ours. The highest RER we found in the literature was 5.96 for an RER_{6Gy} using 50 μg/mL $NaCeF_4:Gd^{3+},Tb^{3+}$ nanoparticles coupled to Rose Bengal in A549 cells.[47] This is much higher than any of the enhancements reported herein using 50 μg/mL nanoparticles, even taking into account the different cell line and radiation parameters. The combination of Tb^{3+} and Rose Bengal in X-PDT is by far the most well-established pairing, as discussed in Section 3.6. However, Rose Bengal is a synthetic photosensitizer, thus the Tb^{3+}/Rose Bengal X-PDT systems are less specific than what can be achieved with 5-ALA X-PDT since PPIX is only accumulated in malignant cells. In this case, a tradeoff between specificity and enhancement are mainly what distinguish the two systems.

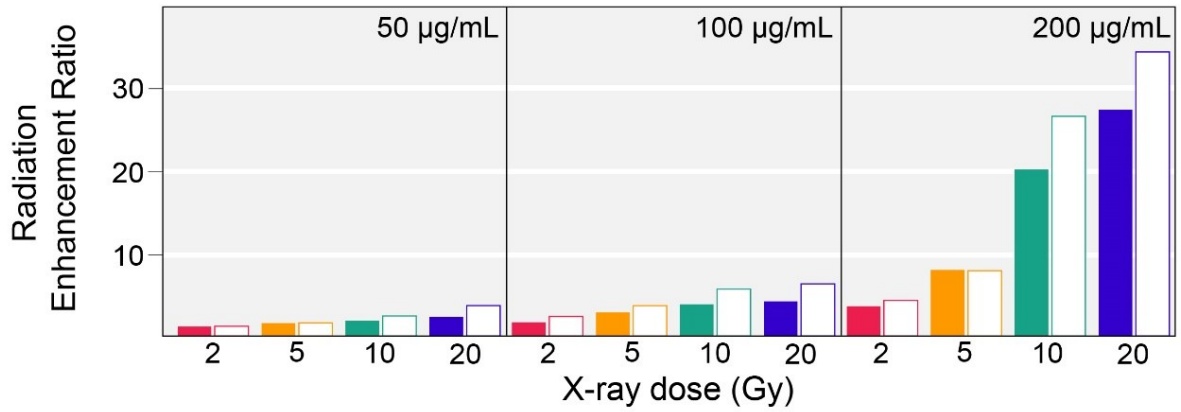

Figure 63. Radiation enhancement ratios as a function of $NaLuF_4:Pr^{3+}$ RLNP concentration (0, 50, 100, and 200 µg/mL) and X-ray dose (0, 2, 5, 10, and 20 Gy). Filled bars represent results for RLNPs alone, outlined bars represent treatment with RLNPs and 5-ALA.

8.9.5. Dose Modifying Ratio

Whereas the previous three enhancement factors are focused on the survival outcomes at a specific radiation dose, the DMR_x gives information on what radiation dose is required to achieve a desired biological effect. The DMR is the ratio of radiation doses where *x* is the survival fraction of interest. DMR values are usually reported at either high or low survival values (ex. 80% survival and 20% survival), as this can give insight into the effect of the treatment on the radiosensitive and radioresistant cell populations, respectively.[266] An outcome of 80% survival means that only the most radiosensitive cells have been eradicated; the majority of the population survived the treatment. In contrast, at 20% survival, the majority of the population was eradicated, and only the most robust, treatment-resistant population remains.

DMR_{10} values are more commonly reported in the literature (Table 21 in Appendix 7), however these could not be obtained for our data because our lowest survival fraction for the untreated controls was above 10%, and we did not explore higher radiation doses as 20 Gy is already substantial. The DMR_{80} and DMR_{20} values were calculated by interpolation of the survival curves to obtain the radiation dose at x% survival, *D*. Then the DMR is calculated using equation 14, where D_{CT} is the dose required to obtain 80 or 20% survival for the control population (either untreated or treated only with 5-ALA), and D_{NP} is the dose required to obtain 80 or 20% survival

after treatment with 50, 100 or 200 μg/mL RLNPs and/or 5-ALA.

$$\boldsymbol{DMR_{X\%}} = \frac{\boldsymbol{D_{CT}}}{\boldsymbol{D_{NP}}} \tag{14}$$

The DMR_{80} and DMR_{20} are reported in Table 19 and shown in Figure 65. DMR_{20} values have been reported for two systems. First, AGuiX® gives a DMR_{20} of 1.31 in Panc1 cells[515], where our system again outperforms it by this metric under all tested conditions. The second system is a nano-X-PDT system. Self-sensitized, Hf-based nanoMOFs with porphyrin linkers in three cell lines (CT26, SQ20B and HeLa), gave DMR_{20} values ranging from 1.56 to 2.83 (Table 21 in Appendix 7).[341] As such, their DMR_{20} values are on par with or lower than what we have obtained. Additionally, they also obtain concave survival curves. Anecdotally, it is interesting that both our system and the nanoMOFs exhibit steep dose-responses using porphyrins as a photosensitizer. Similar to the Tb^{3+}/Rose Bengal combination discussed above, the nanoMOFs will perform X-PDT non-specifically, thus there may be an advantage to our system given the similar performance but improved specificity.

Table 19. Dose modifying ratios at 80% and 20% (DMR_{80} and DMR_{20} respectively) survival derived from the dose-response curves in Figure 62.

RLNPs (μg/mL)	**DMR_{80}**		**DMR_{20}**	
	(-) 5-ALA	**(+) 5-ALA**	**(-) 5-ALA**	**(+) 5-ALA**
50	1.5	1.3	1.5	2.2
100	2.2	1.9	3.3	4.9
200	3.2	2.2	8.2	8.3

Beyond the absolute values of the DMR results, an interesting trend was observed. Graphically, it is easier to understand the implications of the results. In the case of the DMR_{80}, across all RLNP concentrations, the RLNP-only treatment results in a higher DMR than the X-PDT scenario. In contrast, the DMR_{20} is greater for the X-PDT treatment than for the RLNPs alone. This implies that the effect of radiosensitization is sufficient to eradicate the radiosensitive

subpopulation, while the RLNP/5-ALA combination is better able to eliminate the majority of the population, which is radioresistant. Indeed, the response at 80% survival is less important, as the majority of the cancer cells remain in that scenario.

The improvement in treating the majority of the cells shown by the DMR_{20} is of practical clinical importance since the goal is to kill as many cells as possible, especially those that are highly radioresistant. We postulate the added benefit of the X-PDT approach occurs due to the additional modes of damage caused by the simultaneous DNA damage from the radiosensitization effect and UV emissions from Pr^{3+}, and the oxidative damage to other intracellular targets caused by the PDT effect upon activation of PPIX. This further strengthens the notion that adjuvant therapies like X-PDT are better able to treat aggressive cancers, as the damage caused to multiple parts of the cell through different modes of action makes it difficult for cell repair machinery to mitigate damage on all fronts.

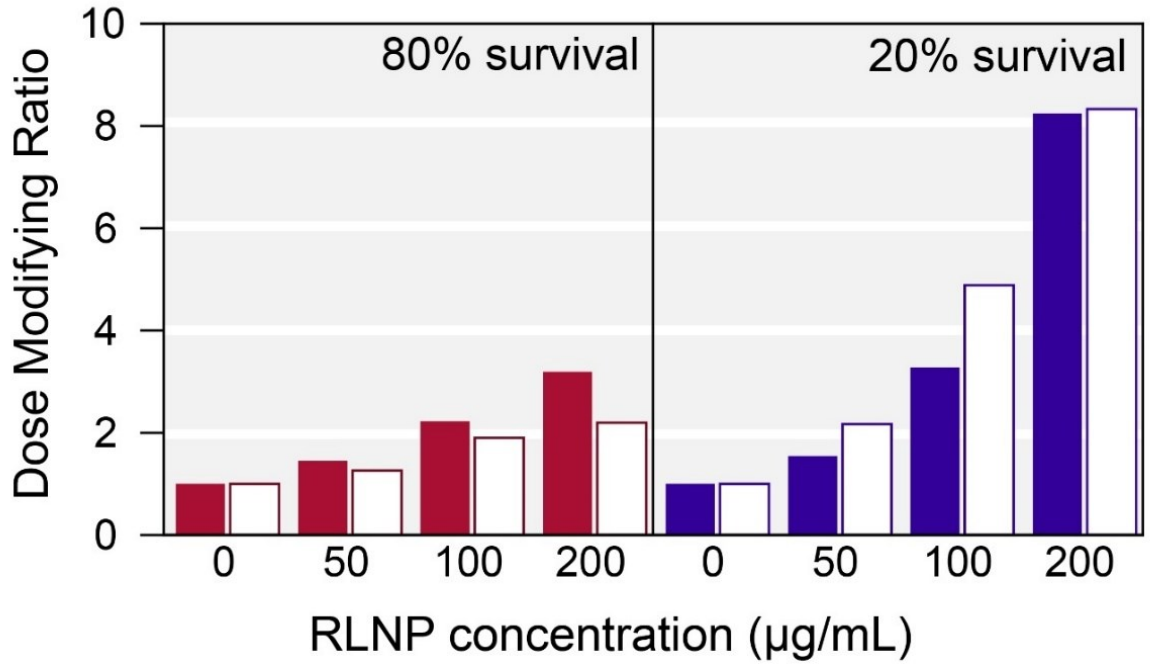

Figure 64. Dose modifying ratios at 80 and 20% survival depicted graphically based on the data in Table 21. Filled in bars represent cells treated with RLNPs only and outlined bars represent cells treated with RLNPs and 5-ALA.

Chapter 9. Conclusions and Future Directions

9.1. Conclusions

Herein, we set out to develop a proof-of-concept toward improving the treatment outcomes of glioblastoma patients using nanomedicine. Toward this goal, we developed Pr^{3+}-doped nanoparticles and studied their synthesis and fundamental spectroscopic properties. Once a thorough understanding of the nanoparticle properties was achieved, we undertook *in vitro* studies to evaluate the potential for these nanoparticles in treating the U251 glioblastoma cell line. The work in this thesis combines aspects of chemistry, physics and biology in a truly interdisciplinary approach that yielded promising results.

The synthesis of $NaLuF_4$:Pr^{3+} nanoparticles was developed with the objective of obtaining uniform nanoparticles at sizes relevant for cell uptake (sub-100 nm) and maximum emission from the $^1S_0 \rightarrow {}^1I_6$ transition of Pr^{3+}, which is resonant with the Soret band of PPIX. A concentration study was carried out across a wide range of Pr^{3+} concentrations (1-40 mol%), revealing $NaLuF_4$:25 mol% Pr^{3+} provided the most intense emissions from the $^1S_0$-$^1I_6$ transition. Persistent luminescence was from the LOLs for over 30 minutes, which warranted further investigation. The persistent luminescence was observed only from the lower excited optical levels and could be induced *via* direct excitation into the $^1S_0$ level of Pr^{3+} in addition to X-ray excitation. Moreover, the persistent luminescence duration was found to increase with decreasing nanoparticle size; at the sub-100 nm sizes relevant for cellular uptake, persistent luminescence was observed for nearly 45 minutes. Using a combination of spectroscopic techniques, a local (de-)trapping mechanism that excludes participation of the valence and conduction bands was determined to explain the radioluminescence and persistent luminescence properties of these nanoparticles. Finally, the optimized composition, $NaLuF_4$:25% Pr^{3+}, also exhibited persistent luminescence which could contribute to the observed therapeutic effects.

The $NaLuF_4$:25 mol% Pr^{3+} nanoparticles were then studied for their potential to achieve X-ray mediated photodynamic therapy (X-PDT) *in vitro* in the U251 glioblastoma cell line using 5-ALA-mediated PPIX as a photosensitizer. Monolayer cultures were used as a proof-of-concept to simulate the thin layer of cells that remain after resection of glioblastoma using fluorescence-

guided surgery. The therapeutic effect of the nanoparticles in the absence and presence of PPIX was studied at three nanoparticle concentrations using an incubation time of 1 hour. The radiosensitization and X-PDT effects were evaluated at a range of radiation doses, from 2 Gy used in fractionated radiotherapy to 20 Gy used in intraoperative radiotherapy. Metabolic activity assays, FACS assays and Western blotting 24 hours post-treatment were used to independently ascertain the effects of the treatments on the short-term. Western blotting analysis was used to evaluate biomarkers associated with DNA damage, cell stress, senescence and markers of apoptosis, and indicated the cells were prone to death after treatment with the nanoparticles and ionizing radiation. At 24 hours, the effects of the treatment were not fully obviated, and it was difficult to establish differences between treatment with and without 5-ALA. However, this project is proof that in many cases, good things take time. The long-term proliferative capacity of the cells was evaluated *via* the clonogenic assay and demonstrated that the X-PDT system provided promising treatment outcomes, as did treatment with the nanoparticles alone, illustrating their strong radiosensitizing effect. Treatment of the cells with 200 μg/mL nanoparticles and 5-ALA with a 2 Gy radiation dose provided the same outcome as irradiation of the cells with 20 Gy of X-rays alone, demonstrating the strong potential of this system at a proof-of-concept level.

We wish to underscore that this X-PDT system was deliberately studied under parameters relevant for the clinical workflow for fluorescence-guided resection of glioblastoma and subsequent intraoperative radiotherapy of the tumor margin. We developed a nanoparticle system with rapid uptake times that are appropriate for an intraoperative setting, and tested their therapeutic efficacy using X-ray radiation parameters that were as close as possible to the clinically-used INTRABEAM® device. These preliminary results aim to establish a strong foundation for subsequent translation to more complex biological models.

9.2. Future Directions

The potential future directions stemming from this work are numerous, but can be generally categorized into fundamental studies of the physicochemical and luminescence properties of the nanoparticles, and studies that bring about their translation to successively more complex biological models.

9.2.1. Future directions from a materials perspective

As demonstrated by the persistent luminescence studies, the luminescence properties of the $NaLuF_4:Pr^{3+}$ nanoparticles likely change as a function of size. As such, it would be of major interest to determine synthetic parameters that enable the synthesis of $NaLuF_4$:25% Pr^{3+} in a range of sizes without significantly altering the degree of crystallinity. Moreover it would be helpful to work toward large-scale synthesis of the particles, such that there is a commercially-viable route to their production.

Upon synthesis of the RLNPs at different sizes, radioluminescence and persistent luminescence spectroscopy should be performed. Ideally, it would be helpful to quantify their radioluminescence yields in both the solid and colloidal forms. Moreover, we have only characterized the radioluminescence properties using orthovoltage X-ray sources; it would be highly interesting evaluate their properties both spectroscopically and therapeutically using a clinical linear particle accelerator (LINAC) source that emits MV photons.

Additionally, there is potential to further maximize the persistent luminescence intensity and duration. Construction of a HRBE/VRBE diagram and subsequent trap depth engineering using additional dopants may provide a means toward improving this property of the material. Given that there are several recent demonstrations of persistent luminescence PDT *in vivo* in the literature[516,517], this may be an attractive means toward achieving an enhanced therapeutic effect without delivering more ionizing radiation to healthy tissue.

9.2.2. *In vitro* future directions

Prior to translation to an *in vivo* model, we believe there are a number of fundamental studies that should still be carried out on cell cultures. Despite the promising results described in this work, we feel at this time it would be unethical to move toward *in vivo* studies, in line with

the principles of reduction, replacement and refinement.[518,519] As such, the majority of the directions described here pertain to fundamental studies on cell cultures such that as much as possible can be learned prior to involving animals in the work.

With regard to U251 cells, studies on the X-PDT effect using the different sizes of nanoparticles as described earlier would be informative for truly optimizing the therapeutic effect of the nanoparticles. Moreover, studies using different X-ray energies such as those from a LINAC source would provide information on the difference in therapeutic outcome when using photon energies that interact with matter primarily *via* Compton scattering and pair production rather than the photoelectric effect.[7] Additionally, there could be benefit to investigating the potential of this system with extremely high single radiation doses (>40 Gy/s) such as those used in FLASH-radiotherapy.[520] Modelling dose-deposition using the different radiation sources would also help to elucidate differences between the treatments in line with the work of Bulin and colleagues.[35,263]

Moreover, studies in different glioblastoma cell lines such as U87-MG, which is a p53 wild-type line[484], would help to gain a better understanding of how effective the system is when the cells exhibit a different mutation profile. In line with using different cell lines, there is increasing evidence that nanoparticle uptake may differ for the same cancers derived from the male and female sex, as well as modes of cell death in a variety of cancers including glioblastoma.[521,522] The U251 cell line is derived from a male patient, while the original U87-MG is derived from a female patient; both are from Uppsala, Sweden and thus have similar ethnic profiles.[177,178,523] Studies on glioblastoma lines from under-sampled communities such as the African-American population would also be of merit toward providing treatments that consider a diverse population. Ideally, if collaboration with a hospital can be obtained, studies should be performed on cells derived from a living patient with glioblastoma, thus providing the most realistic *in vitro* model possible. Immortal cells are a convenient and essential means of studying cancer, but can be prone to genetic drift if proper care is not taken to prevent it.[176]

With regard to *in vivo* models, we feel it would be important to take advantage of the services offered by the Nanoparticle Characterization Laboratory (NCL) at the National Cancer Institute and apply for the free preclinical testing of well-characterized formulations.[524] After this stage, it would be necessary to develop a protocol in a relevant animal model involving

fluorescence-guided resection of a tumor, and subsequent precise irradiation of the tumor bed after nanoparticle administration. Developing a means of administering the nanoparticles, whether *via* local injection, aerosol or topical administration of a gel and evaluating uptake as a function of time would be an essential step in optimizing the procedure. To our knowledge, *in vivo* X-PDT for treatment of the tumor bed has not been investigated; thus there is little prior evidence to begin from in this treatment regime. However, much like the design of the *in vitro* proof-of-concept, current clinical practice should inform on the experimental design.

References

1 J. S. Klein, C. Sun and G. Pratx, Radioluminescence in biomedicine: physics, applications, and models, *Phys. Med. Biol.*, 2019, **64**, 04TR01.

2 S. Wang, R. Tian, X. Zhang, G. Cheng, P. Yu, J. Chang and X. Chen, Beyond Photo: Xdynamic Therapies in Fighting Cancer, *Adv. Mater.*, 2021, **33**, 1–33.

3 L. Larue, A. Ben Mihoub, Z. Youssef, L. Colombeau, S. Acherar, J. C. André, P. Arnoux, F. Baros, M. Vermandel and C. Frochot, Using X-rays in photodynamic therapy: An overview, *Photochem. Photobiol. Sci.*, 2018, **17**, 1612–1650.

4 S. Mallick, G. K. Rath and R. Benson, *Practical Radiation Oncology*, .

5 G. Blasse, in *Springer Handbook of Electronic and Photonic Materials*, Springer International Publishing, Cham, 2017, pp. 1–1.

6 M. Tschurlovits, *What is ionizing radiation?*, Seville, 1997.

7 E. B. Podgorsak, Radiation Physics for Medical Physicists, *Med. Phys.*, 2005, **33**, 249–249.

8 M. L. Taylor, R. L. Smith, F. Dossing and R. D. Franich, Robust calculation of effective atomic numbers: The Auto- Z eff software, *Med. Phys.*, 2012, **39**, 1769–1778.

9 Q. Liu, F. Schneider, L. Ma, F. Wenz and C. Herskind, Relative biologic effectiveness (RBE) of 50 kV X-rays measured in a phantom for intraoperative tumor-bed irradiation, *Int. J. Radiat. Oncol. Biol. Phys.*, 2013, **85**, 1127–1133.

10 K. Kobayashi, N. Usami, E. Porcel, S. Lacombe and C. Le Sech, Enhancement of radiation effect by heavy elements, *Mutat. Res. - Rev. Mutat. Res.*, 2010, **704**, 123–131.

11 J. Choi, G. Kim, S. Bin Cho and H.-J. Im, Radiosensitizing high-Z metal nanoparticles for enhanced radiotherapy of glioblastoma multiforme, *J. Nanobiotechnology*, 2020, **18**, 122.

12 G. Blasse, Reviews: Scintillator Materials, *Chem. Mater.*, 1994, **6**, 1465–1475.

13 P. Lecoq, A. Gektin and M. Korzhik, *Inorganic Scintillators for Detector Systems*, Springer International Publishing, Cham, 2017.

14 A. J. Wojtowicz, Some aspects of solid state radioluminescence, *Acta Phys. Pol. Ser. A*, 1999, **95**, 165–179.

15 M. Nikl and A. Yoshikawa, Recent R&D Trends in Inorganic Single-Crystal Scintillator Materials for Radiation Detection, *Adv. Opt. Mater.*, 2015, **3**, 463–481.

16 M. Nikl, E. Mihokova, J. Pejchal, A. Vedda, M. Fasoli, I. Fontana, V. V. Laguta, V. Babin,

K. Nejezchleb, A. Yoshikawa, H. Ogino and G. Ren, in *IEEE Transactions on Nuclear Science*, 2008, vol. 55, pp. 1035–1041.

17 C. L. Melcher, Scintillators for well logging applications, *Nucl. Instruments Methods Phys. Res. Sect. B Beam Interact. with Mater. Atoms*, 1989, **40**–**41**, 1214–1218.

18 J. Glodo, Y. Wang, R. Shawgo, C. Brecher, R. H. Hawrami, J. Tower and K. S. Shah, New Developments in Scintillators for Security Applications, *Phys. Procedia*, 2017, **90**, 285–290.

19 *Wide-Gap Luminescent Materials: Theory and Applications*, 1997.

20 J. Y. Jung, G. A. Hirata, G. Gundiah, S. Derenzo, W. Wrasidlo, S. Kesari, M. T. Makale and J. McKittrick, Identification and development of nanoscintillators for biotechnology applications, *J. Lumin.*, 2014, **154**, 569–577.

21 C. Dujardin, E. Auffray, E. Bourret-Courchesne, P. Dorenbos, P. Lecoq, M. Nikl, A. N. Vasil'Ev, A. Yoshikawa and R. Y. Zhu, Needs, trends, and advances in inorganic scintillators, *IEEE Trans. Nucl. Sci.*, 2018, **65**, 1977–1997.

22 P. A. Rodnyi, P. Dorenbos and C. W. E. Van Euk, Creation of Electron-Hole Pairs in Inorganic Scintillators, *MRS Proc.*, 1994, **348**, 379.

23 R. H. Bartram and A. Lempicki, Efficiency of electron-hole pair production in scintillators, *J. Lumin.*, 1996, **68**, 225–240.

24 M. Korzhik, G. Tamulaitis and A. N. Vasil'ev, *Physics of Fast Processes in Scintillators*, Springer International Publishing, Cham, 1st edn., 2020.

25 M. J. Weber, Spontaneous Emission Probabilities and Quantum Efficiencies for Excited States of Pr 3+ in LaF 3, *J. Chem. Phys.*, 1968, **48**, 4774–4780.

26 G. A. Ozin, A. Arsenault and L. Cademartiri, *Nanochemistry: A Chemical Approach to Nanomaterials*, The Royal Society of Chemistry, 2nd edn., 2015.

27 S. Bonvalot, P. L. Rutkowski, J. Thariat, S. Carrère, A. Ducassou, M. P. Sunyach, P. Agoston, A. M. Hong, A. Mervoyer, M. Rastrelli, V. Moreno, R. K. Li, B. J. Tiangco, A. C. Herráez, A. Gronchi, T. Sy-Ortin, P. Hohenberger, T. de Baère, A. Le Cesne, S. Helfre, E. Saada-Bouzid, R. M. Anghel, G. Kantor, A. Montero, H. H. Loong, R. Vergés, G. Kacso, L. Austen, V. F. Servois, E. Wardelmann, M. Dimitriu, P. Said, A. J. Lazar, J. V. M. G. Bovée, C. Le Péchoux and Z. Pápai, Final Safety and HRQoL Results of the Phase 2/3 Act.In.Sarc Study With Preoperative NBTXR3 Plus Radiation Therapy Versus Radiation

Therapy in Locally Advanced Soft-Tissue Sarcoma, *Int. J. Radiat. Oncol. Biol. Phys.*, 2022, **114**, 422–432.

28 F. Lux, V. L. Tran, E. Thomas, S. Dufort, F. Rossetti, M. Martini, C. Truillet, T. Doussineau, G. Bort, F. Denat, F. Boschetti, G. Angelovski, A. Detappe, Y. Crémillieux, N. Mignet, B.-T. Doan, B. Larrat, S. Meriaux, E. Barbier, S. Roux, P. Fries, A. Müller, M.-C. Abadjian, C. Anderson, E. Canet-Soulas, P. Bouziotis, M. Barberi-Heyob, C. Frochot, C. Verry, J. Balosso, M. Evans, J. Sidi-Boumedine, M. Janier, K. Butterworth, S. McMahon, K. Prise, M.-T. Aloy, D. Ardail, C. Rodriguez-Lafrasse, E. Porcel, S. Lacombe, R. Berbeco, A. Allouch, J.-L. Perfettini, C. Chargari, E. Deutsch, G. Le Duc and O. Tillement, AGuIX ® from bench to bedside—Transfer of an ultrasmall theranostic gadolinium-based nanoparticle to clinical medicine, *Br. J. Radiol.*, 2018, **92**, 20180365.

29 L. G. Jacobsohn, K. B. Sprinkle, S. A. Roberts, C. J. Kucera, T. L. James, E. G. Yukihara, T. A. Devol and J. Ballato, Fluoride nanoscintillators, *J. Nanomater.*, , DOI:10.1155/2011/523638.

30 A. Belsky, K. Ivanovskikh, A. Vasil'ev, M.-F. Joubert and C. Dujardin, Estimation of the Electron Thermalization Length in Ionic Materials, *J. Phys. Chem. Lett.*, 2013, **4**, 3534–3538.

31 V. Vistovskyy, Y. Chornodolskyy, A. Gloskovskii, S. Syrotyuk, T. Malyi, M. Chylii, P. Zhmurin, A. Gektin, A. Vasil'ev and A. Voloshinovskii, Modeling of X-ray excited luminescence intensity dependence on the nanoparticle size, *Radiat. Meas.*, 2016, **90**, 174–177.

32 L. G. Jacobsohn, C. L. McPherson, K. B. Sprinkle, E. G. Yukihara, T. A. Devol and J. Ballato, Scintillation of rare earth doped fluoride nanoparticles, *Appl. Phys. Lett.*, , DOI:10.1063/1.3638484.

33 N. V. Klassen, V. V. Kedrov, V. N. Kurlov, Y. A. Ossipyan, S. Z. Shmurak, I. M. Shmyt'ko, G. K. Strukova, N. P. Kobelev, E. A. Kudrenko, O. A. Krivko, A. P. Kiselev, A. V. Bazhenov and T. N. Fursova, Advantages and Problems of Nanocrystalline Scintillators, *IEEE Trans. Nucl. Sci.*, 2008, **55**, 1536–1541.

34 A. N. Belsky, R. A. Glukhov, I. A. Kamenskikh, P. Martin, V. V. Mikhailin, I. H. Munro, C. Pedrini, D. A. Shaw, I. N. Shpinkov and A. N. Vasil'ev, Luminescence quenching as a probe for the local density of electronic excitations in insulators, *J. Electron Spectros. Relat.*

Phenomena, 1996, **79**, 147–150.

35 A. L. Bulin, A. Vasil'Ev, A. Belsky, D. Amans, G. Ledoux and C. Dujardin, Modelling energy deposition in nanoscintillators to predict the efficiency of the X-ray-induced photodynamic effect, *Nanoscale*, 2015, **7**, 5744–5751.

36 T. Kawaguchi, Noriaki, Kimura, Hiromi, Nakauchi, Daisuke, Kato, Takumi, Yanagada, in *Phosphors for Radiation Detectors*, eds. T. Yanagida and M. Koshimizu, Wiley, 2022, pp. 91–120.

37 R. Naccache, Q. Yu and J. A. Capobianco, The Fluoride host: Nucleation, growth, and upconversion of lanthanide-doped nanoparticles, *Adv. Opt. Mater.*, 2015, 3, **4**, 482–509.

38 H. X. Mai, Y. W. Zhang, R. Si, Z. G. Yan, L. D. Sun, L. P. You and C. H. Yan, High-quality sodium rare-earth fluoride nanocrystals: Controlled synthesis and optical properties, *J. Am. Chem. Soc.*, 2006, **128**, 6426–6436.

39 D. M. Samhadaneh, G. A. Mandl, Z. Han, M. Mahjoob, S. C. Weber, M. Tuznik, D. A. Rudko, J. A. Capobianco and U. Stochaj, Evaluation of Lanthanide-Doped Upconverting Nanoparticles for in Vitro and in Vivo Applications, *ACS Appl. Bio Mater.*, 2020, **3**, 4358–4369.

40 T. Sabri, P. D. Pawelek and J. A. Capobianco, Dual Activity of Rose Bengal Functionalized to Albumin-Coated Lanthanide-Doped Upconverting Nanoparticles: Targeting and Photodynamic Therapy, *ACS Appl. Mater. Interfaces*, 2018, **10**, 26947–26953.

41 Y. Ren, J. G. Rosch, M. R. Landry, H. Winter, S. Khan, G. Pratx and C. Sun, Tb-Doped core-shell-shell nanophosphors for enhanced X-ray induced luminescence and sensitization of radiodynamic therapy, *Biomater. Sci.*, 2021, **9**, 496–505.

42 H. Wang, W. Lu, T. Zeng, Z. Yi, L. Rao, H. Liu and S. Zeng, Multi-functional NaErF 4 :Yb nanorods: enhanced red upconversion emission, in vitro cell, in vivo X-ray, and T 2 -weighted magnetic resonance imaging, *Nanoscale*, 2014, **6**, 2855–2860.

43 A. Gnach, T. Lipinski, A. Bednarkiewicz, J. Rybka and J. A. Capobianco, *Chem. Soc. Rev.*, 2015, 44, 1561–1584.

44 G. Tessitore, G. A. Mandl, S. L. Maurizio and J. A. Capobianco, Springer, Cham, 2021, pp. 1–36.

45 U. Stochaj, D. C. Rodríguez Burbano, D. R. Cooper, M. Kodiha and J. A. Capobianco, The effects of lanthanide-doped upconverting nanoparticles on cancer cell biomarkers,

Nanoscale, 2018, **10**, 14464–14471.

46 P. A. Rojas-Gutierrez, D. Bekah, J. Seuntjens, C. Dewolf and J. A. Capobianco, Cellular Uptake, Cytotoxicity and Trafficking of Supported Lipid-Bilayer-Coated Lanthanide Upconverting Nanoparticles in Alveolar Lung Cancer Cells, *ACS Appl. Bio Mater.*, 2019, **2**, 4527–4536.

47 X. Zhong, X. Wang, G. Zhan, Y. Tang, Y. Yao, Z. Dong, L. Hou, H. Zhao, S. Zeng, J. Hu, L. Cheng and X. Yang, NaCeF 4 :Gd,Tb Scintillator as an X-ray Responsive Photosensitizer for Multimodal Imaging-Guided Synchronous Radio/Radiodynamic Therapy, *Nano Lett.*, 2019, **19**, 8234–8244.

48 D. R. Cooper, J. A. Capobianco and J. Seuntjens, Radioluminescence studies of colloidal oleate-capped β-Na(Gd,Lu)F4:Ln3+ nanoparticles (Ln = Ce, Eu, Tb), *Nanoscale*, 2018, **10**, 7821–7832.

49 J.-C. G. Bünzli, in *Handbook on the Physics and Chemistry of Rare Earths*, Elsevier, 2016, pp. 141–176.

50 A. J. Wojtowicz, in *Nuclear Instruments and Methods in Physics Research, Section A: Accelerators, Spectrometers, Detectors and Associated Equipment*, 2002.

51 J. C. G. Bünzli and C. Piguet, *Chem. Soc. Rev.*, 2005, 34, 1048–1077.

52 F. Szabadvary, in *Handbook on the Physics and Chemistry of Rare Earths*, Elsevier, 1988, pp. 33–80.

53 Government of Canda, Rare earth elements facts, https://www.nrcan.gc.ca/our-natural-resources/minerals-mining/minerals-metals-facts/rare-earth-elements-facts/20522.

54 C. Lu, Why Rare Earths Are The Key To Just About Everything, *Foreign Policy*, 2021.

55 K. Bradsher, China's Supply of Minerals for iPhones and Missiles Could Be a Risky Trade Weapon, *New York Times*, 2019.

56 A. Stevenson, 'Weaponized' Currency and Mining Limits: China's Responses to Trump Take Shape, *New York Times*, 2019.

57 P. Dorenbos, The 4f ↔4f − 5d transitions of the trivalent lanthanides in halogenides and chalcogenides, *J. Lumin.*, 2000, **91**, 91–106.

58 J.-C. G. Bünzli and S. V. Eliseeva, in *Lanthanide Luminescence*, Springer Berlin Heidelberg, 2010, pp. 1–45.

59 S. Hüfner, *Optical Spectra of Transparent Rare Earth Compounds*, Academic Press, 1978.

60 J. H. Van Vleck, The puzzle of rare-earth spectra in solids, *J. Phys. Chem.*, 1937, **41**, 67–80.

61 M. P. Hehlen, M. G. Brik and K. W. Krämer, 50th anniversary of the Judd–Ofelt theory: An experimentalist's view of the formalism and its application, *J. Lumin.*, 2013, **136**, 221–239.

62 M. H. V. Werts, Making sense of Lanthanide Luminescence, *Sci. Prog.*, 2005, **88**, 101–131.

63 C. H. Evans, Ed., *Episodes from the History of the Rare Earth Elements*, Springer Netherlands, Dordrecht, 1996.

64 M. Fontani, M. Costa and M. V Orna, *The Lost Elements: The Periodic Table's Shadow Side*, Oxford University Press, 2015.

65 A. M. Srivastava, Aspects of Pr3+ luminescence in solids, *J. Lumin.*, 2016, **169**, 445–449.

66 R. Naccache, F. Vetrone, A. Speghini, M. Bettinelli and J. A. Capobianco, Cross-Relaxation and Upconversion Processes in Pr 3+ Singly Doped and Pr 3+ /Yb 3+ Codoped Nanocrystalline Gd3Ga5O12 : The Sensitizer/Activator Relationship, , DOI:10.1021/jp711494d.

67 P. Dorenbos, A Review on How Lanthanide Impurity Levels Change with Chemistry and Structure of Inorganic Compounds, *ECS J. Solid State Sci. Technol.*, 2013, **2**, R3001–R3011.

68 A. M. Srivastava, A. A. Setlur, H. A. Comanzo, M. E. Hannah, P. A. Schmidt and U. Happek, Luminescence from the Pr3+ 4f15d1 and 1S0 states in LiLaP4O12, *J. Lumin.*, 2009, **129**, 126–129.

69 A. P. Vink, P. Dorenbos, J. T. M. De Haas, H. Donker, P. A. Rodnyi, A. G. Avanesov and C. W. E. Van Eijk, Photon cascade emission in SrAlF5:Pr3+, *J. Phys. Condens. Matter*, 2002, **14**, 8889–8899.

70 P. A. Rodnyi, S. B. Mikhrin, P. Dorenbos, E. Van Der Kolk, C. W. E. Van Eijk, A. P. Vink and A. G. Avanesov, The observation of photon cascade emission in Pr3+-doped compounds under X-ray excitation, *Opt. Commun.*, 2002, **204**, 237–245.

71 S. Kück, I. Sokólska, M. Henke, M. Döring and T. Scheffler, in *Journal of Luminescence*, North-Holland, 2003, vol. 102–103, pp. 176–181.

72 W. W. Piper, J. A. DeLuca and F. S. Ham, Cascade fluorescent decay in Pr3+-doped fluorides: Achievement of a quantum yield greater than unity for emission of visible light,

J. Lumin., 1974, **8**, 344–348.

73 R. Naccache, Colloidal Upconverting Nanoparticle Systems for Integration in Targeting, Therapeutics and Imaging Applications, Concordia University, 2012.

74 R. Balda, J. R. Fernandez, A. Mendioroz, M. Voda and M. Al-Saleh, in *Rare-Earth-Doped Materials and Devices VI*, eds. S. Jiang and R. W. Keys, 2002, vol. 4645, p. 97.

75 M. Malinowski, M. F. Joubert and B. Jacquier, Dynamics of the IR-to-blue wavelength upconversion in Pr3+-doped yttrium aluminum garnet and LiYF4 crystals, *Phys. Rev. B*, 1994, **50**, 12367–12374.

76 N. Martin, P. Boutinaud, M. Malinowski, R. Mahiou and J. C. Cousseins, Optical spectra and analysis of Pr3+ in β-NaYF4, *J. Alloys Compd.*, 1998, **275**–**277**, 304–306.

77 A. Remillieux and B. Jacquier, IR-to-visible up-conversion mechanisms in Pr3+-doped ZBLAN fluoride glasses and fibers, *J. Lumin.*, 1996, **68**, 279–289.

78 L. L. Noto, S. K. K. Shaat, D. Poelman, M. S. Dhlamini, B. M. Mothudi and H. C. Swart, Cathodoluminescence mapping and thermoluminescence of Pr3+ doped in a CaTiO3/CaGa2O4 composite phosphor, *Ceram. Int.*, 2016, **42**, 9779–9784.

79 S. Gharouel, L. Labrador-Páez, A. Urbieta, P. Fernández, P. Haro-González, K. Horchani-Naifer and M. Férid, Luminescence and cathodoluminescence properties of MIPr(PO3)4 (MI=Na, Li, K) and PrP5O14, *Phys. B Condens. Matter*, 2019, **554**, 121–125.

80 A. Leto, F. Piccinelli, G. Pezzotti, A. Speghini, L. Nodari, S. Polizzi and M. Bettinelli, Single crystal and nanocrystalline Pr3+ doped LuPO4: Synthesis, structural characterization, photo- and cathodoluminescence, *Mater. Res. Bull.*, 2014, **51**, 24–27.

81 P. Xiong, M. Peng, K. Qin, F. Xu and X. Xu, Visible to Near-Infrared Persistent Luminescence and Mechanoluminescence from Pr^{3+} -Doped $LiGa_5O_8$ for Energy Storage and Bioimaging, *Adv. Opt. Mater.*, 2019, **7**, 1901107.

82 J. J. Joos, K. Lejaeghere, K. Korthout, A. Feng, D. Poelman and P. F. Smet, Charge transfer induced energy storage in CaZnOS:Mn - Insight from experimental and computational spectroscopy, *Phys. Chem. Chem. Phys.*, 2017, **19**, 9075–9085.

83 A. Lecointre, A. Bessière, A. J. J. Bos, P. Dorenbos, B. Viana and S. Jacquart, Designing a red persistent luminescence phosphor: The example of YPO 4:Pr3+,Ln3+ (Ln = Nd, Er, Ho, Dy), *J. Phys. Chem. C*, 2011, **115**, 4217–4227.

84 A. Abdukayum, J. T. Chen, Q. Zhao and X. P. Yan, Functional near infrared-emitting

Cr3+/Pr3+ Co-doped zinc gallogermanate persistent luminescent nanoparticles with superlong afterglow for in vivo targeted bioimaging, *J. Am. Chem. Soc.*, 2013, **135**, 14125–14133.

85 X. Zhang, X. Zhang, J. Zhang, M. Wang, H. Zhao, S. Lu and X. J. Wang, Size manipulated photoluminescence and phosphorescence in CaTiO 3:Pr3+ nanoparticles, *J. Phys. Chem. C*, 2007, **111**, 18044–18048.

86 E. Dell'Orto, M. Fasoli, G. Ren and A. Vedda, Defect-Driven Radioluminescence Sensitization in Scintillators: The Case of Lu 2 Si 2 O 7 :Pr, *J. Phys. Chem. C*, 2013, **117**, 20201–20208.

87 P. Dorenbos, 5d level positions of the trivalent lanthanides in inorganic compounds, *J. Lumin.*, 2000, **91**, 155–176.

88 P. Dorenbos, Systematic behaviour in trivalent lanthanide charge transfer energies, *J. Phys. Condens. Matter*, 2003, **15**, 8417–8434.

89 A. H. Krumpel, E. Van Der Kolk, D. Zeelenberg, A. J. J. Bos, K. W. Krämer and P. Dorenbos, Lanthanide 4f -level location in lanthanide doped and cerium-lanthanide codoped NaLaF4 by photo- and thermoluminescence, *J. Appl. Phys.*, 2008, **104**, 1–10.

90 P. Dorenbos, Ce3+ 5d-centroid shift and vacuum referred 4f-electron binding energies of all lanthanide impurities in 150 different compounds, *J. Lumin.*, 2013, **135**, 93–104.

91 P. Dorenbos, J. Andriessen and C. W. E. van Eijk, 4fn−15d centroid shift in lanthanides and relation with anion polarizability, covalency, and cation electronegativity, *J. Solid State Chem.*, 2003, **171**, 133–136.

92 A. J. J. Bos, P. Dorenbos, A. Bessière and B. Viana, Lanthanide energy levels in YPO4, *Radiat. Meas.*, 2008, **43**, 222–226.

93 P. Dorenbos, Lanthanide 4f-electron binding energies and the nephelauxetic effect in wide band gap compounds, *J. Lumin.*, 2013, **136**, 122–129.

94 W. Jia, D. Jia, T. Rodriguez, D. R. Evans, R. S. Meltzer and W. M. Yen, UV excitation and trapping centers in CaTiO3:Pr3+, *J. Lumin.*, 2006, **119**–**120**, 13–18.

95 L. Zhang, J. Lei, J. Liu, F. Ma and H. Ju, Persistent luminescence nanoprobe for biosensing and lifetime imaging of cell apoptosis via time-resolved fluorescence resonance energy transfer, *Biomaterials*, 2015, **67**, 323–334.

96 J. Hölsä, Persistent Luminescence Beats the Afterglow: 400 Years of Persistent

Luminescence, *Electrochem. Soc. Interface*, 2009, **18**, 42–45.

97 D. C. R. Burbano, Development of CaS:Eu2+/Dy3+ Persistent and NIR Photo-Stimulated Nanophosphors, Concordia University, 2017.

98 DHi Nearing Goal Line In Installation of Pentagon Photoluminescent Safety Marking Systems, https://www.dh-inc.com/archive/35-dhi-nearing-goal-line-in-pentagon-pl-installation, (accessed 12 February 2023).

99 J. Xu and S. Tanabe, Persistent luminescence instead of phosphorescence: History, mechanism, and perspective, *J. Lumin.*, 2019, **205**, 581–620.

100 Y. Li, M. Gecevicius and J. Qiu, Long persistent phosphors - From fundamentals to applications, *Chem. Soc. Rev.*, 2016, 45, **8**, 2090–2136.

101 K. Van den Eeckhout, P. F. Smet and D. Poelman, Persistent luminescence in Eu2+-doped compounds: A review, *Materials (Basel).*, 2010, **3**, 2536–2566.

102 K. Van den Eeckhout, D. Poelman and P. Smet, Persistent Luminescence in Non-Eu2+-Doped Compounds: A Review, *Materials (Basel).*, 2013, **6**, 2789–2818.

103 T. Laamanen, *Defects in persistent luminescence materials*, 2011.

104 A. J. J. Bos, Theory of thermoluminescence, *Radiat. Meas.*, 2006, **41**, S45–S56.

105 Z. He, X. Wang and W. M. Yen, Investigation on charging processes and phosphorescent efficiency of SrAl2O4:Eu,Dy, *J. Lumin.*, 2006, **119**–**120**, 309–313.

106 A. Bessière, J.-O. Durand and C. Noûs, Persistent luminescence materials for deep photodynamic therapy, 2021, **10**, 2999–3029.

107 K. Van Den Eeckhout, A. J. J. Bos, D. Poelman and P. F. Smet, Revealing trap depth distributions in persistent phosphors, *Phys. Rev. B - Condens. Matter Mater. Phys.*, 2013, **87**, 045126.

108 A. Feng, J. J. Joos, J. Du and P. F. Smet, Revealing trap depth distributions in persistent phosphors with a thermal barrier for charging, *Phys. Rev. B*, 2022, **105**, 1–14.

109 K. van den Eeckhout, Persistent luminescence : kinetics and compounds.

110 J. Ueda, A. Meijerink, P. Dorenbos, A. J. J. Bos and S. Tanabe, Thermal ionization and thermally activated crossover quenching processes for 5d-4f luminescence in Y3Al5-xGaxO12:Pr3+, *Phys. Rev. B*, 2017, **95**, 014303.

111 J. Ueda, P. Dorenbos, A. J. J. Bos, A. Meijerink and S. Tanabe, Insight into the Thermal Quenching Mechanism for Y3Al5O12:Ce3+ through Thermoluminescence Excitation

Spectroscopy, *J. Phys. Chem. C*, 2015, **119**, 25003–25008.

112 S. W. S. McKeever, *Thermoluminescence of Solids*, Cambridge University Press, 1985.

113 A. Bos, Thermoluminescence as a Research Tool to Investigate Luminescence Mechanisms, *Materials (Basel).*, 2017, **10**, 1357.

114 F. Urbach, Messungmethoden Zur Luminescence der Alkalihalogenide, *Sitzungsberichte Akad. der Wissenshaften*, 1930, **139**, 363–483.

115 J. T. Randall, M. H. F. Wilkins and M. L. E. Oliphant, Phosphorescence and electron traps II. The interpretation of long-period phosphorescence, *Proc. R. Soc. London. Ser. A. Math. Phys. Sci.*, 1997, **184**, 390–407.

116 G F J Garlick and A F Gibson, The Electron Trap Mechanism of Luminescence in Sulphide and Silicate Phosphors, *Proc. Phys. Soc.*, 1948, **60**, 574.

117 W. Hoogenstraaten, Electron traps in zinc sulphide phosphors, *Philips Res. Rep.*, 1958, **13**, 515–693.

118 R. Chen, On the calculation of activation energies and frequency factors from glow curves, *J. Appl. Phys.*, 1969, **40**, 570–585.

119 R. Chen, Glow curves with general order kinetics, *J. Electrochem. Soc.*, 1969, **116**, 1254.

120 M A S Sweet and D Urquhart, A new procedure for analysing complex thermoluminescence, *J. Phys. C Solid State Phys.*, 1981, **14**, 773.

121 R. Visocekas, Tunnelling in Afterglow: its Coexistence and Interweaving with Thermally Stimulated Luminescence, *Radiat. Prot. Dosimetry*, 2002, **100**, 45–53.

122 A. Vedda and M. Fasoli, Tunneling recombinations in scintillators, phosphors, and dosimeters, *Radiat. Meas.*, 2018, **118**, 86–97.

123 P. Dorenbos and A. J. J. Bos, Lanthanide level location and related thermoluminescence phenomena, *Radiat. Meas.*, 2008, **43**, 139–145.

124 P. Boutinaud, L. Sarakha and R. Mahiou, NaNbO3:Pr3+: a new red phosphor showing persistent luminescence, *J. Phys. Condens. Matter*, 2009, **21**, 25901.

125 M. Wei, S. Feng, X. Tian, C. Ji, Z. Huang, J. Wen, X. Liu, F. Luo, C. Li, J. Li and Y. Peng, Albumin assisted sol-gel synthesized SrSnO3: Pr3+ red persistent phosphors for temperature sensing, *J. Lumin.*, 2021, **239**, 118328.

126 Y. Katayama, J. Ueda and S. Tanabe, Photo-electronic properties and persistent luminescence in Pr3+ doped (Ca,Sr)TiO3 ceramics, *J. Lumin.*, 2014, **148**, 290–295.

127 Y. Jin, Y. Hu, R. Chen, Y. Fu, G. Ju, Z. Mu, J. Lin, Z. Wang, F. Xue and Q. Zhang, Synthesis and luminescence properties of a novel yellowish-pink emissive long persistent luminescence phosphor Cd2GeO4:Pr3+, *J. Alloys Compd.*, 2015, **623**, 255–260.

128 X. Wang and Y. Mao, Recent advances in Pr3+-activated persistent phosphors, *J. Mater. Chem. C*, 2022, **10**, 3626–3646.

129 E. Pinel, P. Boutinaud and R. Mahiou, in *Journal of Alloys and Compounds*, Elsevier, 2004, vol. 380, pp. 225–229.

130 B. Wang, X. Li, Y. Chen, Y. Chen, J. Zhou and Q. Zeng, Long persistent and photo-stimulated luminescence in Pr3+-doped layered perovskite phosphor for optical data storage, *J. Am. Ceram. Soc.*, 2018, **101**, 4598–4607.

131 B. Wang, H. Lin, J. Xu, H. Chen, Z. Lin, F. Huang and Y. Wang, Design, Preparation, and Characterization of a Novel Red Long-Persistent Perovskite Phosphor: Ca3Ti2O7:Pr3+, *Inorg. Chem.*, 2015, **54**, 11299–11306.

132 L. Feng, Z. Wang, C. Cao, T. Zhang, J. Zhang, Z. Ci, Z. Zhao and Y. Wang, Warm-white persistent luminescence of Lu3Al2Ga3O12:Pr3+ phosphor, *J. Rare Earths*, 2017, **35**, 47–52.

133 N. Li, P. Zhang, Z. Wang, Z. Wei, Z. Jiang, Y. Shang, M. Zhang, Q. Qiang, L. Zhao and W. Chen, Novel UV and X-ray irradiated white-emitting persistent luminescence and traps distribution of Ca5Ga6O14: Pr3+ phosphors, *J. Alloys Compd.*, 2021, **858**, 157719.

134 X. Fu, S. Zheng, Y. Meng, W. Sun and H. Zhang, Long afterglow yellow luminescence from Pr3+ doped SrSc2O4, *J. Rare Earths*, 2022, **40**, 567–571.

135 S. Yan, Q. Gao, X. Zhao, A. Wang, Y. Liu, J. Zhang, X. Wang and F. Liu, Charging Gd3Ga5O12:Pr3+ persistent phosphor using blue lasers, *J. Lumin.*, 2020, **226**, 117427.

136 W. B. Dai, Y. F. Lei, J. Zhou, M. Xu, L. L. Chu, L. Li, P. Zhao and Z. H. Zhang, Near-infrared quantum-cutting and long-persistent phosphor Ca3Ga2Ge3O12: Pr3+, Yb3+ for application in in vivo bioimaging and dye-sensitized solar cells, *J. Alloys Compd.*, 2017, **726**, 230–239.

137 S. Zhang, Y. Hu, L. Chen, G. Ju, T. Wang and Z. Wang, Luminescence properties of the pink emitting persistent phosphor Pr 3+ -doped La 3 GaGe 5 O 16, *RSC Adv.*, 2015, **5**, 37172–37179.

138 L. Ji, J. Zhou, J. Zhang, Z. Zhang, Z. Ma, W. Wang, H. Li and C. Wu, A multicolor

persistent luminescent phosphor Sr2Ga2GeO7:Pr3+ for dynamic anticounterfeiting, *J. Am. Ceram. Soc.*, 2019, **102**, 5465–5470.

139 Z. Zou, C. Cao, T. Zhang, L. Feng, J. Zhang, Z. Ci, Z. Zhang and Y. Wang, Structure, long persistent luminescent properties and mechanism of a novel efficient red emitting Ca2Ga2GeO7:Pr3+ phosphor, *J. Alloys Compd.*, 2016, **680**, 397–405.

140 Y. M. Yang, Z. Y. Li, J. Y. Zhang, Y. Lu, S. Q. Guo, Q. Zhao, X. Wang, Z. J. Yong, H. Li, J. P. Ma, Y. Kuroiwa, C. Moriyoshi, L. L. Hu, L. Y. Zhang, L. R. Zheng and H. T. Sun, X-ray-activated long persistent phosphors featuring strong UVC afterglow emissions, *Light Sci. Appl.*, 2018, **7**, 2047–7538.

141 N. Shiran, S. Neicheva, A. Gektin, Y. Boyarintseva, G. Stryganyuk, K. Shimamura and E. Villora, Luminescence of Pr-doped LiCaAlF6 and LiSrAlF6 crystals, *J. Lumin.*, 2009, **129**, 1542–1545.

142 P. Dorenbos, Lanthanide charge transfer energies and related luminescence, charge carrier trapping, and redox phenomena, *J. Alloys Compd.*, , DOI:10.1016/j.jallcom.2008.09.059.

143 A. H. Krumpel, A. J. J. Bos, A. Bessière, E. Van Der Kolk and P. Dorenbos, Controlled electron and hole trapping in YPO4: Ce3+, Ln3+ and LuPO4: Ce3+, Ln3+ (Ln=Sm, Dy, Ho, Er, Tm), *Phys. Rev. B - Condens. Matter Mater. Phys.*, 2009, **80**, 1–10.

144 C. Richard and B. Viana, Persistent X-ray-activated phosphors: mechanisms and applications, *Light Sci. Appl.*, 2022, **11**, 123.

145 H. F. Brito, J. Hölsä, T. Laamanen, Mi. Lastusaari, M. Malkamäki and L. C. V. Rodrigues, Persistent luminescence mechanisms: human imagination at work, *Opt. Mater. Express*, 2012, **2**, 371.

146 P. Boutinaud, E. Pinel, M. Dubois, A. P. Vink and R. Mahiou, UV-to-red relaxation pathways in CaTiO3:Pr3+, *J. Lumin.*, 2005, **111**, 69–80.

147 T. Matsuzawa, Y. Aoki, N. Takeuchi and Y. Murayama, A New Long Phosphorescent Phosphor with High Brightness, SrAl2 O 4 : Eu2 + , Dy3 + , *J. Electrochem. Soc.*, 1996, **143**, 2670.

148 H. Takasaki, S. Tanabe And T. Hanada, Long-Lasting Afterglow Characteristics of Eu, Dy Codoped SrO-Al_2O_3 Phosphor, *J. Ceram. Soc. Japan*, 1996, **104**, 322–326.

149 T. Aitasalo, P. Dereń, J. Hölsä, H. Jungner, J.-C. Krupa, M. Lastusaari, J. Legendziewicz, J. Niittykoski and W. Stręk, Persistent luminescence phenomena in materials doped with

rare earth ions, *J. Solid State Chem.*, 2003, **171**, 114–122.

150 P. Dorenbos, Mechanism of Persistent Luminescence in Eu[sup 2+] and Dy[sup 3+] Codoped Aluminate and Silicate Compounds, *J. Electrochem. Soc.*, 2005, **152**, H107.

151 F. Clabau, X. Rocquefelte, S. Jobic, P. Deniard, M.-H. Whangbo, A. Garcia and T. Le Mercier, Mechanism of Phosphorescence Appropriate for the Long-Lasting Phosphors Eu2+-Doped SrAl2O4 with Codopants Dy3+ and B3+, *Chem. Mater.*, 2005, **17**, 3904–3912.

152 T. Aitasalo, J. Hölsä, H. Jungner, M. Lastusaari and J. Niittykoski, Thermoluminescence Study of Persistent Luminescence Materials: Eu2+- and R3+-Doped Calcium Aluminates, CaAl2O4:Eu2+,R3+, *J. Phys. Chem. B*, 2006, **110**, 4589–4598.

153 P. Boutinaud, E. Pinel and R. Mahiou, Luminescence and afterglow in CaTiO3:Pr3+ films deposited by spray pyrolysis, *Opt. Mater. (Amst).*, 2008, **30**, 1033–1038.

154 M. Rizwan, Z. Usman, M. Shakil, S. S. A. Gillani, S. Azeem, H. B. Jin, C. B. Cao, R. F. Mehmood, G. Nabi and M. A. Asghar, Electronic and optical behaviour of lanthanum doped CaTiO3 perovskite, *Mater. Res. Express*, 2020, **7**, 015920.

155 R. Chen and V. Pagonis, *Thermally and Optically Stimulated Luminescence: A Simulation Approach*, John Wiley and Sons, 2011.

156 Y. Wu and G. Ren, Energy transfer and radiative recombination processes in (Gd,Lu)3Ga3Al2O12:Pr3+ scintillators, *Opt. Mater. (Amst).*, 2013, **35**, 2146–2154.

157 E. Mihóková, M. Fasoli, F. Moretti, M. Nikl, V. Jary´b, J. Jary´b, G. Ren and A. Vedda, Defect states in Pr 3+ doped lutetium pyrosilicate, , DOI:10.1016/j.optmat.2011.11.029.

158 D. Poelman, N. Avci and P. F. Smet, Measured luminance and visual appearance of multi-color persistent phosphors, *Opt. Express*, 2009, **17**, 358.

159 P. F. Smet, N. Avci, K. Van den Eeckhout and D. Poelman, Extending the afterglow in CaAl_2O_4:Eu,Nd persistent phosphors by electron beam annealing, *Opt. Mater. Express*, 2012, **2**, 1306.

160 J. Yang, Y. Liu, Y. Zhao, Z. Gong, M. Zhang, D. Yan, H. Zhu, C. Liu, C. Xu and H. Zhang, Ratiometric Afterglow Nanothermometer for Simultaneous in Situ Bioimaging and Local Tissue Temperature Sensing, *Chem. Mater.*, 2017, **29**, 8119–8131.

161 D. C. Rodríguez Burbano, S. K. Sharma, P. Dorenbos, B. Viana and J. A. Capobianco, Persistent and Photostimulated Red Emission in CaS:Eu $^{2+}$,Dy $^{3+}$ Nanophosphors, *Adv. Opt.*

Mater., 2015, **3**, 551–557.

162 W. Fan, N. Lu, C. Xu, Y. Liu, J. Lin, S. Wang, Z. Shen, Z. Yang, J. Qu, T. Wang, S. Chen, P. Huang and X. Chen, Enhanced Afterglow Performance of Persistent Luminescence Implants for Efficient Repeatable Photodynamic Therapy, *ACS Nano*, 2017, **11**, 5864–5872.

163 S. K. Sharma, D. Gourier, B. Viana, T. Maldiney, E. Teston, D. Scherman and C. Richard, in *Nanoscale Imaging, Sensing, and Actuation for Biomedical Applications XII*, SPIE, 2015, vol. 9337, p. 93370I.

164 C. G. Hadjipanayis and W. Stummer, 5-aminolevulinic acid photodynamic therapy for the treatment of high-grade gliomas, *J. Neurooncol.*, 2019, 141, **3**, 479–486.

165 A. Shergalis, A. Bankhead, U. Luesakul, N. Muangsin and N. Neamati, Current challenges and opportunities in treating glioblastomas, *Pharmacol. Rev.*, 2018, **70**, 412–445.

166 P. Y. Wen, M. Weller, E. Q. Lee, B. M. Alexander, J. S. Barnholtz-Sloan, F. P. Barthel, T. T. Batchelor, R. S. Bindra, S. M. Chang, E. A. Chiocca, T. F. Cloughesy, J. F. DeGroot, E. Galanis, M. R. Gilbert, M. E. Hegi, C. Horbinski, R. Y. Huang, A. B. Lassman, E. Le Rhun, M. Lim, M. P. Mehta, I. K. Mellinghoff, G. Minniti, D. Nathanson, M. Platten, M. Preusser, P. Roth, M. Sanson, D. Schiff, S. C. Short, M. J. B. Taphoorn, J.-C. Tonn, J. Tsang, R. G. W. Verhaak, A. von Deimling, W. Wick, G. Zadeh, D. A. Reardon, K. D. Aldape and M. J. van den Bent, Glioblastoma in adults: a Society for Neuro-Oncology (SNO) and European Society of Neuro-Oncology (EANO) consensus review on current management and future directions, *Neuro. Oncol.*, 2020, **22**, 1073–1113.

167 K. D. Miller, Q. T. Ostrom, C. Kruchko, N. Patil, T. Tihan, G. Cioffi, H. E. Fuchs, K. A. Waite, A. Jemal, R. L. Siegel and J. S. Barnholtz-Sloan, Brain and other central nervous system tumor statistics, 2021, *CA. Cancer J. Clin.*, 2021, **71**, 381–406.

168 S. Gritsch, T. T. Batchelor and L. N. Gonzalez Castro, Diagnostic, therapeutic, and prognostic implications of the 2021 World Health Organization classification of tumors of the central nervous system, *Cancer*, 2022, **128**, 47–58.

169 M. E. Davis, Glioblastoma: Overview of disease and treatment, *Clin. J. Oncol. Nurs.*, 2016, **20**, 1–8.

170 P. D. Delgado-López and E. M. Corrales-García, Survival in glioblastoma: a review on the impact of treatment modalities, *Clin. Transl. Oncol.*, 2016, **18**, 1062–1071.

171 V. M. Lu, T. R. Jue, K. L. McDonald and R. A. Rovin, The Survival Effect of Repeat

Surgery at Glioblastoma Recurrence and its Trend: A Systematic Review and Meta-Analysis, *World Neurosurg.*, 2018, **115**, 453-459.e3.

172 K. L. Chaichana, P. Zadnik, J. D. Weingart, A. Olivi, G. L. Gallia, J. Blakeley, M. Lim, H. Brem and A. Quiñones-Hinojosa, Multiple resections for patients with glioblastoma: prolonging survival, *J. Neurosurg.*, 2013, **118**, 812–820.

173 Y. Jiang and L. Uhrbom, On the origin of glioma, *Ups. J. Med. Sci.*, 2012, **117**, 113–121.

174 F. Seker-Polat, N. P. Degirmenci, I. Solaroglu and T. Bagci-Onder, Tumor Cell Infiltration into the Brain in Glioblastoma: From Mechanisms to Clinical Perspectives, *Cancers (Basel).*, , DOI:10.3390/cancers14020443.

175 Q. Xie, S. Mittal and M. E. Berens, Targeting adaptive glioblastoma: An overview of proliferation and invasion, *Neuro. Oncol.*, 2014, **16**, 1575–1584.

176 A. Torsvik, D. Stieber, P. O. Enger, A. Golebiewska, A. Molven, A. Svendsen, B. Westermark, S. P. Niclou, T. K. Olsen, M. Chekenya Enger and R. Bjerkvig, U-251 revisited: Genetic drift and phenotypic consequences of long-term cultures of glioblastoma cells, *Cancer Med.*, 2014, **3**, 812–824.

177 A. Bairoch, The Cellosaurus, a Cell-Line Knowledge Resource, *J. Biomol. Tech.*, 2018, **29**, 25–38.

178 Cellosaurus U-251MG (CVCL_0021), https://www.cellosaurus.org/CVCL_0021, (accessed 4 February 2023).

179 S. Zhang, S. Endo, H. Koga, T. Ichikawa, X. Feng, K. Onda, K. Washiyama and T. Kumanishi, A Comparative Study of Glioma Cell Lines for p16, p15, p53 and p21 Gene Alterations, *Japanese J. Cancer Res.*, 1996, **87**, 900–907.

180 J. J. Lee, B. C. Kim, M. J. Park, Y. S. Lee, Y. N. Kim, B. L. Lee and J. S. Lee, PTEN status switches cell fate between premature senescence and apoptosis in glioma exposed to ionizing radiation, *Cell Death Differ.*, 2011, **18**, 666–677.

181 N. Ishii, D. Maier, A. Merlo, M. Tada, Y. Sawamura, A.-C. Diserens and E. G. Van Meir, Frequent Co-Alterations of TP53, p16/CDKN2A, p14 ARF , PTEN Tumor Suppressor Genes in Human Glioma Cell Lines., *Brain Pathol.*, 1999, **9**, 469–479.

182 M. Brázdová, T. Quante, L. Tögel, K. Walter, C. Loscher, V. Tichý, L. Činčárová, W. Deppert and G. V. Tolstonog, Modulation of gene expression in U251 glioblastoma cells by binding of mutant p53 R273H to intronic and intergenic sequences, *Nucleic Acids Res.*,

2009, **37**, 1486–1500.

183 W. Wang, B. Cheng, L. Miao, Y. Mei and M. Wu, Mutant p53-R273H gains new function in sustained activation of EGFR signaling via suppressing miR-27a expression, *Cell Death Dis.*, 2013, **4**, e574–e574.

184 R. Kotecha, Y. Odia, A. A. Khosla and M. S. Ahluwalia, Key Clinical Principles in the Management of Glioblastoma, *JCO Oncol. Pract.*, 2023, OP.22.00476.

185 R. Stupp, W. P. Mason, M. J. van den Bent, M. Weller, B. Fisher, M. J. B. Taphoorn, K. Belanger, A. A. Brandes, C. Marosi, U. Bogdahn, J. Curschmann, R. C. Janzer, S. K. Ludwin, T. Gorlia, A. Allgeier, D. Lacombe, J. G. Cairncross, E. Eisenhauer and R. O. Mirimanoff, Radiotherapy plus Concomitant and Adjuvant Temozolomide for Glioblastoma, *N. Engl. J. Med.*, 2005, **352**, 987–996.

186 A. C. Tan, D. M. Ashley, G. Y. López, M. Malinzak, H. S. Friedman and M. Khasraw, Management of glioblastoma: State of the art and future directions, *CA. Cancer J. Clin.*, 2020, **70**, 299–312.

187 L. Bonosi, S. Marrone, U. E. Benigno, F. Buscemi, S. Musso, M. Porzio, M. P. Silven, F. Torregrossa and G. Grasso, Maximal Safe Resection in Glioblastoma Surgery : A Systematic Review of Advanced Intraoperative Image-Guided Techniques, *Brain Sci.*, , DOI:10.17605/OSF.IO/3FDP9.

188 A. J. Schupper, J. A. Roa and C. G. Hadjipanayis, Contemporary intraoperative visualization for GBM with use of exoscope, 5-ALA fluorescence-guided surgery and tractography, *Neurosurg. Focus Video*, 2022, **6**, V5.

189 L. C. Ahrens, M. G. Krabbenhøft, R. W. Hansen, N. Mikic, C. B. Pedersen, F. R. Poulsen and A. R. Korshoej, Effect of 5-Aminolevulinic Acid and Sodium Fluorescein on the Extent of Resection in High-Grade Gliomas and Brain Metastasis, *Cancers (Basel).*, 2022, **14**, 617.

190 D. Von Wettstein, S. Gough and C. G. Kannangara, Chlorophyll biosynthesis, *Plant Cell*, 1995, **7**, 1039–1057.

191 Y. Ohgari, Y. Nakayasu, S. Kitajima, M. Sawamoto, H. Mori, O. Shimokawa, H. Matsui and S. Taketani, Mechanisms involved in δ-aminolevulinic acid (ALA)-induced photosensitivity of tumor cells: Relation of ferrochelatase and uptake of ALA to the accumulation of protoporphyrin, *Biochem. Pharmacol.*, 2005, **71**, 42–49.

192 N. B. Dadario, D. Khatri, N. Reichman, C. D. Nwagwu and R. S. D'Amico, 5-

Aminolevulinic Acid–Shedding Light on Where to Focus, *World Neurosurg.*, 2021, **150**, 9–16.

193 K. McNicholas, M. N. MacGregor and J. M. Gleadle, In order for the light to shine so brightly, the darkness must be present—why do cancers fluoresce with 5-aminolaevulinic acid?, *Br. J. Cancer*, 2019, **121**, 631–639.

194 Aminolevulinic acid hydrochloride, known as ALA HCl (Gleolan, NX Development Corp.) as an optical imaging agent indicated in patients with gliomas, https://www.fda.gov/drugs/resources-information-approved-drugs/aminolevulinic-acid-hydrochloride-known-ala-hcl-gleolan-nx-development-corp-optical-imaging-agent.

195 W. Wang, K. Tabu, Y. Hagiya, Y. Sugiyama, Y. Kokubu, Y. Murota, S. I. Ogura and T. Taga, Enhancement of 5-aminolevulinic acid-based fluorescence detection of side population-defined glioma stem cells by iron chelation, *Sci. Rep.*, 2017, **7**, 1–12.

196 R. Sailer, W. S. L. Strauss, M. Wagner, H. Emmert and H. Schneckenburger, Relation between intracellular location and photodynamic efficacy of 5-aminolevulinic acid-induced protoporphyrin IX in vitro. Comparison between human glioblastoma cells and other cancer cell lines, *Photochem. Photobiol. Sci.*, 2007, **6**, 145–151.

197 T. Kitagawa, J. Yamamoto, T. Tanaka, Y. Nakano, D. Akiba, K. Ueta and S. Nishizawa, 5-Aminolevulinic acid strongly enhances delayed intracellular production of reactive oxygen species (ROS) generated by ionizing irradiation: Quantitative analyses and visualization of intracellular ROS production in glioma cells in vitro, *Oncol. Rep.*, 2015, **33**, 583–590.

198 K. Ueta, J. Yamamoto, T. Tanaka, Y. Nakano, T. Kitagawa and S. Nishizawa, 5-Aminolevulinic acid enhances mitochondrial stress upon ionizing irradiation exposure and increases delayed production of reactive oxygen species and cell death in glioma cells, *Int. J. Mol. Med.*, 2017, **39**, 387–398.

199 S. M. Wu, Q. G. Ren, M. O. Zhou, Q. Peng and J. Y. Chen, Protoporphyrin IX production and its photodynamic effects on glioma cells, neuroblastoma cells and normal cerebellar granule cells in vitro with 5-aminolevulinic acid and its hexylester, *Cancer Lett.*, 2003, **200**, 123–131.

200 M. Mischkulnig, T. Roetzer-Pejrimovsky, D. Lötsch-Gojo, N. Kastner, K. Bruckner, R. Prihoda, A. Lang, M. Martinez-Moreno, J. Furtner, A. Berghoff, A. Woehrer, W. Berger, G. Widhalm and B. Kiesel, Heme Biosynthesis Factors and 5-ALA Induced Fluorescence:

Analysis of mRNA and Protein Expression in Fluorescing and Non-fluorescing Gliomas, *Front. Med.*, 2022, **9**, 1–12.

201 Z. Li, M. Teng, Y. Wang, Q. Wang, Y. Feng, Z. Xiao, C. Li and K. Zeng, The mechanism of 5-aminolevulinic acid photodynamic therapy in promoting endoplasmic reticulum stress in the treatment of HR-HPV-infected HeLa cells, *Photodermatol. Photoimmunol. Photomed.*, 2021, **37**, 348–359.

202 S. G. Zhao, X. F. Chen, L. G. Wang, G. Yang, D. Y. Han, L. Teng, M. C. Yang, D. Y. Wang, C. Shi, Y. H. Liu, B. J. Zheng, C. Bin Shi, X. Gao and N. G. Rainov, Increased expression of ABCB6 enhances protoporphyrin ix accumulation and photodynamic effect in human glioma, *Ann. Surg. Oncol.*, 2013, **20**, 4379–4388.

203 S. W. Cramer and C. C. Chen, Photodynamic Therapy for the Treatment of Glioblastoma, *Front. Surg.*, 2020, **6**, 1–11.

204 T. Ogino, H. Kobuchi, K. Munetomo, H. Fujita, M. Yamamoto, T. Utsumi, K. Inoue, T. Shuin, J. Sasaki, M. Inoue and K. Utsumi, Serum-dependent export of protoporphyrin IX by ATP-binding cassette transporter G2 in T24 cells, *Mol. Cell. Biochem.*, 2011, **358**, 297–307.

205 T. Amo, N. Kawanishi, M. Uchida, H. Fujita, E. Oyanagi, T. Utsumi, T. Ogino, K. Inoue, T. Shuin, K. Utsumi and J. Sasaki, Mechanism of cell death by 5-aminolevulinic acid-based photodynamic action and its enhancement by ferrochelatase inhibitors in human histiocytic lymphoma cell line U937, *Cell Biochem. Funct.*, 2009, **27**, 503–515.

206 M. Abdel-Wahab, S. S. Gondhowiardjo, A. A. Rosa, Y. Lievens, N. El-Haj, J. A. Polo Rubio, G. Ben Prajogi, H. Helgadottir, E. Zubizarreta, A. Meghzifene, V. Ashraf, S. Hahn, T. Williams and M. Gospodarowicz, Global Radiotherapy: Current Status and Future Directions—White Paper, *JCO Glob. Oncol.*, 2021, 827–842.

207 E. P. Sulman, N. Ismaila and S. M. Chang, Radiation Therapy for Glioblastoma: American Society of Clinical Oncology Clinical Practice Guideline Endorsement of the American Society for Radiation Oncology Guideline, *J. Oncol. Pract.*, 2017, **13**, 123–127.

208 M. C. Joiner and A. J. van der Kogel, *Basic Clinical Radiobiology*, CRC Press, Boca Raton, 5th edn., 2018.

209 E. J. Hall, *Radiobiology for the radiologist*, Lippincott Williams & Wilkins, 5th edn., 2000.

210 C. S. Sureka and C. Ampilia, *Radiation Biology for Medical Physicists*, Taylor & Francis,

Boca Raton, 2557, vol. 4.

211 T. R. Munro, The Relative Radiosensitivity of the Nucleus and Cytoplasm of Chinese Hamster Fibroblasts, *Radiat. Res.*, 1970, **42**, 451–470.

212 S. Powell and T. J. McMillan, DNA damage and repair following treatment with ionizing radiation, *Radiother. Oncol.*, 1990, **19**, 95–108.

213 R. X. Huang and P. K. Zhou, *Signal Transduct. Target. Ther.*, 2020, 5, 1–27.

214 M. Podhorecka, A. Skladanowski and P. Bozko, H2AX Phosphorylation: Its Role in DNA Damage Response and Cancer Therapy, *J. Nucleic Acids*, 2010, **2010**, 1–9.

215 D. Grebeňová, K. Kuželová, K. Smetana, M. Pluskalová, H. Cajthamlová, I. Marinov, O. Fuchs, J. Souček, P. Jarolím and Z. Hrkal, Mitochondrial and endoplasmic reticulum stress-induced apoptotic pathways are activated by 5-aminolevulinic acid-based photodynamic therapy in HL60 leukemia cells, *J. Photochem. Photobiol. B Biol.*, 2003, **69**, 71–85.

216 T. Ozaki and A. Nakagawara, Role of p53 in cell death and human cancers, *Cancers (Basel).*, 2011, **3**, 994–1013.

217 L. Xia, S. Tan, Y. Zhou, J. Lin, H. Wang, L. Oyang, Y. Tian, L. Liu, M. Su, H. Wang, D. Cao and Q. Liao, Role of the NFkB-signaling pathway in cancer, *Onco. Targets. Ther.*, 2018, **11**, 2063–2073.

218 T. Liu, L. Zhang, D. Joo and S.-C. Sun, NF-κB signaling in inflammation, *Signal Transduct. Target. Ther.*, 2017, **2**, 17023.

219 T. M. Pawlik and K. Keyomarsi, Role of cell cycle in mediating sensitivity to radiotherapy, *Int. J. Radiat. Oncol. Biol. Phys.*, 2004, **59**, 928–942.

220 S. Zhou, W. Ye, Q. Shao, M. Zhang and J. Liang, Nrf2 is a potential therapeutic target in radioresistance in human cancer, *Crit. Rev. Oncol. Hematol.*, 2013, **88**, 706–715.

221 L. Galluzzi, I. Vitale, S. A. Aaronson, J. M. Abrams, D. Adam, P. Agostinis, E. S. Alnemri, L. Altucci, I. Amelio, D. W. Andrews, M. Annicchiarico-Petruzzelli, A. V. Antonov, E. Arama, E. H. Baehrecke, N. A. Barlev, N. G. Bazan, F. Bernassola, M. J. M. Bertrand, K. Bianchi, M. V. Blagosklonny, K. Blomgren, C. Borner, P. Boya, C. Brenner, M. Campanella, E. Candi, D. Carmona-Gutierrez, F. Cecconi, F. K. M. Chan, N. S. Chandel, E. H. Cheng, J. E. Chipuk, J. A. Cidlowski, A. Ciechanover, G. M. Cohen, M. Conrad, J. R. Cubillos-Ruiz, P. E. Czabotar, V. D'Angiolella, T. M. Dawson, V. L. Dawson, V. De Laurenzi, R. De Maria, K. M. Debatin, R. J. Deberardinis, M. Deshmukh, N. Di Daniele, F.

Di Virgilio, V. M. Dixit, S. J. Dixon, C. S. Duckett, B. D. Dynlacht, W. S. El-Deiry, J. W. Elrod, G. M. Fimia, S. Fulda, A. J. García-Sáez, A. D. Garg, C. Garrido, E. Gavathiotis, P. Golstein, E. Gottlieb, D. R. Green, L. A. Greene, H. Gronemeyer, A. Gross, G. Hajnoczky, J. M. Hardwick, I. S. Harris, M. O. Hengartner, C. Hetz, H. Ichijo, M. Jäättelä, B. Joseph, P. J. Jost, P. P. Juin, W. J. Kaiser, M. Karin, T. Kaufmann, O. Kepp, A. Kimchi, R. N. Kitsis, D. J. Klionsky, R. A. Knight, S. Kumar, S. W. Lee, J. J. Lemasters, B. Levine, A. Linkermann, S. A. Lipton, R. A. Lockshin, C. López-Otín, S. W. Lowe, T. Luedde, E. Lugli, M. MacFarlane, F. Madeo, M. Malewicz, W. Malorni, G. Manic, J. C. Marine, S. J. Martin, J. C. Martinou, J. P. Medema, P. Mehlen, P. Meier, S. Melino, E. A. Miao, J. D. Molkentin, U. M. Moll, C. Muñoz-Pinedo, S. Nagata, G. Nuñez, A. Oberst, M. Oren, M. Overholtzer, M. Pagano, T. Panaretakis, M. Pasparakis, J. M. Penninger, D. M. Pereira, S. Pervaiz, M. E. Peter, M. Piacentini, P. Pinton, J. H. M. Prehn, H. Puthalakath, G. A. Rabinovich, M. Rehm, R. Rizzuto, C. M. P. Rodrigues, D. C. Rubinsztein, T. Rudel, K. M. Ryan, E. Sayan, L. Scorrano, F. Shao, Y. Shi, J. Silke, H. U. Simon, A. Sistigu, B. R. Stockwell, A. Strasser, G. Szabadkai, S. W. G. Tait, D. Tang, N. Tavernarakis, A. Thorburn, Y. Tsujimoto, B. Turk, T. Vanden Berghe, P. Vandenabeele, M. G. Vander Heiden, A. Villunger, H. W. Virgin, K. H. Vousden, D. Vucic, E. F. Wagner, H. Walczak, D. Wallach, Y. Wang, J. A. Wells, W. Wood, J. Yuan, Z. Zakeri, B. Zhivotovsky, L. Zitvogel, G. Melino and G. Kroemer, Molecular mechanisms of cell death: Recommendations of the Nomenclature Committee on Cell Death 2018, *Cell Death Differ.*, 2018, **25**, 486–541.

222 G. Kroemer, L. Galluzzi, P. Vandenabeele, J. Abrams, E. S. Alnemri, E. H. Baehrecke, M. V. Blagosklonny, W. S. El-Deiry, P. Golstein, D. R. Green, M. Hengartner, R. A. Knight, S. Kumar, S. A. Lipton, W. Malorni, G. Nuñez, M. E. Peter, J. Tschopp, J. Yuan, M. Piacentini, B. Zhivotovsky and G. Melino, Classification of cell death: recommendations of the Nomenclature Committee on Cell Death 2009, *Cell Death Differ.*, 2009, **16**, 3–11.

223 Y. Woo, H. J. Lee, Y. M. Jung and Y. J. Jung, Regulated Necrotic Cell Death in Alternative Tumor Therapeutic Strategies, *Cells*, 2020, **9**, 1–17.

224 M. S. D'Arcy, Cell death: a review of the major forms of apoptosis, necrosis and autophagy, *Cell Biol. Int.*, 2019, **43**, 582–592.

225 D. R. Green, Apoptotic Pathways: Ten Minutes to Dead, *Cell*, 2005, **121**, 671–674.

226 N. Shinomiya, New concepts in radiation-induced apoptosis: 'premitotic apoptosis' and

'postmitotic apoptosis', *J. Cell. Mol. Med.*, 2001, **5**, 240–253.

227 P. Price and T. J. McMillan, The use of non-clonogenic assays in measuring the response of cells in vitro to ionising radiation, *Eur. J. Cancer*, 1994, **30**, 838–841.

228 P. P. Connell and S. Hellman, Advances in radiotherapy and implications for the next century: A historical perspective, *Cancer Res.*, 2009, **69**, 383–392.

229 M. Lederman, The early history of radiotherapy: 1895-1939, *Int. J. Radiat. Oncol. Biol. Phys.*, 1981, **7**, 639–648.

230 D. G. Petereit, S. J. Frank, A. N. Viswanathan, B. Erickson, P. Eifel, P. L. Nguyen and D. E. Wazer, Brachytherapy: Where Has It Gone?, *J. Clin. Oncol.*, 2015, **33**, 980–982.

231 H. R. Withers, *The Four R's of Radiotherapy*, ACADEMIC PRESS, INC., 1975, vol. 5.

232 M. D. Walker, T. A. Strike and G. E. Sheline, An analysis of dose-effect relationship in the radiotherapy of malignant gliomas, *Int. J. Radiat. Oncol. Biol. Phys.*, 1979, **5**, 1725–1731.

233 G. Minniti, V. De Sanctis, R. Muni, F. Filippone, A. Bozzao, M. Valeriani, M. F. Osti, U. De Paula, G. Lanzetta, V. Tombolini and R. Maurizi Enrici, Radiotherapy plus concomitant and adjuvant temozolomide for glioblastoma in elderly patients, *J. Neurooncol.*, 2008, **88**, 97–103.

234 C. Herskind, L. Ma, Q. Liu, B. Zhang, F. Schneider, M. R. Veldwijk and F. Wenz, Biology of high single doses of IORT: RBE, 5 R's, and other biological aspects, *Radiat. Oncol.*, 2017, **12**, 1–14.

235 F. A. Calvo, R. M. Meirino and R. Orecchia, Intraoperative radiation therapy. First part: Rationale and techniques, *Crit. Rev. Oncol. Hematol.*, 2006, **59**, 106–115.

236 C. P. Cifarelli and G. M. Jacobson, Intraoperative Radiotherapy in Brain Malignancies: Indications and Outcomes in Primary and Metastatic Brain Tumors, *Front. Oncol.*, , DOI:10.3389/fonc.2021.768168.

237 J. A. Vargo, K. M. Sparks, R. Singh, G. M. Jacobson, J. D. Hack and C. P. Cifarelli, Feasibility of dose escalation using intraoperative radiotherapy following resection of large brain metastases compared to post-operative stereotactic radiosurgery, *J. Neurooncol.*, 2018, **140**, 413–420.

238 K.-H. Kahl, N. Balagiannis, M. Höck, S. Schill, Z. Roushan, E. Shiban, H. Müller, U. Grossert, I. Konietzko, B. Sommer, C. J. Maurer, A. Berlis, V. Heidecke, T. Janzen and G. Stüben, Intraoperative radiotherapy with low-energy x-rays after neurosurgical resection of

brain metastases—an Augsburg University Medical Center experience, *Strahlentherapie und Onkol.*, 2021, **197**, 1124–1130.

239 F. A. Giordano, S. Brehmer, B. Mürle, G. Welzel, E. Sperk, A. Keller, Y. Abo-Madyan, E. Scherzinger, S. Clausen, F. Schneider, C. Herskind, M. Glas, M. Seiz-Rosenhagen, C. Groden, D. Hänggi, P. Schmiedek, B. Emami, L. Souhami, K. Petrecca and F. Wenz, Intraoperative Radiotherapy in Newly Diagnosed Glioblastoma (INTRAGO): An open-label, dose-escalation Phase I/II trial, *Clin. Neurosurg.*, 2019, **84**, 41–49.

240 C. P. Cifarelli, S. Brehmer, J. A. Vargo, J. D. Hack, K. H. Kahl, G. Sarria-Vargas and F. A. Giordano, Intraoperative radiotherapy (IORT) for surgically resected brain metastases: outcome analysis of an international cooperative study, *J. Neurooncol.*, 2019, **145**, 391–397.

241 C. Herskind and F. Wenz, Radiobiological aspects of intraoperative tumour-bed irradiation with low-energy X-rays (LEX-IORT), *Transl. Cancer Res.*, 2014, **3**, 3–17.

242 A. Sethi, B. Emami, W. Small and T. O. Thomas, Intraoperative Radiotherapy With INTRABEAM: Technical and Dosimetric Considerations, *Front. Oncol.*

243 G. R. Sarria, E. Sperk, H. Xiaodi, G. J. Sarria, F. Wenz, S. Brehmer, B. Fu, S. Min, H. Zhang, S. Qin, X. Qiu, Y. Abo-Madyan, D. Hänggi, D. A. Martinez, C. Cabrera and F. A. Giordano, Intraoperative Radiotherapy for Glioblastoma: An International Pooled Analysis, *Int. J. Radiat. Oncol.*, 2019, **105**, E107–E108.

244 Y. Saleh and H. Zhang, Technical Note: Dosimetric impact of spherical applicator size in Intrabeam^{TM} IORT for treating unicentric breast cancer lesions, *Med. Phys.*, 2017, **44**, 6706–6714.

245 P. Schueller, O. Micke, S. Palkovic, J. Schroeder, C. Moustakis, F. Bruns, A. Schuck, H. Wassmann and N. Willich, 12 Years' experience with intraoperative radiotherapy (IORT) of malignant gliomas, *Strahlentherapie und Onkol.*, 2005, **181**, 500–506.

246 M. R. Veldwijk, B. Zhang, F. Wenz and C. Herskind, The biological effect of large single doses: A possible role for non-targeted effects in cell inactivation, *PLoS One*, 2014, **9**, 1–8.

247 L. Minafra and V. Bravatà, Cell and molecular response to IORT treatment, *Transl. Cancer Res.*, 2014, **3**, 32–47.

248 N. B. Pepper, W. Stummer and H. T. Eich, *Strahlentherapie und Onkol.*, 2022, 198, 507–526.

249 B. T. Oronsky, S. J. Knox and J. Scicinski, Six degrees of separation: The oxygen effect in the development of radiosensitizers, *Transl. Oncol.*, 2011, **4**, 189–198.

250 L. J. Ostruszka and D. S. Shewach, The Role of Cell Cycle Progression in Radiosensitization by 2′,2′-Difluoro-2′-deoxycytidine1, *Cancer Res.*, 2000, **60**, 6080–6088.

251 Y. Harasaki and A. Waziri, Potential Usefulness of Radiosensitizers in Glioblastoma, *Neurosurg. Clin. N. Am.*, 2012, **23**, 429–437.

252 A. Yokoya and T. Ito, Photon-induced Auger effect in biological systems: a review, *Int. J. Radiat. Biol.*, 2017, **93**, 743–756.

253 D. Larson, W. J. Bodell, C. Ling, T. L. Phillips, M. Schell, D. Shrieve and T. Troxel, Auger electron contribution to bromodeoxyuridine cellular radiosensitization, *Int. J. Radiat. Oncol.*, 1989, **16**, 171–176.

254 D. R. Cooper, D. Bekah and J. L. Nadeau, Gold nanoparticles and their alternatives for radiation therapy enhancement, *Front. Chem.*, 2014, **2**, 86.

255 H. Pan, X. Wang, A. Feng, Q. Cheng, X. Chen, X. He, X. Qin, X. Sha, S. Fu, C. Chi and X. Wang, Nanoparticle radiosensitization: From extended local effect modeling to a survival modification framework of compound Poisson additive killing and its carbon dots validation, *Phys. Med. Biol.*, , DOI:10.1088/1361-6560/ac4c48.

256 S. J. McMahon, H. Paganetti and K. M. Prise, Optimising element choice for nanoparticle radiosensitisers, *Nanoscale*, 2016, **8**, 581–589.

257 E. Brun and C. Sicard-Roselli, Actual questions raised by nanoparticle radiosensitization, *Radiat. Phys. Chem.*, 2016, **128**, 134–142.

258 J. Schuemann, A. F. Bagley, R. Berbeco, K. Bromma, K. T. Butterworth, H. L. Byrne, B. D. Chithrani, S. H. Cho, J. R. Cook, V. Favaudon, Y. H. Gholami, E. Gargioni, J. F. Hainfeld, F. Hespeels, A. C. Heuskin, U. M. Ibeh, Z. Kuncic, S. Kunjachan, S. Lacombe, S. Lucas, F. Lux, S. McMahon, D. Nevozhay, W. Ngwa, J. D. Payne, S. Penninckx, E. Porcel, K. M. Prise, H. Rabus, S. M. Ridwan, B. Rudek, L. Sanche, B. Singh, H. M. Smilowitz, K. V. Sokolov, S. Sridhar, Y. Stanishevskiy, W. Sung, O. Tillement, N. Virani, W. Yantasee and S. Krishnan, Roadmap for metal nanoparticles in radiation therapy: Current status, translational challenges, and future directions, *Phys. Med. Biol.*, , DOI:10.1088/1361-6560/ab9159.

259 S. J. McMahon, W. B. Hyland, M. F. Muir, J. A. Coulter, S. Jain, K. T. Butterworth, G.

Schettino, G. R. Dickson, A. R. Hounsell, J. M. O'Sullivan, K. M. Prise, D. G. Hirst and F. J. Currell, Biological consequences of nanoscale energy deposition near irradiated heavy atom nanoparticles, *Sci. Rep.*, 2011, **1**, 1–10.

260 L. Meitner, Über dieβ-Strahl-Spektra und ihren Zusammenhang mit der γ-Strahlung, *Zeitschrift für Phys.*, 1922, **11**, 35–54.

261 L. Meitner, Das β-Strahlenspektrum von UX1 und seine Deutung, *Zeitschrift für Phys.*, 1923, **17**, 54–66.

262 P. Auger, Sur l'effet photoélectrique composé, *J. Phys. le Radium*, 1925, **6**, 205–208.

263 A. Bulin, M. Broekgaarden, F. Chaput, V. Baisamy, J. Garrevoet, B. Busser, D. Brueckner, A. Youssef, J. Ravanat, C. Dujardin, V. Motto-Ros, F. Lerouge, S. Bohic, L. Sancey and H. Elleaume, Radiation Dose-Enhancement Is a Potent Radiotherapeutic Effect of Rare-Earth Composite Nanoscintillators in Preclinical Models of Glioblastoma, *Adv. Sci.*, 2020, **7**, 2001675.

264 J. F. Hainfeld, D. N. Slatkin, T. M. Focella and H. M. Smilowitz, Gold nanoparticles: a new X-ray contrast agent, *Br. J. Radiol.*, 2006, **79**, 248–253.

265 James F Hainfeld, Daniel N Slatkin and Henry M Smilowitz, The use of gold nanoparticles to enhance radiotherapy in mice, *Phys. Med. Biol.*, 2004, **49**, N309.

266 A. Subiel, R. Ashmore and G. Schettino, Standards and Methodologies for Characterizing Radiobiological Impact of High-Z Nanoparticles, *Theranostics*, 2016, **6**, 1651–1671.

267 S. Bonvalot, E. Wardelmann and C. Le Péchoux, High Z nanoparticles and radiotherapy: a critical view – Authors' reply, *Lancet Oncol.*, 2019, **20**, e558.

268 L. Maggiorella, G. Barouch, C. Devaux, A. Pottier, E. Deutsch, J. Bourhis, E. Borghi and L. Levy, Nanoscale radiotherapy with hafnium oxide nanoparticles, *Futur. Oncol.*, 2012, **8**, 1167–1181.

269 L. Maggiorella, G. Barouch, C. Devaux, A. Pottier, E. Deutsch, J. Bourhis, E. Borghi and L. Levy, Nanoscale radiotherapy with hafnium oxide nanoparticles, *Futur. Oncol.*, 2012, **8**, 1167–1181.

270 F. Lux, A. Mignot, P. Mowat, C. Louis, S. Dufort, C. Bernhard, F. Denat, F. Boschetti, C. Brunet, R. Antoine, P. Dugourd, S. Laurent, L. Vander Elst, R. Muller, L. Sancey, V. Josserand, J.-L. Coll, V. Stupar, E. Barbier, C. Rémy, A. Broisat, C. Ghezzi, G. Le Duc, S. Roux, P. Perriat and O. Tillement, Ultrasmall Rigid Particles as Multimodal Probes for

Medical Applications, *Angew. Chemie Int. Ed.*, 2011, **50**, 12299–12303.

271 C. Verry, S. Dufort, J. Villa, M. Gavard, C. Iriart, S. Grand, J. Charles, B. Chovelon, J.-L. Cracowski, J.-L. Quesada, C. Mendoza, L. Sancey, A. Lehmann, F. Jover, J.-Y. Giraud, F. Lux, Y. Crémillieux, S. McMahon, P. J. Pauwels, D. Cagney, R. Berbeco, A. Aizer, E. Deutsch, M. Loeffler, G. Le Duc, O. Tillement and J. Balosso, Theranostic AGuIX nanoparticles as radiosensitizer: A phase I, dose-escalation study in patients with multiple brain metastases (NANO-RAD trial), *Radiother. Oncol.*, 2021, **160**, 159–165.

272 M. Toussaint, S. Pinel, F. Auger, N. Durieux, M. Thomassin, E. Thomas, A. Moussaron, D. Meng, F. Plénat, M. Amouroux, T. Bastogne, C. Frochot, O. Tillement, F. Lux and M. Barberi-Heyob, Proton MR Spectroscopy and Diffusion MR Imaging Monitoring to Predict Tumor Response to Interstitial Photodynamic Therapy for Glioblastoma, *Theranostics*, 2017, **7**, 436–451.

273 J. Daouk, M. Iltis, B. Dhaini, D. Béchet, P. Arnoux, P. Rocchi, A. Delconte, B. Habermeyer, F. Lux, C. Frochot, O. Tillement, M. Barberi-Heyob and H. Schohn, Terbium-based AGuiX-design nanoparticle to mediate x-ray-induced photodynamic therapy, *Pharmaceuticals*, 2021, **14**, 1–21.

274 A. F. McDonagh, Phototherapy: From ancient egypt to the new millennium, *J. Perinatol.*, 2001, **21**, S7–S12.

275 J. D. Spikes, in *Primary Photo-Processes in Biology and Medicine*, eds. R. V. Bensasson, G. Jori, E. J. Land and T. G. Truscott, Springer US, Boston, MA, 1985, pp. 209–227.

276 M. D. Daniell and J. S. Hill, A HISTORY OF PHOTODYNAMIC THERAPY, *ANZ J. Surg.*, 1991, **61**, 340–348.

277 S. Maehara and N. Ikeda, *Photodynamic Therapy*, Springer Berlin Heidelberg, Berlin, Heidelberg, 2014, vol. 71.

278 L. I. Grossweiner, *The Science of Phototherapy*, 2005.

279 H. Bloch, Solar Theology, heliotherapy and biologic effects: a historical overview, *J. Natl. Med. Abbrogation*.

280 A. Grzybowski, J. Sak and J. Pawlikowski, A brief report on the history of phototherapy, *Clin. Dermatol.*, 2016, **34**, 532–537.

281 H. Hönigsmann, History of phototherapy in dermatology, *Photochem. Photobiol. Sci.*, 2013, **12**, 16–21.

282 O. RAAB, Uber die wirkung fluoreszierender stoffe auf infusorien, *Zeitschr Biol*, 1900, **39**, 524–546.

283 R. R. Allison, G. H. Downie, R. Cuenca, X. H. Hu, C. J. H. Childs and C. H. Sibata, Photosensitizers in clinical PDT, *Photodiagnosis Photodyn. Ther.*, 2004, **1**, 27–42.

284 M. H. Abdel-kader, Chapter 1. The Journey of PDT Throughout History: PDT from Pharos to Present, *Journey PDT Throughout Hist. PDT from Pharos to Present*, 2016, 1–21.

285 A. Jodlbauer and H. Von Tappeiner, On the participation of oxygen in the photodynamic effect of fluorescent substances, *Münch Med Wochenschr*, 1904, **52**, 1139–1141.

286 A. Jesionek and H. Von Tappeiner, On the treatment of skin cancers with fluorescent substances, *Arch Klin Med*, 1905, **82**, 223–227.

287 A. Policard, Etude sur les aspects offerts par des tumeurs experimentales examinees a la lumiere de Wood, *Comptes Rendus des Séances la Société Biol.*, 1924, **91**, 1423–1424.

288 H. Auler and G. Banzer, Untersuchungen über die Rolle der Porphyrine bei geschwulstkranken Menschen und Tieren, *Z. Krebsforsch.*, 1942, **53**, 65–68.

289 C. A. Robertson, D. H. Evans and H. Abrahamse, Photodynamic therapy (PDT): A short review on cellular mechanisms and cancer research applications for PDT, *J. Photochem. Photobiol. B Biol.*, 2009, **96**, 1–8.

290 A. P. Castano, T. N. Demidova and M. R. Hamblin, Mechanisms in photodynamic therapy: part one—photosensitizers, photochemistry and cellular localization, *Photodiagnosis Photodyn. Ther.*, 2004, **1**, 279–293.

291 C. S. Foot, Definition of Type I and Type I1, *Photochem. Photobiol.*, 1991, **54**, 659.

292 M. S. Baptista, J. Cadet, P. Di Mascio, A. A. Ghogare, A. Greer, M. R. Hamblin, C. Lorente, S. C. Nunez, M. S. Ribeiro, A. H. Thomas, M. Vignoni and T. M. Yoshimura, Type I and Type II Photosensitized Oxidation Reactions: Guidelines and Mechanistic Pathways, *Photochem. Photobiol.*, 2017, **93**, 912–919.

293 A. Baker and J. R. Kanofsky, Quenching of singlet oxygen by biomolecules from L1210 leukemia cells, *Photochem. Photobiol.*, 1992, **55**, 523–528.

294 S. Callaghan and M. O. Senge, The good, the bad, and the ugly-controlling singlet oxygen through design of photosensitizers and delivery systems for photodynamic therapy, *Photochem. Photobiol. Sci.*, 2018, **17**, 1490–1514.

295 H. Ding, H. Yu, Y. Dong, R. Tian, G. Huang, D. A. Boothman, B. D. Sumer and J. Gao,

Photoactivation switch from type II to type I reactions by electron-rich micelles for improved photodynamic therapy of cancer cells under hypoxia, *J. Control. Release*, 2011, **156**, 276–280.

296 S. Bonnet, Why develop photoactivated chemotherapy?, *Dalt. Trans.*, 2018, **47**, 10330–10343.

297 D. Kessel, Photodynamic Therapy: Critical PDT Theory †, *Photochem. Photobiol.*, , DOI:10.1111/php.13616.

298 G. M. Cramer, K. A. Cengel and T. M. Busch, Forging Forward in Photodynamic Therapy, *Cancer Res.*, 2022, **82**, 534–536.

299 K. Moghissi and R. R. Allison, *A narrative history of photodynamic therapy*, LTD, 2023.

300 G. Kroemer, L. Galluzzi, O. Kepp and L. Zitvogel, Immunogenic Cell Death in Cancer Therapy, *Annu. Rev. Immunol.*, 2013, **31**, 51–72.

301 T. Mishchenko, I. Balalaeva, A. Gorokhova, M. Vedunova and D. V. Krysko, Which cell death modality wins the contest for photodynamic therapy of cancer?, *Cell Death Dis.*, 2022, **13**, 1–16.

302 A. D. Garg, L. Galluzzi, L. Apetoh, T. Baert, R. B. Birge, J. M. Bravo-San Pedro, K. Breckpot, D. Brough, R. Chaurio, M. Cirone, A. Coosemans, P. G. Coulie, D. De Ruysscher, L. Dini, P. de Witte, A. M. Dudek-Peric, A. Faggioni, J. Fucikova, U. S. Gaipl, J. Golab, M. L. Gougeon, M. R. Hamblin, A. Hemminki, M. Herrmann, J. W. Hodge, O. Kepp, G. Kroemer, D. V. Krysko, W. G. Land, F. Madeo, A. A. Manfredi, S. R. Mattarollo, C. Maueroder, N. Merendino, G. Multhoff, T. Pabst, J. E. Ricci, C. Riganti, E. Romano, N. Rufo, M. J. Smyth, J. Sonnemann, R. Spisek, J. Stagg, E. Vacchelli, P. Vandenabeele, L. Vandenberk, B. J. Van den Eynde, S. Van Gool, F. Velotti, L. Zitvogel and P. Agostinis, Molecular and translational classifications of DAMPs in immunogenic cell death, *Front. Immunol.*, 2015, **6**, 1–24.

303 S. W. Cramer and C. C. Chen, Photodynamic Therapy for the Treatment of Glioblastoma, *Front. Surg.*, , DOI:10.3389/fsurg.2019.00081.

304 C. Ash, M. Dubec, K. Donne and T. Bashford, Effect of wavelength and beam width on penetration in light-tissue interaction using computational methods, *Lasers Med. Sci.*, 2017, **32**, 1909–1918.

305 F. H. Mustafa and M. S. Jaafar, Comparison of wavelength-dependent penetration depths

of lasers in different types of skin in photodynamic therapy, *Indian J. Phys.*, 2013, **87**, 203–209.

306 V. Torres and L. Torezan, Light treatment and photodynamic therapy in acne patients with pigmented skin, *Light. Ther. Ski. Color*, 2009, 249–261.

307 S. Schipmann, M. Müther, L. Stögbauer, S. Zimmer, B. Brokinkel, M. Holling, O. Grauer, E. S. Molina, N. Warneke and W. Stummer, in *Journal of Neurosurgery*, American Association of Neurological Surgeons, 2021, vol. 134, pp. 426–436.

308 R. R. Allison and K. Moghissi, Photodynamic therapy (PDT): PDT mechanisms, *Clin. Endosc.*, 2013, **46**, 24–29.

309 A. E. O'Connor, W. M. Gallagher and A. T. Byrne, Porphyrin and nonporphyrin photosensitizers in oncology: Preclinical and clinical advances in photodynamic therapy, *Photochem. Photobiol.*, 2009, **85**, 1053–1074.

310 M. R. Hamblin, Photodynamic Therapy for Cancer: What's Past is Prologue, *Photochem. Photobiol.*, 2020, **96**, 506–516.

311 J. C. Kennedy, R. H. Pottier and D. C. Pross, Photodynamic therapy with endogenous protoporphyrin. IX: Basic principles and present clinical experience, *J. Photochem. Photobiol. B Biol.*, 1990, **6**, 143–148.

312 B. Krammer and K. Plaetzer, ALA and its clinical impact, from bench to bedside, *Photochem. Photobiol. Sci.*, 2008, **7**, 283–289.

313 H. A. Leroy, L. Guérin, F. Lecomte, G. Baert, A. S. Vignion, S. Mordon and N. Reyns, Is interstitial photodynamic therapy for brain tumors ready for clinical practice? A systematic review, *Photodiagnosis Photodyn. Ther.*, , DOI:10.1016/j.pdpdt.2021.102492.

314 P.-J. Lou, H. R. Jäger, L. Jones, T. Theodossy, S. G. Bown and C. Hopper, Interstitial photodynamic therapy as salvage treatment for recurrent head and neck cancer, *Br. J. Cancer*, 2004, **91**, 441–446.

315 G. Shafirstein, D. Bellnier, E. Oakley, S. Hamilton, M. Potasek, K. Beeson and E. Parilov, *Cancers (Basel).*, 2017, 9.

316 K. Komolibus, C. Fisher, J. Swartling, S. Svanberg, K. Svanberg and S. Andersson-Engels, Perspectives on interstitial photodynamic therapy for malignant tumors, *J. Biomed. Opt.*, 2021, **26**, 1–23.

317 M. Vermandel, C. Dupont, F. Lecomte, H. A. Leroy, C. Tuleasca, S. Mordon, C. G.

Hadjipanayis and N. Reyns, Standardized intraoperative 5-ALA photodynamic therapy for newly diagnosed glioblastoma patients: a preliminary analysis of the INDYGO clinical trial, *J. Neurooncol.*, 2021, **152**, 501–514.

318 R. R. Allison, Photodynamic therapy: Oncologic horizons, *Futur. Oncol.*, 2014, **10**, 123–142.

319 R. R. Allison, G. H. Downie, R. Cuenca, X. H. Hu, C. J. Childs and C. H. Sibata, Photosensitizers in clinical PDT, *Photodiagnosis Photodyn. Ther.*, 2004, **1**, 27–42.

320 B. W. Pogue, J. T. Elliott, S. C. Kanick, S. C. Davis, K. S. Samkoe, E. V. Maytin, S. P. Pereira and T. Hasan, Revisiting photodynamic therapy dosimetry: Reductionist & surrogate approaches to facilitate clinical success, *Phys. Med. Biol.*, 2016, **61**, R57–R89.

321 A. Johansson, F. Faber, G. Kniebühler, H. Stepp, R. Sroka, R. Egensperger, W. Beyer and F.-W. Kreth, Protoporphyrin IX Fluorescence and Photobleaching During Interstitial Photodynamic Therapy of Malignant Gliomas for Early Treatment Prognosis, *Lasers Surg. Med.*, 2013, **45**, 225–234.

322 S. Mallidi, S. Anbil, S. Lee, D. Manstein, S. Elrington, G. Kositratna, D. Schoenfeld, B. Pogue, S. J. Davis and T. Hasan, Photosensitizer fluorescence and singlet oxygen luminescence as dosimetric predictors of topical 5-aminolevulinic acid photodynamic therapy nduced clinical erythema, *J. Biomed. Opt.*, 2014, **19**, 028001.

323 Y. Liu, W. Chen, S. Wang and A. G. Joly, Investigation of water-soluble x-ray luminescence nanoparticles for photodynamic activation, *Appl. Phys. Lett.*, 2008, **92**, 1–4.

324 N. Y. Morgan, G. Kramer-Marek, P. D. Smith, K. Camphausen and J. Capala, Nanoscintillator conjugates as photodynamic therapy-based radiosensitizers: Calculation of required physical parameters, *Radiat. Res.*, 2009, **171**, 236–244.

325 J. C. Finlay, PDT driven by energy-converting materials: a theoretical analysis, in *Proc.SPIE*, 2009, vol. 7164, p. 71640Y.

326 D. L. Andrews and J. Rodríguez, Resonance energy transfer: Spectral overlap, efficiency, and direction, *J. Chem. Phys.*, , DOI:10.1063/1.2759489.

327 P. R. Selvin, Lanthanide-Based Resonance Energy Transfer, *IEEE J. Sel. Top. QUANTUM Electron.*, 1996, **2**, 1077–1087.

328 Forster, Energiewanderung und Fluoreszenz, *Naturwissenschaften*, 1946, **33**, 166–175.

329 T. Förster, Energy migration and fluorescence, *J. Biomed. Opt.*, 2012, **17**, 011002.

330 H. Sahoo, *J. Photochem. Photobiol. C Photochem. Rev.*, 2011, 12, 20–30.

331 J. C. G. Bünzli, On the design of highly luminescent lanthanide complexes, *Coord. Chem. Rev.*, 2015, **293**–**294**, 19–47.

332 O. L. Malta, Mechanisms of non-radiative energy transfer involving lanthanide ions revisited, *J. Non. Cryst. Solids*, 2008, **354**, 4770–4776.

333 Y. Tang, J. Hu, A. H. Elmenoufy and X. Yang, Highly Efficient FRET System Capable of Deep Photodynamic Therapy Established on X-ray Excited Mesoporous LaF3:Tb Scintillating Nanoparticles, *ACS Appl. Mater. Interfaces*, 2015, **7**, 12261–12269.

334 W. Zhang, X. Zhang, Y. Shen, F. Shi, C. Song, T. Liu, P. Gao, B. Lan, M. Liu, S. Wang, L. Fan and H. Lu, Ultra-high FRET efficiency NaGdF4: Tb3+-Rose Bengal biocompatible nanocomposite for X-ray excited photodynamic therapy application, *Biomaterials*, 2018, **184**, 31–40.

335 X. Zhang, B. Lan, S. Wang, P. Gao, T. Liu, J. Rong, F. Xiao, L. Wei, H. Lu, C. Pang, L. Fan, W. Zhang and H. Lu, Low-Dose X-ray Excited Photodynamic Therapy Based on NaLuF 4 :Tb 3 + –Rose Bengal Nanocomposite, *Bioconjug. Chem.*, 2019, **30**, 2191–2200.

336 F. Ahmad, X. Wang, Z. Jiang, X. Yu, X. Liu, R. Mao, X. Chen and W. Li, Codoping Enhanced Radioluminescence of Nanoscintillators for X-ray-Activated Synergistic Cancer Therapy and Prognosis Using Metabolomics, *ACS Nano*, 2019, **13**, 10419–10433.

337 R. W. Redmond and J. N. Gamlin, A Compilation of Singlet Oxygen Yields from Biologically Relevant Molecules, *Photochem. Photobiol.*, 1999, **70**, 391–475.

338 X. Chen, J. Liu, Y. Li, N. K. Pandey, T. Chen, L. Wang, E. H. Amador, W. Chen, F. Liu, E. Xiao and W. Chen, Study of copper-cysteamine based X-ray induced photodynamic therapy and its effects on cancer cell proliferation and migration in a clinical mimic setting, *Bioact. Mater.*, 2022, **7**, 504–514.

339 F. Jiang, C. Lee, W. Zhang, W. Jiang, Z. Cao, H. B. Chong, W. Yang, S. Zhan, J. Li, Y. Teng, Z. Li and J. Xie, Radiodynamic therapy with CsI(na)@MgO nanoparticles and 5-aminolevulinic acid, *J. Nanobiotechnology*, 2022, **20**, 330.

340 K. Kirakci, P. Kubát, K. Fejfarová, J. Martinčík, M. Nikl and K. Lang, X-ray Inducible Luminescence and Singlet Oxygen Sensitization by an Octahedral Molybdenum Cluster Compound: A New Class of Nanoscintillators, *Inorg. Chem.*, 2016, **55**, 803–809.

341 K. Lu, C. He, N. Guo, C. Chan, K. Ni, G. Lan, H. Tang, C. Pelizzari, Y.-X. Fu, M. T.

Spiotto, R. R. Weichselbaum and W. Lin, Low-dose X-ray radiotherapy–radiodynamic therapy via nanoscale metal–organic frameworks enhances checkpoint blockade immunotherapy, *Nat. Biomed. Eng.*, 2018, **2**, 600–610.

342 N. Shah, J. Squire, M. Guirguis, D. Saha, K. Hoyt, K. K.-H. Wang, V. Agarwal and G. Obaid, Deep-Tissue Activation of Photonanomedicines: An Update and Clinical Perspectives, *Cancers (Basel).*, 2022, **14**, 2004.

343 M. J. Niedre, A. J. Secord, M. S. Patterson and B. C. Wilson, In Vitro Tests of the Validity of Singlet Oxygen Luminescence Measurements as a Dose Metric in Photodynamic Therapy, *Cancer Res.*, 2003, **63**, 7986–7994.

344 A. L. Bulin, C. Truillet, R. Chouikrat, F. Lux, C. Frochot, D. Amans, G. Ledoux, O. Tillement, P. Perriat, M. Barberi-Heyob and C. Dujardin, X-ray-induced singlet oxygen activation with nanoscintillator-coupled porphyrins, *J. Phys. Chem. C*, , DOI:10.1021/jp4077189.

345 S. Clement, W. Deng, E. Camilleri, B. C. Wilson and E. M. Goldys, X-ray induced singlet oxygen generation by nanoparticle-photosensitizer conjugates for photodynamic therapy: determination of singlet oxygen quantum yield, *Sci. Rep.*, 2016, **6**, 19954.

346 X. Zou, M. Yao, L. Ma, M. Hossu, X. Han, P. Juzenas and W. Chen, X-ray-induced nanoparticle-based photodynamic therapy of cancer, *Nanomedicine*, 2014, **9**, 2339–2351.

347 C. Zhang, K. Zhao, W. Bu, D. Ni, Y. Liu, J. Feng and J. Shi, Marriage of scintillator and semiconductor for synchronous radiotherapy and deep photodynamic therapy with diminished oxygen dependence, *Angew. Chemie - Int. Ed.*, 2015, **54**, 1770–1774.

348 A. H. Elmenoufy, Y. Tang, J. Hu, H. Xu and X. Yang, A novel deep photodynamic therapy modality combined with CT imaging established via X-ray stimulated silica-modified lanthanide scintillating nanoparticles, *Chem. Commun.*, 2015, **51**, 12247–12250.

349 F. Rossi, E. Bedogni, F. Bigi, T. Rimoldi, L. Cristofolini, S. Pinelli, R. Alinovi, M. Negri, S. C. Dhanabalan, G. Attolini, F. Fabbri, M. Goldoni, A. Mutti, G. Benecchi, C. Ghetti, S. Iannotta and G. Salviati, Porphyrin conjugated SiC/SiOx nanowires for X-ray-excited photodynamic therapy, *Sci. Rep.*, 2015, **5**, 7606.

350 G. D. Wang, H. T. Nguyen, H. Chen, P. B. Cox, L. Wang, K. Nagata, Z. Hao, A. Wang, Z. Li and J. Xie, X-ray induced photodynamic therapy: A combination of radiotherapy and photodynamic therapy, *Theranostics*, 2016, **6**, 2295–2305.

351 S. Clement, W. Chen, W. Deng and E. M. Goldys, X-ray radiation-induced and targeted photodynamic therapy with folic acid-conjugated biodegradable nanoconstructs, *Int. J. Nanomedicine*, 2018, **13**, 3553–3570.

352 X. Yu, X. Liu, W. Wu, K. Yang, R. Mao, F. Ahmad, X. Chen and W. Li, CT/MRI-Guided Synergistic Radiotherapy and X-ray Inducible Photodynamic Therapy Using Tb-Doped Gd-W-Nanoscintillators, *Angew. Chemie Int. Ed.*, 2019, **58**, 2017–2022.

353 W. Sun, T. Shi, L. Luo, X. Chen, P. Lv, Y. Lv, Y. Zhuang, J. Zhu, G. Liu, X. Chen and H. Chen, Monodisperse and Uniform Mesoporous Silicate Nanosensitizers Achieve Low-Dose X-Ray-Induced Deep-Penetrating Photodynamic Therapy, *Adv. Mater.*, 2019, **31**, 1808024.

354 X. Zhong, X. Wang, G. Zhan, Y. Tang, Y. Yao, Z. Dong, L. Hou, H. Zhao, S. Zeng, J. Hu, L. Cheng and X. Yang, NaCeF4:Gd,Tb Scintillator as an X-ray Responsive Photosensitizer for Multimodal Imaging-Guided Synchronous Radio/Radiodynamic Therapy, *Nano Lett.*, 2019, **19**, 8234–8244.

355 M. Müller, Y. Wang, M. R. Squillante, K. D. Held, R. R. Anderson and M. Purschke, UV scintillating particles as radiosensitizer enhance cell killing after X-ray excitation, *Radiother. Oncol.*, 2018, **129**, 589–594.

356 M. Müller, S. Espinoza, T. Jüstel, K. D. Held, R. R. Anderson and M. Purschke, UVC-Emitting LuPO4:Pr3+ Nanoparticles Decrease Radiation Resistance of Hypoxic Cancer Cells, *Radiat. Res.*, 2019, **193**, 82.

357 S. Espinoza, M. Müller, H. Jenneboer, L. Peulen, T. Bradley, M. Purschke, M. Haase, R. Rahmanzadeh and T. Jüstel, Characterization of Micro- and Nanoscale LuPO4:Pr3+,Nd3+ with Strong UV-C Emission to Reduce X-Ray Doses in Radiation Therapy, *Part. Part. Syst. Charact.*, 2019, **36**, 1900280.

358 S. Espinoza, M. F. Volhard, H. Kätker, H. Jenneboer, A. Uckelmann, M. Haase, M. Müller, M. Purschke and T. Jüstel, Deep Ultraviolet Emitting Scintillators for Biomedical Applications: The Hard Way of Downsizing LuPO4:Pr3+, *Part. Part. Syst. Charact.*, 2018, **35**, 1–8.

359 M. R. Squillante, T. Jüstel, R. R. Anderson, C. Brecher, D. Chartier, J. F. Christian, N. Cicchetti, S. Espinoza, D. R. McAdams, M. Müller, B. Tornifoglio, Y. Wang and M. Purschke, Fabrication and characterization of UV-emitting nanoparticles as novel radiation sensitizers targeting hypoxic tumor cells, *Opt. Mater. (Amst).*, 2018, **80**, 197–202.

360 K. Ni, G. Lan, S. S. Veroneau, X. Duan, Y. Song and W. Lin, Nanoscale metal-organic frameworks for mitochondria-targeted radiotherapy-radiodynamic therapy, *Nat. Commun.*, 2018, **9**, 4321.

361 D. M. Samhadaneh, K. A. Alqarni, A. Smart, M. Kuang, O. Moujaber, D. Maysinger and U. Stochaj, Gold nanourchins induce cellular stress, impair proteostasis and damage RNA, *Nanomedicine Nanotechnology, Biol. Med.*, 2019, **22**, 102083.

362 N. A. P. Franken, H. M. Rodermond, J. Stap, J. Haveman and C. van Bree, Clonogenic assay of cells in vitro, *Nat. Protoc.*, 2006, **1**, 2315–2319.

363 N. Brix, D. Samaga, R. Hennel, K. Gehr, H. Zitzelsberger and K. Lauber, The clonogenic assay: robustness of plating efficiency-based analysis is strongly compromised by cellular cooperation, *Radiat. Oncol.*, 2020, **15**, 1–12.

364 N. Brix, D. Samaga, C. Belka, H. Zitzelsberger and K. Lauber, Analysis of clonogenic growth in vitro, *Nat. Protoc.*, 2021, **16**, 4963–4991.

365 R. E. Thoma, H. Insley and G. M. Hebert, The Sodium Fluoride-Lanthanide Trifluoride Systems, *Inorg. Chem.*, 1966, **5**, 1222–1229.

366 R. D. Shannon, Revised Effective Ionic Radii and Systematic Studies of Interatomic Distances in Halides and Chalcogenides, *Acta Cryst.*, 1976, **32**, 751.

367 S. Behzadi, V. Serpooshan, W. Tao, M. A. Hamaly, M. Y. Alkawareek, E. C. Dreaden, D. Brown, A. M. Alkilany, O. C. Farokhzad and M. Mahmoudi, Cellular uptake of nanoparticles: journey inside the cell, *Chem. Soc. Rev.*, 2017, **46**, 4218–4244.

368 R. Shi, C. D. S. Brites and L. D. Carlos, *Nanoscale*, 2021, 13, 19771–19782.

369 B. Herden, A. Meijerink, F. T. Rabouw, M. Haase and T. Jüstel, On the efficient luminescence of β-Na(La1-xPr x)F4, *J. Lumin.*, 2014, **146**, 302–306.

370 B. Herden, J. Nordmann, R. Komban, M. Haase and T. Jüstel, Vacuum-UV excitation and visible luminescence of nano-scale and micro-scale NaLnF4:Pr3+ (Ln = Y, Lu), *Opt. Mater. (Amst).*, 2013, **35**, 2062–2067.

371 P. Ptacek, H. Schäfer, K. Kömpe and M. Haase, Crystal Phase Control of Luminescing α-NaGdF4:Eu3+and β-NaGdF4:Eu3+ Nanocrystals, *Adv. Funct. Mater.*, 2007, **17**, 3843–3848.

372 T. Rinkel, J. Nordmann, A. N. Raj and M. Haase, Ostwald-ripening and particle size focussing of sub-10 nm NaYF4 upconversion nanocrystals, *Nanoscale*, 2014, **6**, 14523–

14530.

373 M. Nikl, K. Kamada, S. Kurosawa, Y. Yokota, A. Yoshikawa, J. Pejchal and V. Babin, Luminescence and scintillation mechanism in Ce3+ and Pr3+ doped (Lu,Y,Gd)3(Ga,Al)5O12 single crystal scintillators, *Phys. Status Solidi Curr. Top. Solid State Phys.*, 2013, **10**, 172–175.

374 V. Babin, M. Nikl, K. Kamada, A. Beitlerova and A. Yoshikawa, Effect of the Pr3+ → Gd3+ energy transfer in multicomponent garnet single crystal scintillators, *J. Phys. D. Appl. Phys.*, , DOI:10.1088/0022-3727/46/36/365303.

375 T. Hirai, H. Yoshida, S. Sakuragi, S. Hashimoto and N. Ohno, Transfer of Excitation Energy from Pr3+ to Gd3+ in YF3:Pr3+,Gd3+, *Jpn. J. Appl. Phys.*, 2007, **46**, 660.

376 Y. Sun, Y. Wang, C. Hu, X. Zhou, J. Hao, W. Li and H. Li, *Materials (Basel).*, 2022, 15.

377 S. Okamoto, R. Uchino, K. Kobayashi and H. Yamamoto, Luminescent properties of Pr3+-sensitized LaPO4:Gd3+ ultraviolet-B phosphor under vacuum-ultraviolet light excitation, *J. Appl. Phys.*, 2009, **106**, 13522.

378 S. Zeng, G. Ren, C. Xu and Q. Yang, High uniformity and monodispersity of sodium rare-earth fluoride nanocrystals: controllable synthesis, shape evolution and optical properties, *CrystEngComm*, 2011, **13**, 1384–1390.

379 T. Rinkel, A. N. Raj, S. Dühnen and M. Haase, Synthesis of 10 nm β-NaYF4:Yb,Er/NaYF4 core/shell upconversion nanocrystals with 5 nm particle cores, *Angew. Chemie - Int. Ed.*, 2016, **55**, 1164–1167.

380 D. LI, Q. SHAO, Y. DONG and J. JIANG, Phase-, shape- and size-controlled synthesis of NaYF4:Yb3+,Er3+ nanoparticles using rare-earth acetate precursors, *J. Rare Earths*, 2014, **32**, 1032–1036.

381 D. Li, W.-Y. Lai, Q. Shao and W. Huang, A facile methodology for regulating the size of hexagonal NaYF4:Yb3+,Er3+ upconversion nanocrystals, *New J. Chem.*, 2017, **41**, 11521–11524.

382 J. Ryu, H.-Y. Park, K. Kim, H. Kim, J. H. Yoo, M. Kang, K. Im, R. Grailhe and R. Song, Facile Synthesis of Ultrasmall and Hexagonal NaGdF4: Yb3+, Er3+ Nanoparticles with Magnetic and Upconversion Imaging Properties, *J. Phys. Chem. C*, 2010, **114**, 21077–21082.

383 G. Tessitore, S. L. Maurizio, T. Sabri and J. A. Capobianco, Intrinsic Time-Tunable

Emissions in Core–Shell Upconverting Nanoparticle Systems, *Angew. Chemie Int. Ed.*, 2019, **58**, 9742–9751.

384 F. T. Rabouw, P. T. Prins, P. Villanueva-Delgado, M. Castelijns, R. G. Geitenbeek and A. Meijerink, Quenching Pathways in $NaYF_4:Er^{3+},Yb^{3+}$ Upconversion Nanocrystals, *ACS Nano*, 2018, **12**, 4812–4823.

385 T. Rinkel, A. N. Raj, S. Dühnen and M. Haase, Synthesis of 10 nm β-NaYF4:Yb,Er/NaYF4 Core/Shell Upconversion Nanocrystals with 5 nm Particle Cores, *Angew. Chemie Int. Ed.*, 2016, **55**, 1164–1167.

386 B. Herden, Untersuchungen zum Einfluss optischer Elektronegativität fluoridischer Wirtsstrukturen auf die Position der Kristallfeldkomponenten von trivalentem Praseodym, *Thesis*, 2014, 240.

387 S. Soltani, A. Ojaghi and F. E. Robles, Deep UV dispersion and absorption spectroscopy of biomolecules, *Biomed. Opt. Express*, 2019, **10**, 487.

388 M. Taniguchi, H. Du and J. S. Lindsey, PhotochemCAD 3: Diverse Modules for Photophysical Calculations with Multiple Spectral Databases, *Photochem. Photobiol.*, 2018, **94**, 277–289.

389 A. M. Srivastava and W. W. Beers, Luminescence of Pr3+ in SrAl12O19: Observation of two photon luminescence in oxide lattice, *J. Lumin.*, 1997, **71**, 285–290.

390 J. L. Sommerdijk, A. Bril and A. W. de Jager, Luminescence of Pr3+-Activated fluorides, *J. Lumin.*, 1974, **9**, 288–296.

391 M. De Jong, A. Meijerink and F. T. Rabouw, Non-Poissonian photon statistics from macroscopic photon cutting materials, *Nat. Commun.*, 2017, **8**, 1–6.

392 M. A. Gusowski, H. C. Swart, L. S. Karlsson and M. Trzebiatowska-Gusowska, NaYF 4:Pr 3+ nanocrystals displaying photon cascade emission, *Nanoscale*, 2012, **4**, 541–546.

393 A. M. Srivastava and S. J. Duclos, On the luminescence of YF3-Pr3+ under vacuum ultraviolet and X-ray excitation, *Chem. Phys. Lett.*, 1997, **275**, 453–456.

394 J. Pejchal, M. Nikl, E. Mihókov, J. A. Mare, A. Yoshikawa, H. Ogino, K. M. Schillemat, A. Krasnikov, A. Vedda, K. Nejezchleb and V. Mka, Pr3+-doped complex oxide single crystal scintillators, *J. Phys. D. Appl. Phys.*, 2009, **42**, 10.

395 M. R. Brown, J. S. S. Whiting and W. A. Shand, Ion—Ion Interactions in Rare-Earth-Doped LaF 3, *J. Chem. Phys.*, 1965, **43**, 1–9.

396 G. Tessitore, G. A. Mandl, M. G. Brik, W. Park and J. A. Capobianco, Recent insights into upconverting nanoparticles: spectroscopy, modeling, and routes to improved luminescence, *Nanoscale*, 2019, **11**, 12015–12029.

397 Y. Zhuang, Y. Katayama, J. Ueda and S. Tanabe, A brief review on red to near-infrared persistent luminescence in transition-metal-activated phosphors, *Opt. Mater. (Amst).*, 2014, **36**, 1907–1912.

398 E. H. Otal, A. E. Maegli, N. Vogel-Schäuble, B. Walfort, H. Hagemann, S. Yoon, A. Zeller and A. Weidenkaff, The influence of defects formed by Ca excess and thermal post-treatments on the persistent luminescence of CaTiO3:Pr, *Opt. Mater. Express*, 2012, **2**, 405.

399 M. Fasoli, N. Chiodini, A. Lauria, F. Moretti and A. Vedda, Effect of deep traps on the optical properties of Tb3+ doped sol-gel silica, *Phys. status solidi c*, 2007, **4**, 1056–1059.

400 F. Moretti, G. Patton, A. Belsky, A. G. Petrosyan and C. Dujardin, Deep traps can reduce memory effects of shallower ones in scintillators, *Phys. Chem. Chem. Phys.*, 2015, **18**, 1178–1184.

401 P. Leblans, D. Vandenbroucke and P. Willems, Storage phosphors for medical imaging, *Materials (Basel).*, 2011, **4**, 1034–1086.

402 T. Yanagida, G. Okada and N. Kawaguchi, Ionizing-radiation-induced storage-luminescence for dosimetric applications, *J. Lumin.*, , DOI:10.1016/j.jlumin.2018.11.004.

403 D. Van der Heggen, D. R. Cooper, M. Tesson, J. J. Joos, J. Seuntjens, J. A. Capobianco and P. F. Smet, Optically Stimulated Nanodosimeters with High Storage Capacity, *Nanomaterials*, 2019, **9**, 1127.

404 B. Huang, H. Dong, K. L. Wong, L. D. Sun and C. H. Yan, Fundamental View of Electronic Structures of β-NaYF4, β-NaGdF4, and β-NaLuF4, *J. Phys. Chem. C*, 2016, 120, **33**, 18858–18870.

405 I. Kamenskikh, C. Pedrini, A. Petrosyan and A. Vasil'ev, Trapping and self-trapping in ytterbium-doped oxides with charge transfer luminescence, *J. Lumin.*, 2009, **129**, 1509–1513.

406 N. Y. Kirikova, M. Kirm, J. C. Krupa, V. N. Makhov, E. Negodin and J. Y. Gesland, Low-temperature high-resolution VUV spectroscopy of Ce3+ doped LiYF4, LiLuF4 and LuF3 crystals, *J. Lumin.*, 2004, **110**, 135–145.

407 J. W. M. Verweij, M. T. Cohen-Adad, D. Bouttet, H. Lautesse, B. Moine and C. Pédrini,

Luminescence properties of GdAlO3: Ce powders. Dependence on reduction conditions, *Chem. Phys. Lett.*, 1995, **239**, 51–55.

408 A. J. Cohen, P. Mori-Sánchez and W. Yang, Challenges for Density Functional Theory, *Chem. Rev.*, 2012, **112**, 289–320.

409 C. Freysoldt, B. Grabowski, T. Hickel, J. Neugebauer, G. Kresse, A. Janotti and C. G. Van De Walle, First-principles calculations for point defects in solids, *Rev. Mod. Phys.*, 2014, **86**, 253–305.

410 V. I. Anisimov, F. Aryasetiawan and A. I. Lichtenstein, *First-principles calculations of the electronic structure and spectra of strongly correlated systems: the LDA + U method*, 1997, vol. 9.

411 J. J. Joos, D. Poelman and P. F. Smet, Energy level modeling of lanthanide materials: review and uncertainty analysis, *Phys. Chem. Chem. Phys.*, 2015, **17**, 19058–19078.

412 L. Vegard, Die Konstitution der Mischkristalle und die Raumfüllung der Atome, *Zeitschrift für Phys.*, 1921, **5**, 17–26.

413 A. R. Denton and N. W. Ashcroft, Vegards law, *Phys. Rev. A*, 1991, **43**, 3161–3164.

414 K. T. Jacob, S. Raj and L. Rannesh, Vegard's law: a fundamental relation or an approximation?, 2007, **98**, 776–779.

415 M. J. Winiarski and D. A. Kowalska, Band gap bowings of ternary REN (RE = Sc, Y, La, and Lu) alloys, *J. Alloys Compd.*, 2020, **824**, 153961.

416 T. Wen, Y. Zhou, Y. Guo, C. Zhao, B. Yang and Y. Wang, Color-tunable and single-band red upconversion luminescence from rare-earth doped Vernier phase ytterbium oxyfluoride nanoparticles, *J. Mater. Chem. C*, 2015, **4**, 684–690.

417 R. Khemici, Z. Chouahda, L. Tairi, F. Semari, B. Amimour, S. Benlamari, H. Meradji and S. Ghemid, First principles calculations of the structural, electronic and optical properties of the mixed fluorides SrxCd1−xF2, *Chinese J. Phys.*, 2018, **56**, 1033–1044.

418 B. P. Sobolev, V. S. Sidorov and D. D. Ikrami, Phase Diagrams of Binary Systems Formed By Rare Earth Trifluorides., *Growth of Cryst*, 1986, **13**, 229–236.

419 R. E. Nahory, M. A. Pollack, W. D. Johnston and R. L. Barns, Band gap versus composition and demonstration of Vegard's law for In 1-xGaxAsyP1-y lattice matched to InP, *Appl. Phys. Lett.*, 1978, **33**, 659–661.

420 R. Dalven, Empirical relation between energy gap and lattice constant in cubic

semiconductors, *Phys. Rev. B*, 1973, **8**, 6033–6034.

421 M. Kirm, J. C. Krupa, V. N. Makhov, M. True, S. Vielhauer and G. Zimmerer, High-resolution vacuum ultraviolet spectroscopy of 5d-4f transitions in Gd and Lu fluorides, *Phys. Rev. B - Condens. Matter Mater. Phys.*, 2004, **70**, 1–4.

422 S. G. Lim, S. Kriventsov, T. N. Jackson, J. H. Haeni, D. G. Schlom, A. M. Balbashov, R. Uecker, P. Reiche, J. L. Freeouf and G. Lucovsky, Dielectric functions and optical bandgaps of high- K dielectrics for metal-oxide-semiconductor field-effect transistors by far ultraviolet spectroscopic ellipsometry, *J. Appl. Phys.*, 2002, **91**, 4500–4505.

423 E. van der Kolk, P. Dorenbos, C. W. E. van Eijk, A. P. Vink, C. Fouassier and F. Guillen, VUV excitation and emission of Pr3+ in BaSiF6 and selecting host lattices with emission, *J. Lumin.*, 2002, **97**, 212–223.

424 Y. V. Zorenko, A. S. Voloshinovskiĭ and I. V. Konstankevych, Luminescence of F+ and f centers in YAlO3, *Opt. Spectrosc. (English Transl. Opt. i Spektrosk.*, 2004, **96**, 532–537.

425 J. Andriessen, E. Van Der Kolk and P. Dorenbos, Lattice relaxation study of the 4f-5d excitation of Ce3+ -doped la Cl3, la Br3, and NaLa F4: Stokes shift by pseudo Jahn-Teller effect, *Phys. Rev. B - Condens. Matter Mater. Phys.*, 2007, **76**, 075124.

426 J. J. Schuyt, G. V. M. Williams, K. Shinohara, T. Shimizu, K. Yamanoi and M. Cadatal-Raduban, Vacuum ultraviolet photoluminescence of NaMgF3:Sm and NaMgF3:Sm,Ce: energy levels of the lanthanides in NaMgF3:Ln compounds, *Methods Appl. Fluoresc.*, 2022, **10**, 35006.

427 Z. Barandiarán, A. Meijerink and L. Seijo, Configuration coordinate energy level diagrams of intervalence and metal-to-metal charge transfer states of dopant pairs in solids, *Phys. Chem. Chem. Phys.*, 2015, **17**, 19874–19884.

428 J. J. Joos, I. Neefjes, L. Seijo and Z. Barandiarán, Charge transfer from Eu2+to trivalent lanthanide co-dopants: Systematic behavior across the series, *J. Chem. Phys.*, 2021, **154**, 064704.

429 S. Schweizer, Physics and Current Understanding of X-Ray Storage Phosphors, *Phys. Status Solidi*, 2001, **187**, 335–393.

430 M. Secu, S. Schweizer, U. Rogulis and J.-M. Spaeth, Radiation-induced defects and their recombination processes in the x-ray storage phosphor BaBr 2 :Eu 2, *J. Phys. Condens. Matter*, 2003, **15**, 2061–2070.

431 A. J. Wojtowicz, K. Brylew, P. Palczewski and M. E. Witkowski, *Excited Pr3+-Pr3+-Trapped Exciton Conversion in BaF2*

432 J. Botterman, J. J. Joos and P. F. Smet, Trapping and detrapping in SrAl2 O4:Eu,Dy persistent phosphors: Influence of excitation wavelength and temperature, *Phys. Rev. B - Condens. Matter Mater. Phys.*, 2014, **90**, 085147.

433 D. Van Der Heggen, J. J. Joos and P. F. Smet, Importance of Evaluating the Intensity Dependency of the Quantum Efficiency: Impact on LEDs and Persistent Phosphors, *ACS Photonics*, 2018, **5**, 4529–4537.

434 Y. Wang, R. Huang, J. Zhang, G. Cheng and H. Yang, Lanthanide(Tb3+, Eu3+)-functionalized a new one dimensional Zn-MOF composite as luminescent probe for highly selectively sensing Fe3+, *Polyhedron*, 2018, **148**, 178–183.

435 I. Norrbo, P. Gluchowski, I. Hyppänen, T. Laihinen, P. Laukkanen, J. Mäkelä, F. Mamedov, H. S. Santos, J. Sinkkonen, M. Tuomisto, A. Viinikanoja and M. Lastusaari, Mechanisms of Tenebrescence and Persistent Luminescence in Synthetic Hackmanite Na8Al6Si6O24(Cl,S)2, *ACS Appl. Mater. Interfaces*, 2016, **8**, 11592–11602.

436 J. Schubert and M. Chanana, Coating Matters: Review on Colloidal Stability of Nanoparticles with Biocompatible Coatings in Biological Media, Living Cells and Organisms, *Curr. Med. Chem.*, 2018, **25**, 4553–4586.

437 P. Foroozandeh and A. A. Aziz, Insight into Cellular Uptake and Intracellular Trafficking of Nanoparticles, *Nanoscale Res. Lett.*, 2018, **13**, 339.

438 S. Wilhelm, M. Kaiser, C. Würth, J. Heiland, C. Carrillo-Carrion, V. Muhr, O. S. Wolfbeis, W. J. Parak, U. Resch-Genger and T. Hirsch, Water dispersible upconverting nanoparticles: effects of surface modification on their luminescence and colloidal stability, *Nanoscale*, 2015, **7**, 1403–1410.

439 V. K. Sharma, K. M. Siskova, R. Zboril and J. L. Gardea-Torresdey, Organic-coated silver nanoparticles in biological and environmental conditions: Fate, stability and toxicity, *Adv. Colloid Interface Sci.*, 2014, **204**, 15–34.

440 Poly-L-Lysine Cell Attachment Protocol, https://www.sigmaaldrich.com/CA/en/technical-documents/protocol/cell-culture-and-cell-culture-analysis/3d-cell-culture/poly-lysine-product, (accessed 23 December 2022).

441 M. Babič, D. Horák, M. Trchová, P. Jendelová, K. Glogarová, P. Lesný, V. Herynek, M.

Hájek and E. Syková, Poly(L-lysine)-modified iron oxide nanoparticles for stem cell labeling, *Bioconjug. Chem.*, 2008, **19**, 740–750.

442 G. Minigo, A. Scholzen, C. K. Tang, J. C. Hanley, M. Kalkanidis, G. A. Pietersz, V. Apostolopoulos and M. Plebanski, Poly-l-lysine-coated nanoparticles: A potent delivery system to enhance DNA vaccine efficacy, *Vaccine*, 2007, **25**, 1316–1327.

443 M. Kaliszewski, M. Kwaśny, J. Kamiński, Z. Dabrowski and E. Burdziakowska, The stability of 5-aminolevulinic acid and its ester derivatives., *Acta Pol. Pharm.*, 2004, **61**, 15–9.

444 A. Bunke, O. Zerbe, H. Schmid, G. Burmeister, H. P. Merkle and B. Gander, Degradation mechanism and stability of 5-aminolevulinic acid, *J. Pharm. Sci.*, 2000, **89**, 1335–1341.

445 B. Elfsson, I. Wallin, S. Eksborg, K. Rudaeus, A. M. Ros and H. Ehrsson, Stability of 5-aminolevulinic acid in aqueous solution, *Eur. J. Pharm. Sci.*, 1999, **7**, 87–91.

446 H. Babich, E. J. Liebling, R. F. Burger, H. L. Zuckerbraun and A. G. Schuck, Choice of DMEM, formulated with or without pyruvate, plays an important role in assessing the in vitro cytotoxicity of oxidants and prooxidant nutraceuticals, *Vitr. Cell. Dev. Biol. - Anim.*, 2009, **45**, 226–233.

447 P. Rosenkranz, Q. Chaudhry, V. Stone and T. F. Fernandes, A comparison of nanoparticle and fine particle uptake by Daphnia magna, *Environ. Toxicol. Chem.*, 2009, **28**, 2142–2149.

448 J. Jin, Z. Xu, Y. Zhang, Y. J. Gu, M. H. W. Lam and W. T. Wong, Upconversion nanoparticles conjugated with Gd3+-DOTA and RGD for targeted dual-modality imaging of brain tumor xenografts, *Adv. Healthc. Mater.*, 2013, **2**, 1501–1512.

449 M. Norouzi, V. Yathindranath, J. A. Thliveris, B. M. Kopec, T. J. Siahaan and D. W. Miller, Doxorubicin-loaded iron oxide nanoparticles for glioblastoma therapy: a combinational approach for enhanced delivery of nanoparticles, *Sci. Rep.*, 2020, **10**, 1–18.

450 Y. Xin, T. Liu and C. L. Yang, Development of PLGA-lipid nanoparticles with covalently conjugated indocyanine green as a versatile nanoplatform for tumor-targeted imaging and drug delivery, *Int. J. Nanomedicine*, 2016, **11**, 5807–5821.

451 A. Neshastehriz, Z. Khosravi, H. Ghaznavi and A. Shakeri-Zadeh, Gold-coated iron oxide nanoparticles trigger apoptosis in the process of thermo-radiotherapy of U87-MG human glioma cells, *Radiat. Environ. Biophys.*, 2018, **57**, 405–418.

452 K. Präbst, H. Engelhardt, S. Ringgeler and H. Hübner, eds. D. F. Gilbert and O. Friedrich,

Springer New York, New York, NY, 2017, pp. 1–17.

453 *10993-5: 2009 Biological evaluation of medical devices— part 5: tests for in vitro cytotoxicity*, International Organization for Standardization, Geneva, 2009.

454 C. He, Y. Hu, L. Yin, C. Tang and C. Yin, Effects of particle size and surface charge on cellular uptake and biodistribution of polymeric nanoparticles, *Biomaterials*, 2010, **31**, 3657–3666.

455 E. Fröhlich, The role of surface charge in cellular uptake and cytotoxicity of medical nanoparticles, *Int. J. Nanomedicine*, 2012, **7**, 5577.

456 N. Schary, B. Novak, L. Kämper, A. Yousf and H. Lübbert, Identification and pharmacological modification of resistance mechanisms to protoporphyrin-mediated photodynamic therapy in human cutaneous squamous cell carcinoma cell lines, *Photodiagnosis Photodyn. Ther.*, 2022, **39**, 103004.

457 M. Schwake, S. Kaneko, E. Suero Molina, M. Müther, S. Schipmann, M. Köchling, A. Brentrup and W. Stummer, Spectroscopic measurement of 5-ALA-induced intracellular protoporphyrin IX in pediatric brain tumors, *Acta Neurochir. (Wien).*, 2019, **161**, 2099–2105.

458 J. Yamamoto, S. I. Ogura, T. Tanaka, T. Kitagawa, Y. Nakano, T. Saito, M. Takahashi, D. Akiba and S. Nishizawa, Radiosensitizing effect of 5-aminolevulinic acid-induced protoporphyrin IX in glioma cells in vitro, *Oncol. Rep.*, 2012, **27**, 1748–1752.

459 M. Schwake, A. Nemes, J. Dondrop, J. Schroeteler, S. Schipmann, V. Senner, W. Stummer and C. Ewelt, In-Vitro Use of 5-ALA for Photodynamic Therapy in Pediatric Brain Tumors, *Neurosurgery*, 2018, **83**, 1328–1337.

460 W. Stummer, S. Stocker, A. Novotny, A. Heimann, O. Sauer, O. Kempski, N. Plesnila, J. Wietzorrek and H. J. Reulen, In vitro and in vivo porphyrin accumulation by C6 glioma cells after exposure to 5-aminolevulinic acid, *J. Photochem. Photobiol. B Biol.*, 1998, **45**, 160–169.

461 S. Sharma, A. Jajoo and A. Dube, 5-Aminolevulinic acid-induced protoporphyrin-IX accumulation and associated phototoxicity in macrophages and oral cancer cell lines, *J. Photochem. Photobiol. B Biol.*, 2007, **88**, 156–162.

462 H. S. De Bruijn, A. G. Casas, G. Di Venosa, L. Gandara, H. J. C. M. Sterenborg, A. Batlle and D. J. Robinson, Light fractionated ALA-PDT enhances therapeutic efficacy in vitro; the

influence of PpIX concentration and illumination parameters, *Cite this Photochem. Photobiol. Sci*, 2013, **12**, 241.

463 M. Morita, H. Tanaka, Y. Kumamoto, A. Nakamura, Y. Harada, T. Ogata, K. Sakaguchi, T. Taguchi and T. Takamatsu, Fluorescence-based discrimination of breast cancer cells by direct exposure to 5-aminolevulinic acid, *Cancer Med.*, 2019, **8**, 5524–5533.

464 B. Zhang, R. Xue and C. Sun, Rational design of ROS-responsive nanocarriers for targeted X-ray-induced photodynamic therapy and cascaded chemotherapy of intracranial glioblastoma, *Nanoscale*, 2022, **14**, 5054–5067.

465 R. Chouikrat, F. Baros, J. C. André, R. Vanderesse, B. Viana, A. L. Bulin, C. Dujardin, P. Arnoux, M. Verelst and C. Frochot, A Photosensitizer Lanthanide Nanoparticle Formulation that Induces Singlet Oxygen with Direct Light Excitation, But Not By Photon or X-ray Energy Transfer, *Photochem. Photobiol.*, 2017, **93**, 1439–1448.

466 A. N. DuRoss, M. J. Neufeld, S. Rana, C. R. Thomas and C. Sun, Integrating nanomedicine into clinical radiotherapy regimens, *Adv. Drug Deliv. Rev.*, 2019, **144**, 35–56.

467 P. Retif, S. Pinel, M. Toussaint, C. Frochot, R. Chouikrat, T. Bastogne and M. Barberi-Heyob, Nanoparticles for radiation therapy enhancement: The key parameters, *Theranostics*, 2015, **5**, 1030–1044.

468 J. P. Gérard, C. Dejean, L. Montagne, K. Benezery, J. Doyen and J. M. Hannoun Levi, A brief history of contact X-ray brachytherapy 50 kVp, *Cancer/Radiotherapie*, 2020, **24**, 222–225.

469 J. Takahashi and M. Misawa, Characterization of reactive oxygen species generated by protoporphyrin IX under X-ray irradiation, *Radiat. Phys. Chem.*, 2009, **78**, 889–898.

470 U. Kraus-Tiefenbacher, A. Scheda, V. Steil, B. Hermann, T. Kehrer, L. Bauer, F. Melchert and F. Wenz, Intraoperative Radiotherapy (Iort) for Breast Cancer Using the Intrabeam™ System, *Tumori J.*, 2005, **91**, 339–345.

471 R. Li, H. Wang, Q. Liang, L. Chen and J. Ren, Radiotherapy for glioblastoma: clinical issues and nanotechnology strategies, *Biomater. Sci.*, 2022, **10**, 892–908.

472 D. Banasiak, A. R. Barnetson, R. A. Odell, H. Mameghan and P. J. Russell, Comparison between the clonogenic, MTT, and SRB assays for determining radiosensitivity in a panel of human bladder cancer cell lines and a ureteral cell line, *Radiat. Oncol. Investig.*, 1999, **7**, 77–85.

473 R. Mirzayans, B. Andrais and D. Murray, Do Multiwell Plate High Throughput Assays Measure Loss of Cell Viability Following Exposure to Genotoxic Agents?, *Int. J. Mol. Sci.*, , DOI:10.3390/ijms18081679.

474 C. Riccardi and I. Nicoletti, Analysis of apoptosis by propidium iodide staining and flow cytometry, *Nat. Protoc.*, 2006, **1**, 1458–1461.

475 J. P. Aubry, A. Blaecke, S. Lecoanet-Henchoz, P. Jeannin, N. Herbault, G. Caron, V. Moine and J. Y. Bonnefoy, Annexin V used for measuring apoptosis in the early events of cellular cytotoxicity, *Cytometry*, 1999, **37**, 197–204.

476 R. Kumar, A. Saneja and A. K. Panda, in *Lung Cancer*, Humana, New York, NY, 2021, pp. 213–223.

477 X. Hong, K. Chedid and S. N. Kalkanis, Glioblastoma cell line-derived spheres in serum-containing medium versus serum-free medium: A comparison of cancer stem cell properties, *Int. J. Oncol.*, 2012, **41**, 1693–1700.

478 B. Stea, R. Falsey, K. Kislin, J. Patel, H. Glanzberg, S. Carey, A. A. Ambrad, E. J. Meuillet and J. D. Martinez, Time and dose-dependent radiosensitization of the glioblastoma multiforme U251 cells by the EGF receptor tyrosine kinase inhibitor ZD1839 ('Iressa'), *Cancer Lett.*, 2003, **202**, 43–51.

479 M. T. Chew, A. Nisbet, M. Suzuki, N. Matsufuji, T. Murakami, B. Jones and D. A. Bradley, Potential lethal damage repair in glioblastoma cells irradiated with ion beams of various types and levels of linear energy transfer, *J. Radiat. Res.*, 2019, **60**, 59–68.

480 V. Turinetto and C. Giachino, Multiple facets of histone variant H2AX: a DNA double-strand-break marker with several biological functions, *Nucleic Acids Res.*, 2015, **43**, 2489–2498.

481 K. Rothkamm and S. Horn, gamma-H2AX as protein biomarker for radiation exposure., *Ann. Ist. Super. Sanita*, 2009, **45**, 265–71.

482 F. S. Pardo, D. W. Hsu, R. Zeheb, J. T. Efird, P. G. Okunieff and D. M. Malkin, Mutant, wild type, or overall p53 expression: freedom from clinical progression in tumours of astrocytic lineage, *Br. J. Cancer*, 2004, **91**, 1678–1686.

483 X. Chen, T. Zhang, W. Su, Z. Dou, D. Zhao, X. Jin, H. Lei, J. Wang, X. Xie, B. Cheng, Q. Li, H. Zhang and C. Di, Mutant p53 in cancer: from molecular mechanism to therapeutic modulation, *Cell Death Dis.*, 2022, **13**, 974.

484 Y. Zhang, C. Dube, M. Gibert, N. Cruickshanks, B. Wang, M. Coughlan, Y. Yang, I. Setiady, C. Deveau, K. Saoud, C. Grello, M. Oxford, F. Yuan and R. Abounader, The p53 Pathway in Glioblastoma, *Cancers (Basel).*, 2018, **10**, 297.

485 A. Zanotto-Filho, R. M. Gonçalves, K. Klafke, P. O. de Souza, F. C. Dillenburg, L. Carro, D. P. Gelain and J. C. F. Moreira, Inflammatory landscape of human brain tumors reveals an NFκB dependent cytokine pathway associated with mesenchymal glioblastoma, *Cancer Lett.*, 2017, **390**, 176–187.

486 J. Obacz, T. Avril, P.-J. Le Reste, H. Urra, V. Quillien, C. Hetz and E. Chevet, Endoplasmic reticulum proteostasis in glioblastoma—From molecular mechanisms to therapeutic perspectives, *Sci. Signal.*, , DOI:10.1126/scisignal.aal2323.

487 W. A. Awuah, A.-R. Toufik, R. Yarlagadda, T. Mikhailova, A. Mehta, H. Huang, M. Kundu, L. Lopes, S. Benson, L. Mykola, S. Vladyslav, A. Alexiou, B. S. Alghamdi, A. M. Hashem and G. Md Ashraf, Exploring the role of Nrf2 signaling in glioblastoma multiforme, *Discov. Oncol.*, 2022, **13**, 94.

488 H. Pan, H. Wang, L. Zhu, X. Wang, Z. Cong, K. Sun and Y. Fan, The involvement of Nrf2–ARE pathway in regulation of apoptosis in human glioblastoma cell U251, *Neurol. Res.*, 2013, **35**, 71–78.

489 D. Y. A. Dadey, V. Kapoor, A. Khudanyan, F. Urano, A. H. Kim, D. Thotala and D. E. Hallahan, The ATF6 pathway of the ER stress response contributes to enhanced viability in glioblastoma, *Oncotarget*, 2016, **7**, 2080–2092.

490 K. Liu, K. Tsung and F. J. Attenello, Characterizing Cell Stress and GRP78 in Glioma to Enhance Tumor Treatment, *Front. Oncol.*, , DOI:10.3389/fonc.2020.608911.

491 D. Eletto, D. Dersh and Y. Argon, GRP94 in ER quality control and stress responses, *Semin. Cell Dev. Biol.*, 2010, **21**, 479–485.

492 T. Hu, N. Xie, C. Qin, J. Wang and Y. You, Glucose-regulated protein 94 is a novel glioma biomarker and promotes the aggressiveness of glioma via Wnt/β-catenin signaling pathway, *Tumor Biol.*, 2015, **36**, 9357–9364.

493 S. Inoue, G. Browne, G. Melino and G. M. Cohen, Ordering of caspases in cells undergoing apoptosis by the intrinsic pathway, *Cell Death Differ.*, 2009, **16**, 1053–1061.

494 M. P. Mongiardi, M. Pellegrini, R. Pallini, A. Levi and M. L. Falchetti, Cancer Response to Therapy-Induced Senescence: A Matter of Dose and Timing, *Cancers (Basel).*, 2021, **13**,

484.

495 A. Freund, R.-M. Laberge, M. Demaria and J. Campisi, Lamin B1 loss is a senescence-associated biomarker, *Mol. Biol. Cell*, 2012, **23**, 2066–2075.

496 D. M. Razmik Mirzayans, Role of Therapy-Induced Cellular Senescence in Tumor Cells and its Modification in Radiotherapy: The Good, The Bad and The Ugly, *J. Nucl. Med. Radiat. Ther.*, , DOI:10.4172/2155-9619.S6-018.

497 J. Kaur and J. N. Farr, Cellular senescence in age-related disorders, *Transl. Res.*, 2020, **226**, 96–104.

498 S. Lee and C. A. Schmitt, The dynamic nature of senescence in cancer, *Nat. Cell Biol.*, 2019, **21**, 94–101.

499 J.-J. Lee, B. C. Kim, M.-J. Park, Y.-S. Lee, Y.-N. Kim, B. L. Lee and J.-S. Lee, PTEN status switches cell fate between premature senescence and apoptosis in glioma exposed to ionizing radiation, *Cell Death Differ.*, 2011, **18**, 666–677.

500 C. P. Cifarelli, A. Jacques and A. Bobko, Heterogeneity of radiation response in mesenchymal subtype glioblastoma: molecular profiling and reactive oxygen species generation, *J. Neurooncol.*, 2021, **152**, 245–255.

501 D. Kessel, Critical PDT Theory: Preclinical Translation, *Photochem. Photobiol.*, 2023, 0–2.

502 D. Kessel, Adventures in Photodynamic Therapy: Location, Location, Location, *Photochem. Photobiol.*, 2023, 0–2.

503 C. Guardiola, Y. Prezado, C. Roulin and J. W. J. Bergs, Effect of X-ray minibeam radiation therapy on clonogenic survival of glioma cells, *Clin. Transl. Radiat. Oncol.*, 2018, **13**, 7–13.

504 S. Unkel, C. Belka and K. Lauber, On the analysis of clonogenic survival data: Statistical alternatives to the linear-quadratic model, *Radiat. Oncol.*, 2016, **11**, 1–11.

505 L. Bodgi, A. Canet, L. Pujo-Menjouet, A. Lesne, J.-M. Victor and N. Foray, Mathematical models of radiation action on living cells: From the target theory to the modern approaches. A historical and critical review, *J. Theor. Biol.*, 2016, **394**, 93–101.

506 P. Alexander, W. M. Dale, W. Dittrich, O. Hug, A. M. Kellerer, W. Minder, J. S. Mitchell, H. B. Newcombe and A. Zuppinger, *Strahlenbiologie / Radiation Biology*, Springer Berlin Heidelberg, Berlin, Heidelberg, 1966, vol. 2 / 1.

507 S. J. McMahon, The linear quadratic model: Usage, interpretation and challenges, *Phys. Med. Biol.*, 2019, **64**, aaf26a.

508 B. Emami, G. Woloschak and W. Small, Beyond the linear quadratic model: Intraoperative radiotherapy and normal tissue tolerance, *Transl. Cancer Res.*, 2015, 4, 140–147.

509 A. M. Kellerer and O. Hug, Springer, Berlin, Heidelberg, 1972, pp. 1–42.

510 B. Fertil, H. Dertinger, A. Courdi and E. P. Malaise, Mean inactivation dose: A useful concept for intercomparison of human cell survival curves, *Radiat. Res.*, 1984, **99**, 73–84.

511 *Quantitative concepts in dosimetry and radiobiology*, Washington, 1979.

512 P. D. Liu, H. Jin, Z. Guo, J. Ma, J. Zhao, D. Li, H. Wu and N. Gu, Silver nanoparticles outperform gold nanoparticles in radiosensitizing U251 cells in vitro and in an intracranial mouse model of glioma, *Int. J. Nanomedicine*, 2016, **Volume 11**, 5003–5014.

513 X. Bai, Y. Wang, Z. Song, Y. Feng, Y. Chen, D. Zhang and L. Feng, *Int. J. Mol. Sci.*, 2020, 21, 2480.

514 M. Misawa and J. Takahashi, Generation of reactive oxygen species induced by gold nanoparticles under x-ray and UV Irradiations, *Nanomedicine Nanotechnology, Biol. Med.*, 2011, **7**, 604–614.

515 A. Detappe, S. Kunjachan, J. Rottmann, J. Robar, P. Tsiamas, H. Korideck, O. Tillement and R. Berbeco, AGuIX nanoparticles as a promising platform for image-guided radiation therapy, *Cancer Nanotechnol.*, 2015, **6**, 4.

516 H. Chen, X. Sun, G. D. Wang, K. Nagata, Z. Hao, A. Wang, Z. Li, J. Xie and B. Shen, LiGa5O8:Cr-based theranostic nanoparticles for imaging-guided X-ray induced photodynamic therapy of deep-seated tumors, *Mater. Horizons*, 2017, **4**, 1092–1101.

517 L. Song, P.-P. Li, W. Yang, X.-H. Lin, H. Liang, X.-F. Chen, G. Liu, J. Li and H.-H. Yang, Low-Dose X-ray Activation of W(VI)-Doped Persistent Luminescence Nanoparticles for Deep-Tissue Photodynamic Therapy, *Adv. Funct. Mater.*, 2018, **28**, 1707496.

518 Hubrecht and Carter, The 3Rs and Humane Experimental Technique: Implementing Change, *Animals*, 2019, **9**, 754.

519 S. K. Doke and S. C. Dhawale, Alternatives to animal testing: A review, *Saudi Pharm. J.*, 2015, **23**, 223–229.

520 M.-C. Vozenin, J. Bourhis and M. Durante, Towards clinical translation of FLASH radiotherapy, *Nat. Rev. Clin. Oncol.*, 2022, **19**, 791–803.

521 R. R. Colen, J. Wang, S. K. Singh, D. A. Gutman and P. O. Zinn, Glioblastoma: Imaging Genomic Mapping Reveals Sex-specific Oncogenic Associations of Cell Death, *Radiology*, 2014, **275**, 215–227.

522 V. Serpooshan, S. Sheibani, P. Pushparaj, M. Wojcik, A. Y. Jang, M. R. Santoso, J. H. Jang, H. Huang, R. Safavi-Sohi, N. Haghjoo, H. Nejadnik, H. Aghaverdi, H. Vali, J. M. Kinsella, J. Presley, K. Xu, P. C.-M. Yang and M. Mahmoudi, Effect of Cell Sex on Uptake of Nanoparticles: The Overlooked Factor at the Nanobio Interface, *ACS Nano*, 2018, **12**, 2253–2266.

523 Cellosaurus U87-MG Uppsala (CVCL_GP63), https://www.cellosaurus.org/CVCL_GP63.

524 Assay Cascade Characterization Program, https://www.cancer.gov/nano/research/ncl/assay-cascade.

525 R. Naccache, Cross-relaxation and energy transfer processes in praseodymium-doped gadolinium gallium garnet, Concordia University, 2007.

526 B. A. Weaver, How Taxol/paclitaxel kills cancer cells, *Mol. Biol. Cell*, 2014, **25**, 2677–2681.

527 S. W. Ham, H.-Y. Jeon, X. Jin, E.-J. Kim, J.-K. Kim, Y. J. Shin, Y. Lee, S. H. Kim, S. Y. Lee, S. Seo, M. G. Park, H.-M. Kim, D.-H. Nam and H. Kim, TP53 gain-of-function mutation promotes inflammation in glioblastoma, *Cell Death Differ.*, 2019, **26**, 409–425.

528 Y. Li, Y. Zhang, X. Li, S. Yi and J. Xu, Gain-of-Function Mutations: An Emerging Advantage for Cancer Biology, *Trends Biochem. Sci.*, 2019, **44**, 659–674.

529 P. J. Cimino, Y. Kim, H. J. Wu, J. Alexander, H. G. Wirsching, F. Szulzewsky, K. Pitter, T. Ozawa, J. Wang, J. Vazquez, S. Arora, R. Rabadan, R. Levine, F. Michor and E. C. Holland, Increased HOXA5 expression provides a selective advantage for gain of whole chromosome 7 in IDH wild-type glioblastoma, *Genes Dev.*, 2018, **32**, 512–523.

530 A. K. Yadav, Monosomy of Chromosome 10 Associated With Dysregulation of Epidermal Growth Factor Signaling in Glioblastomas, *JAMA*, 2009, **302**, 276.

531 H.-G. Wirsching and M. Weller, eds. J. Moliterno Gunel, J. M. Piepmeier and J. M. Baehring, Springer International Publishing, Cham, 2017, pp. 265–288.

532 G. Karpel-Massler and M.-E. Halatsch, in *Tumors of the Central Nervous System: Primary and Secondary*, ed. L. R. Morgan, IntechOpen, Rijeka, 2014.

533 J. Hu, J. Cao, W. Topatana, S. Juengpanich, S. Li, B. Zhang, J. Shen, L. Cai, X. Cai and M.

Chen, Targeting mutant p53 for cancer therapy: direct and indirect strategies, *J. Hematol. Oncol.*, 2021, **14**, 157.

534 I. Crespo, A. L. Vital, M. Gonzalez-Tablas, M. del C. Patino, A. Otero, M. C. Lopes, C. de Oliveira, P. Domingues, A. Orfao and M. D. Tabernero, Molecular and Genomic Alterations in Glioblastoma Multiforme, *Am. J. Pathol.*, 2015, **185**, 1820–1833.

535 E. G. Van Meir, C. G. Hadjipanayis, A. D. Norden, H.-K. Shu, P. Y. Wen and J. J. Olson, Exciting New Advances in Neuro-Oncology: The Avenue to a Cure for Malignant Glioma, *CA. Cancer J. Clin.*, 2010, **60**, 166–193.

536 S. Tanaka, D. N. Louis, W. T. Curry, T. T. Batchelor and J. Dietrich, Diagnostic and therapeutic avenues for glioblastoma: no longer a dead end?, *Nat. Rev. Clin. Oncol.*, 2013, **10**, 14–26.

537 Z. G. Liu and D. Jiao, Necroptosis, tumor necrosis and tumorigenesis, *Cell Stress*, 2020, **4**, 1–8.

538 P. Golstein and G. Kroemer, Cell death by necrosis: towards a molecular definition, *Trends Biochem. Sci.*, 2007, **32**, 37–43.

539 J. Sia, R. Szmyd, E. Hau and H. E. Gee, Molecular Mechanisms of Radiation-Induced Cancer Cell Death: A Primer, *Front. Cell Dev. Biol.*, 2020, **8**, 41.

540 L. Galluzzi and G. Kroemer, Necroptosis: A Specialized Pathway of Programmed Necrosis, *Cell*, 2008, **135**, 1161–1163.

541 J. F. R. Kerr, A. H. Wyllie and A. R. Currie, Apoptosis: A Basic Biological Phenomenon with Wideranging Implications in Tissue Kinetics, *Br. J. Cancer*, 1972, **26**, 239–257.

542 M. S. D'Arcy, Cell death: a review of the major forms of apoptosis, necrosis and autophagy, *Cell Biol. Int.*, 2019, **43**, 582–592.

543 B. Huppertz, H. G. Frank and P. Kaufmann, The apoptosis cascade - Morphological and immunohistochemical methods for its visualization, *Anat. Embryol. (Berl).*, 1999, **200**, 1–18.

544 G. M. Cohen, Caspases: The executioners of apoptosis, *Biochem. J.*, 1997, **326**, 1–16.

545 L. Galluzzi, A. López-Soto, S. Kumar and G. Kroemer, *Immunity*, 2016, 44, 221–231.

546 Q. Bao and Y. Shi, Apoptosome: a platform for the activation of initiator caspases, *Cell Death Differ.*, 2007, **14**, 56–65.

547 K. A. Pyrshev, S. O. Yesylevskyy, Y. Mély, A. P. Demchenko and A. S. Klymchenko,

Caspase-3 activation decreases lipid order in the outer plasma membrane leaflet during apoptosis: A fluorescent probe study, *Biochim. Biophys. Acta - Biomembr.*, 2017, **1859**, 2123–2132.

548 O. T. Fackler and R. Grosse, Cell motility through plasma membrane blebbing , *J. Cell Biol.*, 2008, **181**, 879–884.

549 D. Westphal, R. M. Kluck and G. Dewson, Building blocks of the apoptotic pore: how Bax and Bak are activated and oligomerize during apoptosis, *Cell Death Differ.*, 2014, **21**, 196–205.

550 C. L. Brunet, R. H. Gunby, R. S. P. Benson, J. A. Hickman, A. J. M. Watson and G. Brady, Commitment to cell death measured by loss of clonogenicity is separable from the appearance of apoptotic markers, *Cell Death Differ.*, 1998, **5**, 107–115.

551 C. A. Messam and R. N. Pittman, Asynchrony and commitment to die during apoptosis, *Exp. Cell Res.*, 1998, **238**, 389–398.

552 N. J. McCarthy, M. K. B. Whyte, C. S. Gilbert and G. I. Evan, Inhibition of Ced-3/ICE-related proteases does not prevent cell death induced by oncogenes, DNA damage, or the Bcl-2 homologue Bak, *J. Cell Biol.*, 1997, **136**, 215–227.

553 A. Saraste and K. Pulkki, Morphologic and biochemical hallmarks of apoptosis, *Cardiovasc. Res.*, 2000, **45**, 528–537.

554 C. Yun and S. Lee, The Roles of Autophagy in Cancer, *Int. J. Mol. Sci.*, 2018, **19**, 3466.

555 S. Y. Tam, V. W. C. Wu and H. K. W. Law, Influence of autophagy on the efficacy of radiotherapy, *Radiat. Oncol.*, 2017, **12**, 57.

556 S. Palumbo, L. Pirtoli, P. Tini, G. Cevenini, F. Calderaro, M. Toscano, C. Miracco and S. Comincini, Different involvement of autophagy in human malignant glioma cell lines undergoing irradiation and temozolomide combined treatments, *J. Cell. Biochem.*, 2012, **113**, 2308–2318.

557 W. Wang, L. Long, N. Yang, Q. Zhang, W. Ji, J. Zhao, Z. Qin, Z. Wang, G. Chen and Z. Liang, NVP-BEZ235, a novel dual PI3K/mTOR inhibitor, enhances the radiosensitivity of human glioma stem cells in vitro, *Acta Pharmacol. Sin.*, 2013, **34**, 681–690.

558 L. Hayflick and P. S. Moorhead, The serial cultivation of human diploid cell strains, *Exp. Cell Res.*, 1961, **25**, 585–621.

559 Autophagy Is Pro-Senescence When Seen in Close-Up, but Anti-Senescence in Long-Shot,

Mol. Cells, , DOI:10.14348/molcells.2017.0151.

560 R. Kumari and P. Jat, Mechanisms of Cellular Senescence: Cell Cycle Arrest and Senescence Associated Secretory Phenotype, *Front. Cell Dev. Biol.*, 2021, **9**, 1–24.

561 P. P. Shah, G. Donahue, G. L. Otte, B. C. Capell, D. M. Nelson, K. Cao, V. Aggarwala, H. A. Cruickshanks, T. S. Rai, T. McBryan, B. D. Gregory, P. D. Adams and S. L. Berger, Lamin B1 depletion in senescent cells triggers large-scale changes in gene expression and the chromatin landscape, *Genes Dev.*, 2013, **27**, 1787–1799.

562 A. F. S. Tabasso, D. J. L. Jones, G. D. D. Jones and S. Macip, Radiotherapy-Induced Senescence and its Effects on Responses to Treatment, *Clin. Oncol.*, 2019, **31**, 283–289.

563 J. L. Kirkland and T. Tchkonia, Senolytic drugs: from discovery to translation, *J. Intern. Med.*, 2020, **288**, 518–536.

564 C. A. Schmitt, T. Tchkonia, L. J. Niedernhofer, P. D. Robbins, J. L. Kirkland and S. Lee, COVID-19 and cellular senescence, *Nat. Rev. Immunol.*, 2023, **23**, 251–263.

565 C. Gzell, M. Back, H. Wheeler, D. Bailey and M. Foote, Radiotherapy in Glioblastoma: the Past, the Present and the Future, *Clin. Oncol.*, 2017, **29**, 15–25.

566 S. ei Noda, T. Lautenschlaeger, M. R. Siedow, D. R. Patel, A. El-Jawahri, Y. Suzuki, J. S. Loeffler, M. R. Bussiere and A. Chakravarti, Technological Advances in Radiation Oncology for Central Nervous System Tumors, *Semin. Radiat. Oncol.*, 2009, **19**, 179–186.

567 P. T. E. Board, *PDQ Adult Treatment Editorial Board. Adult Central Nervous System Tumors Treatment (PDQ®): Health Professional Version.*, Bethesda, 2023.

568 M. T. Eschwège Francois, Conformal Radiotherapy and Intensity-modulated Radiotherapy: Clinical Data, *Acta Oncol. (Madr).*, 2000, **39**, 555–567.

569 A. Narayana, J. Yamada, S. Berry, P. Shah, M. Hunt, P. H. Gutin and S. A. Leibel, Intensity-modulated radiotherapy in high-grade gliomas: Clinical and dosimetric results, *Int. J. Radiat. Oncol. Biol. Phys.*, 2006, **64**, 892–897.

570 J. Raizer and A. Parsa, *Current Understanding and Treatment of Gliomas*, 2015, vol. 163.

571 C. Verry, L. Sancey, S. Dufort, G. Le Duc, C. Mendoza, F. Lux, S. Grand, J. Arnaud, J. L. Quesada, J. Villa, O. Tillement and J. Balosso, Treatment of multiple brain metastases using gadolinium nanoparticles and radiotherapy: NANO-RAD, a phase I study protocol, *BMJ Open*, , DOI:10.1136/bmjopen-2018-023591.

572 D. Khosla, Concurrent therapy to enhance radiotherapeutic outcomes in glioblastoma, *Ann.*

Transl. Med. Vol 4, No 3 (February 02, 2016) Ann. Transl. Med. (STARD Guidel. Newer Agents to Enhanc. Radiother. Outcomes).

573 F. A. Giordano, S. Brehmer, Y. Abo-Madyan, G. Welzel, E. Sperk, A. Keller, F. Schneider, S. Clausen, C. Herskind, P. Schmiedek and F. Wenz, INTRAGO: Intraoperative radiotherapy in glioblastoma multiforme - A Phase I/II dose escalation study, *BMC Cancer*, 2014, **14**, 1–9.

574 J. S. Vaidya, M. Bulsara, M. Baum, F. Wenz, S. Massarut, S. Pigorsch, M. Alvarado, M. Douek, C. Saunders, H. L. Flyger, W. Eiermann, C. Brew-Graves, N. R. Williams, I. Potyka, N. Roberts, M. Bernstein, D. Brown, E. Sperk, S. Laws, M. Sütterlin, T. Corica, S. Lundgren, D. Holmes, L. Vinante, F. Bozza, M. Pazos, M. Le Blanc-Onfroy, G. Gruber, W. Polkowski, K. J. Dedes, M. Niewald, J. Blohmer, D. McCready, R. Hoefer, P. Kelemen, G. Petralia, M. Falzon, D. J. Joseph and J. S. Tobias, Long term survival and local control outcomes from single dose targeted intraoperative radiotherapy during lumpectomy (TARGIT-IORT) for early breast cancer: TARGIT-A randomised clinical trial, *BMJ*, 2020, **370**, m2836.

575 S. Bonvalot, P. L. Rutkowski, J. Thariat, S. Carrère, A. Ducassou, M.-P. Sunyach, P. Agoston, A. Hong, A. Mervoyer, M. Rastrelli, V. Moreno, R. K. Li, B. Tiangco, A. C. Herraez, A. Gronchi, L. Mangel, T. Sy-Ortin, P. Hohenberger, T. de Baère, A. Le Cesne, S. Helfre, E. Saada-Bouzid, A. Borkowska, R. Anghel, A. Co, M. Gebhart, G. Kantor, A. Montero, H. H. Loong, R. Vergés, L. Lapeire, S. Dema, G. Kacso, L. Austen, L. Moureau-Zabotto, V. Servois, E. Wardelmann, P. Terrier, A. J. Lazar, J. V. M. G. Bovée, C. Le Péchoux and Z. Papai, NBTXR3, a first-in-class radioenhancer hafnium oxide nanoparticle, plus radiotherapy versus radiotherapy alone in patients with locally advanced soft-tissue sarcoma (Act.In.Sarc): a multicentre, phase 2–3, randomised, controlled trial, *Lancet Oncol.*, 2019, **20**, 1148–1159.

576 Nanobiotix, Clinical trials, https://www.nanobiotix.com/clinical-trials/.

577 P. Zhang, J. Marill, A. Darmon, N. Mohamed Anesary, B. Lu and S. Paris, NBTXR3 Radiotherapy-Activated Functionalized Hafnium Oxide Nanoparticles Show Efficient Antitumor Effects Across a Large Panel of Human Cancer Models, *Int. J. Nanomedicine*, 2021, **16**, 2761–2773.

578 M. Luchette, H. Korideck, M. Makrigiorgos, O. Tillement and R. Berbeco, Radiation dose

enhancement of gadolinium-based AGuIX nanoparticles on HeLa cells, *Nanomedicine Nanotechnology, Biol. Med.*, 2014, **10**, 1751–1755.

579 P. Mowat, A. Mignot, W. Rima, F. Lux, O. Tillement, C. Roulin, M. Dutreix, D. Bechet, S. Huger, L. Humbert, M. Barberi-Heyob, M. T. Aloy, E. Armandy, C. Rodriguez-Lafrasse, G. Le Duc, S. Roux and P. Perriat, In vitro radiosensitizing effects of ultrasmall gadolinium based particles on tumour cells, *J. Nanosci. Nanotechnol.*, 2011, **11**, 7833–7839.

580 R. Baskaran, J. Lee and S. G. Yang, Clinical development of photodynamic agents and therapeutic applications, *Biomater. Res.*, 2018, **22**, 1–8.

581 V. J. Pizzuti, D. Viswanath, S. E. Torregrosa-Allen, M. P. Currie, B. D. Elzey and Y. Y. Won, Bilirubin-Coated Radioluminescent Particles for Radiation-Induced Photodynamic Therapy, *ACS Appl. Bio Mater.*, 2020, **3**, 4858–4872.

582 M. Nakayama, C. L. Smith, B. N. Feltis, T. J. Piva, F. Tabatabaie, P. D. Harty, F. M. Gagliardi, K. Platts, S. Otto, A. Blencowe, K. Morita and M. Geso, Samarium doped titanium dioxide nanoparticles as theranostic agents in radiation therapy, *Phys. Medica*, 2020, **75**, 69–76.

583 R. R. Anderson and J. A. Parrish, The optics of human skin, *J. Invest. Dermatol.*, 1981, **77**, 13–19.

584 A. Cios, M. Ciepielak, Ł. Szymański, A. Lewicka, S. Cierniak, W. Stankiewicz, M. Mendrycka and S. Lewicki, Effect of Different Wavelengths of Laser Irradiation on the Skin Cells, *Int. J. Mol. Sci.*, 2021, **22**, 1–19.

585 N. Kollias and A. H. Baqer, Absorption Mechanisms of Human Melanin in the Visible, 400–720nm, *J. Invest. Dermatol.*, 1987, **89**, 384–388.

586 N. Kollias and A. Baqer, Spectroscopic Characteristics of Human Melanin In Vivo, *J. Invest. Dermatol.*, 1985, **85**, 38–42.

587 R. L. P. van Veen, H. J. C. M. Sterenborg, A. Pifferi, A. Torricelli, E. Chikoidze and R. Cubeddu, Determination of visible near-IR absorption coefficients of mammalian fat using time- and spatially resolved diffuse reflectance and transmission spectroscopy, *J. Biomed. Opt.*, 2005, **10**, 54004.

588 B. Pahari, S. Chakraborty, B. Sengupta, S. Chaudhuri, W. Martin, J. Taylor, J. Henley, D. Davis, P. K. Biswas, A. K. Sharma and P. K. Sengupta, Biophysical Characterization of Genistein in Its Natural Carrier Human Hemoglobin Using Spectroscopic and

Computational Approaches, *Food Nutr. Sci.*, 2013, **04**, 83–92.

Appendix 1: Cross-relaxation mechanisms

Cross-relaxation is an energy transfer process involving two identical ions. When multiple resonant energy gaps are present in an ion, de-excitation of one state and concurrent population of another state may occur. This is common in the LOLs of Pr^{3+} where there are several resonant energy gaps. The cross-relaxation mechanisms known for Pr^{3+} ions are depicted in Figure 66.

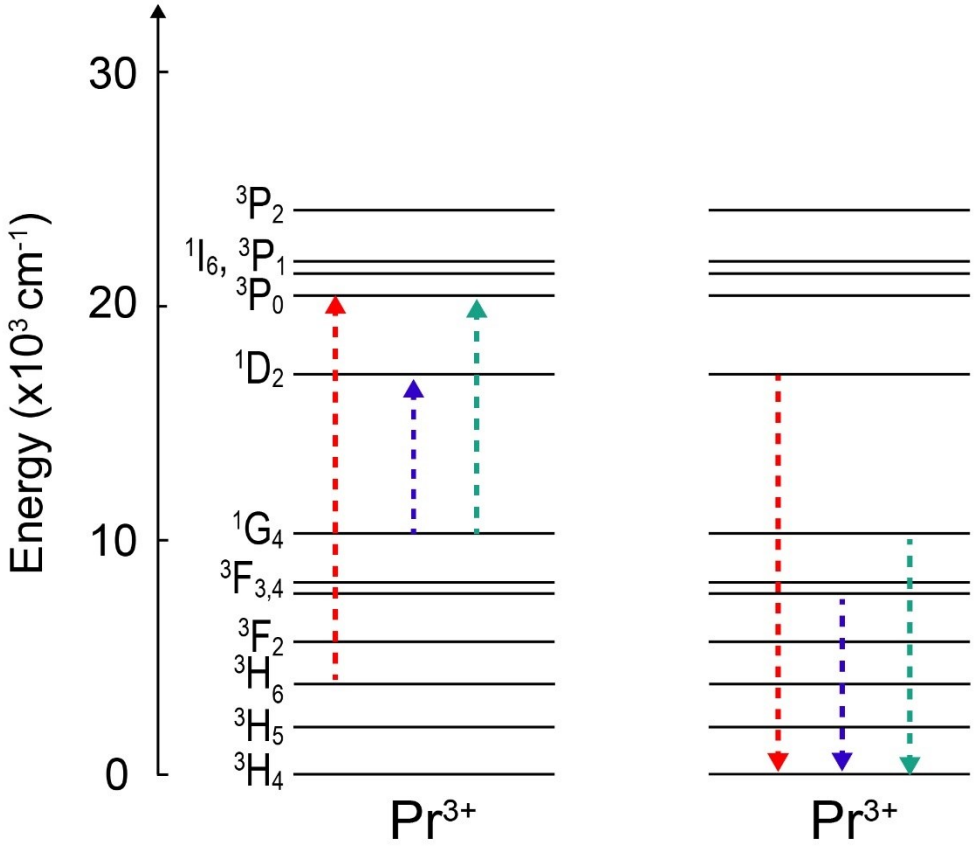

Figure 66. Established cross-relaxation mechanisms between the LOLs of Pr^{3+}.[66,525] The mechanisms correspond to $^3H_6 + {}^1D_2 \rightarrow {}^3P_0 + {}^3H_4$ (red), $^1G_4 + {}^3F_{3,4} \rightarrow {}^1D_2 + {}^3H_4$ (blue), $^1G_4 + {}^1G_4 \rightarrow {}^1D_2 + {}^3P_0$ (teal).

Appendix 2: Additional molecular biology considerations

A2.1. The cell cycle

The cell cycle is shown in Figure 67. There are 4 checkpoints, one that prevents transition from G1 into S phase, one that prevents the progression from S to G2, one at the early stage of G2, and one at late-stage G2 that prevents cells from undergoing mitosis.[208] Each checkpoint either functions as an opportunity for damage to be repaired or for death to be initiated. Activation of these checkpoints prevents the cells from transitioning into the next phase of the cycle, and the cells may be stalled at these checkpoints for hours. The part of the cycle the cell is in when it is irradiated also affects the outcome of the treatment. Cells which are irradiated in the G2/M phases have a higher DNA content and thus are more radiosensitive, while cells in the S phase tend to be more radioresistant.[219] Paclitaxel, a popular chemotherapy drug used for a wide variety of cancers, partially functions as a treatment by arresting cells at the G2/M phase, thereby improving the efficacy of radiotherapy.[219,526] DNA is replicated during the S phase, thus the G1/S cell cycle checkpoint is activated when DNA damage is detected to give the cell the opportunity to repair the DNA damage or to initiate apoptosis. In many cancers, including glioblastoma, p53 is mutated.[216,482,527] This makes it substantially easier for cancer cells to evade death and continue proliferating and it contributes to the radioresistance of many cancers. Moreover, in U251 cells, the gene encoding p21 is deleted (section 3.1.2). Since p53 induces G1 cell cycle arrest through activation of p21, the loss of this protein contributes to radioresistance and survival despite the

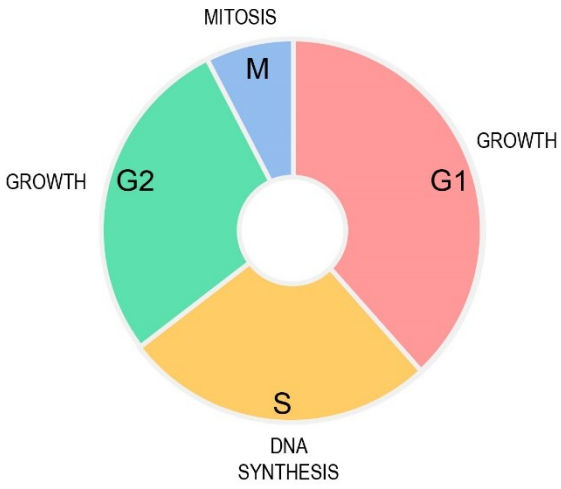

Figure 65. The cell cycle

accumulation of DNA damage.[216,219]

A2.2. Molecular features of glioblastoma

Cancer, in the most basic sense, is a disease caused by genetic mutations. These mutations allow for cells to continue proliferating in an uncontrolled fashion, giving rise to a tumor. Mutations can either result in gain-of-function or loss-of-function events.[528] A gain-of-function mutation means that a gene or protein is endowed with a new function or a new expression pattern, whereas a loss-of-function mutation prevents a gene or protein from performing its intended function or from being produced at all. This is important because if the mutations can be identified, it is easier to understand how the tumor may respond to a certain treatment.

According to the 2021 WHO classification scheme, to be classified as glioblastoma, cells must be wildtype for isocitrate dehydrogenase (IDH) expression; IDH mutant cells are diagnosed as astrocytomas or oligodendrogliomas. Cells which exhibit a concurrent gain of chromosome 7 and loss of chromosome 10, mutations in the (TERT) promoter, and/or epidermal growth factor receptor (EGFR) amplification are now also classified as glioblastoma, even if the histological presentation of the tumor doesn't appear to be high grade (ie. no necrotic core).[168] Trisomy 7 is associated with increased radiation resistance and increased proliferation, attributed to the overexpression of HOXA5 genes, which are responsible for producing transcription factors that affect cell proliferation and fate decisions.[529] The loss of one copy of chromosome 10 (monoploidy 10) is thought to favor the overexpression of EGFR on chromosome 7 due to the loss of sufficient annexin 7, which regulates EGFR signaling.[530] Hence, the loss of a copy of chromosome 10 by these cells is used to favor the addition of a copy chromosome 7, which gives rise to the genes that cause aggressive tumorigenesis.

There are four genes that appear to give rise to gliomagenesis based on population studies: tumor suppressor 53 (TP53), epidermal growth factor receptor (EGFR), telomerase reverse transcriptase (TERT) and regulator of telomere elongation helicase 1 (RTEL1).[531] TERT and RTEL1 are associated with increased prevalence of gliomagenesis at older ages. Mutations in TP53 and EGFR are common in many different kinds of cancers, and are ultimately associated

with poor prognosis and treatment resistance.

EGFR regulates a large number of downstream pathways, ultimately affecting cell signaling and proliferation. The overexpression of EGFR is associated with increased cell proliferation leading to tumorigenesis, and increased cell survival (ie. treatment resistance). Unfortunately, EGFR-targeting drugs like erlotinib, which are a first-line treatment for non-small cell lung cancer, are not effective for glioblastoma.[532] TP53 encodes the p53 protein, which plays a major role in cell signalling in response to stress and damage, and ultimately affects cell fate (Figure 13).[484] Important to the work herein, the stress induced by PDT and DNA damage induced by radiotherapy both initiate a response from p53 under normal (healthy) circumstances. Because of its multitude of functions, p53 is known as the "Guardian of the Genome". In glioblastoma, p53 exhibits a gain-of-function mutation that causes accumulation of the mutant p53 protein, which results in enhanced migration and invasion, as well as more rapid cell proliferation[533] and enhanced inflammation.[483,484,527] Perhaps the most prominent effect of the EGFR and TP53 mutations is that, combined, they result in drastically enhanced proliferation and reduced apoptosis.[534] Finally, there is also a known alteration in the retinoblastoma (Rb) tumor suppressor, which does not affect gliomagenesis like EGFR and TP53, but is a common feature in glioblastoma that affects cell proliferation by altering the progression of cells through the cell cycle as described above.[535] Together these three alterations are considered to be the essential molecular features of glioblastoma.[536]

Moreover, glioblastoma tumors exhibit a high degree of heterogeneity within a single tumor, and within different tumors in the same patient.[165,168] In other words, the cells within the tumor can vary greatly in terms of their protein expressions, mutations and even their morphology. This makes it difficult to effectively eradicate all of the cells based on a single treatment strategy.

A2.3. Modes of cell death

A2.3.1 Necrosis

Necrosis is the main spontaneous (unprogrammed) form of cell death, caused by overwhelming trauma to the cell. Physically, necrosis is characterized by condensation of the nucleus and rupture of the cell membrane, causing the contents of the cell to leak into the

extracellular environment.[224] This happens quickly, such that the cell does not have time to attempt recovery or initiate a programmed death pathway. Necrosis is often considered to be an undesirable mode of cell death, since the biomolecules that leak out of the damaged cell are still active and can therefore induce interactions within nearby cells, leading to inflammation and an immune response.[537]

Notably, in the past 15 years, the understanding of programmed necrosis, known as necroptosis, has demonstrated that necrosis is not as unregulated as previously thought.[538] There is conflicting evidence as to whether the induced inflammation and immune response contribute to a poor prognosis overall, or if they may contribute anti-tumorigenic effects.[539,540] The role of radiotherapy in inducing immunogenic cell death is currently under investigation because of these new advancements in the understanding of molecular biology. In contrast, immunogenic cell death is a well-established outcome of photodynamic therapy (section 3.5.2).

A2.3.2 Apoptosis

Apoptosis is perhaps the best-known mode of programmed cell death, first described in 1972.[541] In stark contrast to necrosis, apoptosis is carried out in such a way that the cell dies without leaking any of its contents.[542] Thus, it does not cause inflammation. Apoptosis is carefully orchestrated, and occurs in three phases: the initiation phase, the commitment to cell death, and the actual execution of the process. The initiation phase is regulated by a variety of biomolecules, such as p53 discussed below. The commitment and execution phases are carried out by molecules known as caspases, which are responsible for initiating the degradation of all cellular components and the eventual dissolution of the cell membrane as the final stage of death.[493,543,544] Because apoptosis involves the entire cell, and the pathways are relatively well-understood, it is possible to detect a cell undergoing apoptosis through evaluation of a variety of biomarkers and molecular changes that may occur at different stages of the process.

Molecularly, caspases can be divided by their roles as initiators and effectors.[493,544–546] Caspases 2, 8, 9 and 10 are the initiators, while caspases 3, 6 and 7 are the effectors. The other caspases (ex. Caspase 1, 4, 5, 11 etc) have roles in other types of cell death and in inflammation. Briefly, as mentioned earlier, p53 can mediate apoptosis through the activation of BAX and

PUMA, which activate caspase 9. These initial processes cause the depolarization of the mitochondrial membrane, and formation of a structure called an apoptosome. Caspase 9 then activates caspases 3 and 7, both of which execute the activation of hundreds of different processes leading to the eventual completion of the process. As such, if p53 is mutated, this early part of the apoptosis cascade is de-railed; this is the major anti-apoptotic effect of p53 mutations.

Of relevance to this work, in the early stages of apoptosis, caspases 3 and 7 inhibit the proteins responsible for the structural integrity of the cytoskeleton and cell membrane.[547,548] This results in the translocation of phosphatidylserine from the inner leaflet of the cell membrane to the outer leaflet, which is a hallmark of early-stage apoptosis.[475] The phosphatidylserine in the outer leaflet acts as a signal to neighboring cells to phagocytize the soon-to-be apoptotic bodies produced in later stages of the cascade.[222] Morphologically, these changes are visualized by membrane blebbing, in which small sphere-like pieces of the cell membrane (called blebs) are pinched off from the cell in order to decouple it from the cytoskeleton and provide more flexibility within the cell to carry out the degradation processes.[208,543,548] Caspases 3 and 7 also cleave PARP1, which signals for DNA damage repair, as mentioned in section 3.2.3.2. Thus, the process of DNA cleavage can begin without any signaling for repairs. Also in the early stages of the process, condensation of chromatin occurs to facilitate the DNA cleavage process. Degradation of the nuclear envelope is initiated after caspases 3 and 7 activate caspase 6, which cleaves nuclear lamins A and C.[544] Lamins are crucial structural proteins of the nuclear envelope, thus their cleavage leads to collapse of the nucleus.[543] Since PARP1 and the lamins are cleaved by different caspases, detection of their cleavage provides independent means of confirming apoptosis has been initiated. In the later stages of apoptosis, membrane blebbing transitions into full membrane permeability, and apoptotic bodies are formed that contain fragments of organelles and the degradation products from the apoptosis process. These bodies are consumed by macrophages, thus eliminating the cells without any interaction of the contents with the extracellular environment. Notably, apoptosis is an ATP-dependent process, and cells may run out of ATP prior to the completion of the process, leading to what is known as secondary necrosis, which is energy-independent.[221,542] As such, cell death mechanisms are highly inter-related.

The initiation phase is carried out by proteins like p53 and the Bcl-2 protein family, which eventually activate BAX and PUMA.[549] This phase is extremely variable and occurs hours to days

before any morphological changes are observed, and before the activation of caspases.[550,551] Interestingly, it is not known precisely why it takes such a long time between the initiation and commitment phases. The commitment phase is considered to start with activation of BAX, followed by depolarization of the outer mitochondrial membrane and immediate release of its contents, and activation of caspase-9, all of which occurs on a timescale of ten minutes.[225] Notably, Messam *et al.* don't describe this stage, but describe a second stage characterized by membrane bubbling that lasts anywhere from 10 minutes to 40 hours, but appears to still be reversible based on serum rescue experiments.[551] The subsequent execution phase then proceeds in less than two hours, as evidenced by video microscopy from different researchers in different cell lines.[551–553]

A3.3 Autophagy and Senescence

Autophagy is particularly interesting because it likely occurs in an attempt to ensure cell survival, thus it is both anti-tumorigenic and pro-tumorigenic depending on the scenario.[208,554] This process, as suggested by its name, is the process of a cell digesting itself, often to generate energy or recycle damaged components; cells often do this in response to stress. For these reasons, autophagy plays a highly complex role in the outcome of cancer therapy. Of relevance to this work, autophagy is linked to the PTEN and p53 genes, both of which are mutated in the U251 cell line (and commonly in glioblastoma in general) as previously mentioned. This is thought to be a potential contributor to radiation resistance, as the ability for autophagy to occur is reduced by these mutations.[208] Autophagy may also be triggered by endoplasmic reticulum stress after irradiation with ionizing radiation, *via* the unfolded protein response (UPR). The UPR plays a major role in stress response and homeostasis, ensuring that proteins that are misfolded are sent for degradation and mediating the accumulation of other proteins in the endoplasmic reticulum.[490] Glucose-related proteins 78 and 94 (Grp78 and Grp94, respectively) contribute to modulating the UPR.[489,491] Grp78 in particular is implicated in radiation-induced autophagy, as are Nf-κB and Nrf2, since they mediate cell stress, as mentioned previously. However, since these proteins are usually involved in cell survival, their involvement in autophagy strengthens the notion that autophagy occurs to facilitate survival in many cases.[555] Attempts to inhibit autophagy through modulating the UPR, and to activate it through modulating endoplasmic reticulum stress and other pathways have both been studied as a route to improving glioblastoma treatment by increasing radiosensitivity.[556,557]

As mentioned above, with regard to radiotherapy, the goal is to ensure cells cannot reproduce, and thus cells which are under proliferative arrest are considered indirectly dead.[208] Cellular senescence was first described by Leonard Hayflick in 1961, where he reported that cultured cells can only divide for a certain number of times before they are simply no longer able to do so; ie. they become senescent.[558] This number of divisions, known as the Hayflick limit, is the basis of aging, and is the natural progression that cells usually follow (unless they die by other mechanisms). Senescence can also be initiated in cells prematurely as a response to stress or injury, and has a complex relationship with autophagy.[498,559] Senescence is induced primarily by the activation of p16 and p21.[208,560] The p16 protein acts in concert with Rb to initiate senescence, and mentioned earlier, p21 is activated by p53 in response to DNA damage, leading to proliferative arrest at the G1/S checkpoint. Senescence is induced when one or more of these four factors is overexpressed for a prolonged time.[560] Senescence is accompanied by the loss of production of lamin B1, a nuclear envelope protein that is essential for DNA replication.[495,561] As such, lamin B1 loss is the gold-standard hallmark of identifying senescent cells.

The proliferative arrest of senescent cells is a common outcome of radiotherapy.[562] The inability for these cells to divide is a positive outcome in the sense that they cannot directly contribute to tumorigenesis, and therefore improve progression-free survival of patients. However, these cells are still metabolically active and thus can contribute to disease progression *via* signalling. Senescent cells transition into a phenotype known as the senescence-associated secretory phenotype (SASP).[496] The SASP, as described by its name, involves the secretion of a large number of pro-inflammatory biomolecules that stimulate the upregulation of stress-response proteins such as Nf-κB. Inflammation can either aid in stimulating the immune system to attack cancer cells, or it can contribute to increased treatment resistance and proliferation. As such, senescence is not the optimal solution for tumor control but does help in the short term.[559,562] Importantly, while natural senescence is permanent, premature senescence may not be. There is mounting evidence that senescent cells can become reactivated and proliferate at a later timepoint. To this end, drugs have been developed to eliminate senescent cells. Senolytics are meant to selectively kill senescent cells, and are in clinical trials for testing their effects in a variety of diseases from Alzheimer's to long COVID-19, and of course, cancer.[563,564]

Appendix 3: Techniques in post-operative treatment of glioblastoma

It is important to note that the overarching goal of involved-field radiotherapy is to encompass as much of the tumor and margin as possible, while simultaneously avoiding damage to eloquent structures such as the optic chiasm or the brain stem, for example. Additionally, conventional radiotherapy has not greatly improved treatment outcomes at the prescribed 60 Gy dose, as mentioned earlier. Thus, the state-of-the-art in radiotherapy for glioblastoma has been to avoid as much healthy tissue as possible while altering the precision, intensity and local dose delivered within the resection cavity and to the tumor margin.[508,565,566]

Conformal radiotherapy has yielded improvements in delivering radiation more precisely to the resection cavity, especially once 3-dimensional treatment mapping was introduced; it is now the standard mode of radiotherapy for glioblastoma patients.[169,566,567] 3D-Conformal radiotherapy utilizes multiple radiation beams at different angles to precisely irradiate the tumor field based on the 3D image constructed from CT, MR and PET images prior to radiotherapy. Intensity-modulated radiotherapy is a type of 3D conformal radiotherapy where an irregular radiation dose is administered based on the position of the tumor and nearby delicate healthy tissue. This has led to the ability to deliver precise amounts of radiation to irregularly-shaped cavities, and to the ability to achieve dose escalation at the center of the tumor site, while administrating lower doses at the margins where healthy tissues are known to reside.[568] While intensity-modulated radiotherapy has reduced side effects due to toxicity in healthy tissues, it is not expected to provide a higher degree of tumor control for glioblastoma patients.[569] This is partially because the diffuse nature of glioblastoma still makes it difficult to delineate the edges of the tumor *via* imaging, and because these techniques are used after a 3-4 week delay post-resection.

In these techniques, the use of high-energy radiation beams (in the MV range) facilitate the administration of radiation to the target while attempting to spare the skin and healthy tissues in the beam path. Despite advances that have enabled a greater tissue-sparing ability, it is simply not possible to perform external beam therapy while completely avoiding irradiation of healthy tissue. To this end, intraoperative radiotherapy has become an attractive technique.

A3.1 Fractionated Radiotherapy: The 4 R's

The *repair* principle is meant to spare healthy cells and give them time to repair sub-lethal DNA damage. Typically, healthy cells repair DNA damage more quickly than malignant ones, thus the goal is to administer the next radiation fraction after the healthy cells have repaired but before the cancerous ones are able to. The *redistribution* principle is based on the idea that cells are arrested at different stages of the cell cycle, and some cycles are more radioresistant than others, as previously mentioned. Thus, the idea is to provide enough time to regain an even distribution of cells in all of the cycles such that the proportion of cells in the radioresistant phases are decreased before the next fraction. *Regeneration* follows a similar principle as *repair* but on a tissue-level; careful timing of fractionation must be used to ensure clonogenic cells cannot repopulate the tumor while also ensuring healthy tissue has time to regrow. Finally, the damage caused by ionizing radiation is mainly due to the formation of reactive oxygen species. Thus, it is important to allow time for *reoxygenation* to occur such that the fraction can induce effective cell killing. Since tumors tend to be hypoxic, this is an extensively studied consideration for dose timing schedules.[208] The use of 2 Gy fractions for glioblastoma is based on the balance between healthy tissue damage and achieving a significant dose response. The total dose has been historically limited to 60 Gy based on a study in 1970's (before computed tomography imaging was even implemented) that established doses beyond this induce too much damage to healthy tissues to be considered useful.[570]

A3.2 Radiotherapy field size in glioblastoma treatment

Prior to the 1970's, whole-brain radiotherapy (WBRT) was performed based on the assumption that there could be multiple tumors, and imaging techniques had not advanced enough to fully determine the size and location of the disease.[570] However, the cognitive deficits incurred during WBRT preclude its widespread use today for primary glioblastoma, as there has been no significant advantage in outcomes observed relative to localized radiation treatments that spare healthy tissues. Importantly, WBRT remains important for the treatment of metastatic brain cancer, since there are generally many lesions present.[571] Since 90% of tumor recurrence occurs within 2 cm of the primary tumor site[169,570,572], conventional fractionated radiotherapy involves radiation of the tumor bed plus a margin of 2-3 cm to encompass the potential recurrence sites. This is known

as involved-field radiotherapy, and is the standard practice today.

A3.3 Chemotherapeutics for glioblastoma

The only chemotherapeutics that have proven beneficial for treatment of glioblastoma are temozolomide (the standard of care) lomustine (administered orally), and carmustine, which is implanted as a wafer inside the resection cavity.[184,186] All are DNA alkylating agents, meant to prevent DNA replication or silence certain genes that aid in DNA repair. Marginal improvements in survival (~2 months with temozolomide) are achieved. Bevacizumab is also given during palliative care but has shown no survival benefit.[184] Alkylating agents are used as an adjuvant treatment with radiotherapy, since their mode of action is to prevent DNA repair.

Appendix 4: Relevant Clinical Trials

A4.1 Intraoperative Radiotherapy for Glioblastoma

With respect to glioblastoma, IORT is currently under phase III of clinical trials, known as INTRAGO: Intraoperative Radiotherapy in Newly-Diagnosed Glioblastoma.[237,239,240,243] Phases I and II of the INTRAGO trial were introduced in 2014 and published in 2019, with the primary goal of establishing the maximum safe and tolerable radiation dose of kV X-rays that could be administered for glioblastoma; doses between 20 and 40 Gy were studied.[239,573] As such, the INTRAGO trial is based on LEX-IORT; electron beam IORT for glioblastoma had previously demonstrated worse outcomes than conventional radiotherapy due to insufficient coverage of the tumor bed.[245] Additionally, the goal was to evaluate the overall and progression-free survival when this technique was incorporated into the standard treatment regimen. Notably, it is the first IORT trial since the addition of temozolomide was widely adopted as the standard of care (Stupp protocol); there is hope that the effects of both therapies together may further potentiate the treatment. The trial was based on findings from the TARGIT (Targeted Intraoperative Radiotherapy) trial for breast cancer using the same radiation instrument, the Zeiss INTRABEAM®.[574] It consisted of 15 patients treated at the University of Heidelberg Medical Center in Mannheim, Germany, and was overseen by clinicians from Mannheim, Germany, Chicago, Illinois, and Montréal, Canada.

Notably, none of the patients exhibited dose-limiting toxicity up to 40 Gy, confirming the IORT protocol was safe. No treatment related deaths occurred, and of the two patients that exhibited radiation necrosis requiring surgery, no active cancer was found upon operation. The median local progression-free survival was 17.8 months, and overall progression-free survival was 14.3 months. Notably, whereas most recurrence is observed within 2 cm of the primary tumor, all but two of the patients saw local recurrence (one of them did not receive the 60 Gy fractionated radiotherapy post-surgery). This is suggestive that IORT does effectively treat the tumor margin. As mentioned in Section 3.1, the median *overall* survival of glioblastoma patients is 16-18 months, underscoring the impressive length of progression-free survival attained in this study (approximately 3 times longer than the standard treatment).[239] However, the average overall

survival was 17.8 months, due to several of the patients exhibiting distant tumor recurrence in other regions of the brain. The INTRAGO trial is currently at phase III and actively recruiting patients according to its listing on ClinicalTrials.gov (INTRAGO-II Clinical trial identifier NCT02685605).

Subsequently, the same technique (and same instrumentation) has been used in several international studies in China, Peru, Germany, and the United States on hundreds of patients with primary, recurrent and metastatic brain cancer.[240,243] These studies have shown similar promising results to the initial INTRAGO trial, with longer local and distant progression-free survival times; an estimated overall survival rate of 20.5% at 4 years post-treatment was reported for the primary glioblastoma study; a larger clinical trial is underway as reported by the authors. In 2017, the German Society for Radiation Oncology (DEGRO) decreed 50 kVp IORT with the INTRABEAM® to be the standard of care for resectable metastatic brain cancer.[238] However, all of the reports mention distant progression. As such, there is still a need to improve treatment outcomes despite the favorable advancements demonstrated.

A4.2 NBTXR3 Clinical trials

As of 2023, there are six clinical trials under active recruitment for NBTXR3® (trade name Hensify®), one active trial not recruiting, and two completed trials (NCT01433068, NCT02379845). In the completed phase II/III trial, for soft-tissue sarcoma, the radiotherapy prescribed was 50 Gy delivered in 2 Gy fractions as either 3D conformal or intensity-modulated radiotherapy. NBTXR3® was administered only one time, 1-5 days before the start of radiotherapy, at a dose of 10% of the tumor volume *via* intratumoral injection (initial concentration of 53.3 g/L).[575] The trial was completed across 11 countries in Europe and Asia, with 87 patients being given the full prescribed treatment. 19% of the patients given the treatment exhibited a complete response to the treatment (< 5 % residual cancer cells) versus the 9% receiving standard care (radiotherapy alone). NBTXR3® is currently under review by the FDA and awaiting final approval for use in Head and Neck cancer, and the clinical trials have shown clinical activity and safety of it across multiple solid tumor types, including *in vitro* trials in five glioblastoma lines.[576,577] Notably, the executioners of the trial suggest that all patients with solid tumors eligible for pre-operative radiotherapy may benefit from its use, but do not specify why it would not be

useful for post-operative radiotherapy.[575] Since pre- and post-operative radiotherapy generate similar survival rates in soft-tissue sarcoma patients, the choice for pre-operative radiotherapy appears to be based on clinical evidence of better long-term outcomes and not based on the use of the nanoparticles.

A4.3 AGuIX Clinical trials

The first AGuIX® clinical trial, Nano-RAD (NCT02820454), was completed in 2019 and, relevant to this thesis, was indicated for the treatment of multiple brain metastases.[271] It was studied in the context of whole brain radiotherapy, owing to the treatment of multiple tumors simultaneously. A total dose of 30 Gy across 10 sessions was performed, with an intravenous injection of the nanoparticles four hours prior to the radiotherapy session. 13 out of 14 patients achieved a positive clinical outcome, with either a reduction of tumor volume or a stabilization of disease progression. As of 2023, there are six clinical trials for AGuIX underway, currently all are recruiting patients and one trial, Nano-GBM (NCT04881032) is a phase I/II trial specified for patients with primary glioblastoma. The mode of action of AGuIX® is through the Auger effect, as previously described.[578] Notably, *in vitro* studies of AGuIX have demonstrated non-specific accumulation in the cytoplasm and no accumulation in the nucleus. The apparent clinical success of these nanoparticles thus far suggests it is not necessary for nanoparticles to reach the nucleus to achieve increased DNA damage *via* the Auger cascade.[579] This is an important demonstration, as there is a common presupposition within the nanomedicine community that it is essential for all nanoparticles to exit the lysosomes or that a specific organelle must be targeted to achieve a clinically-relevant therapeutic effect.[367]

Appendix 5: Clinically approved photosensitizers

For a photosensitizer to be effective and clinically-relevant, there are several properties that clinicians agree it should exhibit.[283,297,309,318] The most obvious property perhaps is that the photosensitizer should generate a powerful photodynamic effect. The type II photoreaction is generally more lethal, thus a high singlet oxygen yield is desired (number of $^1O_2$ molecules produced per photon absorbed). There are a huge number of photosensitizers that generate a powerful photodynamic reaction; it is usually the remaining parameters which preclude their translation to the clinic.[297] The efficacy of the photodynamic effect should be reliable across different patients and tumor locations for the same tumor type, which relies upon its uptake and distribution properties. It should also be excited in the optical window so that sufficient tissue penetration can be achieved to yield a therapeutic effect. Ideally, it has either rapid pharmacokinetics or is selectively uptaken by the tumor, such that the patient does not experience prolonged systemic photosensitivity but not such fast clearance that it is impractical to use in the clinic. It should also not cause toxicity in the absence of irradiation, and its photoproducts should also be non-toxic. Finally, with respect to commercial translation, it should be reliably and easily synthesized, have acceptable storage stability and ideally be a singular pure substance that is well characterized.[309]

The clinically-approved photosensitizers have similar absorption profiles, with a strong absorption band around 400 nm called the Soret band and weaker Q-bands throughout the visible-red region. They are all excited with red light, and thus achieve reasonable tissue depth penetration in the optical window. The major downfall of Photofrin® is it's low absorption coefficient and its extremely slow and unspecific pharmacokinetics; patients are rendered photosensitive for months after treatment.[309] Foscan® also causes prolonged photosensitivity for weeks, but in contrast to Photofrin®, it is extremely potent and was rejected by the FDA because of the high likelihood of accidental damage to healthy tissues, but is used regularly in Asian and European markets. Foscan® is thus a good example that a strong photodynamic effect is not the only predictor of clinical success. Verteporfin®, and Laserphryin® exhibit advancements such as photosensitivity reduced to days rather than weeks, and are less powerful than Foscan®. Tookad® is a particularly interesting photosensitizer that has only been approved for use in the past five years; it was also declined by the FDA for failing to achieve a clinical benefit greater than other options, but is

approved in other markets.[299,310] Despite failing to gain approval by the FDA, it exhibits many benefits[283,309,580]: it is activated at 762 nm and thus has improved depth penetration relative to older photosensitizers, is rapidly eliminated by the body within a few hours so no prolonged skin sensitivity is observed, and interestingly, its primary mechanism of action is via the type I mechanism rather than type II.

Appendix 6: Additional Data

A6.1 Spectrum corrected for the sensitivity of the detector

Intensity correction was performed using a deuterium/halogen lamp from Ocean Optics. The NIST-calibrated spectrum file provided by the manufacturer was used to generate a correction factor as a function of wavelength. This was done by comparing to the emission spectrum of the same lamp as obtained using the same spectrometer, grating and blazing wavelength used to obtain the emission spectrum.

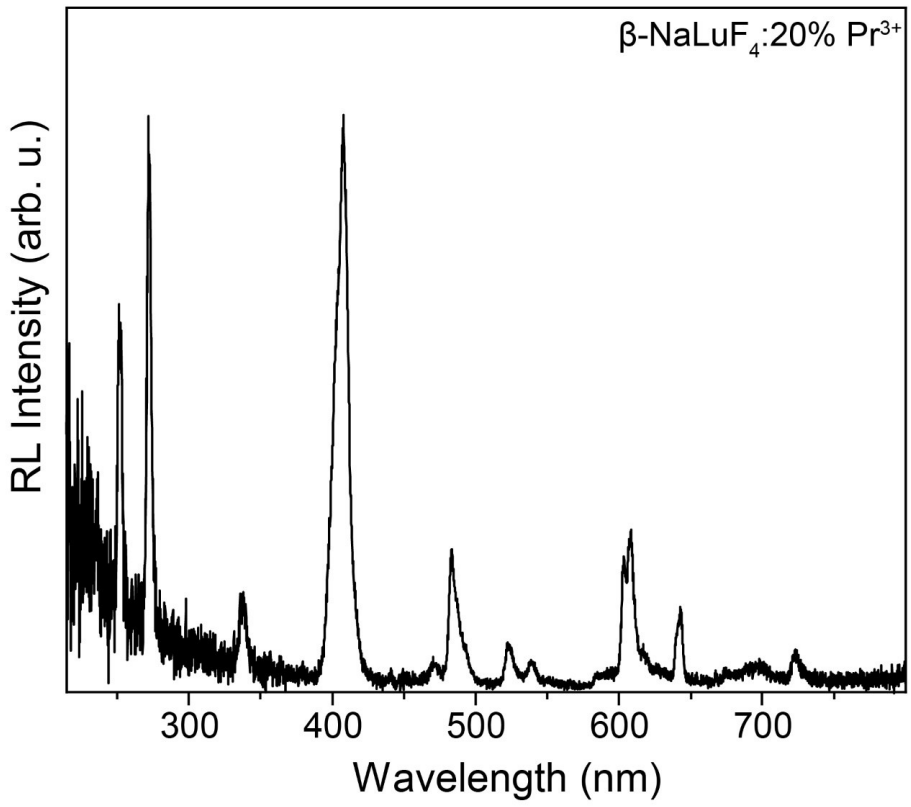

Figure 66. Radioluminescence spectrum of $NaLuF_4$: 20% Pr^{3+} nanoparticles that has been corrected for the spectral sensitivity of the detector. The original spectrum is displayed in Figure 20, section 7.1.

A6.2 Amptek MINI-X output spectrum

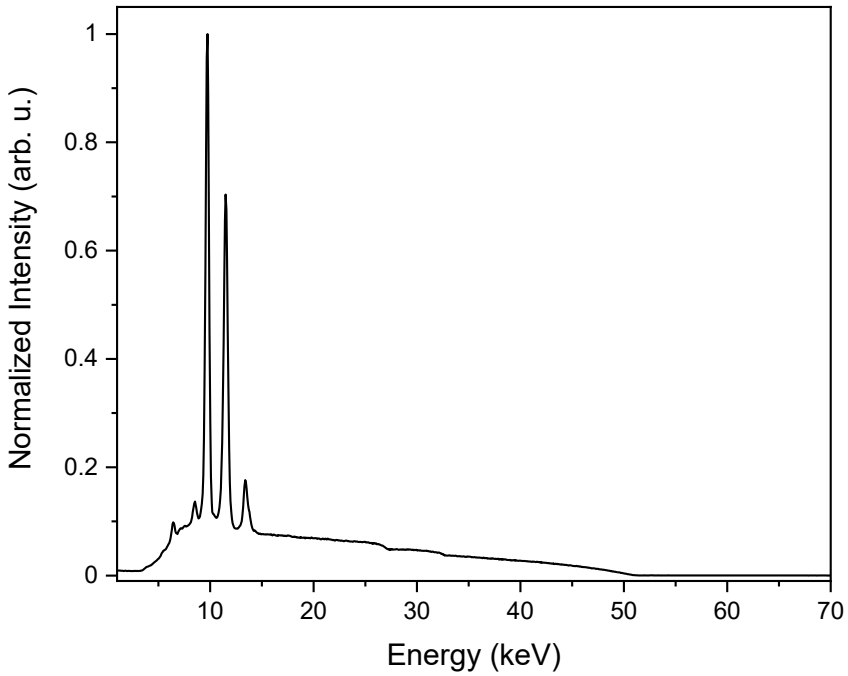

Figure 67. Emission spectrum of the Amptek Mini-X portable X-ray source (Au target, uncollimated, unfiltered beam, 50 kVp, 80 μA). Spectrum provided by the manufacturer.

A6.3 Raw survival fraction data

Table 20. Raw survival fraction (SF) values from the clonogenic assays used to generate Figure 62 in Section 8.9.

0 μg/mL RLNPs				
Dose (Gy)	**(-) 5-ALA**		**(+) 5-ALA**	
	SF (%)	**% Uncertainty**	**SF (%)**	**% Uncertainty**
0	100.00	0.00	100.00	0.00
2	75.17	11.09	60.78	17.43
5	60.43	6.93	42.41	11.89
10	42.32	10.02	28.41	10.43
20	14.38	2.49	13.14	4.96

50 µg/mL RLNPs				
Dose (Gy)	**(-) 5-ALA**		**(+) 5-ALA**	
	SF (%)	**% Uncertainty**	**SF (%)**	**% Uncertainty**
0	100.00	0.00	100.00	0.00
2	63.85	10.86	50.75	8.51
5	38.59	13.42	26.31	6.46
10	22.73	5.46	11.61	1.65
20	6.19	1.66	3.54	1.38
100 µg/mL RLNPs				
Dose (Gy)	**(-) 5-ALA**		**(+) 5-ALA**	
	SF (%)	**% Uncertainty**	**SF (%)**	**% Uncertainty**
0	100.00	0.00	100.00	0.00
2	44.79	9.44	25.45	3.48
5	20.97	4.05	11.47	1.54
10	10.98	1.76	4.97	2.06
20	3.41	0.55	2.07	0.46
200 µg/mL RLNPs				
Dose (Gy)	**(-) 5-ALA**		**(+) 5-ALA**	
	SF (%)	**% Uncertainty**	**SF (%)**	**% Uncertainty**
0	100.00	0.00	100.00	0.00
2	20.84	4.46	14.06	2.25
5	7.52	1.63	5.33	0.75
10	2.09	0.53	1.06	0.19
20	0.52	0.13	0.38	0.04

Appendix 7: Literature values – enhancement factors

Table 21 outlines the enhancements reported in the literature and relevant experimental details for ease of comparison to the data in Chapter 7.

Table 21. Summary of the reported enhancement factors for radiosensitizers, self-sensitized X-PDT agents and traditional X-PDT agents.

Type[A]	NP composition	PS	Cell line	Radiation	Enhancement[B]	Ref
RS	NBTXR3® (HfO_2)	--	T98G	200 kVp	RER_{2Gy} 1.22	[577]
RS	AGuiX® (Gd-DOTA-PS)	--	Panc1, HeLa	220 kVp	DMR_{20} 1.31 SER 1.46	[515,578]
RS	AuNP	--	U251	6 MeV	SER 1.23	[512]
RS	AgNP	--	U251	6 MeV	SER 1.64	[512]
Self	DPB-Hf	DPB linker	CT26	120 kVp	DMR_{20} 2.82	[341]
Self	DPB-Hf	DPB linker	SQ20B	120 kVp	DMR_{20} 2.36	[341]
Self	DPB-Hf	DPB linker	HeLa	120 kVp	DMR_{20} 2.83	[341]
RS	HfO_2	--	CT26		DMR_{20} 1.02	[341]
RS	HfO_2	--	SQ20B		DMR_{20} 1.275	[341]
RS	HfO_2	--	HeLa		DMR_{20} 1.13	[341]
Self	DBA-Hf	DBA linker	HeLa	120 kVp	DMR_{20} 1.56	[341]
Self	DBA-Hf	DBA	MC38	250 kVp	DMR_{10} 1.50	[360]
Self	Hf-DBB-Ru	DBB	MC38	250 kVp	DMR_{10} 2.68	[360]
X-PDT	$Gd_2(WO_4)_3:Tb^{3+}$	MC540	4T1	160 kVp	DMR_{10} 1.43	[352]
X-PDT	$NaCeF_4:Gd^{3+},Tb^{3+}$	RB	A549	160 kV	RER_{6Gy} 5.96	[47]
X-PDT	$SAO:Eu^{2+}/mSiO_2$	MC540	U251N	50 kVp	DMR_{10} 1.67	[350]
X-PDT	$mSiO_2:Mn^{2+},Zn^{4+}$	RB	U87-MG	50 kVp	DMR_{10} 3.1	[353]
X-PDT	CsI(Na)@MgO	5-ALA	4T1	320 kVp	DMR_{10} 1.328** DMR_{10} 1.537	[339]

X-PDT	$CaWO_4$	BR	HN31	320 kVp	DMR_{10} 1.39	[581]
RS	$TiO_4:Sm^{3+}$	--	A549	6 MV	SER 1.21	[582]
X-PDT	Tb^{3+}-AGuIX	P1	U251-MG	320 kVp	RER_{2Gy} 1.54	[273]

PS: photosensitizer, NP: nanoparticle, AuNP: gold nanoparticle, AgNP: silver nanoparticle, RB: Rose Bengal, 5-ALA: 5-aminolevulinic acid, BR: bilirubin, DBB: bis (2,2'-bipyridine)(5,5'-di(4-benzoato)-2,2'-bipyridine, DBA: 2,5-di(p-benzoato)aniline, P1: 5-(4-carboxyphenyl succinimide ester)-10,15,20- triphenyl porphyrin

[A]RS: non-luminescent radiosensitizer, Self: luminescent radiosensitizer or PS is a structural component, X-PDT: a luminescent nanoparticle and PS combination

[B]RER_x: radiation enhancement ratio at X Gy, SER: mean inactivation dose-derived sensitizer enhancement ratio, DMR_x: dose modifying ratio at x% survival

**value reported for RLNP-only with no photosensitizer